THE THERMOPHYSICAL PROPERTIES OF GASES DETERMINED USING AN ANNULAR ACOUSTIC RESONATOR

A thesis submitted to the

University of London

for the Degree of Doctor of Philosophy

by

Amanda Jane Buxton.

Department of Chemistry

Christopher Ingold Laboratories

20 Gordon Street

University College London

London WC1H 0AJ

August 1997

ABSTRACT

A novel annular acoustic resonator was constructed for measurements of the speed of sound in gases at pressures below 1 MPa. The resonator was designed to allow measurements of the speed and absorption of sound at low pressure in gases with large bulk viscosities. Measurements in propene, for which the speed of sound is known, served to characterise the geometry of the resonator and provide a test of the acoustic model for the system. A detailed description of the resonator which has an outer radius of 140 mm is given. The large radius provides low frequency resonance modes that minimise acoustic losses in the bulk of the gas. Three substances were studied: trifluoromethane, sulfur hexafluoride and a binary mixture consisting of methane and ethane with mole fraction composition {0.85 CH_4 + 0.15 C_2H_6}. Measurements were conducted over the temperature range 230 to 350 K, and the results analysed to obtain perfect gas heat capacities and second acoustic virial coefficients. The heat capacity data are compared to literature sources. Values for the second *(p,V,T)* virial coefficients were obtained from the second acoustic virial coefficients and the results are compared with previous determinations. Analysis of the acoustic loss mechanisms allows the shear viscosity, thermal conductivity and bulk viscosity of the gas to be estimated. The values obtained do not have the accuracy that may be achieved using specialised techniques and a comparison is made where data is available. The estimates of the thermal conductivity and shear and bulk viscosities provide a new self consistent method for the analysis of the acoustic results which does not rely on literature values for the transport coefficients. Where possible vibrational relaxation times are evaluated from the bulk viscosity and are compared with results from other sources.

ACKNOWLEDGMENTS

I would like to thank my supervisor Dr M B Ewing for giving up his Monday evenings over the past year, and for the guidance and support he has given me during all my years at University College London.

I would like to thank B.P. for the award of a Research Scholarship. Much of the apparatus was expertly fabricated by Mr D Morfett whom, together with his colleagues in the mechanical and electronics workshops at U.C.L. I would like to thank.

Many thanks are due to all my friends and family for all the good times shared, and all the support given during the process of writing this thesis. Special thanks are due my parents and Chris for their constant understanding, encouragement and belief in me.

CONTENTS

List of Tables

List of Figures

1. INTRODUCTION

1.1. Introduction

The fundamental relation between the thermodynamic properties of a fluid and the speed of sound u is

$$u^2 = \left(\frac{\partial p}{\partial \rho}\right)_S, \tag{1.1}$$

where p is the pressure, ρ the mass density and S the entropy. It is convenient to express equation (1.1) in terms of an isothermal and either an isobaric or isochoric partial derivative[1]. Using standard thermodynamic manipulations this leads to

$$u^2 = \left[\left(\frac{\partial \rho}{\partial p}\right)_T - \left(\frac{T}{\rho^2 c_p}\right)\left(\frac{\partial \rho}{\partial T}\right)_p^2\right]^{-1}, \tag{1.2}$$

and

$$u^2 = \left[\left(\frac{\partial \rho}{\partial p}\right)_T - \left(\frac{T}{\rho^2 c_V}\right)\left(\frac{\partial p}{\partial T}\right)_\rho^2\right]^{-1}, \tag{1.3}$$

where T is the thermodynamic temperature, c_p the isobaric and c_V the isochoric specific heat capacity. The heat capacity c_p may be expressed as

$$c_p(T,p) = c_p^{\mathrm{r}}(T) + \int_{p^{\mathrm{r}}}^{p} (\partial c_p/\partial p)_T \, dp \tag{1.4}$$

where c_p^{r} is the value of c_p at the reference pressure p^{r} and $(\partial c_p/\partial p)_T$ is given by

$$(\partial c_p/\partial p)_T = -T\left(\partial^2 \rho^{-1}/\partial T^2\right)_p. \tag{1.5}$$

If the reference pressure is taken as zero, c_p^{r} becomes the specific heat capacity of a perfect gas denoted by c_p^{pg}. In a similar way the isothermal partial derivative of c_V with respect to density may be written as

$$(\partial c_V/\partial \rho)_T = -\left(T/\rho^2\right)\left(\partial^2 p/\partial T^2\right)_\rho . \tag{1.6}$$

The expressions above are required to relate u to an equation of state of the form $\rho = \rho(T,p)$ or $p = p(T,\rho)$.

For a perfect gas, the mass density is simply Mp/RT where M is the molar mass and R the gas constant. When substituted into equation (1.2) this gives

$$u^2 = RT\gamma^{\mathrm{pg}}/M, \tag{1.7}$$

in which the ratio of heat capacities γ^{pg} may be written as

$$\gamma^{\mathrm{pg}} = C_{p,\mathrm{m}}^{\mathrm{pg}}/\left(C_{p,\mathrm{m}}^{\mathrm{pg}} - R\right). \tag{1.8}$$

This is the perfect gas limit of $C_{p,\mathrm{m}}/C_{V,\mathrm{m}}$ where $C_{p,\mathrm{m}}$ and $C_{V,\mathrm{m}}$ denote the molar heat capacities $C_{p,\mathrm{m}} = c_p M$ and $C_{V,\mathrm{m}} = c_V M$ respectively. Equation (1.7) is exact only in the limit as $p \to 0$ for real gases and, at higher pressures there are departures from the simple model. Then, equation (1.7) can be written in terms of an expansion in powers of pressure:

$$u^2 = A_0(T) + A_1(T)\,p + A_2(T)\,p^2 + \cdots, \tag{1.9}$$

where

$$A_0 = RT\gamma^{\mathrm{pg}}/M \tag{1.10}$$

which may be obtained by extrapolation of sound speeds obtained at a number of pressures along an isotherm to the limit as $p \to 0$. Once A_0 is known one of the quantities on the right hand side of (1.10) can be determined provided the others are known. For example, the molar heat capacities C_p^{pg} and C_V^{pg} can be obtained through the relation

$$C_p^{\mathrm{pg}}/R = \gamma^{\mathrm{pg}}/\left(\gamma^{\mathrm{pg}} - 1\right). \tag{1.11}$$

C_p^{pg} can be determined to a precision of better than 0.01 %[2],[5].

1.2. Determination of (p, V, T) Virial Coefficients from the Speed of Sound

Accurate measurement of $\rho(T,p)$ is difficult in experimental thermodynamics and accurate prediction is still not possible from statistical mechanics. Acoustic

measurements provide a route to this quantity as equation (1.1) shows that ρ should be obtainable from an integration of $u^{-2}(T,p)$. The most common method is to postulate an explicit functional form for the equation of state that contains a set of adjustable parameters which may be optimized using non-linear fitting procedures. Often in constructing an equation of state, T and the amount of substance density $\rho_n = 1/V_{\mathrm{m}}$ are chosen as the independent variables in place of $T$and p. The coefficients B, C in the virial equation of state

$$p/\rho_n RT = 1 + B(T)\rho_n + C(T)\rho_n^2 + \cdots \tag{1.12}$$

are related by the theory to the functions that describe the intermolecular potential energy functions of molecular clusters containing two, three, $\cdots$ molecules. The second virial coefficient B is related to the pair potential function U, and, when that depends only on the distance r between the molecules, B is given by[6]

$$B = 2\pi L \int_0^\infty \left[1 - \exp\left(-U/kT\right)\right] r^2 dr, \tag{1.13}$$

where L is the Avogadro constant and k is the Boltzmann constant.

The speed of sound may also be written as a power series in the density,

$$u^2 = \left(RT\gamma^{\mathrm{pg}}/M\right)\left(1 + \beta_{\mathrm{a}}\rho_n + \gamma_{\mathrm{a}}\rho_n^2 + \cdots\right) \tag{1.14}$$

in which the acoustic virial coefficients β_{a}, γ_{a} $\cdots$ are also functions of temperature and are related to the corresponding virial coefficients by second-order differential equations. The second acoustic virial coefficient is given by

$$\beta_{\mathrm{a}} = 2B + 2T\left(\gamma^{\mathrm{pg}} - 1\right)\left(dB/dT\right) + T^2\left(d^2B/dT^2\right)\left[\left(\gamma^{\mathrm{pg}} - 1\right)^2/\gamma^{\mathrm{pg}}\right], \tag{1.15}$$

and the third by

$$\begin{aligned}
\gamma_{\mathrm{a}} \;=\; & \left[\left(\gamma^{\mathrm{pg}} - 1\right)/\gamma^{\mathrm{pg}}\right] \times \\
& \left[B + \left(2\gamma^{\mathrm{pg}} - 1\right) T\left(dB/dT\right) + \left(\gamma^{\mathrm{pg}} - 1\right) T^2\left(d^2B/dT^2\right)\right]^2 \\
& + \left(1/\gamma^{\mathrm{pg}}\right) \times \left\{\left(1 + 2\gamma^{\mathrm{pg}}\right) C + \left[\left(\gamma^{\mathrm{pg}}\right)^2 - 1\right] T\left(dC/dT\right)\right. \\
& \left. + \frac{1}{2}\left(\gamma^{\mathrm{pg}} - 1\right)^2 T^2\left(d^2C/dT^2\right)\right\}.
\end{aligned} \tag{1.16}$$

The coefficients of (1.14) and (1.9) may be related:

$$\left.\begin{aligned}
\left(M/\gamma^{\mathrm{pg}}\right) A_1 &= \beta_{\mathrm{a}} \\
\left(M/\gamma^{\mathrm{pg}}\right) A_2 &= \left(\gamma_{\mathrm{a}} - B\beta_{\mathrm{a}}\right)/RT.
\end{aligned}\right\} \tag{1.17}$$

If the pair potential is known then both β_a and B can be determined from equations (1.13) and (1.15). Alternatively β_a can be used to provide information about $U(r)$. The inversion procedure by which $U(r)$ can be obtained directly from $B(T)$ has been modified to allow its calculation from $\beta_a(T)$[7]. Quite crude models of $U(r)$ with parameters determined using β_a have been found to give excellent results. Not only do they fit the data within experimental error, but several different models give the same values of B even when extrapolated to temperatures well above the experimental range[8],[2]. This method is usually employed in practice as inversion requires results over a very wide temperature range and is mathematically unstable. In principle, the third virial coefficient may also be determined from $U(r)$, however it is more sensitive to the form of the potential function and is also necessarily affected by three molecule interactions. Hence empirical pair potentials that give β_a and B to high accuracy cannot be relied upon to do the same for γ_a and C.

Conventionally, virial coefficients are determined from measurements of the volumes occupied by a given mass of gas at various temperatures and pressures[9]-[17]. Such measurements are subject to systematic errors, some of which may be reduced by recourse to more elaborate experimental techniques[18]. Gas adsorption becomes a significant source of error when the experimental pressure is a large fraction of the vapour pressure[14]. While careful (p, V_m, T) measurements can yield accurate virial coefficients at high reduced temperatures, it has proved very difficult to obtain results free of systematic errors at low reduced temperatures where gas adsorption is a serious problem. (p, V_m, T) methods are discussed in greater detail in chapter 3. Since the speed of sound is formally independent of the amount of substance, acoustics allows the precise determination of β_a at low reduced temperatures where (p, V_m, T) methods are unreliable. Speed of sound experiments are subject to very different systematic errors, which may be identified and greatly reduced leading to very accurate results[5],[8],[19]-[22].

1.3. Other Applications of Speed of Sound Measurements

Speed of sound measurements have many applications, and this work is primarily concerned with utilising sound speeds to yield precise equation of state

information[1] and perfect gas heat capacities. A third application is primary thermometry[21] where the ratio of $A_0(T)$ to that at the triple point of water $A_0(T_t)$, where $T_t = 273.16$ K, for a monatomic gas will give T/T_t without $R\gamma^{pg}/M$ being required. Alternatively using a gas for which γ^{pg} and M are known to sufficient accuracy, $A_0(T_t)$, serves to define the gas constant, R[22]. For a binary gaseous mixture, the mole fraction x may be determined from $A_0(T)$ provided that C_p^{pg} is known for each component. Speed of sound measurements have been used to monitor composition in experiments designed to study the ordinary and thermal diffusion coefficients in binary mixtures[23]. Another application is in the determination of gas-liquid phase boundaries[24]. More importantly, the absorption of sound in the bulk of a gas depends on kinetic effects involving the distribution of energy on a molecular scale, and, under favorable conditions can provide a measure of one or more time constants characterising molecular processes[25], in particular, vibrational relaxation times[8]. Another field of interest is in the estimation of thermal conductivities and shear viscosities. These may sometimes be inferred from the phase changes and energy losses that accompany the reflection of sound waves from a boundary between a gas and a solid surface. These last two effects have been investigated for the gases under study in this work.

(u, T, p) measurements may be used to evaluate any proposed form of the equation of state $V_m = V_m(p, T)$ or assist in optimising an existing (p, V_m, T) surface for a particular application[28]. Equations of state are utilised industrially in the calculation of mass flow rates from sonic nozzle flow meters[29].

1.4. Determination of the Speed of Sound

The resonance technique may be used to measure the speed of sound. This involves exciting a sound field within a cavity of known geometry and measuring the frequencies of the normal modes. Such methods involving the use of a continuous sound source depend on standing waves being formed inside an acoustic cavity and are therefore effective when the walls reflect sound efficiently. This occurs when there is a large difference between the acoustic impedances of the wall and fluid as is the case for metal walled enclosures filled with gas. The reflection coefficient is much lower when the fluid under study is in a liquid state and so these methods

are best applied to gases up to pressures of the order of 10 MPa. This discussion is limited to fixed volume cavity resonators where the normal modes measured are usually resolved from one another, and which are advantageous for low frequency measurements of sound speed and absorption. Until a few years ago, most speed of sound measurements were performed using cylindrical interferometers. For most applications, these have since been superseded by spherical resonators as it has been demonstrated that these afford numerous advantages[5],[20]. When the gas under study has a large absorption coefficient the long pathlength, low frequency annular resonator discussed here provides the most accurate results.

1.4.1. The Spherical Geometry

The spherical geometry is utilized in most studies due to the existence of the radially symmetric (radial) modes which are characterised by the absence of viscous damping at the resonator wall and by resonance frequencies which are insensitive to geometric imperfections of the cavity[30],[31]. These factors, and the favorable surface area to volume ratio leads to the least thermal damping and hence the sharpest resonances under most circumstances compared with resonators of other geometries. This allows the most accurate determination of the resonance frequencies, and thus the speed of sound. A further advantage of the spherical geometry lies in the possibility of solving the shifts in frequency due to coupling of the motion of the gas and cavity wall[32]. Another advantage is that if the gas inlet tube has length a, (where a is the radius of the sphere), this causes the minimum perturbation to the normal modes, which lie approximately $\left(n-\frac{1}{2}\right)\pi$ apart, interspersed by the tube resonances[29]. Using the spherical geometry it is also possible to position the transducers to exclude some resonances by placing them at nodal planes, thereby reducing some of the unwanted effects caused by overlapping modes.

1.4.2. The Cylindrical Geometry

Compared with spherical resonators, cylinders are easier to fabricate and offer an extra degree of freedom in the form of the ratio b/L (where b is the radius of the cylinder and L its length) which can be chosen to suit a particular application[26]. However, due to the less favourable surface area to volume ratio and both viscous

Figure 1.1: A cylindrical annulus with inner radius a, outer radius b and length L.

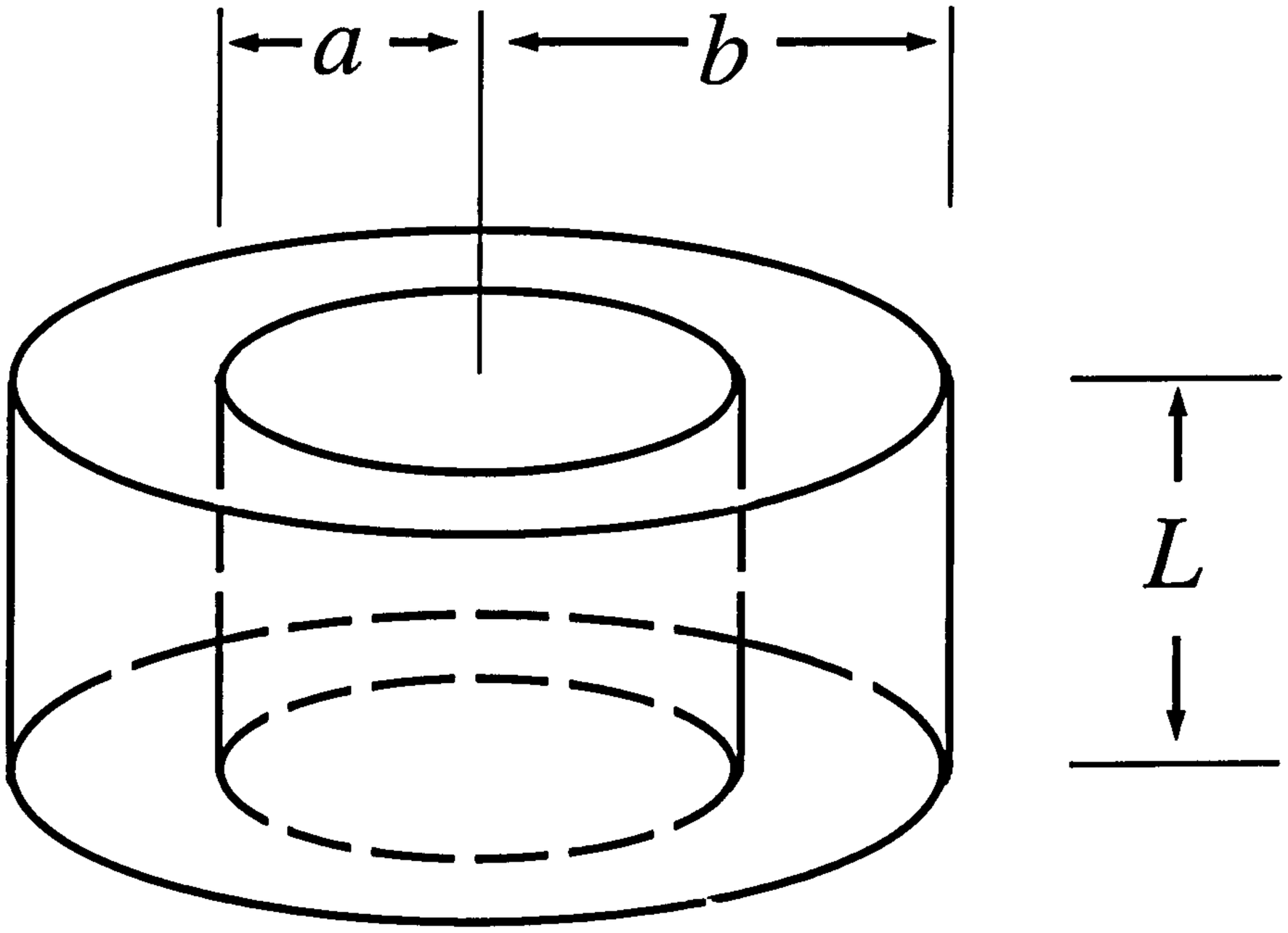

and thermal damping at the resonator wall, the resonances will not be as sharp as in a spherical resonator with the same volume. In the spherical geometry, the resonances are radial, azimuthal or mixed radial-azimuthal. In the cylindrical geometry, longitudinal resonance modes are also possible, so radial, azimuthal, longitudinal, or any of the types of mixed modes may be chosen for study. The location of the transducers will depend on the symmetry of the modes of interest. For longitudinal modes all positions on the end plates are equally efficient and a source located in the centre of the end plate will couple effectively to all axisymmetric modes including all radial, and mixed radial-longitudinal modes but not azimuthal modes. The cylindrical geometry is particularly suited to the determination of the thermal conductivity and shear viscosity[27] as the existence of modes of differing symmetry allows the contributions of the thermal and viscous loss mechanisms at the cavity wall to be separated.

1.4.3. The Annular Geometry

Compared to the cylinder, a cylindrical annulus as shown in figure (1.1) has another degree of freedom in the radius ratio $a/b = \zeta$, but due to the larger surface area to volume ratio, the resonances are correspondingly broader. Yet,

under some conditions the annular geometry becomes favourable; for example, for low pressure measurements of the speed and absorption of sound in relaxing gases such as CO_2. For relaxing gases the time scales of the processes that control the distribution of energy on a molecular scale are comparable with the period of the sound wave within the acoustic cavity. This leads to a large bulk viscosity η_b, resulting in a large absorption coefficient α at low pressures because α is proportional to η_b/ρ. The contribution is frequency dependent because α is also proportional to ω^2, and thus the lower the frequency the sharper the resonance modes. Low frequencies require a long pathlength, and consequently the sphere is not a viable geometry as it would have to be very large for the modes to be resolved at low pressures. The temperature of such a large sphere could not be controlled adequately. A long thin cylinder in which the ratio L/b is such that the first few longitudinal modes would occur at lower frequencies than any other class of modes is a possible solution, but in practice this would have had a very poor surface area to volume ratio causing the modes to be difficult to resolve. Another possibility is a short cylinder of large radius in which the first two azimuthal modes have the lowest frequencies and the ratio L/b is chosen such that the first few radial, azimuthal and mixed radial-azimuthal modes occur at lower frequency than the longitudinal modes. However a problem arises due to overlap of various modes, resulting in it not being possible to resolve key resonances. However in the annulus there is another degree of freedom in the radius ratio ζ, (it can be varied between 0 and 1) and the larger the value of ζ the longer the pathlength of the azimuthal modes and the shorter the pathlength of the radial modes. With this scenario, the first few azimuthal occur at lower frequencies than any of the radial modes. In fact, ζ may be chosen such that the first radial mode lies between two of the azimuthal modes.

An annular resonator with an outer radius $b = 140$ mm, an inner to outer radius ratio $\zeta = a/b = 0.532$, and length $L = 59$ mm has been designed and constructed for this work. In this resonator the first five azimuthal modes occur at lower frequency than the first radial mode. This allows the study of relaxing gases at pressures a factor of ten lower than for a practical sphere. Low pressure measurements are particularly important as the second acoustic virial coefficient is given by the limiting slope of the speed of sound results as the density tends to

zero, and the heat capacity is calculated from the intercept of the speed of sound results.

1.5. The Acoustic Model

The first order perturbation theory developed by Mehl and Moldover[5] for the spherical cavity to make corrections for the presence of the thermal and viscous damping at the cavity wall, and openings in the wall of the resonator has been extended to the annular geometry. Using this method the observed frequency f of the normal mode is shifted from the perfect annulus value given by

$$f = \left(\frac{u}{2\pi}\right)\sqrt{\left(\frac{l\pi}{L}\right)^2 + \left(\frac{\chi}{b}\right)^2}, \tag{1.18}$$

where u is the speed of sound, l is an integer, and χ is an eigenvalue known exactly but dependent on the ratio ζ. In the perturbation model the frequency is represented by the complex quantity

$$F = f + ig = \left(\frac{u}{2\pi}\right)\sqrt{\left(\frac{l\pi}{L}\right)^2 + \left(\frac{\chi}{b}\right)^2} + \sum_j (\Delta f + ig)_j\,, \tag{1.19}$$

in which the sum represents the contributions of the various perturbations to the resonance frequencies and losses observed in the cavity. These are discussed in greater detail in the following chapter.

The second order terms and smaller corrections arising from, for example the slits round the transducer housings were neglected as the magnitude of such effects was negligible when compared to the uncertainty in the calculated first order effects. It is not feasible to calculate the effect of the motion of the cavity wall on the acoustic modes for an annular resonator, as the modes of motion of an annular shell are not known. Additionally, there is no *a priori* way of calculating the coupling constant due to the differing symmetry of the motion of the gas and shell. For a sphere the correction is most simply the case of a breathing motion of the shell which has the same symmetry as the radial modes. This correction is small at low pressures when the frequency of the shell motion is large compared to that of gas, as is the case in the sphere. A similar frequency ratio was expected for the annulus, but unfortunately a shell resonance that overlapped the low order azimuthal modes was detected. The effect of this shell resonance and its

effect on the results is discussed in detail in later chapters. In practice higher order azimuthal modes were also measured for which the shell motion was not important. As for spherical resonators, the gain inherent in the system allowed the use of small inefficient transducers in the resonator wall, thus minimising the perturbation to the resonator/gas boundary.

Measurements of the resonance frequency f for a particular mode yields uk which, as k is given by

$$k = \frac{1}{2\pi}\sqrt{\left(\frac{l\pi}{L}\right)^2 + \left(\frac{\chi}{b}\right)^2} \tag{1.20}$$

depends on the geometry of the cavity. Thus in order to make absolute measurements of the speed of sound u, a knowledge of the geometric parameters ζ, b and L as functions of T and p is required. $\{(uk), T, p\}$ measurements suffice to determine gas imperfections in the form of an equation of state but a knowledge of ζ, b and L at $(T, p = 0)$, allows the evaluation of $C^{\mathrm{pg}}_{p,\mathrm{m}}$. When heat capacity information is combined with equation of state data, it is possible to calculate any thermodynamic quantity for a pure gas or gas mixture.

The values of ζ, b and L at $(T, p = 0)$ can be obtained from dimensional microwave measurements or by calibrating with a gas of known A_0 combined with the pressure dependence determined by auxiliary methods. Both methods have been utilized for spherical resonators. The frequencies of the microwave resonance modes are available in the literature[33] for the annular geometry, allowing the extension of this technique to cover the annular resonator. The geometry of the annular cavity was calibrated using propene as it had sharper resonance modes than the more usual choice of Ar (for which γ^{pg} is known), giving more accurate values for f and leading to more reliable estimates of ζ, b and L.

1.6. Results Reported in this Work

Measurements at pressures up to 1 MPa are reported for propene, sulfur hexafluoride, trifluoromethane and the binary mixture $\{0.85\ CH_4 + 0.15\ C_2H_6\}$, of methane and ethane.

1.6.1. Results Derived from the Speed of Sound

The measurements in propene that served to characterise the resonator are discussed in detail in chapter 6 and the second acoustic virial coefficients and heat capacities obtained from the results are compared with previous measurements in chapter 8. The data on sulfur hexafluoride and trifluoromethane, yielded perfect gas heat capacities, and second acoustic virial coefficients which were used to determine B. The results are presented and a comparison is made with published work. Speed of sound data in the binary mixture yielded second acoustic virial coefficients allowing the extraction of cross and interaction virial coefficients for methane-ethane which are compared to the literature.

1.6.2. Results Derived from Sound Losses in the System

The thermal conductivity, and the viscosity of the gas under study as well as vibrational relaxation times were calculated from an analysis of the loss mechanisms operating in the system. Sound absorption and dispersion determines the breadth of the resonance modes measured in the experiment. The differing density dependencies of the loss mechanisms allows those in the bulk of gas and at the gas/metal interface at the resonator wall to be resolved. Vibrational relaxation times may be calculated from the losses in the bulk of the gas, and the thermal conductivity and shear viscosity from the losses at the cavity walls.

Transport Properties

The usual method for the analysis of acoustic measurements first calculates the contributions to the breadth of the resonances using published values for the thermal conductivities and shear viscosities. The remainder of the breadth of the resonance is then attributed to relaxation effects. In general, transport properties of fluids are difficult to measure experimentally as they describe the relations between gradients of the state variables[35]. Therefore their measurement necessitates bringing the system out of thermodynamic equilibrium. The necessary results for direct calculation of the surface loss mechanisms were not available over the whole of the experimental temperature and pressure range. As functions that adequately describe experimental data cannot reliably be extrapolated

beyond the limits of the T and p ranges quoted, a new analysis technique was developed. Earlier it was mentioned that transport properties had been calculated from acoustic measurements of modes of different symmetry in a cylindrical resonator. In this work, only the low frequency azimuthal modes were measured, hence modes having significantly different ratios of shear to thermal losses were not available. In order to obtain values for the thermal conductivity and shear viscosity, the two were coupled by approximations such as the Euken relation[34]. This method is discussed in greater depth in chapter 7.

Many specialised pieces of equipment have been designed to measure the viscosity of fluids including oscillating body viscometers, capillary viscometers, vibrating viscometers and falling body viscometers[35]. Capillary viscometers only find application for gases at high density and liquids as the pressure drop along a circular tube through which the fluid flows is measured. Falling body viscometers are based on the measurement of the time of free fall under the influence of gravity of a sphere or cylinder through the fluid of interest. Such instruments are generally not among the most accurate, but do find application at very high pressures[35].

It is the class of oscillating body viscometers that have been used with most success for measurements of the shear viscosity of gases at low pressures. Oscillating body viscometers consist of an axially symmetric body suspended from an elastic strand for which the decay of the torsional oscillations gives a measure of the fluid viscosity. The most common types are the oscillating disk and cup viscometers. The viscosity is calculated from measurements of the logarithmic decrease in the amplitude of the oscillation and the increase in its period which are due to the torque generated by the fluid on the surface of the body. The torque is generally described by a theoretical expression, but when this is unknown it may be derived from calibration procedures[36]. This type of viscometer also allows the possibility of simultaneous measurements of the fluid density[37]-[39]. Oscillating body viscometers may be configured to measure a wide range of fluid viscosities ranging from low density gases to molten ores. The accuracy of viscosity measurements for dilute gases achieved with an oscillating disk viscometer is at best 0.1 %.

Vibrating viscometers have also been utilised to measure gas viscosities, but

do not achieve the accuracy of oscillating viscometers. In vibrating viscometers, small amplitude oscillations of the body are induced electrically. There are two types; the vibrating wire viscometer[40] in which transverse oscillations of a thin metal cylinder are monitored, and the torsional quartz crystal viscometer. Such instruments find applications at very low temperatures and high pressures where their small sample volume offers advantages. For example the viscosity of He at temperatures of a few kelvins has been measured using a vibrating wire viscometer[40]-[43], and results have been achieved at pressures up to 700 MPa in liquids using a torsional crystal viscometer[35].

The thermal conductivity of fluids can be measured in two ways, via steady state and transient techniques. Steady state techniques are based on the measurement of the heat flux required to maintain a temperature difference between two surfaces immersed in the fluid. For such techniques, the working equations are relatively simple and available in the literature[35]. Experimental difficulties arise from attaining the alignment of the two surfaces which are usually parallel plates or coaxial cylinders, and the need to avoid contributions to the heat transfer from conductive and radiative processes. Careful absolute measurements using a coaxial cylinder arrangement have an accuracy of around 1-3%[44],[45]. The more complex parallel plate method achieves the same level of accuracy and finds importance in the measurement of thermal conductivities near the critical point[46].

Thermal conductivity evaluations are complicated by the need to set up a temperature gradient in a fluid whilst preventing its motion. Transient techniques rely on the fact that the time scale for setting up convective flow in a fluid is much greater than the propagation time of a temperature wave set up by a large gradient. The transient hot wire technique is applicable over a wide range of conditions whereas the interferrometric method is suited to the critical region as smaller gradients may be applied. For non conducting gases accuracies of 0.3%[35] have been achieved using the hot wire method for determining the thermal conductivity. The ultimate accuracy of methods that measure thermal conductivity may be checked against measurements in low density monatomic gases for which an exact molecular theory exists[6].

Reference data for the transport properties are required to check the reliability

of new techniques and for the calibrations necessary for relative measurements. For viscosity measurements, the establishment of a standard has proved a difficult task[35]. At present there is no agreed international standard for gas viscosities, but measurements from a variety of techniques on monatomic gases are now in good agreement. Nitrogen is readily available at high purity and is inexpensive and is probably the most convenient choice for a standard. The number of gases for which the viscosity has been accurately determined at temperatures below 25 °C and at pressures other than atmospheric is small. In addition, values published before 1945 are often in error. For routine thermal conductivity measurements a reference standard is extremely important as absolute measurements are difficult. The small magnitude of thermal conductivity measurements in gases makes them particularly problematic. Early measurements are often in error due to convection and radiation, but the new techniques have not yet been applied over a wide range of conditions so that directly measured reference data remains rare[35].

The estimates of the shear viscosity and thermal conductivity derived in this work are reported in later chapters, in addition to the vibrational relaxation times, and are compared to previous work. The results do not have the accuracy of the published data, but their importance lies in providing a method for the analysis of the acoustic results that does not require recourse to further specialised equipment.

BIBLIOGRAPHY

[1] Van Dael W. *Experimental Thermodynamics Volume II.* (Butterworths: London, 1968).

[2] Ewing M B, Goodwin A R H, McGlashan M L and Trusler J P M. *J. Chem. Thermodyn.* 1987, **19**, 721.

[3] Ewing M B, Goodwin A R H, McGlashan M L and Trusler J P M. *J. Chem. Thermodyn.* 1987, **20**, 243.

[4] Ewing M B, Goodwin A R H and Trusler J P M. *J. Chem. Thermodyn.* 1989, **21**, 867.

[5] Mehl J B and Moldover M R. *J. Chem. Phys.* 1981, **74**, 4062.

[6] Maitland G C, Rigby M, Smith E B and Wakeham W A. *Intermolecular Forces.* (Clarendon: Oxford, 1981).

[7] Ewing M B, McGlashan M L and Trusler J P M. *Mol. Phys.* 1987, **60**, 681.

[8] Ewing M B and Trusler J P M. *J. Chem. Phys.* 1989, **90**, 1106.

[9] Pieperbeck N, Kleinrahm R, Wagner W and Jacschke M. *J. Chem. Thermodyn.* 1991, **23(2)**, 175.

[10] Kleinrahm R, Duschek W, Wagner W and Jaeschke M. *J. Chem. Thermodyn.* 1988, **20(5)**, 621.

[11] Douslin D R and Harrison R H. *J. Chem. Thermodyn.* 1973, **5**, 491.

[12] Douslin D R, Harrison R H, Moore R T and Mc Cullough J P. *J. Chem. Eng. Data.* 1964, **9**, 358.

[13] Douslin D R, Harrison R H, Moore R T and Mc Cullough J P. *J. Chem. Phys.* 1961, **35**, 1357.

[14] Saville G. *Experimental Thermodynamics Volume II.* (Butterworths: London, 1968).

[15] Brielles J, Dédit A, Lallemand M, Le Neindre B, Leroux Y, Vermesse J and Vidal D. *Experimental Thermodynamics Volume II.* (Butterworths: London, 1968).

[16] Malbrunot P. *Experimental Thermodynamics Volume II.* (Butterworths: London, 1968).

[17] Mc Carty R D. *Experimental Thermodynamics Volume II.* (Butterworths: London, 1968).

[18] Ewing M B and Marsh K N. *J. Chem. Thermodyn.* 1979, **11**, 793.

[19] Ewing M B, Mc Glashan M L and Trusler J P M. *Metrologia* 1986, **22**, 93.

[20] Moldover M R, Mehl J B and Greenspan M. *J. Acoust. Soc. Am.* 1986, **79(2)**, 253.

[21] Moldover M R and Trusler J P M. *Metrologia* 1988, **25**, 165.

[22] Edwards T J, Davis R S, Mehl J B, Moldover M R and Trusler J P M. *J. Res. Nat. Bur. Standards* 1988, **93**, 85.

[23] van Itterbeek A and Nihoul J. *Acustica* 1955, **5**, 142.

[24] Colgate S O, Sivaraman A, Dejsupa C and McGill K. *J. Chem. Thermodyn.* 1991, **23**, 647.

[25] Herzfeld K F and Litovitz T A. *Absorption and Dispersion of Ultrasonic Waves.* (Academic Press: London, 1959).

[26] Trusler J P M. *Physical Acoustics and Metrology of Fluids.* (Adam Hilger: Worcester, 1991).

[27] Carey C, Bradshaw J, Lin E and Carnevale E H. *Experimental Determination of Gas Properties at High Temperatures and/or High Pressures.* (Arnold Engineering Development Center, Arnold Air Force Station, TN 37389, USA 1974) Report no. AEDC-TR-74-33.

[28] Biswas S N and Seldam C A. *J. Chem. Thermodyn.* 1991, **23**, 175.

[29] Goodwin A R H. Ph.D Thesis, University of London 1988.

[30] Mehl J B. *J. Acoust. Soc. Am.* 1982, **71**, 1109.

[31] Mehl J B. *J. Acoust. Soc. Am.* 1986, **79**, 278.

[32] Mehl J B. *J. Acoust. Soc. Am.* 1985, **78**, 782.

[33] Waldron R A. *Theory of Guided Electromagnetic Waves.* (Van Nostrand-Reinhold: New York, 1969).

[34] Reid R C and Sherwood T K. *The Properties of Gases and Liquids.* Second Edition. (McGraw Hill: New York, 1966)

[35] Wakehams W A, Nagashima A and Sengers J V. *Measurement of the Transport Properties of Fluids.* (Blackwell Scientific Publications: Oxford, 1991)

[36] Kestin J and Shankland I R. *J. Appl. Math. Phys. ZAMP.* 1981, **32**, 533.

[37] Nieuwoudt J C, Kestin J and Sengers J V. *Physica.* 1987, **142A**, 53.

[38] Nieuwoudt J C, Kestin J and Sengers J V. *Physica.* 1988, **149A**, 107.

[39] Krall A H, Nieuwoudt J C, Kestin J and Sengers J V. *Fluid Phase Equilibria.* 1987, **36**, 207.

[40] Tough J T, McCormick W D and Dash J G. *Phys. Rev.* 1963, **132**, 2373.

[41] Tough J T, McCormick W D and Dash J G. *Rev. Sci. Instrum.* 1964, **35**, 1345.

[42] Goodwin J M. *J. Phys. E.* 1973, **6**, 452.

[43] Goodwin J M. *Physica.* 1974, **76**, 177.

[44] Lawson A W, Lowell R and Jain A L. *J. Chem. Phys.* 1959, **30**, 643.

[45] Rastorguev Y L and Pugach V V. *Thermal Engineering.* 1970, **17**, 116.

[46] Sirota A M, Latunin V I and Belyaeva G M. *Thermal Engineering.* 1974, **21**, 70.

2. ACOUSTICS

2.1. Introduction

The theory relevant to the propagation of sound within a cavity is extensively covered in the literature[1]-[5], and only a brief outline is included here. The discussion starts with a simplified theory of sound that neglects completely the effects of the mechanisms that result in dissipation. This is applicable only to an ideal fluid in which the shear viscosity and thermal conductivity are negligible, and in which local thermodynamic equilibrium is established instantaneously in the presence of sound. The discussion is then extended to cover propagation in a dissipative fluid. Absorption of sound in the bulk of the fluid, including molecular relaxation is then considered. This may severely perturb the speed of sound from its ideal value, and cause severe dispersion as well as contributing to the attenuation of the sound wave.

Enclosing the fluid in a cavity imposes boundary conditions on the wave equation which must be satisfied. Near the wall of the cavity the shear and thermal waves must also be considered, leading to the dispersion and a consequent perturbation of the speed of sound. When sound is generated continuously within a closed cavity, a steady state is achieved in which the wave motion is that of a standing wave. When the frequency of the sound source is close to that of a natural frequency of the system, resonance occurs. For a simple geometry, such as an annulus, solutions of the wave equation may be found that satisfy the boundary conditions, leading to equations which relate the frequencies of the normal modes of the gas filled cavity to the speed and absorption of sound in a gas, thus providing a basis for their measurement.

Finally, other perturbations to the system such as the effects of openings in the cavity wall, and the motion of the cavity wall in response to sound are considered.

2.2. Propagation in an Idealised Fluid

If dissipation is neglected and it is also assumed that local thermodynamic equilibrium is established instantaneously in the presence of sound, a simple description of the propagation of sound may be derived. A linear acoustic theory is developed[1],[3], by which it is meant that the acoustic variables are sufficiently small for their cross products, squares, and higher powers to be neglected. In the presence of sound the pressure, temperature and density are represented by $p + p_a(\boldsymbol{r}, t)$, $T + T_a(\boldsymbol{r}, t)$, and $\rho + \rho_a(\boldsymbol{r}, t)$ where p_a, T_a and ρ_a are the acoustic contributions to the equilibrium pressure, temperature and density.

In terms of this notation the equation of continuity of mass density is

$$(\partial \rho_a / \partial t) = -(\rho + \rho_a) \nabla \cdot \boldsymbol{\nu} - (\boldsymbol{\nu} \cdot \nabla) \rho_a \tag{2.1}$$

in which $\boldsymbol{\nu}$ is the fluid velocity and $\nabla = \boldsymbol{i}(\partial/\partial x) + \boldsymbol{j}(\partial/\partial y) + \boldsymbol{k}(\partial/\partial z)$ in the Cartesian coordinate system.

Euler's equation for the motion of an ideal fluid is given by

$$-\nabla p_a = (\rho + \rho_a)\left[(\partial \boldsymbol{\nu}/\partial t) + (\boldsymbol{\nu} \cdot \nabla)\boldsymbol{\nu}\right]. \tag{2.2}$$

The fluid velocity is counted among the small acoustic variables as the fluid is assumed to be at rest except for the motion due to sound waves. When approximated to leading order in the small acoustic terms, and using the isentropic equation of state

$$(\partial p/\partial \rho)_S \, \delta\rho = \delta p, \tag{2.3}$$

the equations become

$$\rho^{-1} (\partial \rho/\partial p)_S (\partial p_a/\partial t) = -\nabla \cdot \boldsymbol{\nu}, \tag{2.4}$$

and

$$\rho (\partial \boldsymbol{\nu}/\partial t) = -\nabla p_a. \tag{2.5}$$

Taking the divergence of equation (2.5) and eliminating $\boldsymbol{\nu}$ using (2.4) gives a wave equation,

$$\left[\nabla^2 - \left(1/u_0^2\right)\left(\partial^2/\partial t^2\right)\right] p_a(\boldsymbol{r}, t) = 0 \tag{2.6}$$

in which $\nabla^2 = \nabla \cdot \nabla$ is the Laplacian operator, and $u_0^2 = (\partial \rho/\partial p)_S$ is the speed of sound in an ideal fluid. This linearised wave equation describes the propagation of small amplitude sound waves in a non-dissipative medium.

In the absence of dissipation, the fluid flow is irrotational and hence $\boldsymbol{\nu}$ may be expressed as the gradient of a scalar function $\Psi(\boldsymbol{r},t)$, the velocity potential, giving

$$\boldsymbol{\nu}(\boldsymbol{r},t) = -\boldsymbol{\nabla}\Psi(\boldsymbol{r},t). \tag{2.7}$$

Thus to first order in the acoustic variables the linearised version of Euler's equation (2.5) becomes

$$p_{\mathrm{a}}(\boldsymbol{r},t) = \rho\{\partial\Psi(\boldsymbol{r},t)/\partial t\}, \tag{2.8}$$

and consequently the fluid velocity and acoustic pressure may be simply described in terms of this velocity potential.

2.3. Propagation in a Dissipative Fluid

This linear theory of sound is exact in the limit $p_{\mathrm{a}} \to 0$ and in practice the small amplitude limiting behaviour is easy to achieve. However real fluids are not ideal and hence thermal conduction and friction which are always present must be considered. The model starts with the equations derived by Kirchhoff[5] who assumed that the pressure, temperature and particle velocity were described by the Navier-Stokes equations, the equation of continuity, and Fourier's law of heat flow.

Friction directly effects the equations of motion through the transport coefficients η and η_{b}, the shear and bulk viscosities respectively. The Navier-Stokes equation for a compressible fluid which consists of a relation between the stress and spatial derivatives of the fluid velocity and Newton's second law, may be written correct to first order in the acoustic variables[1] as

$$\left(\frac{\partial\boldsymbol{\nu}}{\partial t}\right) = -\left(\frac{1}{\rho}\right)\boldsymbol{\nabla}p_{\mathrm{a}} + \left[\left(\frac{4D_{\mathrm{s}}}{3}\right) + \left(\frac{\eta_{\mathrm{b}}}{\rho}\right)\right]\boldsymbol{\nabla}\cdot(\boldsymbol{\nabla}\cdot\boldsymbol{\nu}) - D_{\mathrm{s}}\boldsymbol{\nabla}\times(\boldsymbol{\nabla}\times\boldsymbol{\nu}) \tag{2.9}$$

where $(\boldsymbol{\nabla}\times\boldsymbol{\nu})$ is the curl of the velocity $\boldsymbol{\nu}$ and $D_{\mathrm{s}} = \eta/\rho$ is the viscous diffusivity. Equation (2.9) can be resolved into two uncoupled equations[3]:

$$\left(\frac{\partial\boldsymbol{\nu}_{\mathrm{l}}}{\partial t}\right) = -\left(\frac{1}{\rho}\right)\boldsymbol{\nabla}p_{\mathrm{a}} + \left[\left(\frac{4D_{\mathrm{s}}}{3}\right) + \left(\frac{\eta_{\mathrm{b}}}{\rho}\right)\right]\boldsymbol{\nabla}(\boldsymbol{\nabla}\cdot\boldsymbol{\nu}_{\mathrm{l}}), \tag{2.10}$$

in which $\boldsymbol{\nu}_{\mathrm{l}}$ is a longitudinal (or irrotational) component of $\boldsymbol{\nu}$ for which $\boldsymbol{\nabla}\times\boldsymbol{\nu}_{\mathrm{l}} = 0$ and p_{a} contributes only to this longitudinal flow, and

$$\left(\frac{\partial\boldsymbol{\nu}_{\mathrm{r}}}{\partial t}\right) = -D_{\mathrm{s}}\boldsymbol{\nabla}\times(\boldsymbol{\nabla}\times\boldsymbol{\nu}) = D_{\mathrm{s}}\boldsymbol{\nabla}^2\boldsymbol{\nu}_{\mathrm{r}} \tag{2.11}$$

in which ν_r is a rotational (or transverse) component of ν for which $\nabla \cdot \nu_r = 0$. Since (2.11) is independent of the acoustic pressure p_a it can be neglected for the bulk of the fluid but may become important when considering boundary layers.

In addition to the pressure fluctuations, fluctuations in temperature accompany the presence of sound. In response to the resulting temperature gradients, irreversible heat flow occurs from regions of higher temperature to those of lower temperature. This thermal conduction is described by a second-order diffusion equation[1]:

$$D_h \nabla^2 T_a = (\partial/\partial t \{T_a - [(\gamma - 1)/\gamma\beta] p_a\}), \tag{2.12}$$

where $\beta = (\partial p/\partial T)_\rho$, $D_h = \kappa/\rho C_p$ is the thermal diffusivity, and κ is the thermal conductivity.

The acoustic description now includes six quantities: p_a, T_a, ρ_a and the three components of the fluid velocity ν and consequently six equations are required to specify a solution. For irrotational flow, the components of (2.10) provide three equations, a fourth is (2.12), and a fifth is the equation of the continuity of density[1]

$$(\partial \rho_a/\partial t) + \rho \nabla \cdot \nu_l = 0. \tag{2.13}$$

The sixth, and final equation is obtained using the thermodynamic equation of state to interrelate p_a, T_a and ρ_a:

$$\begin{aligned} \rho_a &= (\partial \rho/\partial p)_T p_a + (\partial \rho/\partial T)_p T_a \\ &= (\gamma/u_0^2)(p_a - \beta T_a). \end{aligned} \tag{2.14}$$

Taking the divergence of equation (2.10) and eliminating ν_l using (2.13) gives

$$\nabla^2 p_a = \left(\partial^2 \rho_a/\partial t^2\right) - \left[\left(\frac{4D_s}{3}\right) + \left(\frac{\eta_b}{\rho}\right)\right] \nabla^2 (\partial \rho_a/\partial t), \tag{2.15}$$

and when ρ_a is eliminated using equation (2.14) the following modified wave equation is obtained

$$\nabla^2 p_a = \left(\gamma/u_0^2\right) \left\{\left(\partial^2/\partial t^2\right) - \left[\left(\frac{4D_s}{3}\right) + \left(\frac{\eta_b}{\rho}\right)\right] (\partial/\partial t) \nabla^2\right\} (p_a - \beta T_a). \tag{2.16}$$

Equations (2.16) and (2.12) may be solved exactly for T_a and p_a, but as the dissipative effects are small it is sufficient to consider solutions correct to first order in η, η_b and κ.

The coupling of pressure and temperature leads to the fluid tending to propagate pressure waves and the heat tending to diffuse[3]. For simple harmonic wave motion with angular frequency ω, equations (2.16) and (2.12) may be solved simultaneously to give two positive roots defining the propagational and thermal modes[3]. The propagational mode has a real part equal to u_0 (the adiabatic speed) and a small imaginary part corresponding to the energy loss mechanisms. For the thermal wave which corresponds to heat diffusion, p_a is small compared to βT_a and the wave velocity is proportional to $\sqrt{i}$ indicating rapid attenuation[3]. The shear mode which is also a solution for simple harmonic motion, comes from the rotational components of (2.11). This is used along with the thermal mode to satisfy the boundary conditions that may not be satisfied by the propagational mode alone. For the shear mode, the wave velocity is again proportional to $\sqrt{i}$ such that its attenuation is rapid. The acoustic pressure and temperature associated with the propagational mode are both eigenfunctions of ∇, with eigenvalues $-k^2$. The propagation constant, k for angular frequency ω is

$$k = \left(\frac{\omega}{u}\right) + i\alpha, \tag{2.17}$$

where α is the coefficient of absorption. Before going into more detail about the absorption of sound, the effect of a boundary must be considered in order to describe the fluid contained within a cavity.

2.4. Boundary Conditions

When a fluid is confined to a region by a surface, solutions of the wave equation must also satisfy certain boundary conditions at that surface. For the case of a boundary with a solid medium the complete problem is complicated by elastic shear waves propagating in the solid but, as these transmitted waves are of no particular interest, an acoustic impedance Z_a may simply be assigned to the boundary. In order to do this it is assumed that the motion of any element of the surface is determined solely by the acoustic pressure acting there. Such a boundary is defined as one of local reaction. It is usually more convenient to use the specific acoustic admittance y_0 defined by[1]

$$y_0 = \rho u / Z_a \tag{2.18}$$

where ρu is the acoustic impedance of the adjacent fluid.

2.4.1. Thermal and Viscous Boundary Layers

In the bulk of the fluid only the propagational mode is important but, at an interface with a solid, the thermal and shear waves in the boundary layer give rise to important loss mechanisms for a typical fluid at pressures below 1 MPa. There are four boundary conditions that must be satisfied at the surface[3]: (i) the ratio $\rho u/Z_a$ must equal the specific acoustic admittance y_0 of the boundary surface; (ii) the temperatures of the wall and fluid must be equal at the surface; (iii) there must be continuity of heat flow across the interface; and (iv) the tangential component of the fluid velocity must vanish at the surface. On its own the propagational mode cannot satisfy all four conditions and all three modes are required[3]. The second and third conditions result in thermal waves being generated in the wall and fluid, though those in the wall have a much smaller amplitude and may be ignored[13]. Effectively, the thermal wave at the interface cancels out the temperature fluctuations associated with the propagational mode. The fourth condition demands that a shear wave in the fluid is generated at the surface to cancel the tangential motion of the propagational wave. Consequently near the gas-wall interface, energy is withdrawn from the propagational mode and the amplitudes of the thermal and shear waves increase to a maximum at the boundary. Detailed theory is given in reference [1] and the results are that the specific acoustic admittances of the thermal, y_h and shear, y_s boundary layers are given by

$$y_h = (1+i)\,(\gamma-1)\,(\omega/2u)\,\delta_h \tag{2.19}$$

and

$$y_s = (1+i)\,(k_t/k)^2\,(\omega/2u)\,\delta_s \tag{2.20}$$

where k_t is the tangential propagation constant. Thus the viscous effects on the sound wave near the wall depend on the angle of incidence but the effects of heat flow at the wall are independent of k_t. The thermal, δ_h and viscous, δ_s penetration lengths are given by

$$\delta_h = (2D_h/\omega)^{\frac{1}{2}} \tag{2.21}$$

and

$$\delta_s = (2D_s/\omega)^{\frac{1}{2}} . \tag{2.22}$$

The shear and thermal waves decay very rapidly in the fluid, and the penetration lengths give a measure of the distances over which the boundary layer effects are important. The theory now allows the equations for a fluid contained within an annular cavity and the contributions to the acoustic admittance of the surface to be derived, but first the absorption of sound is considered in greater detail.

2.5. Absorption of Sound

In a gas the absorption of sound is a consequence of kinetic processes. These include the transport of heat and momentum, and vibrational and rotational relaxation[4],[6]-[11]. Hence information may be gained about the time scale of various relaxation processes[12].

The acoustic absorption coefficient, α is defined such that the amplitude of a plane wave decays with distance z proportional to $\exp(-\alpha z)$. Sound in a fluid consists of compression waves and thus imposes cyclic fluctuations in pressure and density associated with fluctuations in local temperature.

At the low frequency limit, where the wavelength and hence the time scale of the fluctuations is long, these processes occur isentropically and none of the sound energy is dissipated. However, at higher frequencies the fluid cannot maintain local equilibrium on a microscopic scale due to the non zero response time to the fluctuations. As a consequence the acoustic cycle no longer occurs reversibly, sound energy is dissipated, and α takes on a non zero value. As the frequency is increased the magnitude of the resulting temperature and velocity gradients in the fluid increase leading to a greater flow of heat and momentum over distances comparable with the wavelength which again causes dissipation. This classical absorption is always present and its magnitude is controlled by the transport properties κ and η which are the coefficients of thermal conductivity and shear viscosity respectively. These result in a contribution α_{cl} to α given by:

$$\alpha_{cl} = \left(\omega^2/2u^3\right)\left[(4D_s/3) + (\gamma - 1)\, D_h\right] . \tag{2.23}$$

where $\omega = 2\pi f$ is the angular frequency and D_s and D_h are the viscous and

thermal diffusivities defined in the previous sections.

Equation (2.23) shows that the absorption coefficient increases as the square of the frequency. Other dissipation mechanisms are generally more important than α_{cl} and usually corrections are made for α_{cl} before such loss mechanisms are investigated.

In the presence of sound the density is fluctuating at a frequency $f = \omega/2\pi$, and as the pressure is dependent on the translational modes of motion, the pressure will adjust almost instantaneously to the fluctuations in the density as only a few collisions are required for the energy within the translational modes to equilibriate. Thus under most conditions, thermodynamic equilibrium will be established rapidly in monatomic gases where only translational modes are accessible. In polyatomic gases however, some of the energy is distributed among the available rotational and vibrational modes of motion. The transfer of energy from translation to rotation (T-R) and translation to vibration (T-V) termed thermal relaxation, requires a finite time and as gas collisions are necessary, thermal relaxation depends on the gas density[8]. Under conditions where thermal relaxation is important the pressure will decay with a time constant governed by the slowest process to its value at thermodynamic equilibrium. Thermal relaxation becomes important when the time constants and $1/\omega$ are comparable, at lower frequencies where $1/\omega$ is much greater than the time constants then T-R and T-V transfers can occur and these effects are not important as a source of sound attenuation and dispersion. At high frequencies, in effect some or all of the internal degrees of freedom cease to participate in the acoustic cycle.

When the sound is harmonic, the amplitude of the energy fluctuation within a given j-th degree of freedom will be reduced from ε_j to $\varepsilon_j/(1 - i\omega\tau_j)$, where ε_j is the energy fluctuation that would be observed if equilibrium were achieved instantaneously, and τ_j is the time constant or relaxation time for the j-th degree of freedom[7]. It follows[3] that the j-th degree of freedom's contribution to the heat capacities C_p and C_V will also be modified by a factor of $(1 - i\omega\tau_j)^{-1}$.

At the temperatures used in most acoustic experiments, many of the closely spaced rotational levels are populated and thus T-R transfer occurs at nearly every collision. The relaxation times are generally only a factor of ten greater than for translational motion and in consequence at audio frequencies, the effect

can usually be ignored[9].

The situation for vibrational modes is very different as the levels are widely spaced and only a few are populated. The vibrational relaxation time τ_{vib} is related to the probabilities $\text{P}_{0\rightarrow 1}$ and $\text{P}_{1\rightarrow 0}$ of transitions between the ground and first vibrational energy levels per molecular collision, and Z which is the number of collisions encountered by a molecule per second:

$$\tau_{\text{vib}} = \left\{\left(\text{P}_{1\rightarrow 0} - \text{P}_{0\rightarrow 1}\right) Z\right\}^{-1}. \tag{2.24}$$

The probability of activation $\text{P}_{0\rightarrow 1}$is related to the probability of deactivation $\text{P}_{1\rightarrow 0}$ via

$$\text{P}_{0\rightarrow 1} = \text{P}_{1\rightarrow 0} \exp\left(-h\nu/kT\right), \tag{2.25}$$

where h is the Planck constant, ν the vibrational frequency and k the Boltzmann constant. Using the last two equations an expression that gives the average number of collisions necessary for a molecule in the first excited state to decay to the ground state may be written

$$Z_{1\rightarrow 0} = \left[Z\tau_{\text{vib}}\left\{1 - \exp\left(-h\nu/kT\right)\right\}\right]^{-1} = \text{P}_{1\rightarrow 0}^{-1}. \tag{2.26}$$

Landau and Teller developed a simple theory of vibrational relaxation that predicts $\text{P}_{1\rightarrow 0}$ is proportional to $\exp\left(-T^{\frac{1}{3}}\right)$[8], and many non polar gases exhibit this behaviour over a wide temperature range[9].

The effective ratio of heat capacities, γ for a gas where rotational relaxation may be ignored but vibrational relaxation is important is given by[7]

$$\gamma\left(\omega, T, p\right) = \frac{\left[\gamma + \sum_j \left\{i\omega\tau_j / \left(1 - i\omega\tau_j\right)\right\} C_{\text{vib},j}\left(T\right) / C_V\left(T, p\right)\right]}{\left[1 + \sum_j \left\{i\omega\tau_j / \left(1 - i\omega\tau_j\right)\right\} C_{\text{vib},j}\left(T\right) / C_V\left(T, p\right)\right]} \tag{2.27}$$

when it is assumed that the degrees of freedom are independent. Here $C_{\text{vib},j}$ denotes the contribution of the j-th vibrational mode to the heat capacity. If it is assumed that there is a single relaxation time, τ_{vib} arising from one vibrational state or from a number of states coupling in series[8],[9], equation (2.27) may be written as

$$\frac{\gamma\left(\omega\right)}{\gamma} = 1 + \frac{\omega\tau_{\text{vib}}\left(\gamma - 1\right)\Delta\left\{\omega\tau_{\text{vib}}\left(1 - \gamma\Delta\right) - i\right\}}{\left\{1 + \left[\omega\tau_{\text{vib}}\left(1 - \gamma\Delta\right)\right]^2\right\}}, \tag{2.28}$$

where $\Delta = C_{\text{vib}}/C_p$ is the fraction of the heat capacity that is relaxing. Most polyatomic molecules show this kind of behaviour[9]. For this work where $\omega\tau_{\text{vib}} \ll 1$,

it is sufficient to employ a series expansion of equation (2.28) in powers of $\omega\tau_{\text{vib}}$ giving

$$\left(\frac{\gamma(\omega)}{\gamma}\right)^{\frac{1}{2}} = 1 - \left(\frac{i}{2}\right)(\gamma-1)\,\Delta\omega\tau_{\text{vib}} + \left[\frac{1}{2}(\gamma-1)\,\Delta\,(\omega\tau_{\text{vib}})^2\left\{1-\frac{1}{4}\Delta\,(1+3\gamma)\right\}\right] + O\,(\omega\tau_{\text{vib}})^3\,. \tag{2.29}$$

The contribution of vibrational relaxation to the coefficient of absorption in terms of this expansion is[11]

$$\alpha_{\text{rel}} = \frac{(\omega/u)}{\text{Im}\left[\{\gamma(\omega)/\gamma\}^{\frac{1}{2}}\right]} = \frac{(\gamma-1)\,\Delta\omega^2\tau_{\text{vib}}}{2u} + O\,(\omega\tau_{\text{vib}})^3\,, \tag{2.30}$$

and the speed of sound is[11]

$$u_\omega = u\cdot\text{Re}\left[\{\gamma(\omega)/\gamma\}^{\frac{1}{2}}\right] = u\left[1+\frac{1}{2}(\gamma-1)\,\Delta\,(\omega\tau_{\text{vib}})^2\left\{1-\frac{1}{4}\Delta\,(1+3\gamma)\right\}\right] + O\,(\omega\tau_{\text{vib}})^3\,, \tag{2.31}$$

where u is the zero frequency sound speed. Vibrational relaxation makes a contribution to the breadth of the resonance modes and causes a shift in the resonance frequencies. These will be discussed in a later section. The bulk viscosity η_{b} is defined by

$$\eta_{\text{b}} = (\gamma-1)\,(\rho\tau_{\text{vib}})\,u^2\Delta, \tag{2.32}$$

and hence the total absorption coefficient can be written as

$$\alpha = \left(\omega^2/2u^3\right)\left[(4D_{\text{s}}/3) + (\gamma-1)\,D_{\text{h}} + (\eta_{\text{b}}/\rho)\right]. \tag{2.33}$$

For a binary mixture $\{x\text{A} + (1-x)\,\text{B}\}$, the vibrational relaxation effects will depend on the relative efficiencies of energy transfer between A-A, B-B and A-B. For the case when only A can relax and A-B energy exchange is efficient compared to A-A, addition of B will have a catalytic effect on the relaxation of A and consequently the relaxation time will decrease. When the efficiencies of energy exchange are reversed then addition of B will have an anti-catalytic effect. When B also relaxes, and both A and B exhibit only one relaxation time, then in the mixture one or two relaxation times will exist[7]. Four types of T-V energy transfer may occur between A and B and one of V-V transfer. The mixture will exhibit two relaxation times if the V-V transfer does not occur. To explain this,

let A have a slow relaxation time τ_A and B a fast characteristic time constant for vibrational relaxation τ_B. If V-V transfer is efficient as is the case when the vibrational frequencies are similar, then only one relaxation time characteristic of B will exist. In this case the situation is analogous to the series coupling of vibrational modes that most polyatomic molecules exhibit. If V-V transfer is slow then A and B relax independently and two characteristic time constants are observed.

In binary gas mixtures diffusion also causes an additional contribution to η_b due to the greater flow of lighter components in the presence of density gradients. This is given by[8]

$$\eta_{b,diff} = \left\{\frac{\gamma^2 x\left(1-x\right) pD_{12}}{u^2}\right\}\left[\left\{\frac{M_A - M_B}{M}\right\} + \left\{\frac{\left(\gamma-1\right) D_T}{\gamma D_{12} x\left(1-x\right)}\right\}\right]^2, \qquad (2.34)$$

where D_{12} is the binary diffusion coefficient and D_T the thermal diffusion factor. In equation (2.34), $M = xM_A + \left(1-x\right) M_B$ is the mole fraction weighted average molar mass of the mixture, and M_A and M_B denote the molar masses of the individual components and thus the effect is small unless the masses are very different.

2.6. Cavities

2.6.1. Normal Modes

The discussion of the acoustic model starts with the time dependent wave equation which is given by

$$\left[\nabla^2 + \left(k/\omega\right)^2 \left(\partial^2/\partial t^2\right)\right] \Psi\left(\boldsymbol{r}, t\right) = 0 \qquad (2.35)$$

in which $\Psi\left(\boldsymbol{r}, t\right)$ is a velocity potential describing the acoustic field for the region of the cavity $\mathcal{R}$. $\Psi\left(\boldsymbol{r}, t\right)$ may be separated into the product $\Psi\left(\boldsymbol{r}, t\right) = A\Phi\left(\boldsymbol{r}\right)\exp\left(i\omega t\right)$ assuming a simple harmonic time dependence[1]. The frequency f is given by $\omega/2\pi$, A is the amplitude of the wave field, and the spatial function $\Phi\left(\boldsymbol{r}\right)$ is a solution of the Helmholtz equation

$$\left(\nabla^2 + k^2\right) \Phi\left(\boldsymbol{r}\right) = 0. \qquad (2.36)$$

Equation (2.35) is satisfied when $\nabla^2\Phi\left(\boldsymbol{r}\right) = -k^2\Phi\left(\boldsymbol{r}\right)$, and the propagation constant is given by $k = \left(\omega/u\right) + i\alpha$, where u is the sound speed and α the

coefficient of absorption. The solutions of (2.36) are the normal modes which form an infinite set of functions that are orthogonal, finite and continuous within the cavity. The eigenfunctions of the normal modes are represented by $\Phi_N(\boldsymbol{r},\omega)$, and corresponding eigenvalues by $K_N(\omega)$, where N is a set of three indices n_1, n_2, n_3 required to specify the solution in three dimensions. The normal modes obey the orthogonality condition[3]

$$\iiint_R \Phi_N(\boldsymbol{r},\omega)\,\Phi_M^*(\boldsymbol{r},\omega)\,dV = V\Lambda_N(\omega)\,\delta_{NM}. \tag{2.37}$$

In equation (2.37) V is the volume of the cavity, $\Lambda_N(\omega)$ is a normalisation constant and δ_{NM} a Dirac delta function. Assuming the surface S is of local reaction the boundary condition is[3].

$$\nu_n(\boldsymbol{r}_S) = p_a(\boldsymbol{r}_S)\,y(\boldsymbol{r}_S,\omega)/\rho u, \tag{2.38}$$

for all positions $\boldsymbol{r}_S$ on S. In (2.38), $\nu_n(\boldsymbol{r}_S)$ is the component of the fluid velocity normal to S, y is the specific acoustic admittance of the boundary, and ρ the fluid density. The boundary condition depends on the frequency ω and hence the eigenfuctions Φ_N and eigenvalues K_N are also functions of ω. Since the acoustic pressure p_a is related to $\Phi(\boldsymbol{r},\omega)$ by

$$p_a(\boldsymbol{r},\omega) = -i\omega\rho\Phi(\boldsymbol{r},\omega), \tag{2.39}$$

the wavefunctions $\Phi(\boldsymbol{r})$ must satisfy

$$(\partial/\partial n)\,\Phi(\boldsymbol{r},\omega)|_{r=r_s} = -i(\omega/u)\,\Phi(\boldsymbol{r}_S,\omega)\,y(\boldsymbol{r}_s,\omega). \tag{2.40}$$

It is the boundary condition that restricts the propagation constant k to the set of values $K_N(\omega)$. The natural frequencies of the system are therefore given by

$$F_N = (f_N + ig_N) = (u/2\pi)(K_N + i\alpha) \tag{2.41}$$

2.6.2. Forced Oscillations

The normal modes define the form of the free oscillations allowed within a cavity, and may be used to derive the steady state response to a source of sound. Using arguments based on a simple harmonic source of infinitesimal size it can be

shown[1] that the acoustic pressure is a complex quantity as the response of the driven cavity and the source are not necessarily in phase. The velocity potential for a cavity driven in the steady state by a source at F_0 is represented by the Green function $G_\omega(r/F_0)$, which may be expanded as an infinite series of the normal modes[3]. When the normal modes are well resolved, a single component (or a set of degenerate components) predominates near resonance and hence a single mode may be studied in near isolation. In this case the background contribution of the other modes is expanded in a Taylor series about some frequency f_0 near the resonance of interest and the acoustic pressure p_ω is given by[4],[5]

$$p_\omega = \left(\frac{A_N}{(F_N/f)^2 - 1}\right) + B + C(f - f_0) + \cdots \tag{2.42}$$

where F_N is defined by equation (2.41) and the coefficients A_N, B, $C\cdots$ are complex constants. The complex natural frequency F_N and other constants in (2.42) may be obtained by measurement of the amplitude and phase of the acoustic pressure over a small frequency band near to the resonance. The higher the quality factor $Q_N = f_N/2g_N$ of the mode, the more precise are the values obtained. In the limit of a sharp singlet without background a Lorentzian line-shape is obtained

$$p_\omega = \frac{ia_N}{g_N + i(f - f_N)} \tag{2.43}$$

The amplitude a_N is reduced to $1/\sqrt{2}$ of its maximum at $f_N \pm g_N$ and g_N is referred to as the resonance half-width. In practice the resonance line-shape closely approximates the Lorentzian function, the amplitude and phase of which are illustrated in figure (2.1).

2.6.3. Boundary Conditions

Eigenfunctions of the Helmholtz operator that satisfy the boundary conditions of the cavity in question must be found before the results obtained in the previous sections can be used. For simple geometries, an appropriate choice of coordinate system allows the wave functions that satisfy the boundary conditions for the ideal cavity to be separated into a product of three terms, each of which is a function of just one coordinate. The ideal case is taken to be a cavity of perfect geometry and zero surface admittance. For the ideal case, the eigenfunctions of the Helmholtz operator are denoted by $\phi_N(r)$, the corresponding eigenvalues by $-k_N^2$ and the normalisation constants by Λ_N^0. Thus:

Figure 2.1: Amplitude and phase for a Lorentzian resonance. The phase is plotted relative to an arbitrary zero at the resonance frequency.

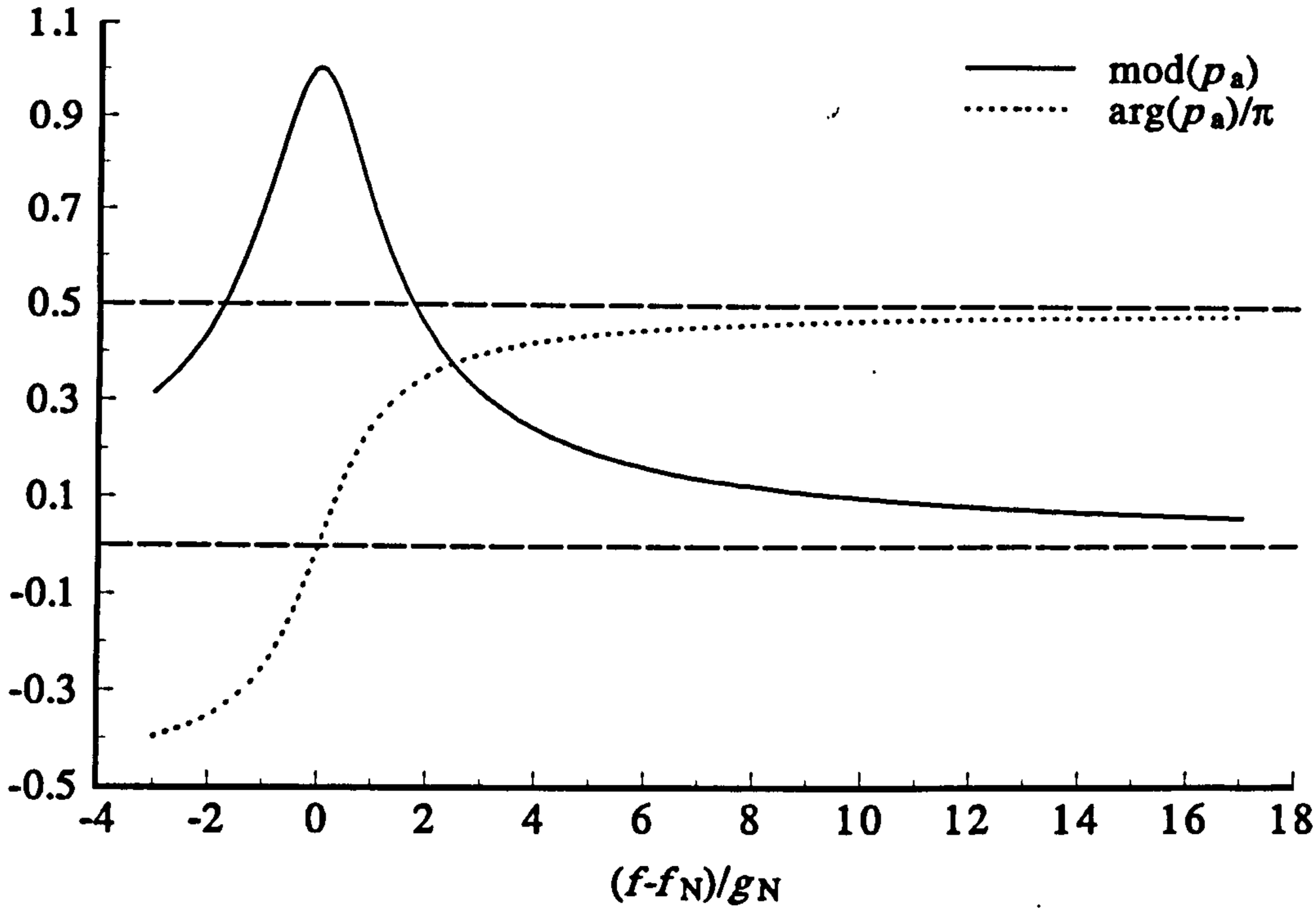

$$\left(\nabla^2 + k^2\right)\phi\left(\boldsymbol{r}\right) = 0 \tag{2.44}$$

within $\mathcal{R}_0$, the region of the ideal cavity and

$$\left(\partial/\partial n\right)\phi\left(\boldsymbol{r}\right)\big|_{r=r_S} = 0 \tag{2.45}$$

on $\mathcal{S}_0$, the surface of the ideal cavity. The boundary conditions given in equations (2.44) and (2.45) are called the homogeneous Neumann conditions[1], and the propagation constant $-k_N^2$ is real and independent of frequency. The real cavity will not have zero surface admittance or perfect geometry and these are dealt with as perturbations to the ideal system. To calculate these effects, solutions are found of the homogeneous wave equation

$$\left(\nabla^2 + k^2\right)\Phi\left(\boldsymbol{r}\right) = 0 \tag{2.46}$$

within $\mathcal{R}$ subject to the inhomogeneous boundary conditions at the surface $\mathcal{S}$ of the real cavity

$$\left(\partial/\partial n\right)\Phi\left(\boldsymbol{r}\right)\big|_{r=r_S} = -i\left(\omega/u\right)\Phi\left(\boldsymbol{r}\right)y\left(\boldsymbol{r}\right). \tag{2.47}$$

Φ_N is the eigenfunction for the real cavity with corresponding eigenvalue K_N.

The solutions are expressed in terms of those for the idealised cavity with surface S_0 (not necessarily coincident with S) and the unperturbed wave functions ϕ_N form the basis set from which Φ_N is expanded. The method employed utilizes Green's functions and is described in references [1] and [3].

Non zero surface admittance and absorption in the bulk of the gas

The result[1] of this method for a cavity of perfect geometry but non zero specific surface acoustic admittance $y(r)_S$ is

$$K_N = k_N + \left(\frac{\omega}{uk_N}\right)\left(\frac{i}{2V\Lambda_N^0}\right)\iint_S y(r)_S \left|\Phi_N(r)_S\right|^2 dS. \tag{2.48}$$

In a first order approximation, Φ may be replaced by ϕ, ω/uk_N by unity and

$$V\Lambda_N^0 = \iiint_R |\phi_N|^2 \, dV. \tag{2.49}$$

This result will be used in the following sections to derive expressions for the resonance frequencies and half-widths, correct to first order, which are given by

$$f_N = (u/2\pi)\, k_N + \Delta f_s + \Delta f_h + \Delta f_b \tag{2.50}$$

and

$$g_N = g_s + g_h + g_b. \tag{2.51}$$

where Δf_s and Δf_h are the frequency shifts and g_s and g_h are the contributions to the half-widths due to the surface admittance caused by the shear and thermal boundary layers. The term g_b in (2.51) is the contribution to the half-width due to absorption and is given by[4]

$$g_b = \left(\frac{u}{2\pi}\right)\alpha, \tag{2.52}$$

where α is defined by equation (2.33). The much smaller correction (as it depends on $(\omega\tau_{vib})^2 \ll 1$), to the resonance frequencies Δf_b due to absorption is given by[11]

$$\Delta f_b \approx \frac{f}{2}(\gamma - 1)\,\Delta\,(\omega\tau_{vib})^2 \left\{1 - \frac{1}{4}\Delta\,(1 + 3\gamma)\right\}. \tag{2.53}$$

Imperfect geometry

This method can also be used to determine the effects of imperfect geometry, but, as for other geometries the perturbations are likely to have a magnitude negligible compared to other sources the results are not quoted here. The theory and some specific examples are given in reference [1].

Figure 2.2: The cylindrical polar coordinates applicable to the annular geometry.

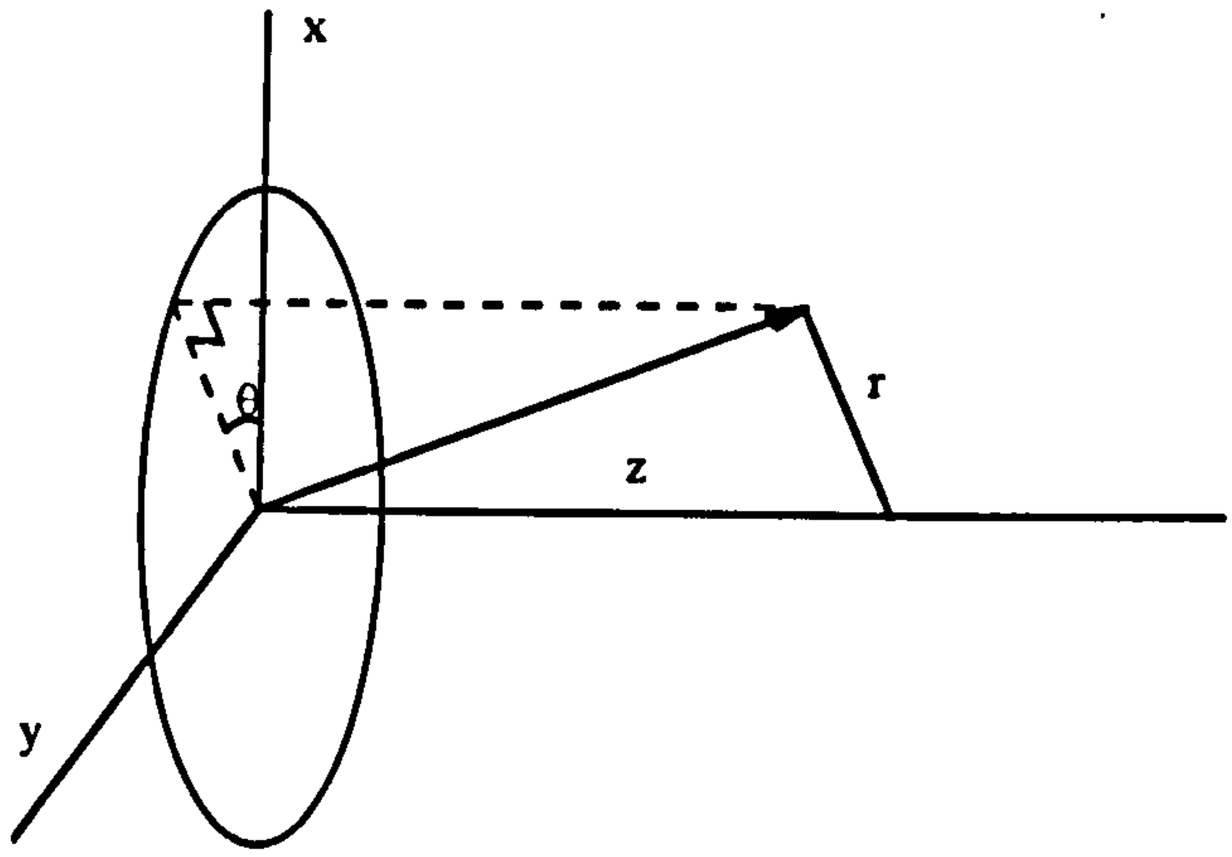

2.7. The Cylindrical Annular Cavity

Cylindrical polar coordinates shown in figure (2.2) are appropriate to this problem and are related to the Cartesian set by

$$\begin{aligned} x &= r\cos\theta \\ y &= r\sin\theta \\ z &= z. \end{aligned} \tag{2.54}$$

2.7.1. The Ideal Case

The wavefunctions for an annulus inner radius a, outer radius b, concentric with the z axis extending from $z = 0$ to $z = L$ are given by the product[2]

$$\phi_N(r,\theta,z) = X_N(r)\,Y_N(\theta)\,Z_N(z)\,. \tag{2.55}$$

When this is substituted into the wave equation, the problem separates into three ordinary differential equations

$$\left.\begin{aligned} (1/X)\,(d^2X/dr^2) + (1/rX)\,(dX/dr) + (k_N^2 - q^2) - (m/r)^2 &= 0 \\ (d^2Y/d\theta^2) + m^2Y &= 0 \\ (d^2Z/dz^2) + k_z^2Z &= 0 \end{aligned}\right\} \tag{2.56}$$

in which $-m^2$ is the separation constant for Y and $-k_z^2$ is the separation constant for Z. The substitution $r = x/\left(k_N^2 - k_x^2\right)^{\frac{1}{2}}$ reveals that the first of the differential equations is Bessel's equation

$$\left(d^2X/dx^2\right) + (1/x)\,(dX/dx) + \left[1 - (m/x)^2\right] = 0, \tag{2.57}$$

for which the solutions are linear combinations of $J_m(x)$, the cylindrical Bessel function of order m and $N_m(x)$, the cylindrical Neumann function of order m. If ξ is the constant for the linear combination of the two solutions, then the radial solution may be written as

$$\phi_r = J_m(kr) + \xi N_m(kr) = R_m(kr). \tag{2.58}$$

The derivative $dR(r)/dr$ must vanish at both radial walls giving

$$[J'_m(kr) + \xi N'_m(kr)]|_{r=a} = 0; \tag{2.59}$$

and

$$[J'_m(kr) + \xi N'_m(kr)]|_{r=b} = 0. \tag{2.60}$$

Using the two equations above, ξ is given by

$$\xi = \frac{J'_m(ka)}{N'_m(ka)} = \frac{J'_m(kb)}{N'_m(kb)}. \tag{2.61}$$

Hence, the equation that needs to be solved is

$$J'_m(ka)\,N'_m(kb) - J'_m(kb)\,N'_m(ka) = 0. \tag{2.62}$$

This still has two variables (a and b) but one may be eliminated by use of the radius ratio $\zeta = a/b$ which is a constant for a given annulus, and equation (2.62) written in terms of ζb is

$$J'_m(k\zeta b)\,N'_m(kb) - J'_m(kb)\,N'_m(k\zeta b) = 0. \tag{2.63}$$

Equation (2.63) is solved to give χ_{mn}, the n^{th} turning point for the m^{th} order solution $R_m(kr)$

$$\chi_{mn} = k_{mn} b. \tag{2.64}$$

This leads to the following expressions for X, Y and Z:

$$\left.\begin{aligned} X_N(r) &= R_m(\chi_{mn} r/b) \\ Y_N(\theta) &= \cos m\theta + \sin m\theta \\ Z_N(z) &= \cos(l\pi z/L)\,. \end{aligned}\right\} \tag{2.65}$$

Hence the wave function for the ideal annular cavity is

$$\phi_N(r,\theta,z) = R_m(\chi_{mn} r/b)\,[\cos m\theta + \sin m\theta]\cos(l\pi z/L)\,, \tag{2.66}$$

and the propagation constant k_N is

$$k_N^2 = (l\pi z/L)^2 + (\chi_{mn}/b)^2\,, \tag{2.67}$$

where $l = 0, 1, 2, 3, \ldots$, and $|m| = 0, 1, 2, \ldots l$. Each value of $|m|$, other than zero corresponds to a pair of degenerate modes, one for $+|m|$ and one for $-|m|$. The N^{th} mode has $(l+1)$ plane nodal surfaces perpendicular to the axis, $|m|$ radial nodal planes and n cylindrical nodal surfaces (except when $m = 0$ and there are $n-1$ cylindrical nodes[5]). Using appropriate properties of Bessel and trigonometric functions the orthogonality of the wavefunctions can be verified[1]. The volume integral I_V given by

$$I_V = \iiint_V \phi^* \phi dV = \iiint_V \phi^2 dV, \tag{2.68}$$

which can be written as the product of three integrals,

$$I_V = I_r I_\theta I_z. \tag{2.69}$$

Axial integral

$$\begin{aligned} I_z &= \int_0^L \cos^2(l\pi z/L)\, dz \\ &= \frac{1}{2}\int_0^L \{1 + \cos^2(2l\pi z/L)\}\, dz \\ &= \frac{L}{\varepsilon} \end{aligned} \tag{2.70}$$

where $\varepsilon = 1$ for $l = 0$ and 2 otherwise.

Angular integral

$$\begin{aligned} I_\theta &= \int_0^{2\pi} (\cos m\theta + \sin m\theta)^2\, d\theta \\ &= \int_0^{2\pi} (\cos^2 m\theta + \sin^2 m\theta + 2\cos m\theta \sin m\theta)\, d\theta \\ &= \int_0^{2\pi} (1 + 2\cos m\theta \sin m\theta)\, d\theta \\ &= \left[\theta + 2 \times \frac{1}{2m} \sin^2 m\theta\right]_0^{2\pi} \\ &= 2\pi \end{aligned} \tag{2.71}$$

Radial integral

This is Lommel's integral (a standard integral of Bessel functions) and using the result from the boundary conditions that

$$R'_m\left(\chi_{mn}r/b\right) = 0, \tag{2.72}$$

the radial integral can be shown to simplify to

$$\begin{aligned}
I_r &= \int_a^b r R_m^2\left(\chi_{mn}r/b\right) dr \\
&= \left[\frac{r^2}{2}\left\{R_m^2\left(\chi_{mn}r/b\right) - R_{m-1}\left(\chi_{mn}r/b\right) R_{m+1}\left(\chi_{mn}r/b\right)\right\}\right]_a^b \\
&= \left[\frac{r^2}{2}\left\{R_m^2\left(\chi_{mn}r/b\right) - \left[1 - \left(\frac{m}{\chi_{mn}r/b}\right)^2\right]\right\}\right]_a^b \\
&= \frac{b^2}{2}\left\{R_m^2\left(\chi_{mn}\right) - \left[1 - \left(\frac{m}{\chi_{mn}}\right)^2\right]\right\} \\
&\quad - \frac{(\zeta b)^2}{2}\left\{R_m^2\left(\chi_{mn}\zeta\right) - \left[1 - \left(\frac{m}{\chi_{mn}\zeta}\right)^2\right]\right\}
\end{aligned} \tag{2.73}$$

Normalisation constant

The normalisation integral is therefore

$$I_V = I_z I_\theta I_r \tag{2.74}$$

which as $V = \pi L\left(b^2 - a^2\right)$, the normalisation constant Λ_N^0 as defined in (2.49) can be shown to be

$$\begin{aligned}
\Lambda_N^0 = \; & \frac{1}{\varepsilon}\left[\frac{1}{1-\zeta^2}\left\{R_m^2\left(\chi_{mn}\right) - \left[1 - \left(\frac{m}{\chi_{mn}}\right)^2\right]\right\}\right. \\
& \left. -\frac{\zeta^2}{1-\zeta^2}\left\{R_m^2\left(\chi_{mn}\zeta\right) - \left[1 - \left(\frac{m}{\chi_{mn}\zeta}\right)^2\right]\right\}\right]
\end{aligned} \tag{2.75}$$

The complex natural frequencies of the resonator are given in terms of the eigenvalues by equation (2.41). When the surface admittance is zero, the eigenvalues are purely real, the complex resonance frequencies F_N equal $(u/2\pi)\,k_N$, and the only term contributing to the resonance half width g_N is that due to bulk absorption g_b given by equation (2.52).

2.7.2. Non Zero Surface Admittance

Both the real and imaginary parts of the eigenvalues will be altered by the non zero surface admittance, and the effective surface admittance changes with the properties of the fluid that fills the cavity. For the annular geometry used in this work the first order theory given in equation (2.48) is sufficient. The expectation value of y is given by

$$\langle y \rangle = \iint_S \phi^* y \phi dS = \iint_S \phi^2 y dS. \tag{2.76}$$

However y will not be the same for each wall of the cavity because the orientation of ϕ at the surface determines whether thermal and/or viscous effects must be taken into account. Hence the surface integral in equation (2.48) must be expressed as a sum of integrals over the sides and two ends of the cylinder.

For the end plates, the wave function reduces to

$$\phi_{r\theta z} = \phi_r \phi_\theta, \tag{2.77}$$

because $\phi_z = \cos(l\pi z/L) = 1$ at $z = 0$ and $z = L$. The surface increment is $dS = rdrd\theta$ on $z = 0$ and $z = L$, and the surface admittance of each end plate is given by

$$\begin{aligned}
\langle y_{\text{end}} \rangle &= y_{\text{end}} \int_0^{2\pi} \phi_\theta^2 d\theta \int_a^b r\phi_r^2 dr \\
&= y_{\text{end}} I_\theta I_r \\
&= y_{\text{end}} \pi \left\{ b^2 R_m^2(\chi_{mn}) \left[1 - \left(\frac{m}{\chi_{mn}} \right)^2 \right] \right. \\
&\qquad \left. - (\zeta b)^2 R_m^2(\chi_{mn}\zeta) \left[1 - \left(\frac{m}{\chi_{mn}\zeta} \right)^2 \right] \right\}.
\end{aligned} \tag{2.78}$$

The wave function on the cylindrical wall at $r = b$ is

$$\phi_{r\theta z} = \phi_r(b)\, \phi_\theta \phi_z, \tag{2.79}$$

where $\phi_r(b) = R_m(\chi_{mn} b/b) = R_m(\chi_{mn})$ is a constant. The surface increment is $dS = bd\theta dz$ for $r = b$. The admittance of the side wall at $r = b$ is therefore

$$\begin{aligned}
\langle y_{\text{side}b} \rangle &= y_{\text{side}b} b \phi_r^2(b) \int_0^{2\pi} \phi_\theta \int_0^L \phi_z dz \\
&= y_{\text{side}b} b R_m^2(\chi_{mn})\, I_\theta I_z \\
&= y_{\text{side}b} b R_m^2(\chi_{mn})\, 2\pi \frac{L}{\varepsilon}.
\end{aligned} \tag{2.80}$$

The wave function on the cylindrical wall at $r = a$ is

$$\phi_{r\theta z} = \phi_r(a)\,\phi_\theta\phi_z, \tag{2.81}$$

where $\phi_r(a) = R_m(\chi_{mn}a/b) = R_m(\chi_{mn}\zeta)$ is a constant. The surface increment is $dS = ad\theta dz$ for $r = a$. The admittance of the side wall at $r = a$ is therefore

$$\begin{aligned}\langle y_{\text{sidea}}\rangle &= y_{\text{sidea}}a\phi_r^2(a)\int_0^{2\pi}\phi_\theta\int_0^L\phi_z dz\\ &= y_{\text{sidea}}aR_m^2(\chi_{mn}\zeta)\,I_\theta I_z\\ &= y_{\text{sidea}}aR_m^2(\chi_{mn}\zeta)\,2\pi\frac{L}{\varepsilon}.\end{aligned} \tag{2.82}$$

The total surface admittance is hence given by a sum of the admittances of the sides and two identical ends:

$$< y >= 2\langle y_{\text{end}}\rangle + \langle y_{\text{sidea}}\rangle + \langle y_{\text{sideb}}\rangle\,. \tag{2.83}$$

Ignoring mechanical terms in the surface admittance and considering only those due to the boundary layers, the specific acoustic admittances are given by equations (2.19) and (2.20) if the effects of molecular slip and the temperature jump are ignored. Equations (2.19) and (2.20) are valid as long as δ_s,$\delta_h \ll b$. Since the viscous damping at the walls depends on the tangential component k_t of the propagation constant the boundary admittance will depend on the mode of cavity resonance. In leading order, k_t^2 is equal to $(l\pi/L)^2 + (m/b)^2$ along side b, $(l\pi/L)^2 + (m/a)^2$ along side a and $(\chi_{mn}/b)^2$ at the ends so, using the results derived above, the specific acoustic admittances are given by

$$y_{\text{sidea}} = (1+i)\left(\frac{\omega}{2u}\right)\left[(\gamma-1)\,\delta_h + \frac{(l\pi/L)^2 + (m/b\zeta)^2}{(l\pi/L)^2 + (\chi_{mn}/b)^2}\delta_s\right], \tag{2.84}$$

$$y_{\text{sideb}} = (1+i)\left(\frac{\omega}{2u}\right)\left[(\gamma-1)\,\delta_h + \frac{(l\pi/L)^2 + (m/b)^2}{(l\pi/L)^2 + (\chi_{mn}/b)^2}\delta_s\right], \tag{2.85}$$

and

$$y_{\text{end}} = (1+i)\left(\frac{\omega}{2u}\right)\left[(\gamma-1)\,\delta_h + \frac{(\chi_{mn}/b)^2}{(l\pi/L)^2 + (\chi_{mn}/b)^2}\delta_s\right]. \tag{2.86}$$

Using the results derived previously this gives

$$\begin{aligned}
\left\{\frac{2\left(g_{\mathrm{h}}+g_{\mathrm{s}}\right)}{f}\right\} V\Lambda_N^0 = & \left[\left(\gamma-1\right)\delta_{\mathrm{h}}+\left\{\frac{\left(l\pi/L\right)^2+\left(m/b\zeta\right)^2}{\left(l\pi/L\right)^2+\left(\chi_{mn}/b\right)^2}\right\}\delta_{\mathrm{s}}\right]\frac{\pi L}{\varepsilon}R_m^2\left(\chi_{mn}\zeta\right) \\
& +\left[\left(\gamma-1\right)\delta_{\mathrm{h}}+\left\{\frac{\left(l\pi/L\right)^2+\left(m/b\right)^2}{\left(l\pi/L\right)^2+\left(\chi_{mn}/b\right)^2}\right\}\delta_{\mathrm{s}}\right]\frac{\pi L}{\varepsilon}R_m^2\left(\chi_{mn}\right) \\
& +\left\{\left[\left(\gamma-1\right)\delta_{\mathrm{h}}+\left\{\frac{\left(\chi_{mn}/b\right)^2}{\left(l\pi/L\right)^2+\left(\chi_{mn}/b\right)^2}\right\}\delta_{\mathrm{s}}\right]\pi\right. \\
& \times\left[b^2\left\{R_m^2\left(\chi_{mn}\right)\left[1-\left(\frac{m}{\chi_{mn}}\right)^2\right]\right\}\right. \\
& \left.\left.\left.-\left(\zeta b\right)^2\left\{R_m^2\left(\chi_{mn}\zeta\right)\left[1-\left(\frac{m}{\chi_{mn}\zeta}\right)^2\right]\right\}\right]\right\},
\end{aligned} \tag{2.87}$$

or

$$\begin{aligned}
g_{\mathrm{h}} = & -\Delta f_{\mathrm{h}} \\
= & \frac{\left(\gamma-1\right)\delta_{\mathrm{h}}\pi f}{2V\Lambda_N^0}\left\{\left[\frac{bL}{\varepsilon}\left(\zeta R_m^2\left(\chi_{mn}\zeta\right)+R_m^2\left(\chi_{mn}\right)\right)\right]\right. \\
& +\left(b^2R_m^2\left(\chi_{mn}\right)\left[1-\left(\frac{m}{\chi_{mn}}\right)^2\right]\right. \\
& \left.\left.-\left(\zeta b\right)^2R_m^2\left(\chi_{mn}\zeta\right)\left[1-\left(\frac{m}{\chi_{mn}\zeta}\right)^2\right]\right)\right\},
\end{aligned} \tag{2.88}$$

and

$$\begin{aligned}
g_{\mathrm{s}} = & -\Delta f_{\mathrm{s}} \\
= & \frac{\delta_{\mathrm{s}}\pi f}{\left[\left(l\pi/L\right)^2+\left(\chi_{mn}/b\right)^2\right]2V\Lambda_N^0}\left\{\left[\frac{bL}{\varepsilon}\left(\left\{\left(l\pi/L\right)^2+\left(m/b\zeta\right)^2\right\}\zeta R_m^2\left(\chi_{mn}\zeta\right)\right.\right.\right. \\
& \left.\left.+\left\{\left(l\pi/L\right)^2+\left(m/b\right)^2\right\}R_m^2\left(\chi_{mn}\right)\right)\right] \\
& +\left[\left(\chi_{mn}/b\right)^2\left(b^2R_m^2\left(\chi_{mn}\right)\left[1-\left(\frac{m}{\chi_{mn}}\right)^2\right]\right.\right. \\
& \left.\left.\left.-\left(\zeta b\right)^2R_m^2\left(\chi_{mn}\zeta\right)\left[1-\left(\frac{m}{\chi_{mn}\zeta}\right)^2\right]\right)\right]\right\}.
\end{aligned} \tag{2.89}$$

Molecular slip and the temperature jump

The boundary layer theory while a good approximation is not exact. In gases at low pressure the finite length of the mean free path becomes important and hence the effects of molecular slip and the temperature jump need to be included.

Details of the theory are given in the literature[14], and the result is that the surface admittance should then be calculated from the equations below:

$$y_h = (\gamma - 1)\,(\omega/2u)\,[(1+i)\,\delta_h - 2il_h] \tag{2.90}$$

$$y_s = (k_t/k)^2\,(\omega/2u)\,[(1+i)\,\delta_s - 2il_s] \tag{2.91}$$

where l_s and l_h are the shear and thermal accommodation lengths respectively. The accommodation coefficients are given by the following expressions;

$$l_h = \left(\frac{\kappa}{p}\right)\sqrt{\frac{\pi MT}{2R}}\left[\frac{(2-h)}{2h}\right], \tag{2.92}$$

and

$$l_s = \left(\frac{\eta}{p}\right)\sqrt{\frac{\pi MT}{2R}}\left[\frac{(2-s)}{s}\right], \tag{2.93}$$

where h and s represent the thermal and shear accommodation coefficients respectively.

The half-widths remain unchanged by inclusion of these effects but the frequency is shifted slightly and hence Δf_s and Δf_h become

$$-\Delta f_h = g_h(1 - 2l_h/\delta_h), \tag{2.94}$$

and

$$-\Delta f_s = g_s(1 - 2l_s/\delta_s). \tag{2.95}$$

However, there is no *a priori* way of calculating the shear and thermal accommodation lengths. For the spherical geometry only l_h is important, the magnitude of which may be estimated as the value that gives the best agreement for the resonance modes measured. This is possible because δ_h is a frequency dependent quantity which therefore differs for each normal mode. This approach is not possible for the annular geometry because both penetration lengths have the same frequency dependence and the contributions from molecular slip and the temperature jump effect cannot be resolved. At the pressures used in this work it is estimated that these effects are negligible when compared to the uncertainties in calculating the correction terms. This is discussed further in later chapters.

2.7.3. Openings in the Resonator Wall

If there is an opening in the wall of the resonator, then the specific acoustic admittance will differ from that given by equation (2.83) over the area S_o of

that opening. In leading order, the shift Δf_o in the resonance frequency and contribution g_o to the half width of a resonance mode will be

$$\Delta f_o + i g_o = \frac{i y_o \iint_{S_o} \phi^2 dS_o}{2V\Lambda_N^0}, \tag{2.96}$$

where y_o is the specific acoustic input admittance of the opening. The sound source and microphone used for the generation and detection of sound necessarily cause openings in the resonator wall as does the gas inlet tube. For narrow tubes such as these operated at frequencies below the cut off where only plane waves can propagate, the admittance is constant over any cross section of the tube. The value at the opening y_o, may be expressed in terms of the value y_L at the termination of the tube of length L and the propagation constant for plane waves travelling through the tube. Losses at the wall of the tube may be allowed for by setting the propagation constant equal to the Kirchhoff-Helmholtz value

$$k_{KH} = (\omega/u) + (1-i)\,\alpha_{KH}, \tag{2.97}$$

where

$$\alpha_{KH} = \frac{(\gamma-1)\,\delta_h + \delta_s}{r_o}, \tag{2.98}$$

and r_o is the tube radius.

If the tube is closed at the end remote from the resonator by a rigid termination then the specific acoustic admittance at the opening is

$$y_o = i \tan(k_{KH} L)\,. \tag{2.99}$$

The sound source and microphone are closed tubes and the admittance of these may be approximated by equation (2.99). For the case of a tube open to free space such as the gas inlet pipe the specific acoustic admittance at the opening in the resonator is

$$y_o = -i \cot(k_{KH} L)\,. \tag{2.100}$$

Modifications to these expressions to account for the complexities of real tubes, such as a flanged open tube or tube ending in a terminal volume have been considered[7]. These effects however, are small in comparison with the uncertainty in the calculated value of the perturbation due to geometric factors and need not be considered here.

At a resonance frequency of the gas filled cavity, (ω/u) is k_N for the normal mode, and under the conditions of the measurements, $\alpha_{KH}L \ll 1$ and negligible compared to $k_N L$. Thus $k_{KII} = k_N$, and the corrections to the resonance frequencies may be calculated if the geometry of the tube is known. The perturbation may be minimised through the length L of the tube or by minimising the surface integral in equation (2.96) through the choice of the position of the opening. These design considerations and the limitations on the accuracy of the calculated perturbation are discussed in later chapters.

2.7.4. Shell Motion

The contribution of the wall itself to the effective acoustic surface admittance is usually small but may not always be neglected. Unfortunately an exact solution for the modes of motion of an annular shell is not possible in closed form and as yet a detailed approximation has not been derived. From general considerations it may be inferred that the coupling of fluid and shell motion must cause a perturbation Δf_{sh} to the resonance frequencies that is linear in the fluid density. At frequencies small compared with that of the lowest resonance frequency of the wall, the mechanical admittance is given by[1]

$$y_{sh} = -i2\pi f \rho u b C \tag{2.101}$$

where C is the static compliance of the tube with respect to variation of the internal pressure which also cannot be calculated exactly for an annular shell. By analogy with a simplification of the exact results for a sphere[5], at frequencies near to a shell resonance, equation (2.101) is likely to become

$$y_{sh} = \frac{i2\pi f \rho u b C x}{\left[1 - (f/f_{sh})^2\right]}. \tag{2.102}$$

In equation (2.102) f_{sh} is the frequency of the nearest shell resonance. x is a coupling constant that arises due to the differing symmetries of the wall and shell motion that is also unknown, and in addition is dependent on the mode of excitation of the fluid in the cavity. Note that iy_{sh} is purely real in this approximation and therefore contributes only a shift in the resonance frequencies of the fluid within the cavity,

$$\Delta f_{sh} = \frac{-f \rho u^2 C x}{\left[1 - (f/f_{sh})^2\right]} \tag{2.103}$$

without a corresponding contribution to the half width. Losses in the wall material itself[5] and the smaller losses due to radiation from the external surface[1] may be accounted for by the inclusion in series with the lossless impedance of the shell an additional term incorporating the quality factor Q_{sh} for the damped shell resonance,

$$\Delta f_{sh} = \frac{-f\rho u^2 C x}{\left[1-(f/f_{sh})^2 + i\,(f/f_{sh}Q_{sh})\right]}. \tag{2.104}$$

The frequencies of any shell resonances may be determined experimentally[7],[15], and the value of C estimated from elastic theory but the values of x, and Q_{sh} can only be determined empirically by fitting these parameters for the affected modes. This is only possible if results are available over a wide range of frequencies and unperturbed modes are also available. As such data were not available the parameters in equation (2.104) could not be determined for the affected modes measured in this work.

BIBLIOGRAPHY

[1] Trusler J P M. *Physical Acoustics and Metrology of Fluids.* (Adam Hilger: Worcester, 1991).

[2] Morse P M. *Vibration and Sound.* (McGraw-Hill: York, 1948).

[3] Morse P M and Ingard K U. *Theoretical Acoustics.* (McGraw-Hill: New York, 1968).

[4] Mehl J B and Moldover M R. *Topics in Current Physics, Volume 46.* (Springer-Verlag: 1989).

[5] Moldover M R, Mehl J B and Greenspan M. *J. Acoust. Soc. Am.* 1986, **79(2)**, 253.

[6] Ewing M B, Goodwin A R H, McGlashan M L and Trusler J P M. *J. Chem. Thermodyn.* 1987, **19**, 721.

[7] Goodwin A R H. Ph.D Thesis, University of London 1988.

[8] Herzfeld K F and Litovitz T A. *Pure and Applied Physics Volume 7: Absorption and Dispersion of Ultrasonic Waves.* Editor: Massey H S W. (Academic Press: London, 1959).

[9] Lambert J D. *Vibrational and Rotational Relaxation in Gases.* (Clarendon Press: Oxford, 1977).

[10] Mehl J B, Moldover M R. *J. Chem. Phys.* 1981, **74**, 4062.

[11] Ewing M B and Trusler J P M. *J. Chem. Phys.* 1989, **90**, 1106.

[12] Colclough A R. *Proc. R. Soc* A 1979, **365**, 349.

[13] Trusler J P M. Ph.D Thesis, University of London 1984.

[14] Ewing M B, Mc Glashan M L and Trusler J P M. *Metrologia* 1986, **22**, 93.

[15] Boyes S J. Ph.D Thesis, University of London 1988.

3. EQUATIONS OF STATE

3.1. Introduction

According to the phase rule, a phase of fixed composition has two degrees of freedom. It follows that a chosen intensive property, X_1 may be described in terms of two other independent intensive properties X_2 and X_3 by an equation of state:

$$X_1 = X_1 (X_2, X_3) \tag{3.1}$$

Using equation (3.1) any intensive property may be described in terms of X_2 and X_3 by using the appropriate thermodynamic relations.

3.2. Equations of State

Classically equations of state for a gaseous phase of fixed composition have related the intensive properties of the system, pressure p, molar volume V_m and temperature T by either:

1) an infinite power series in one of the intensive properties, usually V_m or p, or

2) closed empirical expressions.

The category of closed empirical equations falls into two types, those that are cubic in V_m and closely resemble the van der Waals equation of state, and those that have a variety of functional forms.

3.2.1. The Virial Equation of State

The virial equation of state which may be rigorously derived from statistical mechanics[1], can be written in terms of the molar volume or in a pressure explicit form:

$$Z_m = \frac{pV_m}{RT} = 1 + \frac{B}{V_m} + \frac{C}{V_m^2} + \cdots, \tag{3.2}$$

or

$$Z_{\mathrm{m}} = \frac{pV_{\mathrm{m}}}{RT} = 1 + \frac{B'}{RT}p + \frac{C'}{RT}p^2 + \cdots, \tag{3.3}$$

where R is the gas constant, and B, C, $\cdots$ are second, third, $\cdots$ virial coefficients. The coefficients of the two equations are functions of temperature only and are related by

$$\left.\begin{aligned} B' &= B \\ C' &= \frac{(C - B^2)}{RT} \end{aligned}\right\}. \tag{3.4}$$

The intermolecular energies of clusters of two, three, $\cdots$ molecules are related to B, C, $\cdots$ by a statistical mechanical derivation of equation (3.2). In particular, B is given by

$$B = 2\pi L \int_0^\infty [1 - \exp\{-U(r)/kT\}] r^2 dr, \tag{3.5}$$

in which $U(r)$ is the pair wise intermolecular energy function and r the intermolecular separation[2]. Expressions for the higher order coefficients are complicated by the non pairwise additivity of the intermolecular potential energies.

The second virial coefficient of a gas mixture with components A, B, $\cdots$ in mole fractions x_{A}, x_{B}, $\cdots$ is given by

$$B(T, x_{\mathrm{A}}, x_{\mathrm{B}}, \cdots) = \sum_i \sum_j x_i x_j B(T)_{ij} \tag{3.6}$$

where i, j = A, B, $\cdots$. For the binary gas mixture $\{(1-x)\,\mathrm{A} + x\mathrm{B}\}$, equation (3.6) is written

$$B(T, x) = (1-x)^2 B_{\mathrm{AA}} + 2(1-x)\,x B_{\mathrm{AB}} + x^2 B_{\mathrm{BB}} \tag{3.7}$$

where B_{AA} and B_{BB} are virial coefficients arising from pure A and pure B respectively, and B_{AB}, the cross virial coefficient, arises from interactions between A and B.

Both equations (3.2) and (3.3) suffer from the disadvantage that they must be truncated to represent a given set of experimental data and criteria for determining the number of coefficients that may be justified have been discussed in the literature[3]-[5]. The problem of finding accurate values for the coefficients is more subtle, for example to find reliable values of B, measurements must be extended to sufficiently low pressures that the definition[6],[7]

$$B = \lim_{p \to 0} \left\{ \frac{pV_{\mathrm{m}}}{RT} - 1 \right\} V_{\mathrm{m}}, \tag{3.8}$$

is realised.

3.2.2. Empirical Equations

Many empirical equations of state are elaborations of the van der Waals equation. The simple cubic equations modify the attractive and repulsive terms independently, whereas in the non cubic expressions both are modified simultaneously and, as a consequence they have a variety of functional forms and rapidly become complicated.

Simple cubic equations

The van der Waals equation of state[8] is given by

$$p = \frac{RT}{V_{\mathrm{m}}(1-4y)} - \left(\frac{a}{V_{\mathrm{m}}^2}\right), \tag{3.9}$$

where y the fraction of the volume occupied by the molecules, is

$$y = \frac{b}{4V_{\mathrm{m}}}, \tag{3.10}$$

and b is the volume excluded by the molecules. The first term of equation (3.9) approximates the pressure of a hard sphere gas and the second represents the influence of attractive interactions between molecules. This equation like all analytic expressions for the equation of state breaks down at the critical point where it lacks an appropriate singularity and, in addition is limited in its usefulness because it generally gives only qualitative agreement with experimental data.

If a pure fluid obeys the principle of corresponding states then the compression factor Z_{m} may be written in the form

$$Z_{\mathrm{m}} = \frac{pV_{\mathrm{m}}}{RT} = \phi\left(p/p^{\mathrm{c}}, T/T^{\mathrm{c}}\right), \tag{3.11}$$

in which p^{c} is the critical pressure and T^{c} the critical temperature, and where ϕ is the same function for each fluid. Substances that do not obey the principle of corresponding states may be included by extending equation (3.11) to three variables. An important example is Pitzer's equation[9]

$$Z_{\mathrm{m}} = \frac{pV_{\mathrm{m}}}{RT} = \phi_{\omega}\left(p/p^{\mathrm{c}}, T/T^{\mathrm{c}}, \omega\right), \tag{3.12}$$

in which the acentric factor ω, defined by

$$\omega = \log_{10}\left[p^{\mathrm{c}}/p^{1+\mathrm{g}}\left(T/T^{\mathrm{c}} = 0.7\right)\right] - 1, \tag{3.13}$$

was chosen such that $\omega \approx 0$ for Ar, Kr and Xe. When $\omega = 0$, equation (3.12) reduces to equation (3.11) and substances such as Ar, Kr and Xe have the same compression factor at the same reduced temperatures and pressures. Other important examples may be found in the literature[10]-[12] that include molecular shape factors, however usually they are only useful over the limited ranges for which the additional parameter has been optimised.

The simple cubic equations may be generalised[13] to give

$$p = \frac{RT}{(V_m - b)} - \frac{a(T)}{\{V_m^2 + V_m cb - (c-1)b^2\}}, \quad (3.14)$$

in which c is chosen empirically, and $a(T)$ and b are parameters which have been adjusted using T^c, p^c and ω. When $c = 1$ equation (3.14) becomes the Redlich-Kwong equation[14] for which

$$a(T) = \frac{a(T^c)}{T^{\frac{1}{2}}}, \quad (3.15)$$

and $Z^c = 1/3$. Soave[15] extended the temperature dependence by modifying $a(T)$ to

$$a(T) = a(T)\,\alpha(T/T^c) = a(T^c)\left[1 + \left(e + f\omega + g\omega^2\right)\left\{1 - (T/T^c)^{\frac{1}{2}}\right\}\right]^2. \quad (3.16)$$

Gibbons and Laughton[16] further modified $\alpha(T/T^c)$ to give

$$a(T) = a(T)\,\alpha(T/T^c) = a(T^c)\left[1 + X(T/T^c - 1) + Y\left\{(T/T^c)^{\frac{1}{2}} - 1\right\}\right] \quad (3.17)$$

in which X and Y are substance dependent parameters. The Peng-Robinson equation[17] has $c = 2$ and an $a(T)$ of the same form as Soave. As a final example Harmens et al.[18],[19] developed equations with $c = 3$ and c as an adjustable parameter. Values of the variables in each equation of state are discussed in the relevant papers and in general they predict compression factors for gases to within a few per cent.

The equations discussed above retain the hard sphere term in the van der Waals equation, but modify the attractive term. The alternative is to elaborate the repulsive term. The virial expansion for a hard sphere fluid correct to sixth order in y is[20]

$$Z_H = \frac{pV_m}{RT} = 1 + 4y + 10y^2 + 18.365y^3 + 28.26y^4 + 39.5y^5 + 57y^6 + \cdots, \quad (3.18)$$

in which y is defined as in equation (3.10). The van der Waals expansion

$$Z_{\mathrm{H}} = 1 + 4y + 16y^2 + 64y^3 + \cdots \tag{3.19}$$

is only correct to first order in y by comparison. Carnham and Starling[21] developed a closed form expression

$$\begin{aligned} Z_{\mathrm{H}} &= \frac{(1 + y + y^2 - y^3)}{(1-y)^3} \\ &= 1 + 4y + 10y^2 + 18y^3 + 28y^4 + 40y^5 + 54y^6 + \cdots, \end{aligned} \tag{3.20}$$

that is a much better approximation to equation (3.18).

Non cubic empirical equations

When the repulsive and attractive terms are modified simultaneously, expressions are generated that are no longer cubic in V_{m}. The best known of such equations of state is due to Beattie and Bridgeman[22], and may be written

$$\begin{aligned} p = \ & \frac{RT}{V_{\mathrm{m}}} + \frac{(B_0 RT - A_0 - Rc/T^2)}{V_{\mathrm{m}}^2} \\ & + \frac{(aA_0 - B_0 bRT - RB_0 c/T^2)}{V_{\mathrm{m}}^3} + \frac{RB_0 bc}{V_{\mathrm{m}}^4 T^2}, \end{aligned} \tag{3.21}$$

where a, b, c, A_0 and B_0 are adjustable parameters. The expression only provides a representation of fluids below the critical density. Benedict, Webb and Rubin[23] modified equation (3.21) to extend its applicability up to densities twice the critical value by use of two additional parameters α and γ:

$$\begin{aligned} p = \ & \frac{RT}{V_{\mathrm{m}}} + \frac{(B_0 RT - A_0 - C_0/T^2)}{V_{\mathrm{m}}^2} + \frac{(bRT - a)}{V_{\mathrm{m}}^3} \\ & + \frac{(a\alpha)}{V_{\mathrm{m}}^6} + \frac{[c(\gamma - 1/V_{\mathrm{m}}^2)\exp(-\gamma/V_{\mathrm{m}}^2)]}{V_{\mathrm{m}}^3 T^2}. \end{aligned} \tag{3.22}$$

More precise representations of volumetric results, and more recently other properties have been achieved using further modifications[24],[25] to give expressions with a variety of functional forms but all contain exponential terms.

Equations of state derived solely from experimental results allow good agreement to experimental results by the revision of functional forms and optimisation of the parameters. Equations that are particularly successful when applied to mixtures are due to Schouten *et al.*[26]-[29] and Starling *et al.*[30], but it must be remembered that they are only applicable to the components and composition ranges stated.

3.3. Experimental Techniques

3.3.1. (p, V, T) Methods

Most equation of state information has been acquired using (p, V_m, T) methods. The molar volume $V_m = V/n$, which is an intensive property cannot be measured directly and therefore must be determined from the vessel volume V, and amount of substance n, which are both extensive properties.

Boyle's tube is one of the most simple experimental designs, in which the pressure p is measured of a fixed amount of substance confined within a variable volume V at constant temperature T. The amount of substance is given by $\lim_{p\to 0}\{pV/RT\}$. The apparatus may be calibrated using a gas with a known equation of state, or the experimental volumes may be determined by finding the mass of mercury required to fill each one. Mercury is also used to confine the fluid and to calculate the sample pressure and so such measurements are limited to the range over which mercury is a liquid with an acceptably low vapour pressure.

Expansion methods such as that devised by Burnett[31] avoid the use of mercury. Successive expansions are performed until the pressure can no longer be determined accurately. The Burnett method gives the compression factor Z directly, so such methods have been utilised at high pressures where the truncation of the virial expansion at the appropriate order may be a problem.

Methods such as those described above may also be used to study gas mixtures and have been used to obtain B_{AB} for binary mixtures[13] from measurements of $B(T, x)$ and B_{AA} and B_{BB}. More direct techniques are available based on the measurement of the interaction virial coefficients

$$\delta_{AB}(T) = B_{AB}(T) - \frac{1}{2}\left[B_{AA}(T) + B_{BB}(T)\right], \tag{3.23}$$

from either the pressure change on mixing at constant volume[32], or the volume change on mixing at constant pressure[33].

So far, the effect of adsorption has been neglected but it severely limits the experimental accuracy at pressures approaching the vapour pressure. As adsorption depends on the surface area to volume ratio it varies from one experimental method to another. For example, in methods involving the use of mercury, material is lost by the advancing meniscus in compression methods and in expansion

methods degassed surfaces are exposed. Adsorption models have been used to calculate corrections terms[7], but if information is required under conditions when adsorption is significant then alternatives to (p, V_m, T) methods must be sought.

3.3.2. Calorimetric Methods

The equation of state in the form

$$H_m = H_m(p, T), \tag{3.24}$$

may be studied using a flow calorimeter consisting of a pipe containing a throttle and heater. The molar enthalpy change is given by

$$H_m(p_2, T_2) - H_m(p_1, T_1) = \frac{P}{\partial n/\partial t}, \tag{3.25}$$

when the calorimeter is adiabatic and the changes in the potential and kinetic energies of the gas are small. In equation (3.25), 1 and 2 denote the state of the gas on either side of the throttle, P is the steady state power dissipated in the heater, and $\partial n/\partial t$ is the flow rate of fluid through the calorimeter.

In the isothermal Joule-Thomson experiment, the power P is adjusted such that $T_2 = T_1$, and the isothermal Joule-Thomson coefficient

$$\begin{aligned} \phi_{JT} = \left(\frac{\partial H}{\partial p}\right)_T &= \left[V_m - T\left(\frac{\partial V_m}{\partial T}\right)_p\right] = -\left[\frac{RT^2}{p}\right]\left(\frac{\partial Z}{\partial T}\right)_p \\ &= \lim_{p_1 \to p_2}\left[\frac{\{H(T, p_2) - H(T, p_1)\}}{p_2 - p_1}\right], \end{aligned} \tag{3.26}$$

is useful for obtaining equation of state information where adsorption would be a problem in (p, V_m, T) methods[34]. This method is complicated by the presence of heat leaks near the throttle that compromise the accuracy of experimental measurements.

The isenthalpic Joule-Thomson coefficient

$$\mu_{JT} = \left(\frac{\partial T}{\partial p}\right)_H = -\frac{\left\{V_m - T(\partial V_m/\partial T)_p\right\}}{C_{p,m}}, \tag{3.27}$$

may be determined when no power is supplied to the heater. Equation of state data may also be obtained from this relation provided that the heat capacity is known.

If the calorimeter contains no throttle and energy is dissipated in the heater, then the heat capacity may be obtained directly from the expression

$$C_{p,\mathrm{m}} = \left(\frac{\partial H_{\mathrm{m}}}{\partial T}\right)_p = \lim_{T_1 \to T_2} \left[\frac{\{H(T_2,p) - H(T_1,p)\}}{T_2 - T_1}\right]. \tag{3.28}$$

A combination of isenthalpic and heat capacity calorimeters in the same flow system thus gives ϕ_{JT} from

$$\phi_{\mathrm{JT}} = -C_{p,\mathrm{m}}\mu_{\mathrm{JT}}, \tag{3.29}$$

and this method has been used successfully to obtain equation of state data for both pure gases[35] and binary gas mixtures[36].

3.3.3. Speed of Sound Measurements

As an alternative to (p,V,T) relations, equations of state may be written in the form

$$u^2 = u^2(T,p), \tag{3.30}$$

and, as the speed of sound u is independent of the amount of substance, experimental measurements of this quantity should be immune from the effects of adsorption suffered by other methods. However, anomalous results at pressures approaching the vapour pressure have been observed and interpreted by Mehl and Moldover in terms of a precondensation phenomenon[37]. They observed that the effect was greatest at low frequencies, depended on the surface finish of the resonator, and resulted in an apparent decrease in the resonance frequencies and an accompanying increase in the resonance half-widths at pressures greater than 0.6 of the vapour pressure. As described in chapter 1, the (p,V,T) virial coefficients are related to the acoustic virial coefficients and the method used in this work to obtain values for the second virial coefficient from acoustic measurements is discussed in greater detail in chapter 7.

3.4. Sonic Nozzles

Sonic nozzles[38] consist of a tube of variable cross section through which a steady flow of gas occurs from a large vessel. The importance of sonic nozzles lies in their simplicity and lack of moving parts allowing them to be easily maintained and making them a likely candidate for flow metering standards within the gas

industry. In order to obtain reliable estimates of the speed of sound at the steady state conditions at the throat of the nozzle and thus calculate the mass flow rate, an equation of state and a method of prediction of the perfect gas heat capacities is required. Thus evaluation of equations of state by comparison with speed of sound results are important for obtaining reliable estimates of flow rates. Boyes[39] has made comparisons between the calculated speeds of sound derived from the equations of state described earlier and his speed of sound results for the industrially important gases methane and a binary mixture of methane and ethane. He found that the agreement was better than 1 % over the experimental range and generally better than 0.5 %.

BIBLIOGRAPHY

[1] Mayer J E and Mayer M G. *Statistical Mechanics.* Second Edition (Wiley: New York, 1977).

[2] Maitland G C, Rigby M, Smith E B and Wakeham W A. *Intermolecular Forces. Their Origin and Determination.* (Clarendon: Oxford, 1981).

[3] Hall K R and Canfield FB. *Physica.* 1967, **33,** 481.

[4] Holleran E M. *J. Chem. Thermodyn.* 1970, **2,** 779.

[5] Ewing M B and Marsh K N. *J. Chem. Thermodyn.* 1979, **11,** 793.

[6] Scott R L. *J. Phys. Chem.* 1962, **66,** 639.

[7] Knobler C M. *Pure and Appl. Chem.* 1983, **55,** 455.

[8] van der Waals J D. Thesis: Leydon 1873.

[9] Pitzer K S, Lipman R F, Curl R F, Huggins C M and Peterson D E. *J. Am. Chem. Soc.* 1955, **77,** 3433.

[10] Leland T W and Chappelear P S. *Ind. Eng. Chem.* 1968, **60,** 15.

[11] Leach J W, Chappelear P S and Leland T W. *A. I. Ch. E. J.* 1968, **14,** 568.

[12] Fisher G D and Leland T W. *Ind. Eng. Chem. Fundamentals.* 1970, **9,** 537.

[13] Goodwin A R H. Ph.D. Thesis: London 1988.

[14] Redlich O and Kwong J N S. *Chem. Rev.* 1949, **44,** 223.

[15] Soave G. *Chem. Eng. Sci.* 1972, **27,** 1197.

[16] Gibbons R M and Laughton A P. *J. Chem. Soc. Faraday Trans. 2.* 1984, **80,** 1019.

[17] Peng D Y and Robinson D B. *Ind. Eng. Chem. Fundamentals.* 1976, **15**, 59.

[18] Harmens A. *Cryogenics.* 1977, **17**, 519.

[19] Harmens A and Knapp H. *Ind. Eng. Chem. Fundamentals.* 1980, **19**, 291.

[20] Ree F H and Hoover W G. *J. Chem. Phys.* 1964, **40**, 939.

[21] Carnahan N F and Starling K E. *J. Chem. Phys.* 1969, **51**, 635.

[22] Beattie J A and Bridgeman O C. *Proc. Amer. Acad. Arts Sci.* 1929, **63**, 229.

[23] Benedict M, Webb G B and Rubin L C. *J. Chem. Phys.* 1940, **8**, 334.

[24] McCarty R D. *Experimental Thermodynamics Volume II.* (Butterworths: London, 1968).

[25] Younglove B A and McCarty R D. *J. Chem. Thermodyn.* 1980, **12**, 1121.

[26] Schouten J A, Michels J P J, Prins C, van der Gulik P S and Trappeniers N J. *Report No. 8410-1,* (van der Waals Laboratory: Netherlands, 1984)

[27] Schouten J A, ten Seldam G A, Biswas S N, Michels J P J and Trappeniers N J. *Report No. 8410-2,* (van der Waals Laboratory: Netherlands, 1984)

[28] Schouten J A, ten Seldam G A, Michels J P J and Trappeniers N J. *Report No. 8410-3,* (van der Waals Laboratory: Netherlands, 1984)

[29] Schouten J A and Michels J P J. *Report No. 8410-4,* (van der Waals Laboratory: Netherlands, 1984)

[30] Starling K E, Klein M and Little F G. *Proc. Congress Gas Quality- Specification and Measurement of Physical and Chemical Properties of Natural Gas.* Editor: van Rossum G J. (Elsevier: Oxford, 1986).

[31] Burnett E S. *J. Appl. Mech.* 1936, **3A**, 136

[32] Knobler C M, Beenakker J J M and Knapp H F P. *Physica.* 1959, **25**, 909.

[33] Din F and Burn I. *Trans. Faraday Soc.* 1965, **61**, 1351.

[34] Francis P G and Phutela R C. *J. Chem. Thermodyn.* 1979, **11**, 747.

[35] Bier K, Kunze J and Maurer G. *J. Chem. Thermodyn.* 1976, **8**, 857.

[36] Bier K, Kunze J and Maurer G. *J. Chem. Thermodyn.* 1980, **12**, 151.

[37] Mehl J B and Moldover M R. *J. Chem. Phys.* 1982, **77**, 455.

[38] Landau L D and Lifshitz E M. *Course of Theoretical Physics: Volume 6. Fluid Mechanics.* Second Edition (Permagon Press: 1987)

[39] Boyes S J. Ph.D. Thesis: London 1992.

4. APPARATUS

4.1. Introduction

The novel annular resonator constructed for this work is described in detail below. The design of the inlet tube and the transducers are discussed with reference to minimising the resultant perturbations to the resonance frequencies. The thermal environment of the resonator is discussed with particular attention to the methods used to reduce the heat leaks to the surroundings in order to obtain a uniform temperature distribution throughout the resonator. Finally the temperature control system developed for the apparatus is outlined.

4.2. The Annular Resonator

The cylindrical walls of the resonator were turned from aluminium alloy 6082. The outer cylinder had a nominal inner radius of 139.7 mm and outer radius of 152.4 mm. The inner cylinder had an outer radius of 74.5 mm and inner radius of 61.8 mm before polishing. The cylindrical walls had a final length of 59.0 mm. In choosing the geometry of the resonator a balance was struck between the need for the modes to be resolved and the need for resonances with high quality factors. Increasing the radius ratio allows more azimuthal modes to be at lower frequencies than the radial, longitudinal or mixed modes but increases the surface area to volume ratio thus reducing the quality factors for the resonances. The radii of the cylinders and length of the resonator were chosen such that the first five azimuthal modes $\{(0, m, 1)\ m = 1 - 5\}$ occurred at lower frequency than any other type. In the resonator described here for which the radius ratio $\zeta \simeq 0.532$ the quality factor $Q = 172$ for the $(0, 1, 1)$ mode in Ar at 300 K and 100 kPa. Increasing the radius ratio to $\zeta = 0.9$ would allow the first seven azimuthal modes to occur before any other type of mode but the quality factor would be reduced to $Q = 57$ for the $(0, 1, 1)$ mode in Ar at 300 K and 100 kPa. Decreasing the

Figure 4.1: The frequencies of the resonance modes up to 4.2 kHz in the resonator filled with Ar at 100 kPa and 300 K.

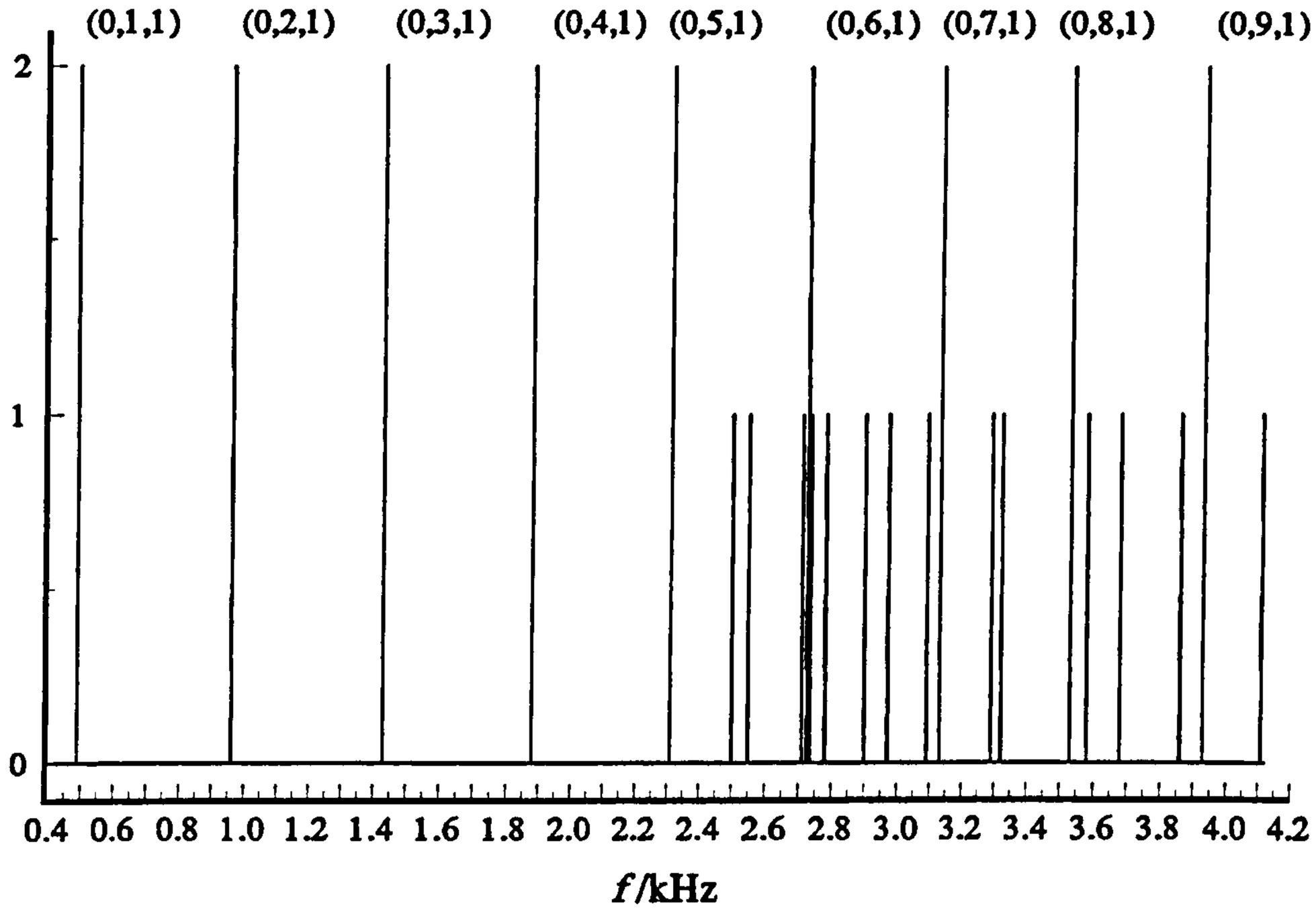

radius ratio to $\zeta = 0.1$ increases the quality factor to $Q = 266$ for the $(0, 1, 1)$ mode in Ar at 300 K and 100 kPa but then only two azimuthal modes would occur at lower frequency than other types of mode. With such a low radius ratio the higher order azimuthal modes cannot be resolved due to overlap with radial and mixed modes.

The frequencies of the resonance modes in Ar at 300 K and 100 kPa up to 4.2 kHz are shown in figure (4.1). The $(0, 6, 1)$ azimuthal mode cannot be resolved as it lies too close to the $(0, 2, 2)$ mixed radial-azimuthal mode and the first $(1, 0, 1)$ longitudinal mode. With this design the first radial $(0, 0, 2)$ mode may be resolved. During the design phase of this work, it was thought that this radial mode would be measured. However initial measurements in He showed it was not possible to find a radius ratio that gave agreement between it and the azimuthal modes and it was hence rejected. The resonance modes finally measured were the $(0, m, 1)$ azimuthal modes where $m = 1 - 5, 7 - 9$. The higher order modes were included in order to avoid the effects of the shell resonance. The first $(0, 1, 1)$ azimuthal mode was not measured as it lay below the cut off frequency of the bandpass amplifier of 0.3 kHz for some of the gases under study.

The bottom plate of the resonator was 15.88 mm thick, calculated to safely withstand a pressure of 1 MPa by comparison with a circular plate of the same surface area. This method probably overestimates the thickness required, but the greater thickness helped to prevent the end plates from deforming when the resonator was pressurised. The top plate of the resonator was 19.05 mm thick to allow for the extra stresses caused where holes were machined to house the transducers and the gas inlet tube.

The surfaces comprising the interior of the resonator were hand polished to remove tooling marks first with emery paper, then with silicon carbide papers of varying grit size and finally with aluminium oxide pastes with particle sizes decreasing from 5 μm down to 0.03 μm. The surface had a near mirror finish viewed with the naked eye. The transducer ports and hole for the inlet tube were then machined in the top plate, and the side cylindrical walls were turned down to their final length of 59.00 mm. As the resonator was constructed from aluminium, welding of the joins to give a pressure tight seal was not feasible, and an additional problem was that threads turned into aluminium are easily deformed. In order to safely withstand the maximum working pressure of 1 MPa, 4 mm diameter stainless steel studding was passed through the full length of the walls and end plates and bolted at either end. The number of pieces of studding used was chosen to allow the full load at the maximum working pressure to be withstood by just one turn of the thread on the studding. Twenty equidistant pieces were bolted through the outer wall and ten through the inner wall. Nitrile O-rings, which may be used over the temperature range 218 K to 398 K, were employed to seal the resonator. The grooves cut into the cylindrical walls to house the O-rings were machined close to the upper size tolerance limit to prevent the O-rings from extruding into the body of the resonator. The interior of the assembled resonator was viewed through the transducer ports to check the four seals. The transducers and inlet pipe were screwed into place using indium wire to provide seals between the components and the resonator. After assembly all the seals were checked using a helium leak tester.

4.3. Inlet Tube

A length of stainless steel tubing (3.18 mm i.d. and 2.58 mm o.d.) was embedded in the top plate of the resonator, which was drilled through with the appropriate diameters to form a gas inlet tube of length $L_i = 67.0$ mm and diameter 2.58 mm. As described in equation (1.96) the correction for a hole in the resonator wall is proportional to the square of the wavefunction ϕ_N^2 over the surface of the hole, so an obvious way to reduce the perturbation is to place the inlet tube at a minimum in the wave function. The tube was placed at $r/b = 0.78$ where the wavefunction for the $(0,0,2)$ radial mode was at a minimum. The tube was positioned at an angle of $\pi/2$ from the two transducers where the wavefunctions for all the azimuthal modes with odd index m (i.e. $(0,m,1)$ modes where $m = 1,3,5,7,9\ldots$) were also at minima. Unfortunately, the azimuthal modes with even index m have maxima at this angle to the transducers. The perturbation to these modes is minimised by using tubing of a small diameter, thus reducing the area over which the squared wavefunction ϕ_N^2 is integrated. The correction can be further reduced by varying the length L_i of the tube because the correction is also proportional to the acoustic admittance, y_o of the hole, which for an open tube is given by $y_o = i\tan(k_{KH}L_i)$. The requirements for pumping the resonator down to vacuum to prevent the contamination of subsequent samples restricts the length of tubing which may be used for a given diameter. A length of 67 mm was chosen from a systematic search because it gave a reasonable values ($-\Delta f_o/f \approx 30$ ppm) for the correction to all the measured modes with even index m (i.e. $(0,m,1)$ modes where $m = 2,4,6,8$), and did not compromise the conductance of gas out of the resonator at low pressures.

4.4. Transducers

Capacitance transducers are very sensitive wide band devices ideal for sound generation and detection in gases as their intrinsic noise level is very small[1]. The parallel plate capacitance transducers employed in this work were machined from brass and took the form of a massive metal back plate, and light front plate of tensioned metallised polymer film. The polymer membrane moves in response to incident sound waves when operated as a detector, or in response to an a.c. signal

Figure 4.2: The squared wavefunction ϕ_N^2 for the first radial mode and first five azimuthal modes along the radial coordinate.

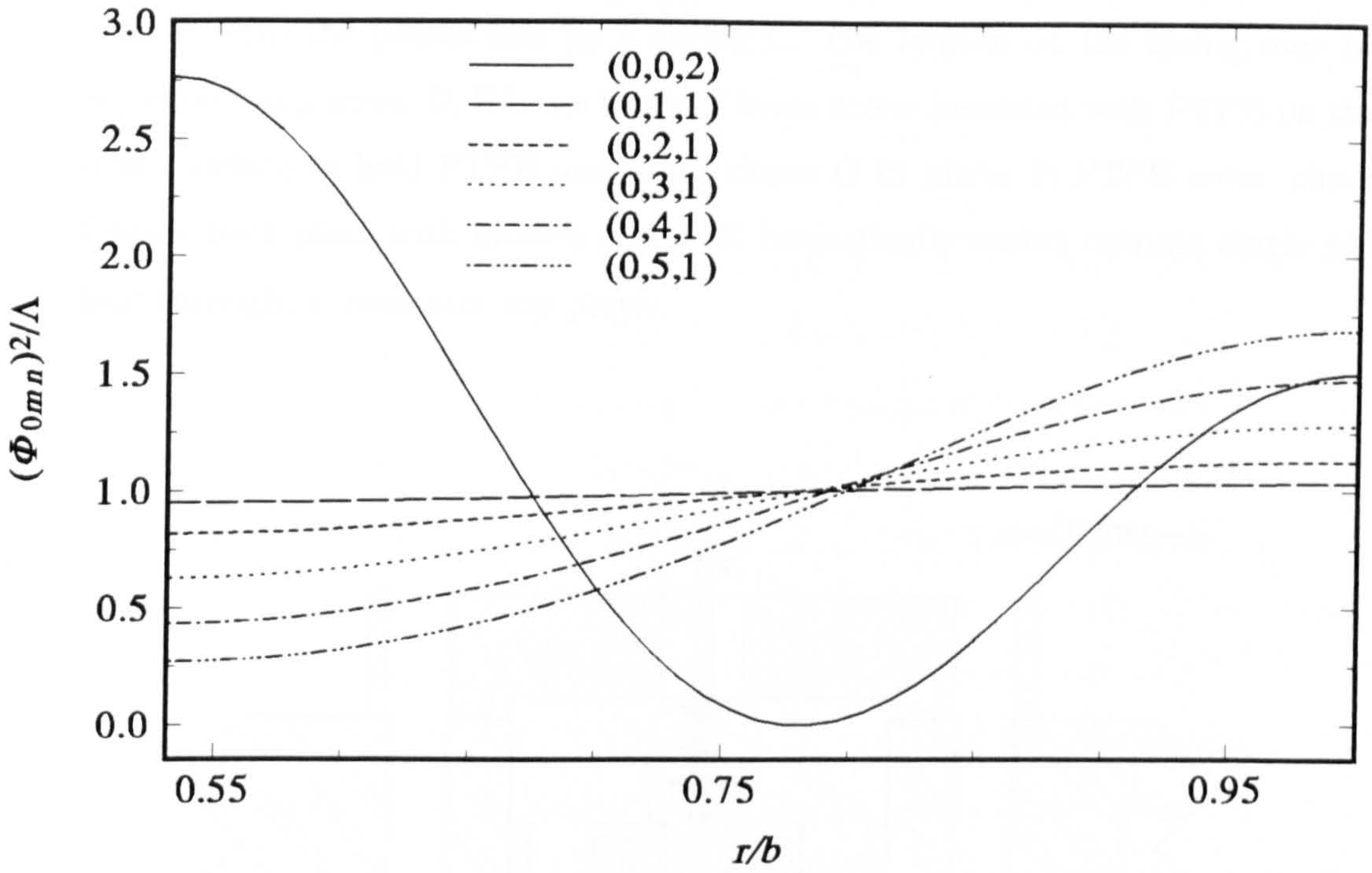

when operated as a sound source. In order to excite and detect the resonance modes most efficiently the sound source and detector must be placed where the square of the wavefunction is large as the acoustic pressure p_{a} is proportional to ϕ_N^2.

As can be seen in figure (4.2) which shows the square of the wavefunction along the r coordinate this occurs for all the modes of interest towards the outer side wall of the resonator. The transducers were placed as close to the wall at $r = b$ as possible in order to obtain the best signals despite the fact that this necessarily maximises the perturbation to the resonance modes due to the holes caused in the resonator wall. The transducers were also placed at an angle of π apart where all the azimuthal modes have maxima in the wavefunction. The transducers form closed tubes in the resonator top plate for which the acoustic admittance y_{o} of the opening is given by $y_{\mathrm{o}} = -i\cot(k_{\mathrm{KH}}L_{\mathrm{t}})$. The only way to reduce this term and minimise the resultant correction to the resonance modes is to make the length L_{t} of the hole as small as possible. Both the position and size of the transducers are determined by other considerations. Even the length of the hole is restricted by the height of metal to which the front of the transducer

Figure 4.3: Detector transducer; A metal coated plastic film; B brass backplate machined on face A with holes of diameter 0.5 mm and depth 1 mm held in contact with the plastic film by a spring C. The tension on the spring may be adjusted using screw D; E brass body; F brass screw insulated with PTFE on the inner surface to hold PTFE insulating sleeve G in place; H PTFE cover plate; I brass back plate with indium seal J; K hermetically sealed ceramic single pin lead-through; L resonator top plate.

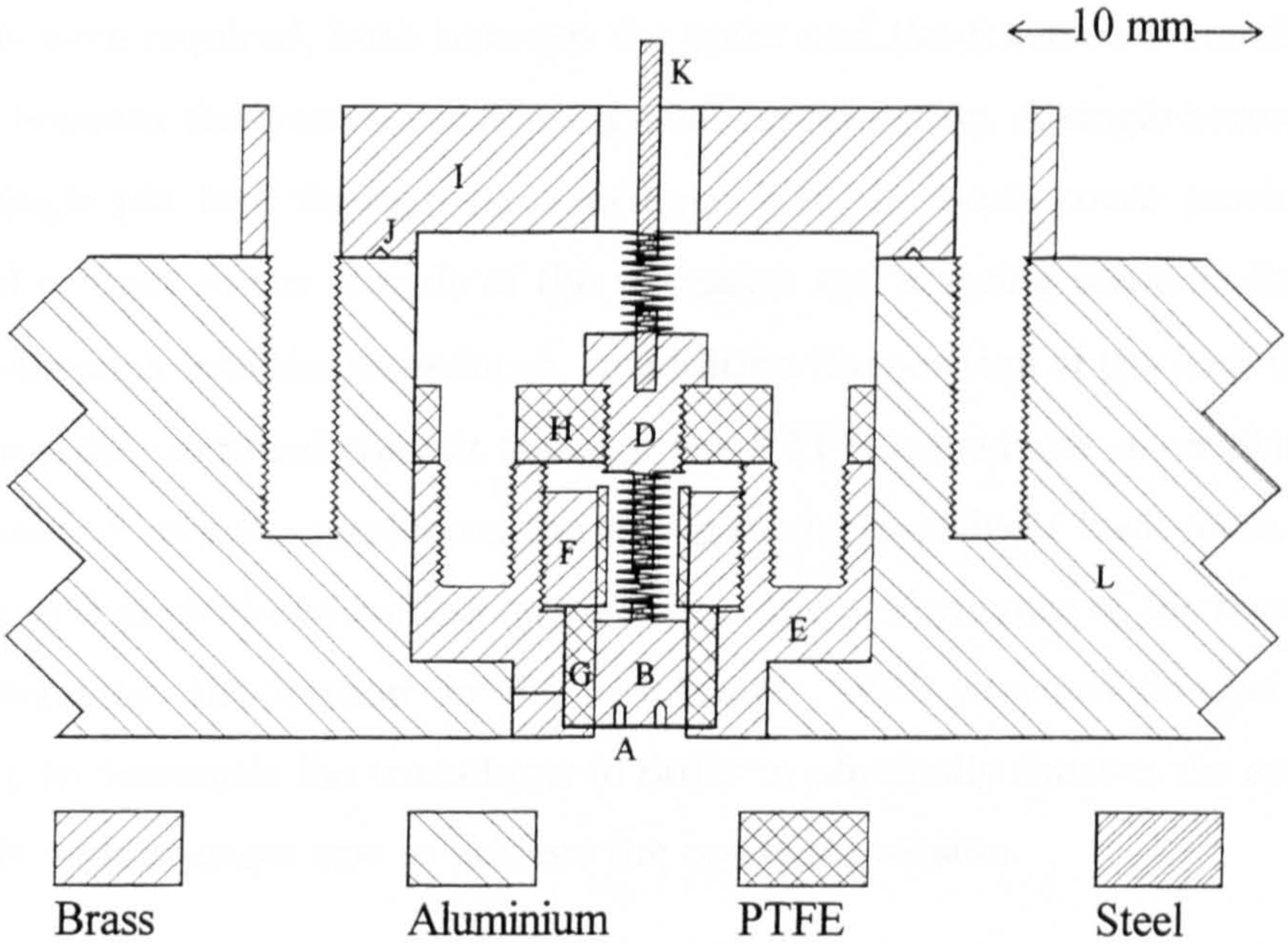

housing may reliably be machined. The smallest length possible is $L_t = 0.5$ mm which was used for the transducers in this work.

Both electroacoustic capacitance transducers were of essentially the same design, the detector is shown in figure (4.3). The thin dielectric membrane was clamped by a PTFE sleeve within the brass housing with the metallised outer surface in contact with the brass. The housings were carefully machined to fit snugly into the transducer ports in the resonator top plate, both in order to minimise the annular slots round the housings, and so that the front faces of the housings were flush with the interior surface when in place. A circular area of the

membrane was exposed to the gas in the resonator by a hole in the front of the housing. A brass electrode of the same cross sectional area as the exposed membrane was held against it by a spring which also served as an electrical connection. Small pressure equalisation vents allowed the small volumes in the transducers to be in equilibrium with the pressure in the resonator to prevent damage to the thin membranes.

Similar transducers are described in references [2] to [5], but the following design modifications were implemented. Only one indium seal was required in this design between the cover which screws into the resonator and the resonator top plate reducing the occurrence of pressure leaks in the system. In previous designs two seals were required, both between the cover and the transducer housing and another between the transducer housing and the resonator. A single hermetically sealed single pin lead-through hard soldered into the brass cover provides the electrical contact to the outside of the resonator and a spring contacts this with the lead-through into the transducer. In addition the position of the lead-through which provides electrical contact through the PTFE transducer cover plate may be adjusted to vary the tension on the spring to the transducer back plate. It has been found that the force on this spring affects the performance of the transducer as it determines the tension on the membrane. With previous designs it was necessary to dismantle the transducer in order to physically shorten the spring or replace it with a longer one to achieve the optimum tension.

4.4.1. Source

The centre of the source was positioned at $r/b = 0.814$ in the resonator top plate. The membrane of the source transducer was cut from 12 μm thick polyester film (Melinex, ICI plc), coated with a 50 nm thick aluminium layer. The active element had an active area of diameter 20 mm in order to excite the large (≈ 3 dm^3) volume of gas in the resonator. The transducer housing and metallised layer of the membrane with which it contacts were held at ground potential and the back plate was excited with an a.c. signal of up to 60 V superimposed on a d.c. bias of about 300 V. The resultant electrostatic force drives the membrane to produce sound at the excitation frequency under these conditions. The back plate of the transducer had a diameter the same as the active element and the front surface

had 19 blind holes of diameter 2 mm and depth 1 mm drilled into it to increase the volume of gas trapped between it and the membrane. These holes increase the compliance of the active element and prevent any natural resonances of the membrane from perturbing the resonance modes of the cavity by damping the motion of the membrane[6].

Due to the diameter of the source being a significant proportion of the diameter of the resonator it was not possible to approximate ϕ_N^2 over the whole of the opening for the source by the value at the centre. This simplification was tolerable for the spherical resonators described in the literature but for the annulus it was necessary to carry out the integration explicitly. Once this was achieved for the source it was easy to extend the program to perform the same calculations for the inlet tube and detector but in these cases ϕ_N^2 did not vary significantly over the opening

4.4.2. Detector

The centre of the detector was positioned at $r/b = 0.886$ in the resonator top plate. In the detector transducer, a 6 μm thick polyvinylidene fluoride membrane coated with aluminium on the outer surface was used. The material required no d.c. bias as it had a permanent dielectric polarisation 'frozen' in. The active area of the element had a diameter of only 3.5 mm as increasing the size does not increase the efficiency of sound detection, in contrast with the increased efficiency with which the source excites the sound field within the gas on increasing the size. This reduces the perturbation to the resonance modes caused by the detector transducer. As for the source, the back plate was the same diameter as the active element and had 4 equally spaced blind holes of diameter 0.5 mm and depth 1 mm drilled into its front surface. These again increased the compliance of the active element thus increasing the sensitivity of the device. When the membrane is set in motion by audio frequency sound it acts as a very high impedance signal source due to its small capacitance of ≈ 5 pF[2]. To prevent loss of the signal which would occur in through coaxial cable a preamplifier is required very close to the transducer[1]. A simple JFET circuit shown in figure (4.4) was soldered directly to the electrical lead-through pin of the cover plate on the resonator. This device has a low power dissipation, a potential difference gain of ≈ 0.6, negligible phase

Figure 4.4: The JFET circuit used as a preamplifier for the detector transducer.

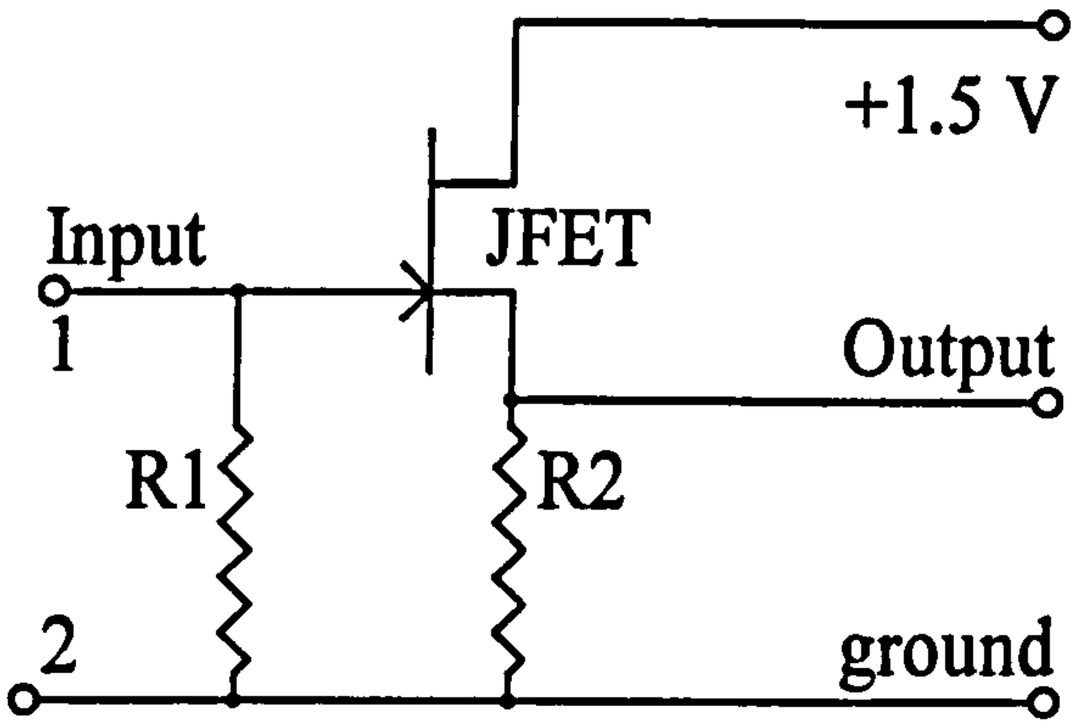

shift at audio frequencies, and a low output impedance[2].

4.5. Thermal Environment of the Resonator

The thermal environment of the resonator is shown schematically in figure (4.5). The resonator was hung within a radiation shield covered with 48 layers of superinsulation. An outer stainless steel can, sealed with a nitrile O-ring served as a vacuum enclosure. With continual pumping the pressure inside the enclosure was less than 5 mPa. This arrangement eliminates the convective and most of the conductive heat losses to the surroundings. The remaining conductive losses occur through the inlet pipe, resonator support and wires which are necessarily connected to the surroundings. To reduce these heat leaks, all the wires were thermally anchored to copper posts on the top of the radiation shield and thin walled 6.35 mm diameter stainless steel tubing was used for the inlet pipe and resonator support rod. Varnish was used to provide thermal contact between the wires and the copper posts round which they were wound. The vacuum can was too large to be suspended in a Dewar, so a bin insulated with polystyrene served to contain dry ice packed round the can for operation at temperatures below ambient.

The resonator was suspended from a bar across the central access pipe. Thin walled 6.35 mm diameter stainless steel tubing connected this bar to a stainless steel central support plate of radius 76 mm and depth of 6.35 mm. The plate was machined to produce three radial arms, to reduce the thermal contact with the resonator, and holes were drilled through those arms to locate the support on the nuts for the studding on the resonator's inner wall. The stainless steel provided the strength necessary for the components as well as reducing the conductive heat

Figure 4.5: Diagram showing the thermal environment of the annular resonator.

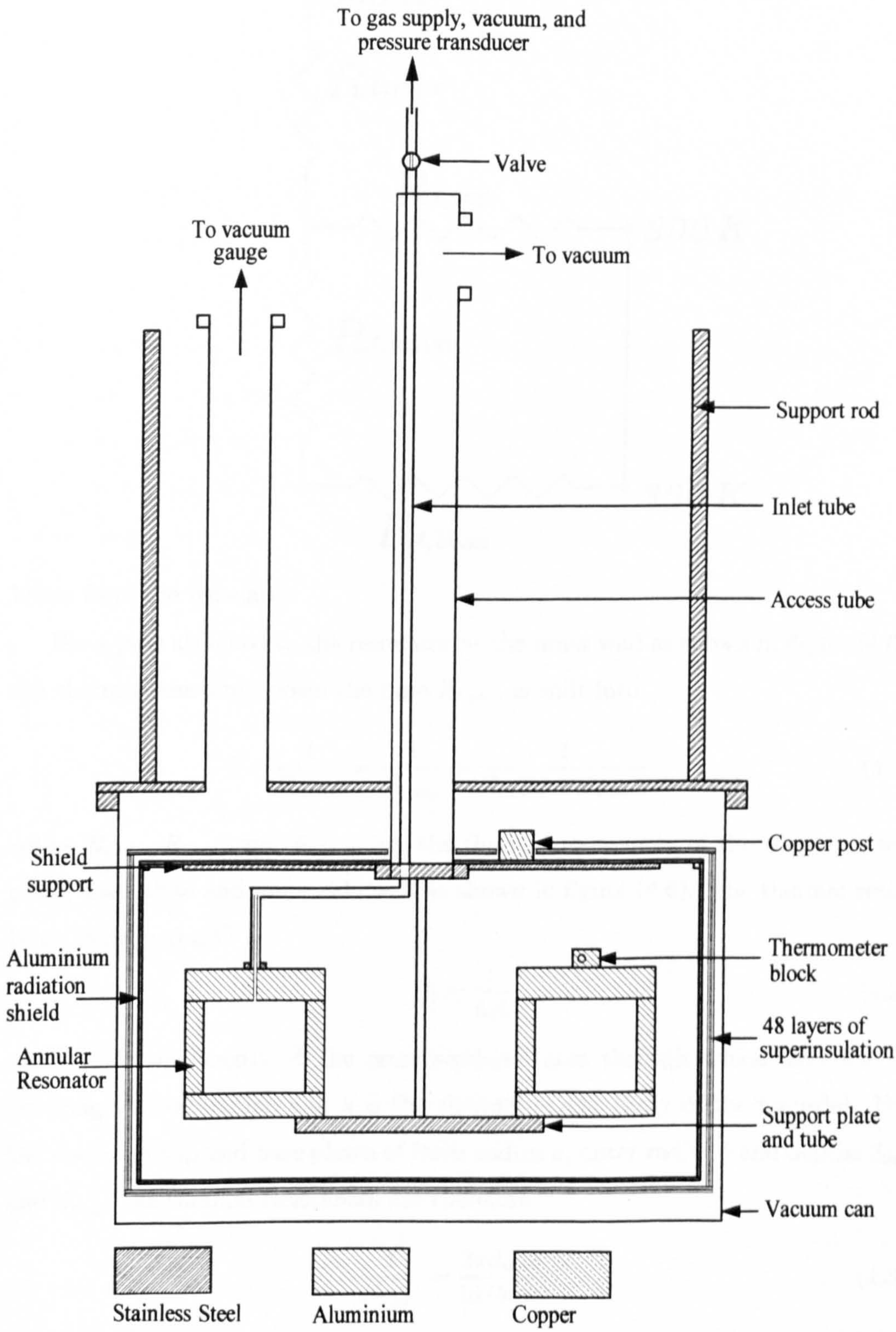

Figure 4.6: The thermal resistances for a pipe attached to the inner rim of the resonator top plate.

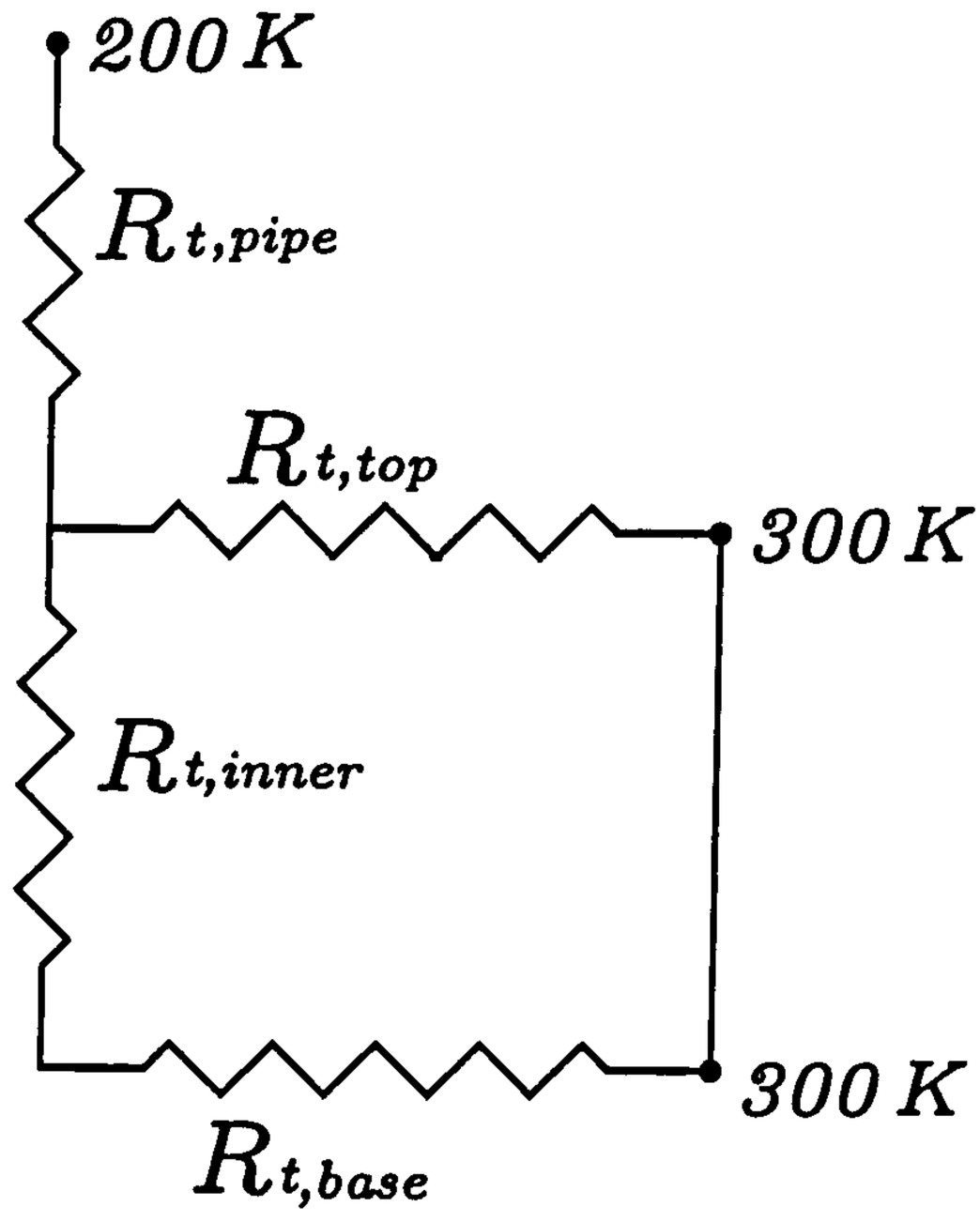

losses from the resonator.

For a pipe attached to the resonator at the inner wall as shown in figure (4.6), the thermal resistance down the pipe $R_{t,\text{pipe}}$ is split into

$$\frac{1}{R_{t,\text{pipe}}} = \frac{1}{R_{t,\text{top}}} + \frac{1}{R_{t,\text{base}} + R_{t,\text{inner}}} \tag{4.1}$$

where $R_{t,\text{top}}$, $R_{t,\text{base}}$ and $R_{t,\text{inner}}$ are the thermal resistances of the resonator top plate, base plate and inner side wall as shown in figure (4.6). The thermal resistance is defined as[7]

$$R_t = \frac{L}{kA} \tag{4.2}$$

where L is the length, A the cross sectional area through which heat loss is occuring via conduction and k is the thermal conductivity of the material. For the resonator top and base plates of inner radius a, outer radius b and depths d_{top} and d_{base}, the thermal resistances are therefore

$$\frac{1}{R_{t,\text{top}}} = \frac{2\pi d_{\text{top}} k}{\ln(b/a)}, \tag{4.3}$$

and

$$\frac{1}{R_{t,\text{base}}} = \frac{2\pi d_{\text{base}} k}{\ln(b/a)}. \tag{4.4}$$

The thermal resistance of the inner wall of thickness ω and height h is given by

$$\frac{1}{R_{t,\text{inner}}} = \frac{\pi\left[(a+\omega)^2 - a^2\right]k}{h}. \tag{4.5}$$

The heat transfer rate q is defined by Fourier's law[7] as

$$q = \frac{kA\Delta T}{\Delta L} = \frac{\Delta T}{R_t}, \tag{4.6}$$

The heat transfer rate q_{pipe} along the pipe of length l inner radius p and outer radius o is therefore

$$q_{\text{pipe}} = \frac{\pi\left[o^2 - p^2\right]k\Delta T_{\text{pipe}}}{l}. \tag{4.7}$$

Matching the transfer rates at the base of the pipe and the inner wall of the resonator assuming that no other modes of heat transport are occuring allows the resulting temperature drops across the resonator and down the inner wall to be calculated. The heat transfer rates q_{top}, q_{inner} and q_{base} are determined by the ratio's of the thermal resistances given in equations (4.3), (4.4) and (4.5). The thermal resistances may be calculated and hence the resulting temperature drops ΔT_{top}, ΔT_{base}, and ΔT_{inner} due to conductive heat losses may be determined for a given ΔT_{pipe}. For a piece of thin walled stainless steel tubing 70 cm long when $\Delta T_{\text{pipe}} = 100$ K and using thermal conductivities taken from reference [7] the resultant temperature gradients across the resonator were calculated to be less than 1 mK.

In order to reduce radiative heat losses from the resonator a 172 mm radius radiation shield of depth 203 mm constructed from 16 gauge aluminium sheet completely surrounded the resonator. Aluminium was chosen for the radiation shield for three reasons: 1) it has a high thermal conductivity allowing heat to be evenly distributed throughout the shield; 2) the surface does not tarnish giving a constant emissivity; and 3) it has a low density. The top plate of the shield was suspended from four 3.18 mm diameter stainless steel rods which were in turn attached to a 9.53 mm thick stainless steel collar hard soldered to the central access pipe. The top plate of the shield was connected to the side wall by brass screws passing through the aluminium into the top and sides of small brass blocks, and the bottom plate was permanently riveted to the side wall. Vacuum grease and aluminium foil were employed to increase the thermal contact between the ends and side wall of the shield where the heaters were located.

The heaters were three 25.4 mm by 1016 mm Watlow flexible silicone rubber heaters with pressure sensitive adhesive. The heaters were connected in parallel and attached around the circumference of the shield at the top, middle and bottom of the side walls. The entire outer surface of the radiation shield was covered with 48 layers of superinsulation which dramatically reduced the radiative losses from the shield to the vacuum can. Modeling of the system indicated that the temperature gradients across the top and bottom of the radiation shield would be reduced by a factor 100. For the top plate, from which most of the heat leaks occur through the central access pipe and wires, the temperature drop across the radiation shield top plate was calculated to be reduced from ≈ 5 K to ≈ 0.05 K when the temperature difference between the shield and the vacuum can was 100 K. This enabled the temperature of the shield to be controlled to within 0.1 K of the resonator temperature. Modeling of the radiative heat losses from the resonator to the radiation shield indicated that the temperature distribution across the resonator will vary by less than 1 mK when the radiation shield is controlled to within 0.1 K of the resonator temperature. The model for the heat flow within the resonator and its thermal environment is outlined in the next section of this chapter.

The temperature difference between the radiation shield and the resonator was sensed using five copper-constantan thermocouples connected to the centre of the shield top plate, the top, middle and bottom of the shield side wall, and the centre of the shield bottom plate. This arrangement gave a measure of the temperature distribution over the whole of the shield. The thermocouples were all referenced to the aluminium thermometer block which was bolted to the centre of the resonator top plate. Vacuum grease was used to provide thermal contact between the block and the resonator, and between the block and the single capsule type platinum resistance measuring thermometer. A final thermocouple was connected across the top plate of the resonator to allow the measurement of any temperature drop across the resonator under the conditions of operation.

The resonator itself was heated via two Watlow flexible silicone rubber heaters with pressure sensitive adhesive connected in parallel. One heater (50.8 mm $\times$ 889 mm) covered most of the outer cylindrical wall of the resonator, and the other heater (25.4 mm $\times$ 356 mm) was attached to the inner wall of the resonator. These

Figure 4.7: The geometric parameters and notation used in the model of the thermal environment of the resonator.

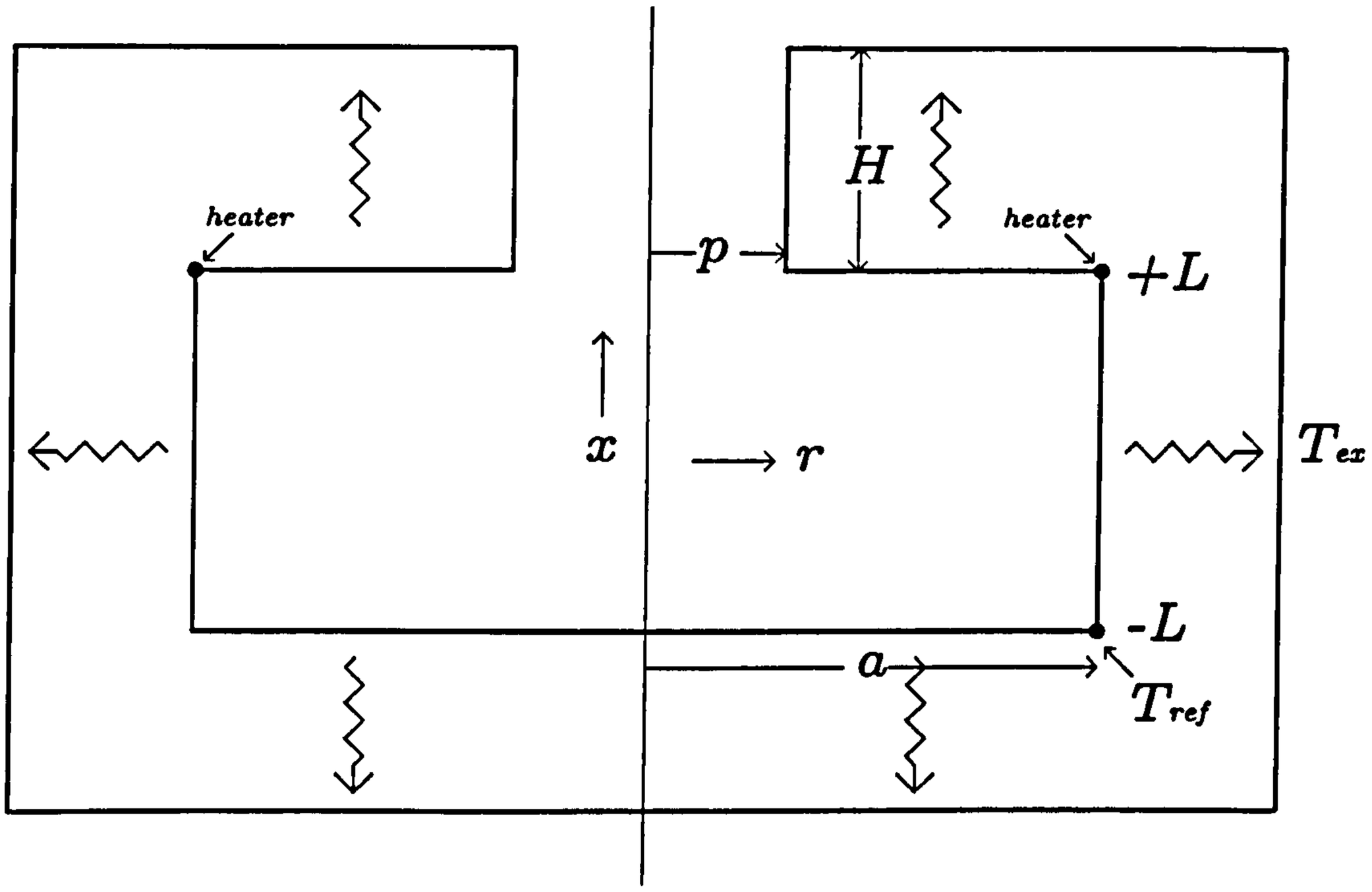

heaters were chosen such that the power per unit area supplied to the inner and outer walls of the resonator was equivalent preventing significant temperature gradients across the resonator. The modeling of the heat flow throughout the resonator and its surroundings was of great importance in the design of the thermal environment of the resonator in order to achieve a temperature uniform to 1 mK across such a large apparatus.

The outer wall of the resonator was also the control block, where the temperature was sensed using three S.D.L. 100 Ω (at 273.15 K) ceramic encased 2 wire platinum resistance thermometers connected in series. The thermometers were located in three equidistant wells machined into the resonator wall; vacuum grease provided thermal contact between them and the control block.

4.5.1. Model for the Thermal Environment of the Resonator

A model was developed for the thermostat to assist with the design because the apparatus was much larger than any that had been thermostatted previously in the laboratory using radiation shields in an evacuated chamber. The basic problem was the temperature distribution over a cylinder that was losing or gaining

Figure 4.8: Heat balance for a cylindrical plate losing heat to another cylindrical plate.

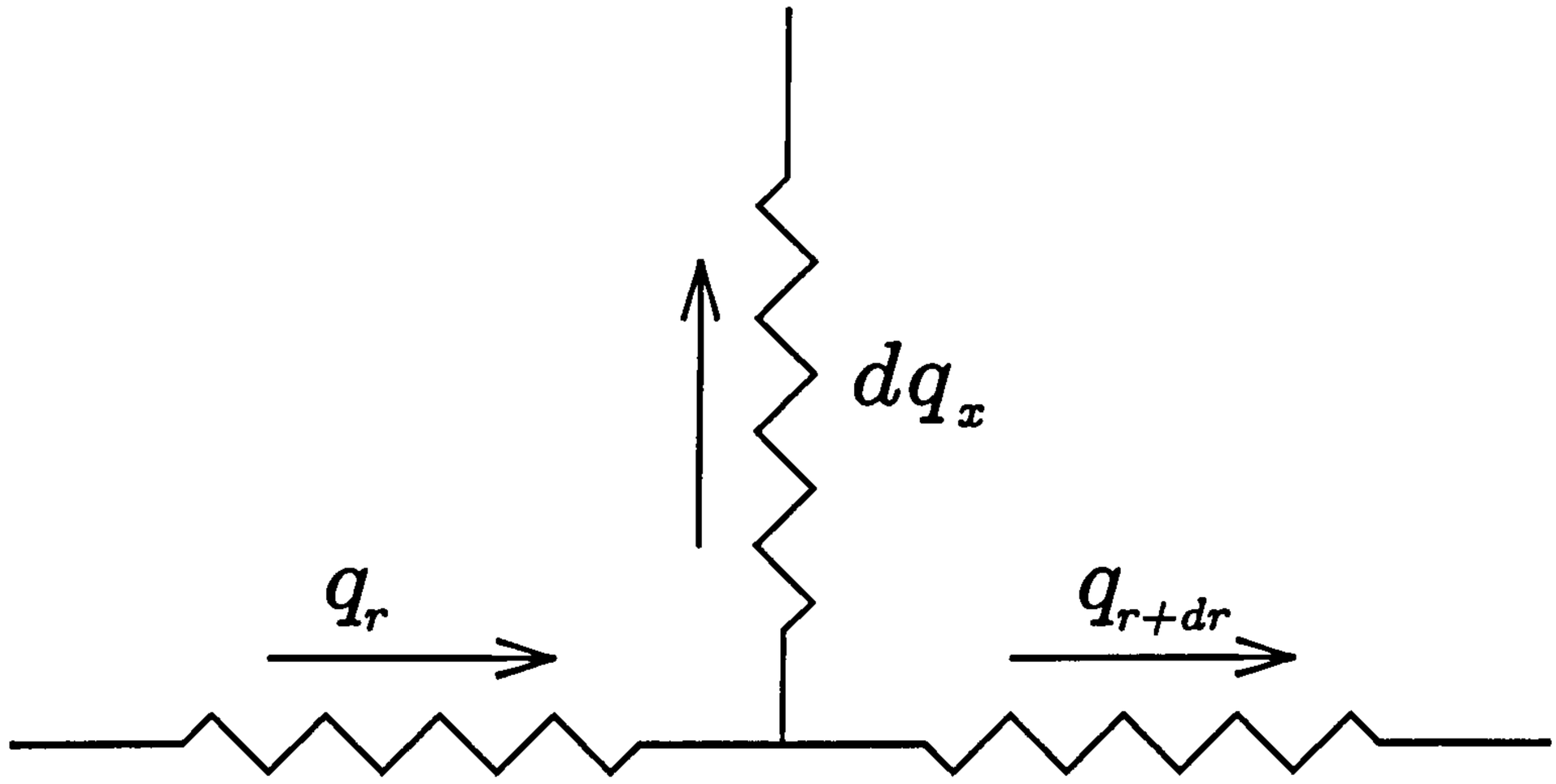

heat from an outer cylinder. The solution would be applied twice. First to the radiation shield within a vacuum jacket and then to the resonator within the radiation shield. In each case the temperature of the container was assumed to be uniform at $T_{\mathbf{ex}}$ and the temperature differences $\theta = T - T_{\mathbf{ref}}$ were calculated relative to the temperature $T_{\mathbf{ref}}$ at the outer rim of the lower plate of the inner vessel. The coordinate system and other notation is defined in figure (4.7) in terms of which the reference point is ($r = a,\ x = -L$) with temperature $T_{\mathbf{ref}}$. The temperature distribution had to be determined for the cylindrical plates with a pipe at the centre (the top plate) and without a pipe (the bottom plate), and for the axial (cylindrical) wall. Temperature and temperature derivatives (proportional to the heat flow) must be continuous at the joins between the different parts of the cylinder and a variety of boundary and initial conditions were considered. Angular variation was neglected so the required temperature distribution was reduced to $T(r, x)$.

Radial differential equation

For a cylindrical plate of thickness t losing heat by radiation to another external cylindrical plate, heat balance relates the radial heat transfer rate q_r (see figure (4.8)) to the axial heat transfer rate q_x by

$$q_r = q_{r+dr} + dq_x, \tag{4.8}$$

and since

$$q_{r+dr} = q_r + \frac{dq_r}{dr}dr, \tag{4.9}$$

it follows that

$$0 = \frac{dq_r}{dr}dr + dq_x. \tag{4.10}$$

The radial heat transfer rate is given by Fourier's law[7]

$$q_r = -2\pi trk\frac{d\theta}{dr}, \tag{4.11}$$

where k is the thermal conductivity of the plate material, $\theta = T - T_{ex}$ and thus

$$\frac{dq_r}{dr} = -2\pi tk\frac{d}{dr}\left(r\frac{d\theta}{dr}\right). \tag{4.12}$$

Equations (4.10) and (4.12) then give

$$2\pi tk\frac{d}{dr}\left(r\frac{d\theta}{dr}\right) - dq_x = 0. \tag{4.13}$$

While the radial heat transfer is by conduction through the plate, the axial heat transfer is by radiation to the surrounding container at temperature T_{ex}. In the simplest case without any layers of superinsulation, the total heat transfer rate q_x is given by[7]

$$q_x = \frac{\sigma\left(T^4 - T_{ex}^4\right)}{\frac{1-\varepsilon}{\varepsilon A} + \frac{1-\varepsilon_{ex}}{\varepsilon_{ex}A_{ex}} + \frac{1}{AF}} \tag{4.14}$$

in which σ is the Stefan-Boltzmann constant, ε and ε_{ex} are the emissivities of the plate and the external surface, A and A_{ex} are the surface areas of the plate and the external surface and F is the view factor. When one layer of superinsulation of area A_I and emissivity ε_I separates the shield plate from the external surface the axial heat transfer rate is given by

$$q_x = \frac{\sigma\left(T^4 - T_{ex}^4\right)}{\frac{1-\varepsilon}{\varepsilon A} + \frac{1}{AF_1} + \frac{1-\varepsilon_I}{\varepsilon_I A_I} + \frac{1-\varepsilon_I}{\varepsilon_I A_I} + \frac{1}{A_I F_2} + \frac{1-\varepsilon_{ex}}{\varepsilon_{ex}A_{ex}}} \tag{4.15}$$

where F_1 is the view factor between the shield and superinsulation F_2 is the view factor between the superinsulation and the external vacuum can. When all the view factors are assumed to be unity, equation (4.15) simplifies to

$$q_x = \frac{\sigma\left(T^4 - T_{ex}^4\right)}{\frac{1}{\varepsilon A} + \frac{2}{\varepsilon_I A_I} - \frac{1}{A_I} + \frac{1-\varepsilon_{ex}}{\varepsilon_{ex}A_{ex}}}. \tag{4.16}$$

Extending equation (4.16) to N layers of superinsulation of average surface area A_{I} gives

$$q_x = \frac{\sigma\left(T^4 - T_{\mathrm{ex}}^4\right)}{\frac{1}{\varepsilon A} + \frac{2N}{\varepsilon_{\mathrm{I}} A_{\mathrm{I}}} - \frac{N}{A_{\mathrm{I}}} + \frac{1-\varepsilon_{\mathrm{ex}}}{\varepsilon_{\mathrm{ex}} A_{\mathrm{ex}}}}. \tag{4.17}$$

Differentiation of equation (4.17) with respect to A gives

$$\frac{dq_x}{dA} = \frac{\sigma\left(T^4 - T_{\mathrm{ex}}^4\right)\theta}{\left[\frac{1}{\varepsilon A} + \frac{2N}{\varepsilon_{\mathrm{I}} A_{\mathrm{I}}} - \frac{N}{A_{\mathrm{I}}} + \frac{1-\varepsilon_{\mathrm{ex}}}{\varepsilon_{\mathrm{ex}} A_{\mathrm{ex}}}\right]^2 \varepsilon A^2 \left(T - T_{\mathrm{ex}}\right)}, \tag{4.18}$$

Expressing dq_x as

$$dq_x = h\theta dA = h\theta 2\pi r dr, \tag{4.19}$$

and using equations (4.8), (4.9) and (4.12) leads to

$$\frac{d}{dr}\left(r\frac{d\theta}{dr}\right) = \frac{hr\theta}{kt}, \tag{4.20}$$

where h is given by

$$h = \frac{\sigma\left(T^4 - T_{\mathrm{ex}}^4\right)}{\left[\frac{1}{\varepsilon A} + \frac{2N}{\varepsilon_N A_N} - \frac{N}{A_N} + \frac{1-\varepsilon_{\mathrm{ex}}}{\varepsilon_{\mathrm{ex}} A_{\mathrm{ex}}}\right]^2 \varepsilon A^2 \left(T - T_{\mathrm{ex}}\right)}. \tag{4.21}$$

Equation (4.20) becomes

$$\frac{d}{dr}\left(r\frac{d\theta}{dr}\right) - \lambda^2 r\theta = 0 \tag{4.22}$$

where λ is defined by $\lambda^2 = h/kt$. Making the substitution $\xi = \lambda r$ and multiplying through by r reveals that equation (4.22) is the modified Bessel equation of order zero

$$\xi^2\frac{d^2\theta}{d\xi^2} + \xi\frac{d\theta}{d\xi} - \xi^2\theta = 0 \tag{4.23}$$

which has the hyperbolic Bessel functions I_0 and Hankel functions K_0 as solutions. The general form of the solution is

$$\theta = c_1 I_0 + c_2 K_0. \tag{4.24}$$

The shield base plate

The shield base plate is at $x = -L$ and has radius a. As the base plate contains the origin, the Hankel function must be rejected as a solution of equation (4.23) because it is infinite at $r = 0$ and the solution is

$$\theta_r\left(r, -L\right) = cI_0\left(\lambda r\right). \tag{4.25}$$

Table 4.1: The temperature difference at nine points across the radiation shield base plate.

r/a	$T - T_{ref}$
0.000	-0.0001
0.125	-0.0001
0.250	-0.0001
0.375	-0.0001
0.500	-0.0001
0.625	0.0000
0.750	0.0000
0.875	0.0000
1.000	0.0000

At the outer edge of the plate where $r = a$, the temperature is fixed at θ_{ref} and thus

$$c = \frac{\theta_{ref}}{I_0(\lambda a)}. \tag{4.26}$$

From equation (4.25) and using the properties of Bessel functions

$$\left.\frac{d\theta_r}{dr}\right|_{r=a,x=-L} = c\lambda I_1(\lambda a) \tag{4.27}$$

Equations (4.25), and (4.26) allow the temperature to be calculated at any point across the shield base plate. The calculated resulting temperature differences $T - T_{ref}$ at nine points across the base plate are given in table (4.1). Values for the thermal conductivities and emissivities were taken from reference [7] and the radiation shield base plate was covered by $N = 48$ layers of superinsulation. T_{ref} was taken as 300 K and T_{ex} as 200 K. The temperature can be seen to vary by less than 0.1 mK across the shield base plate.

Axial differential equation

For a cylindrical shell of outer radius a, inner radius b and length $2L$ losing heat by radiation to another external cylindrical shell heat balance requires that the radial heat transfer rate q_x (see figure (4.9)) is given by

$$q_x = q_{x+dx} + dq_r, \tag{4.28}$$

Figure 4.9: Heat balance for a cylindrical shell losing heat to another cylindrical shell.

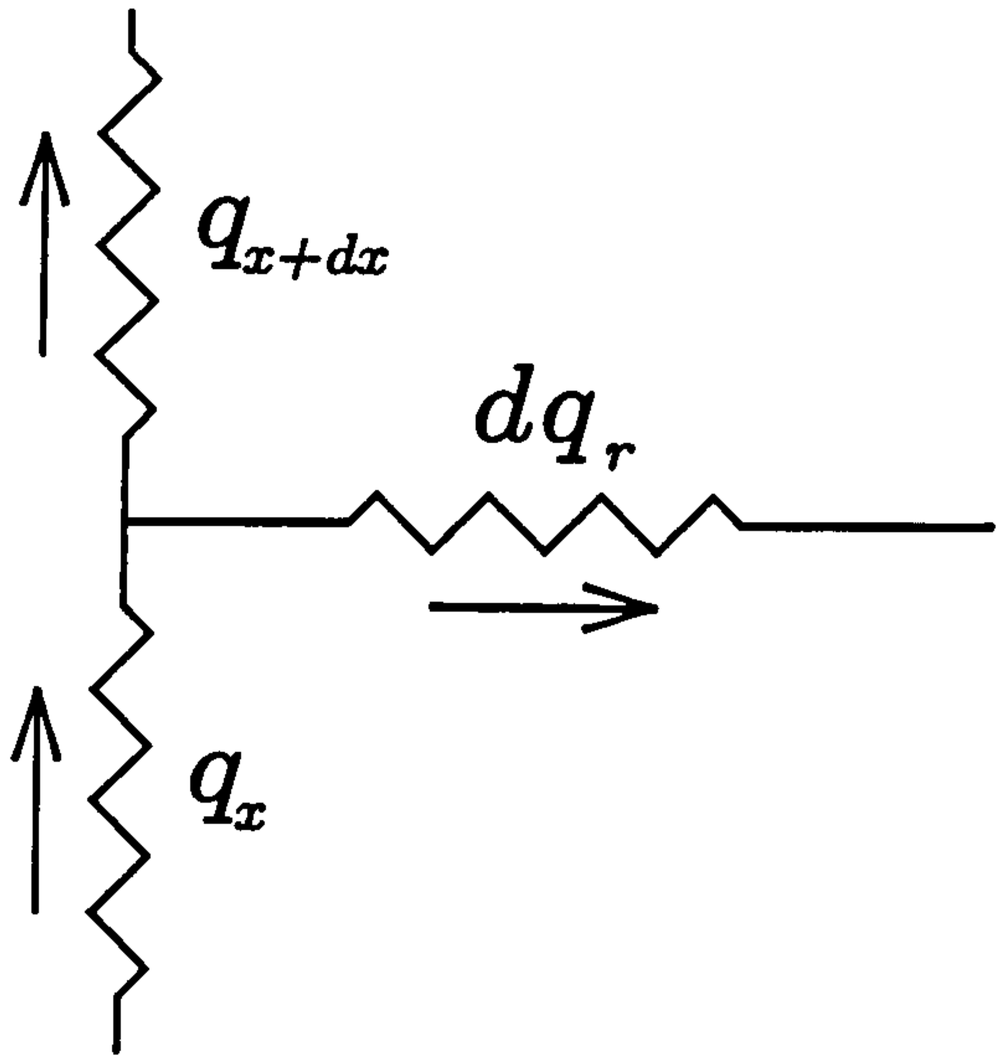

where dq_x is the axial heat transfer,

$$q_{x+dx} = q_x + \frac{dq_x}{dx}dx, \tag{4.29}$$

giving

$$0 = \frac{dq_x}{dx}dx + dq_r. \tag{4.30}$$

The axial heat transfer rate is again given by Fourier's law[7]

$$q_x = -k\pi\left(b^2 - a^2\right)\frac{d\theta}{dx}, \tag{4.31}$$

where k is the thermal conductivity of the cylindrical shell and thus

$$\frac{dq_x}{dx} = -k\pi\left(b^2 - a^2\right)\frac{d^2\theta}{dx^2}. \tag{4.32}$$

The radiative heat transfer rate is again given by

$$\frac{dq_r}{dA} = \frac{\sigma\left(T^4 - T_{ex}^4\right)\theta}{\left[\frac{1}{\varepsilon A} + \frac{2N}{\varepsilon_I A_I} - \frac{N}{A_I} + \frac{1-\varepsilon_{ex}}{\varepsilon_{ex}A_{ex}}\right]^2 \varepsilon A^2\left(T - T_{ex}\right)}, \tag{4.33}$$

in which σ is the Stefan-Boltzmann constant, ε, ε_I and ε_{ex} are the emissivities of the cylindrical shell, the N layers of superinsulation and the external surface respectively, and A, A_I and A_{ex} are the surface areas of the cylindrical shell, the average surface area of the N layers of superinsulation and the external surface. Expressing dq_r as

$$dq_r = h\theta dA = h\theta 2\pi a dx, \tag{4.34}$$

and using (4.32) equation (4.30) becomes

$$0 = -k\pi\left(b^2 - a^2\right)\frac{d^2\theta}{dx^2}dx + h\theta 2\pi a dx, \tag{4.35}$$

which may be written as

$$\frac{d^2\theta}{dx^2} - m^2\theta = 0, \tag{4.36}$$

where

$$m^2 = \frac{2ha}{k\left(b^2 - a^2\right)}. \tag{4.37}$$

The shield side wall

For the radiation shield side wall, using the notation shown in figure (4.7) equation (4.36) has the solution

$$\theta_x\left(a, x\right) = c_1 e^{mx} + c_{-1}e^{-mx}. \tag{4.38}$$

Differentiation of equation (4.38) gives

$$\frac{d\theta_x}{dx}\left(a, x\right) = mc_1 e^{mx} + mc_{-1}e^{-mx}. \tag{4.39}$$

Matching the temperatures and heat fluxes (which is equivalent to matching the derivatives[8]) at the bottom of the shield side wall ($r = a, x = -L$) to those in the shield base plate using equations (4.26) and (4.27) gives

$$\begin{aligned} cI_0\left(\lambda a\right) &= c_1 e^{-mL} + c_{-1}e^{mL} \\ &= c_1 y^{-1} + c_{-1}y, \end{aligned} \tag{4.40}$$

and

$$c\lambda I_1\left(\lambda a\right) = mc_1 y^{-1} - mc_{-1}y, \tag{4.41}$$

where $y = e^{mL}$ and c is defined by equation (4.26). Solving (4.40) and (4.41) for c_1 and c_{-1} gives

$$c_1 = \frac{cy}{2m}\left[mI_0\left(\lambda a\right) + \lambda I_1\left(\lambda a\right)\right] \tag{4.42}$$

and

$$c_{-1} = \frac{cy^{-1}}{2m}\left[mI_0\left(\lambda a\right) - \lambda I_1\left(\lambda a\right)\right]. \tag{4.43}$$

Using the shorthand notation $I_0\left(\lambda a\right) = I_0$ and $I_1\left(\lambda a\right) = I_1$, equations (4.42) and (4.43) may be written in matrix vector form[9] as

$$\begin{pmatrix} c_1 \\ c_{-1} \end{pmatrix} = \frac{c}{2m}\begin{pmatrix} y & 0 \\ 0 & y^{-1} \end{pmatrix}\begin{pmatrix} m & \lambda \\ m & -\lambda \end{pmatrix}\begin{pmatrix} I_0 \\ I_1 \end{pmatrix}. \tag{4.44}$$

Table 4.2: The temperature difference at nine points down the radiation shield side wall.

x/2L	$T - T_{ref}$
0.000	0.0000
0.125	0.0021
0.250	0.0042
0.375	0.0063
0.500	0.0084
0.625	0.0105
0.750	0.0126
0.875	0.0148
1.000	0.0169

At the top of the shield side wall where $(r = a, x = L)$, the temperature is given by

$$\begin{aligned} \theta_x(a, L) &= c_1 e^{mL} + c_{-1} e^{-mL} \\ &= c_1 y + c_{-1} y^{-1}, \end{aligned} \tag{4.45}$$

which may be rewritten as

$$\theta_x(a, L) = \begin{pmatrix} y & y^{-1} \end{pmatrix} . \begin{pmatrix} c_1 \\ c_{-1} \end{pmatrix} . \tag{4.46}$$

Using equation (4.44), equation (4.46) becomes

$$\theta_x(a, L) = \frac{c}{2m} \begin{pmatrix} y^2 & y^{-2} \end{pmatrix} . \begin{pmatrix} m & \lambda \\ m & -\lambda \end{pmatrix} \begin{pmatrix} I_0 \\ I_1 \end{pmatrix} . \tag{4.47}$$

The calculated resulting temperature differences $T - T_{ref}$ at nine points up the side wall are given in table (4.2), again for the radiation shield side wall covered by $N = 48$ layers of superinsulation, and $T_{ref} = 300$ K and $T_{ex} = 200$ K.

The shield top plate

The heater is positioned at the rim of the shield top plate at $(r = a, x = L)$ so there is no longer continuity of heat flow there due to the heat source. Consequently the problem now becomes a boundary value problem rather than an initial value

problem. Because the shield top plate does not contain the origin due to the pipe of radius p (see figure (4.7)), the solution of equation (4.23) has the form

$$\theta_r(r, L) = d_1 I_0(\lambda r) + d_2 K_0(\lambda r), \tag{4.48}$$

and differentiating (4.48) gives

$$\frac{d\theta_r}{dr}(r, L) = d_1 \lambda I_1(\lambda r) - d_2 \lambda K_1(\lambda r). \tag{4.49}$$

Continuity of temperature at $(r = a, x = L)$ leads to

$$d_1 I_0(\lambda a) + d_2 K_0(\lambda a) = \theta_r(a, L) = \theta_x(a, L) \tag{4.50}$$

where $\theta_x(a, L)$ is given by equation (4.47). In order to obtain both d_1 and d_2 it is necessary to specify the heat flux down the pipe. For the pipe of radius p and height H, the heat transfer rate q_p is again given by Fourier's law which may be written as

$$\frac{q_p}{S} = \frac{-k_{\text{pipe}}\theta(p, L)}{H} \tag{4.51}$$

where k_{pipe} is the thermal conductivity of the pipe material and S the cross sectional area of the pipe. Using continuity of heat flow at the rim of the pipe and the inner rim of the shield top plate[8] $(r = p, x = L)$ and Fourier's law for the heat flow across the plate gives

$$\frac{q_p}{S} = -k_{\text{plate}} \frac{d\theta_r}{dr}(p, L). \tag{4.52}$$

From the ratio of (4.51) and (4.52)

$$\frac{k_{\text{pipe}}}{H k_{\text{plate}}} = \frac{1}{\theta_r(p, L)} \frac{d\theta_r}{dr}(p, L). \tag{4.53}$$

If the heat transfer rate q_p is estimated from equation (4.51) using $\theta = \theta_{\text{ref}}$ this is a boundary value problem with $\theta(p, L)$ and $\theta(a, L)$ given. At (p, L)

$$\theta(p, L) = d_1 I_0(\lambda p) + d_2 K_0(\lambda p) = \theta_r(p, L). \tag{4.54}$$

Equations (4.50) and (4.54) may be written as

$$d_1 I_0 + d_2 K_0 = \theta_x(a, L) \tag{4.55}$$

and

$$d_1 \check{I}_0 + d_2 \check{K}_0 = \theta_r(p, L), \tag{4.56}$$

using the shorthand notation $\check{I}_0 = I_0(\lambda p)$ and $\check{K}_0 = K_0(\lambda p)$. Solving (4.55) and (4.56) gives[9]

$$d_1 = \frac{1}{\Delta_{00}}\left[\check{K}_0\theta_x - K_0\theta_r\right] \tag{4.57}$$

and

$$d_2 = \frac{-1}{\Delta_{00}}\left[\check{I}_0\theta_x - I_0\theta_r\right], \tag{4.58}$$

where

$$\Delta_{00} = I_0\check{K}_0 - \check{I}_0 K_0. \tag{4.59}$$

Equations (4.57) and (4.58) may be written in matrix vector form as

$$\begin{pmatrix} d_1 \\ d_2 \end{pmatrix} = \frac{1}{\Delta_{00}} \begin{pmatrix} \check{K}_0 & -K_0 \\ \check{I}_0 & I_0 \end{pmatrix} \begin{pmatrix} \theta_x \\ \theta_r \end{pmatrix}. \tag{4.60}$$

Equation (4.60) was used to calculate the constants required to evaluate the temperature distribution across both the shield top plate containing the pipe and across the resonator inside the radiation shield. The temperature difference $T - T_{\text{ref}}$ at eight points across the shield top plate are given in table (4.3) for $T_{\text{ref}} = 300$ K and $T_{\text{ex}} = 200$ K. Values for the thermal conductivities and emissivities were again taken from reference [7] and the radiation shield top plate was again covered by $N = 48$ layers of superinsulation. $T(p, L)$ was taken as equal to $T_{\text{ref}} = 300$ K in the calculation of q_p and $T(a, L)$ is the resulting temperature at the top of the shield side wall from the calculation of the axial temperature distribution. The temperature drop across the shield top plate is seen to be two orders of magnitude greater than the temperature drop across the shield bottom plate due to the pipe. The temperature across the resonator was found to vary by less than 1 mK when $\theta_{\text{ref}} = 0.1$ K at the outer and inner radii of the resonator and the shield temperature $T_{\text{ex}} = 300$ K.

It must be noted that as the radiation shield side wall was heated by three heaters at the top middle and bottom, the model described above is a worst case scenario and the actual temperature distribution will vary by less than the values estimated in tables (4.1) (4.2) and (4.3).

4.5.2. Temperature Control System

A typical temperature controller would contain several operational amplifiers acting as analogue computers to deliver proportional control and integration. For this

Table 4.3: The temperature difference at eight points across the radiation shield top plate.

r/a	$T - T_{ref}$
0.125	0.0576
0.250	0.0440
0.375	0.0361
0.500	0.0304
0.625	0.0261
0.750	0.0225
0.875	0.0195
1.000	0.0169

experiment the control has been achieved using a digital computer in conjunction with a programmable power supply and appropriate temperature measurement. A Kiethley model 1992 digital multimeter/scanner (d.v.m.) was used to measure the temperature of the thermometers embedded in the outer wall of the resonator and the thermocouples located on the radiation shield and a Thurlby model PL-GP-IEEE-488 programmable power supply capable of delivering up to 25 V on two channels was used to supply power to the heaters on the resonator and the radiation shield. The single program developed to control the temperature of both the shield and resonator was written in QuickBasic to facilitate receiving strings of information from, and sending command strings to the control equipment within a time referenced environment.

The d.v.m. measured the resistance of the control thermometers every three seconds and both proportional and integral control algorithms were utilized to compute the voltage sent to the heaters on the resonator. Integral control was necessary to remove the temperature droop between the steady state and set-point temperature that develops using proportional control alone. Three seconds was chosen as the cycle time between measurements because it is the same order of magnitude as the smallest time constant characterising heat flow through the resonator. The span for the proportional control (i.e. the temperature differences between the control block and the set-point temperature corresponding to full

power and no power to the heaters) could be varied, as could the number of cycles over which the integral control was important. It was found that a span of 0.6 K and an integration time of 24 cycles was robust to varying power requirements and could be used over the whole temperature range. Longer integration times prevented the system from responding quickly to perturbations to the system, for example when gas is being removed from the resonator, and shorter times sometimes amplified small temperature fluctuations. Under steady state conditions the power sent to the heaters was determined mostly by the integral control, and the system provided a temperature on the resonator stable to a few mK over a twenty four hour period.

The e.m.f's of the five thermocouples located on the radiation shield were measured every 10 cycles and the average, combined with the span for the proportional control, was used to compute the voltage sent to the shield heaters. Here, integral control was not useful as some temperature droop between the shield and resonator was necessary to prevent the resonator temperature being influenced too greatly by the shield thus reducing the control on the resonator. It was, however important to have the temperature of the shield close to that of the resonator to reduce the radiative heat losses to the shield. A span of 0.3 K for the proportional control of the shield gave an average shield temperature within 0.1 K of the resonator under steady state conditions. Modeling this situation indicated that the resultant temperature drop across the resonator from radiative heat losses would be of the order of 1 mK. No temperature drop could be detected using the thermocouple across the resonator, which is capable of detecting temperature differences of 1 mK or more.

BIBLIOGRAPHY

[1] Trusler J P M. *Physical Acoustics and Metrology of Fluids.* (Adam Hilger: Worcester, 1991).

[2] Ewing M B and Trusler J P M. *J. Chem. Phys.* 1989, **90**, 1106.

[3] Trusler J P M. Ph.D Thesis, University of London 1984.

[4] Goodwin A R H. Ph.D Thesis, University of London 1988.

[5] Boyes S J. Ph.D Thesis, University of London 1988.

[6] Kudchadker A P and Eubank P T. *J. Chem. Eng. Data.* 1970, **15**, 7.

[7] Incropera F P and De Witt D P. *Fundamentals of Heat and Mass Transfer.* Second Edition (John Wiley and Sons: New York, 1985).

[8] Ewing M B. Private communique 1994.

[9] Buxton B F. Private communique 1994.

5. EXPERIMENTAL TECHNIQUES

5.1. Introduction

The thermophysical and transport properties of the gas under study were determined from the speed and absorption of sound in the gas. The speed of sound was calculated from the resonance frequencies and the absorption from the resonance half-widths. The resonance frequencies and half-widths were determined from comparative measurements, made with a network analyzer, of the amplitude and phase of the signal received from the detector relative to those of the signal transmitted from the source.

The temperature of the sample gas was calculated from the resistance, measured on an a.c. bridge, of a platinum resistance thermometer calibrated on the International Temperature scale of 1968.

Below 115 kPa the pressure of the gas within the resonant cavity was measured using a quartz spiral gauge and at higher pressures a direct reading differential capacitance manometer was used.

5.2. Measurement of Resonance Frequencies

The apparatus used to measure the resonance frequencies and half-widths is shown schematically in figure (5.1). The sine-wave signals used for the acoustic measurements were synthesized by a network analyzer (Hewlet-Packard HP4192A impedance analyzer, serial number 820031), controlled by a microcomputer over an IEEE interface. The HP4192A was phase locked to the 10 MHz time-base of a frequency counter (Hewlet-Packard HP5315B option 004 with thermostatted quartz crystal) ensuring that the fractional accuracy of the signals was better than 10^{-7}. The output from the impedance analyzer, which was variable between 0.005 and 1.1 V r.m.s. and 5 to 13 $\times$ 10^6 Hz in increments of 0.001 V r.m.s. and 0.001 to 1 Hz, was amplified to 60 V r.m.s. and mixed with a d.c. bias which could

Figure 5.1: Schematic diagram of the apparatus used to measure the resonance frequencies and half-widths.

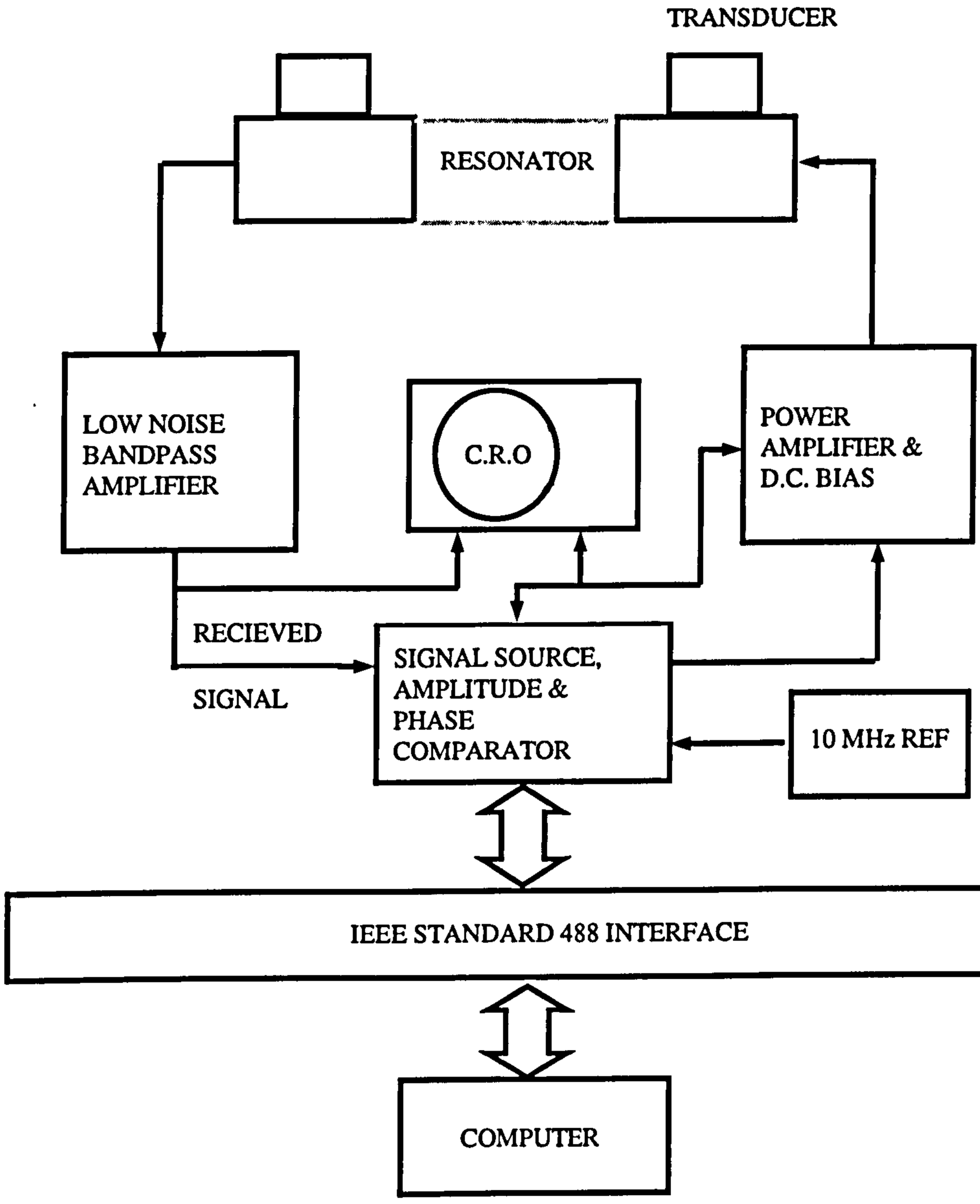

be varied over the range 0 to 300 V, typically operating at 200V, before passing to the source transducer. A resistive-potential divider placed in parallel with the output of the power amplifier supplied a reference signal to the impedance analyzer. The detector output signal was fed to a low noise differential amplifier, based on three operational amplifiers[1] giving a forward potential difference gain of 1000. The signal was further amplified and filtered to remove low and high frequency noise by a 0.3 to 100 kHz band-pass active filter with a potential difference gain variable between 10 and 30, in steps of 10 (usually operated at 10). The signal was then passed to the test input channel of the impedance analyzer where

it typically had a magnitude of 0.1 to 1 V r.m.s. near an acoustic resonance. The amplitude $\bar{a}$ and phase ϕ relative to the reference signal were measured with a time constant of 1 s by the impedance analyzer with a resolution of 0.01 % and 0.0002 rad respectively.

The procedure by which $F_{0,n,1} = f_{0,n,1} + ig_{0,n,1}$ is determined by fitting the data to equation (5.2) is described in the literature[2]-[5]. Once thermal and hydrostatic equilibrium were reached, estimates of $f_{0,n,1}$ and $ig_{0,n,1}$ were obtained from manual scans of the appropriate frequency ranges. The impedance analyzer was then stepped from a frequency near $f_{0,n,1} - ig_{0,n,1}$ to $f_{0,n,1} + ig_{0,n,1}$ in ten equal increments of $g_{0,n,1}/5$. At each discrete frequency a time t was allowed for the acoustic pressure to stabilise such that the fractional systematic error, given approximately by $(g/f)\exp(-2\pi tg)$ in the resonance frequency, was less than 10^{-7} before $\bar{a}$ and ϕ were recorded. The sign of the frequency increment was then reversed and the two sets of measurements were averaged to take account of any small drifts in temperature and pressure. The measurements of $\bar{a}$ and ϕ were then expressed as the real and imaginary parts of the complex potential difference ratio

$$w = \bar{a}\cos(\phi) + i\bar{a}\sin(\phi) = u + iv, \tag{5.1}$$

of the received and reference signals. $\boldsymbol{F_{0,n,1}}$, $\boldsymbol{A_{0,n,1}}$, $\boldsymbol{B}$ and, if significant, $\boldsymbol{C}$ in the theoretical form of the resonance

$$w = \frac{\boldsymbol{A_{0,n,1}} f}{\left(\boldsymbol{F_{0,n,1}^2} - f^2\right)} + \boldsymbol{B} + \boldsymbol{C}f, \tag{5.2}$$

were evaluated using the 11 frequencies and 22 complex potential differences using a non linear fitting procedure similar to that developed by Mehl[4],[5]. As described in chapter 2, $\boldsymbol{A_{0,n,1}}$ is a complex amplitude proportional to the source strength (and any phase shifts between the source and detector), and $\boldsymbol{B}$ and $\boldsymbol{C}$ are the first two terms in a complex Taylor series expansion that can account for any background, due for example, to contributions from other resonance modes. $\boldsymbol{C}$ was not significant except at low pressure where the modes have lower quality factors Q. Using the apparatus and procedure described above, a fractional precision of $10^{-6} f_{0,n,1}$ or better is possible.

Table 5.1: Coefficients for the measurement of temperature on IPTS-68 from the resistances of the PRT.

	B225
R_0/Ω	25.31496
$10^3\alpha/°C^{-1}$	3.925129
$\delta/°C^{-1}$	1.4967
$10^6 e_4/K$	2.824283
$10^6 b_4/K$	-83.78

5.3. Temperature Measurement

The temperature of the resonator and sample gas was measured using a platinum resistance thermometer (PRT) calibrated on the International Practical Temperature Scale of 1968 (IPTS-68)[6],[7] by the National Physical Laboratory (NPL). The PRT was a Tinsley capsule type thermometer (identification number B225) and the constants determined by NPL for the calculation of temperatures in the range 13.81 to 373.15 K are given in table (5.1). The resistance in a triple point of water cell[9] was checked prior to this work. The resistance of the PRT was measured to a precision and resolution of 10 $\mu\Omega$ using an a.c. bridge (Tinsley type 5840, serial number 830037) operating at 375 Hz and a current of 1 mA. A standard Wilkins Resistor (Wilkins type 5685A, serial number 236201) was used to monitor any drifts in the bridge.

5.4. Pressure Measurement

The pressure of the sample gas at pressures above 115 kPa was measured using an MKS Baratron differential capacitance manometer (Baratron), and below 115 kPa Ruska nulling spiral quartz gauge (Ruska) was used. Both gauges were connected in the external pipe work and the reference port of the Baratron was continually evacuated by a mechanical pump.

Both instruments were carefully calibrated using a gas lubricated pressure balance (Ruska, type 2465-751-00, serial number 18510), using the low (0.2 to 15 p.s.i.) or high (2 to 600 p.s.i.) range piston-cylinder combination as appropri-

ate.

5.4.1. Low Pressure

The calibration data for the Ruska gauge (Ruska DDR 6000 type spiral quartz gauge, full scale 115 kPa) could not easily be fitted to a single equation. In order to do this, a four term fit including φ^3 and φ^4 terms was required where $(\varphi/10)$ is the output reading in volts of the gauge on the digital volt meter (Keithley 1992 digital multimeter). These high order terms had not been necessary for previous calibrations[10], and the fit left systematic deviations although no other terms in φ were significant at the 99.5 % level. Systematic regression analysis on truncated sets of the calibration data indicated that it could be split at 91.3 kPa into two regions. The higher and lower sets of pressures could both be fitted to linear equations with lower standard deviations than the global fit. The observed change in slope of the calibration data was probably due to the middle and top pressures not being adjusted to their true values after the gauge was moved in a rearrangement of laboratory equipment. Regression analysis of the low pressure points gave

$$p/\mathrm{kPa} = -(1.134 \pm 0.205) \times 10^{-3} + (0.999494 \pm 0.000004)\,\varphi \qquad (5.3)$$

with a standard deviation of 0.5 Pa, and the high pressure data gave

$$p/\mathrm{kPa} = -(5.447 \pm 0.217) \times 10^{-2} + (1.00008 \pm 0.00002)\,\varphi \qquad (5.4)$$

with a standard deviation of 0.4 Pa. The calibration data consists of three sets of measurements, some with increasing pressures, some with decreasing pressures, and some additional high pressure points which overlapped the other measurements shown in figure (5.2). The gauge was found to be repeatable to better than 1 Pa and the standard deviations of the fits compare favorably with the manufacturers estimate of 3 Pa accuracy for the instrument.

5.4.2. High Pressure

Calibration of the Baratron (MKS type 310CD, 1.3 MPa full scale) was complicated by the gauge showing hysteresis. This effect was observed in previous

Figure 5.2: Deviation plot of the calibration measurements for the Ruska pressure gauge taken with ascending and descending pressure from equations (5.3) and (5.4).

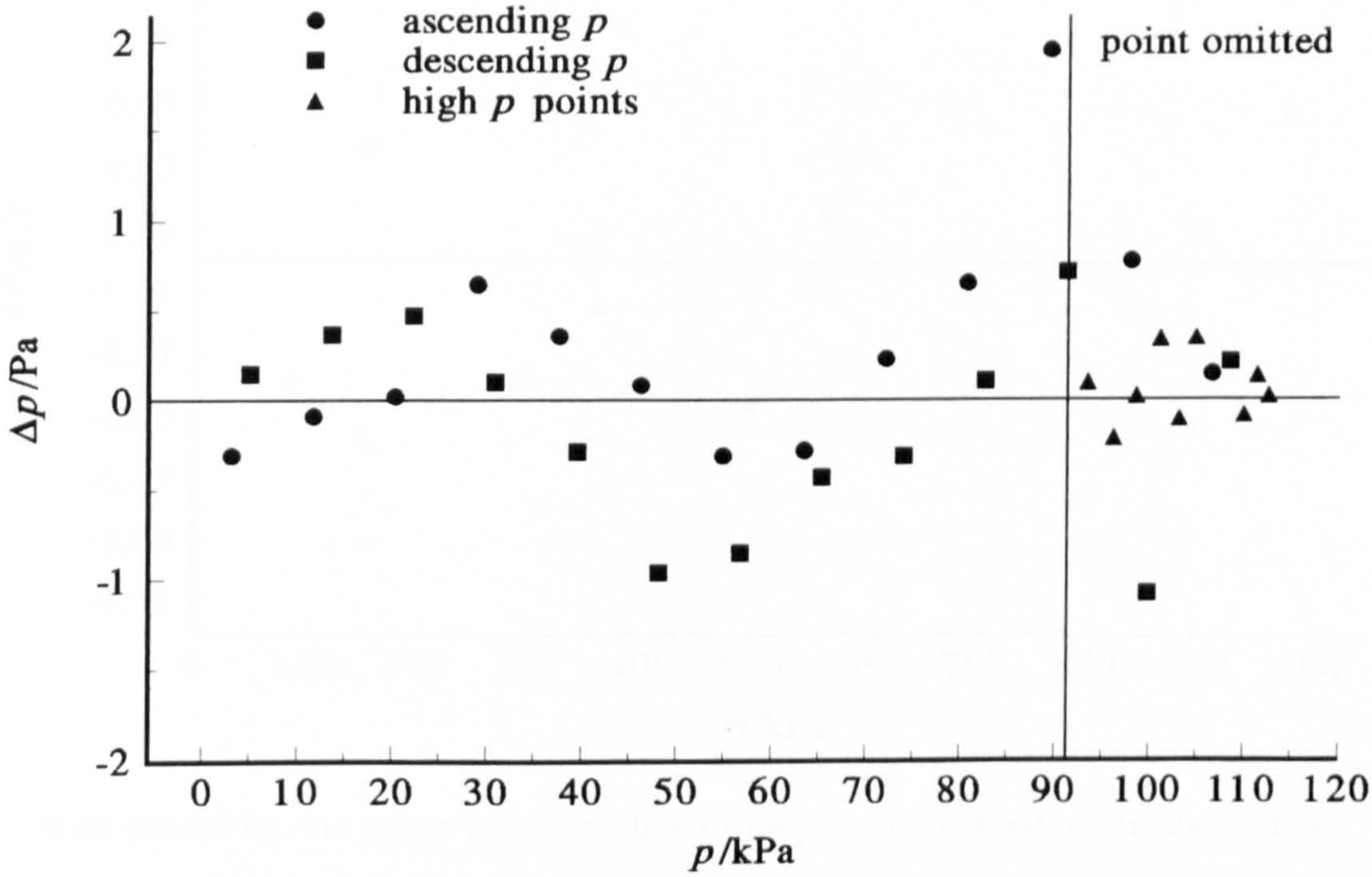

work[10], and during this work the extent of hysteresis was found to depend not only on the initial pressure, but also on the length of time that the gauge had been pressurised. Initially, calibration data were taken with ascending pressures up to 980 kPa and the results could be represented by

$$P/\mathrm{mV} = 999.59 + 7.705p - 3.01 \times 10^{-5}p^2 + 2.05 \times 10^{-24}p^8, \qquad (5.5)$$

with a standard deviation of 0.06 mV (equivalent to 8 Pa). P is the output potential difference of the Baratron on the digital volt meter, and p is the pressure in Pa calculated from the piston and weight combination on the pressure balance. Deviation of the calibration points from this equation are shown in figure (5.3).

Calibration data taken with descending pressures from 980 kPa with the gauge pressurised for 0 hours and 12 hours, are shown in figure (5.4) as deviations from equation (5.5). This shows the relation between the extent of hysteresis and the time the gauge is pressurised, and that at worst the hysteresis has a magnitude of about 5 torr which needs to be accounted for. The hysteresis is likely to have

Figure 5.3: Deviation plot of the calibration measurements for the Baratron pressure gauge taken with ascending pressure from equation (5.5) .

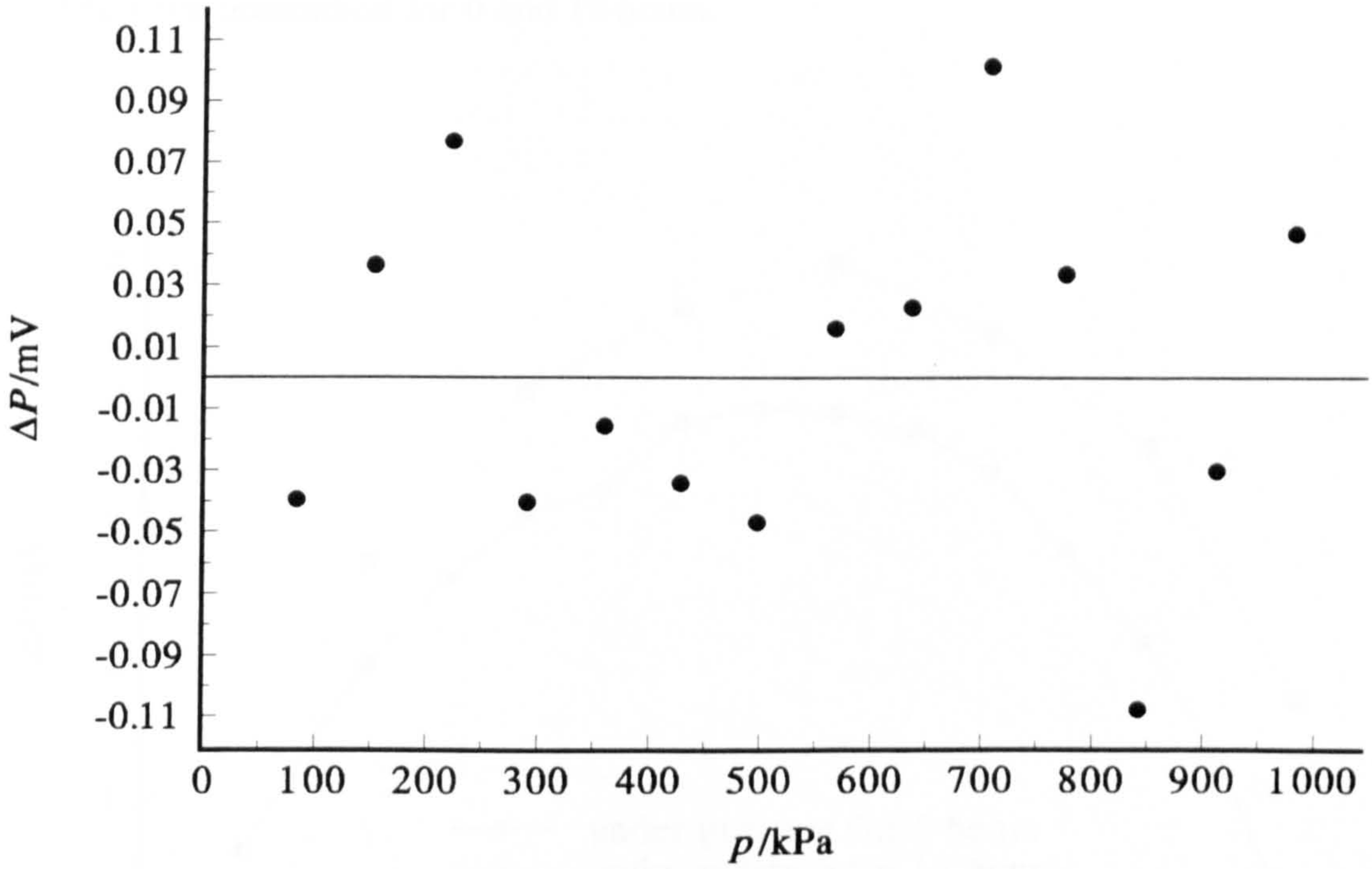

been caused by the gauge being overfilled to a pressure exceeding its elastic limit about 7 years previously.

In the first instance it was necessary to determine at what initial filling pressure negligible hysteresis was observed. Figure (5.5) shows the calibration data (all with the gauge pressurised for 0 hours) taken with descending pressures from 980 kPa, 773 kPa, 497 kPa and 359 kPa as deviations from equation (5.5), the fit of ascending pressures up to 980 kPa. This shows the dependency of the observed hysteresis on initial filling pressure and that negligible hysteresis is observed with initial filling pressures of below 497 kPa. It was also checked that for data collected below 497 kPa, the time the gauge was pressurised had no measurable effect. Regression analysis of all the data showing negligible hysteresis below 497 kPa gave

$$P(\mathrm{DVM})/\mathrm{mV} = 999.78 + 7.704p - 2.95 \times 10^{-5}p^2, \tag{5.6}$$

with a standard deviation of 0.2_8 mV (equivalent to 37 Pa). The standard deviation is about 5 times that for equation (5.5), but the data set combines measurements made over many days and probably gives a more reliable estimate of the error in the pressure determination which reflects the repeatability of the d.v.m.

Figure 5.4: Deviation plot of the calibration measurements from equation (5.5) for the Baratron pressure gauge taken with descending pressure when the gauge had been pressurised for 0 and 12 hours.

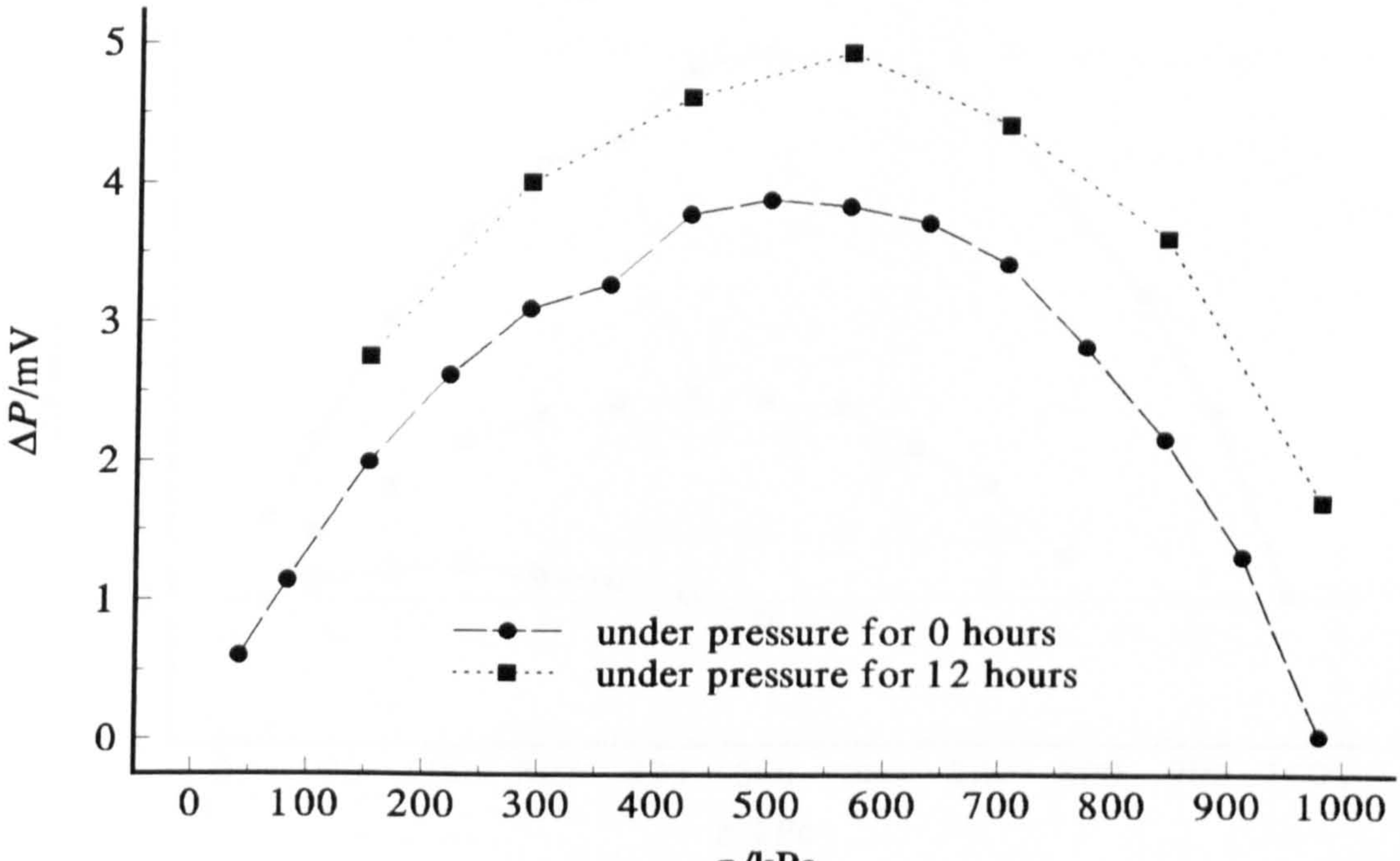

of approximately ±0.2 mV. Equation (5.6) was used to calculate the sample pressure for all Baratron measurements where the initial filling pressure was below 497 kPa.

For Baratron measurements where the initial filling pressure was above 497 kPa, calibration data were collected for every experimental point on the isotherm with the same time lags between the pressure measurements as during the acoustic experiment. This removed any systematic errors due to the unquantified effect of the time for which the gauge is under pressure, which will have an ever decreasing magnitude as the pressure is reduced. This data was then used to correct pressure values calculated from the d.c. potential difference output of the gauge and equation (5.5).

Figure 5.5: Deviation plot of the calibration measurements from equation (5.5) for the Baratron pressure gauge taken with descending pressure with varied maximum filling pressures.

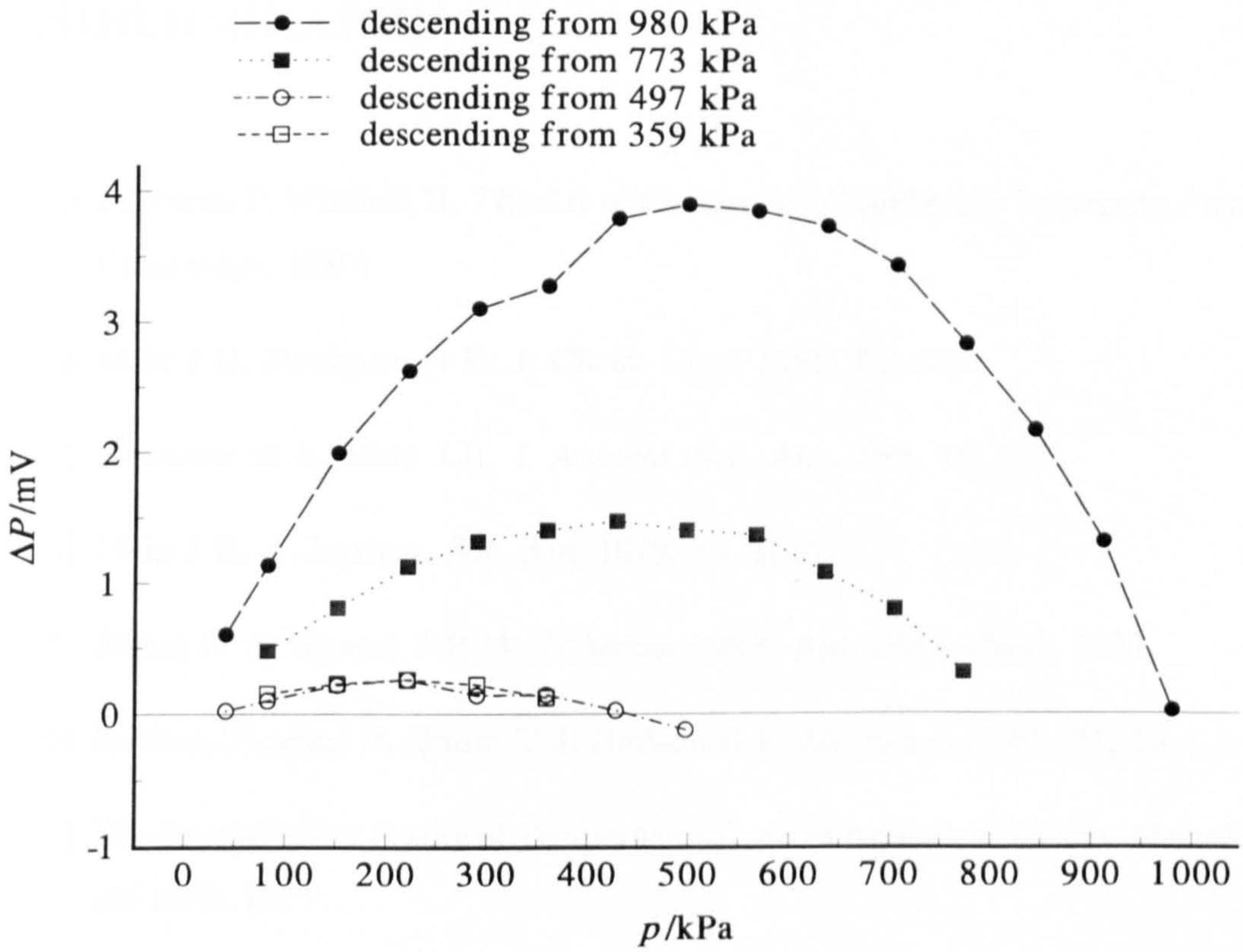

5.5. Samples

The gas samples used in this work all had stated purities of at least 0.995. The samples of propene, argon, sulfur hexafluoride, trifluoromethane and the binary mixture of methane and ethane were used without further purification. The CH_4+C_2H_6 mixture was supplied by Electrochem Ltd. and prepared gravimetrically. They certified that the C_2H_6 content in the mixture had a mole fraction of 0.1500, with the remainder being pure CH_4[11]. The masses used in the sample preparation were traceable to the National Physical Laboratory.

Bibliography

[1] Horowitz P, Winfield H. *The Art of Electronics.* (Cambridge University Press: Cambridge, 1980).

[2] Mehl J B, Moldover M R. *J. Chem. Phys.* 1981, **74**, 4062.

[3] Moldover M R, Mehl J B. *J. Accoust. Soc. Am.* 1986, **79**, 253.

[4] Mehl J B. *J. Accoust. Soc. Am.* 1978, **64**, 1523.

[5] Ewing M B, Trusler J P M. *J. Accoust. Soc. Am.* 1989, **85(4)**, 1780.

[6] Preston-Thomas H, Quinn T J, Hudson R P. *Metrologia* 1985, **21,** 75.

[7] The International Practical Temperature Scale of Amended Edition. *Metrologia* 1976, **12**, 7.

[8] Goodwin A R H. Ph.D Thesis, University of London 1988.

[9] Quinn T J. *Temperature. Monographs in Physical Measurement.* Editor: Cook A H. (Academic Press: London, 1983).

[10] Buxton A J, Bailey C, Ewing M B. Unpublished work 1992.

[11] Electrochem Ltd. Certificate of Composition, 504208, 1991.

6. CHARACTERISATION OF THE RESONATOR GEOMETRY

6.1. Introduction

The geometry of the annular resonator is required to calculate the speed of sound in the gases used in this work. The ratio of the inner to outer radii, $\zeta = a/b$ allows the determination of the eigenvalue χ_{mn} which is a solution of

$$J'_m(k\zeta b)\,N'_m(kb) - J'_m(kb)\,N'_m(k\zeta b) = 0. \tag{6.1}$$

For modes such as azimuthal modes which depend only on the radial solution the propagation constant k_N is given by

$$k_N = \frac{\chi_{mn}}{b}. \tag{6.2}$$

The outer radius, b of the resonator is needed to calculate an absolute value of the speed of sound u from the resonance frequency f_N as

$$u = \frac{2\pi f_N}{k_N}. \tag{6.3}$$

Values for ζ and b were required as functions of temperature and pressure over the whole of the ranges used in this work.

6.1.1. Choice of Calibration gas

The geometry of the annular cavity may be calculated from calibration measurements in a gas for which the speed of sound and density are known to a sufficient accuracy. This is often done using argon, a gas which is very well characterised. However, in this case argon was not the best choice for two reasons. Firstly, the relatively large coefficients of thermal conductivity and viscosity do not allow the resonance frequencies to be determined with sufficient accuracy. A gas with smaller transport coefficients gives resonances with higher quality factors,

$Q = f/2g$ allowing more accurate determinations of the resonance frequencies. Propene was chosen as the calibration gas in this work because a full set of results, covering the whole of the experimental temperature and pressure ranges was available. The speed of sound in propene was determined using a 40 mm radius spherical resonator[1]. At 310 K and 10 kPa the quality factor for the $(0, 5, 1)$ azimuthal mode in the annular resonator is 293 for propene and just 117 for argon allowing the resonance frequency to be determined with an accuracy 2.5 times greater in propene than in argon.

6.2. Calibration Measurements in the Annular Resonator

Isotherms were studied in propene using the annular resonator at temperatures close to 230, 253, 282 and 317 K. In each case the initial pressure p_1 was limited to the highest experimental pressure that would be used for the test gases, or 0.6 of the vapour pressure to avoid the effects of precondensation[2]. The resonance frequencies and half-widths were measured for the seven modes $(0, 2, 1)$ to $(0, 5, 1)$ and $(0, 7, 1)$ to $(0, 9, 1)$ at eleven pressures along the isotherm; p_1/n where $n = 1, 2, 3 \ldots 10$ and $n = 20$.

The measured resonance frequencies and half-widths may be represented by the following equation

$$f_N + ig_N = \left(\frac{u}{2\pi}\right) k_N + \sum_j (\Delta f + ig)_j \,, \tag{6.4}$$

in which the sum represents the contributions of the various corrections to the resonance frequencies and the loss mechanisms described in chapter 2. For propene the largest corrections are those arising from the boundary layers, and there are smaller corrections due to dissipation in the bulk of the fluid and holes in the resonator wall. In addition there is the unknown effect of the coupling of fluid and shell motion. Modes that were adversely affected by the shell motion have been removed from the analysis.

It is important to know the magnitude of the effect of any inaccuracies in the calculated corrections to the resonance frequencies that have been used to calibrate the geometry of the annular cavity. It is also important to know the level of uncertainty that errors in the calculation of the known loss mechanisms

place on the calculation of the excess half-width Δg, which is given by

$$\Delta g = g - (g_h + g_s + g_b)\,. \tag{6.5}$$

If all loss mechanisms had been accounted for accurately, Δg would be exactly zero for all the resonance modes. However, the contribution due to the shell resonance is not known, therefore the experimental Δg is, to a first approximation, a measure of the magnitude of this effect on the resonance half-widths, with associated errors determined by the accuracy of the calculations of the other contributions. The effect of the coupling of gas and shell motion on the resonance half-widths is not as large as the error it will cause to the resonance frequencies, but if a given resonance mode has an excess half-width greater than the expected level of error, it is likely that the mode has been adversely affected by the shell resonance and therefore should be rejected from the analysis.

Some proportion of the resonance half-widths may also be due to the effects of imperfect geometry, because this lifts the degeneracy of the components of the resonance, leading to increased experimental half-widths. Unfortunately, time did not permit the calculation of such effects and an accurate estimation of the magnitude of the splitting of the components. However, by comparison with cylindrical resonators fabricated to the same tolerance as the annular resonator, the contribution is expected to be less than 1 ppm of the resonance frequencies and hence unimportant in limiting the accuracy of the determined experimental excess half-widths.

6.2.1. Sources of Error

The thermal conductivity and viscosity of propene were calculated from values given in reference [3]. This not only gave the most complete set of results that covered the whole of the experimental temperature range, but also seemed to represent an average when compared to other sources of data[4]-[6]. In addition, the paper gave values for both coefficients at pressures of 0.1 and 1.0 MPa allowing linear extrapolation to the limiting values as $p \rightarrow 0$ and determination of the density dependencies. Non linear regression analysis was used to obtain equations for κ and η at the two pressures quoted. For the thermal conductivity of propene

this gave

$$\kappa/\mathrm{mW\cdot m^{-1}\cdot K^{-1}} = 2.10342 + 163.03t^2 + 128.1t^4 - 379t^6 \tag{6.6}$$

at $p = 0.1$ MPa and

$$\kappa/\mathrm{mW\cdot m^{-1}\cdot K^{-1}} = 21.5193 - 136.90t + 528.7t^2 - 318t^3 \tag{6.7}$$

at $p = 1.0$ MPa. The viscosity data for propene were described by

$$\eta/\mu\mathrm{Pa\cdot s} = 27.774t + 7.313t^2 - 12.3t^3 \tag{6.8}$$

at $p = 0.1$ MPa and

$$\eta/\mu\mathrm{Pa\cdot s} = 23.919t + 39.08t^2 - 58.9t^3 \tag{6.9}$$

at $p = 1.0$ MPa. In equations (6.6) to (6.9), $t = 0.001(T/\mathrm{K})$ and from these it was possible to calculate the limiting values of κ and η as $p \rightarrow 0$ using

$$\kappa(p \rightarrow 0) = \kappa(p = 0.1\ \mathrm{MPa}) - \frac{1}{9}\left[\kappa(p = 1.0\ \mathrm{MPa}) - \kappa(p = 0.1\ \mathrm{MPa})\right], \tag{6.10}$$

and

$$\eta(p \rightarrow 0) = \eta(p = 0.1\ \mathrm{MPa}) - \frac{1}{9}\left[\eta(p = 1.0\ \mathrm{MPa}) - \eta(p = 0.1\ \mathrm{MPa})\right]. \tag{6.11}$$

The density dependence of κ and η was calculated using

$$\frac{\partial\kappa}{\partial\rho} = \left[\kappa(p = 1.0\ \mathrm{MPa}) - \kappa(p \rightarrow 0)\right]\frac{RT}{10^6 M}, \tag{6.12}$$

and

$$\frac{\partial\eta}{\partial\rho} = \left[\eta(p = 1.0\ \mathrm{MPa}) - \eta(p \rightarrow 0)\right]\frac{RT}{10^6 M}. \tag{6.13}$$

Assuming this linear dependence introduces an error of approximately 0.5 % in κ and η and by comparison with the data from other sources it was estimated that the calculated thermal conductivities and viscosities for propene are accurate to about 1 %. The corrections to the measured resonance frequencies due to the thermal and viscous boundary layers are largest at low pressures. For the lowest pressure of 4.032 kPa used in the calibration measurements, an error of 1% in both transport properties could result in an error of 20 ppm in the corrected resonance frequencies if the errors are additive. At the highest pressure of 739.228 kPa, the

error introduced is less than 3 ppm. As the calculated boundary layer contributions to the resonance half-widths are of equal magnitude to the corrections to the resonance frequencies, uncertainties of the order of 1 % in the viscosity and thermal conductivity lead to errors again of up to 20 ppm in the calculated excess half-width Δg.

It is not possible to calculate the effects due to molecular slip and the temperature jump which are characterised by the thermal and shear accommodation coefficients h and s in equations (2.92) and (2.93). The accommodation lengths l_h and l_s are of the order of the mean free path when the accommodation coefficients are unity. As the penetration lengths δ_h and δ_s are proportional to $1/p^2$ while the mean free path is proportional to $1/p$, the effects are more significant at low density. Thermal and shear accommodation coefficients of 0.9 result in errors of less than 0.3 % in the calculated boundary layer corrections at the lowest pressure of 4.032 kPa, corresponding to errors of less than 1 ppm in the corrected resonance frequencies. A value of 0.9 was used to estimate the size of the corrections as the value of h has been found to be close to this for many gases in experiments using the 40 mm radius aluminium spherical resonator[7]. The magnitude of the accommodation coefficients depend on the interior surface of the resonator, they are close to unity except for perfectly smooth surfaces which have been completely degassed under high vacuum prior to experimental work[8]. Since the interior surface of the annular resonator was treated in exactly the same way as the 40 mm sphere, it is reasonable to suppose the accommodation coefficients will be comparable. Therefore compared to the limitations on the experimental accuracy due to likely errors in the transport properties, molecular slip and the temperature jump are not important under the experimental conditions.

The transport properties κ and η are also used to calculate the correction to the resonance frequencies and half-widths due to holes in the resonator walls. These corrections were never greater than 30 ppm and hence conceivable uncertainties both in the transport properties and the geometry of the holes of around 1 % result in errors in the calculated corrections of less than 1 ppm.

Values for the vibrational relaxation time $\tau\rho$ and its density dependence $\partial(\tau\rho)/\partial\rho$ for propene were taken from reference [1]. From the standard deviations of the quoted values, it is estimated that $\tau\rho$ is known to an accuracy of

3 %. The corrections to the resonance frequencies due to absorption in the bulk of the fluid never exceeded 0.2 ppm, and although they were calculated they are not important at the level of accuracy of the experiment. The correction term depends on $(\omega\tau)^2$ and in these measurements $(\omega\tau) \ll 1$. The contribution g_b to the resonance half-width is in comparison much greater as it depends on $(\omega\tau)$ and so is largest at high frequencies. The contribution is again largest at low density because it contains a term in ρ^{-1}. At the lowest pressure of 4.032 kPa for the highest frequency $(0, 9, 1)$ mode, the contribution to the resonance half-width (g_b/f) is 35 ppm. Thus a 3 % error in the vibrational relaxation time never results in an uncertainty in the reduced calculated excess half-width $(\Delta g/f)$ of more than 1 ppm, and again is not significant at the level of accuracy of the experiment.

In most acoustic measurements, the purity of the working gas is a significant factor in limiting the accuracy of the results. For calibration purposes because the same grade of propene was used for both the measurements on which the calibration was based and the calibration measurements, such errors do not exist.

In conclusion, the calculated corrected resonance frequencies and hence the associated error in the calculated geometric parameters is limited to 20 ppm for modes not affected by the shell resonance, and modes showing an excess half-width significantly greater than 20 ppm (particularly at high pressures) should be rejected from the analysis. Unfortunately, until the geometric parameters, a/b, b, and L/b are known, the corrections to the resonance frequencies, and contributions to the resonance half-widths cannot be calculated accurately and thus the modes which were significantly affected by the shell resonance was not known in the first instance.

6.3. Determination of the radius ratio $\zeta = a/b$

As only azimuthal modes were used, the radius ratio for a given temperature and pressure should be the value that gives the best agreement between the values of u/b calculated for each mode. However, it was known that there was a shell resonance at about 500 Hz with a half-width of around 150 Hz that perturbed the lower order modes with which it overlapped. The amplitude $\mathrm{Re}(W)$ and phase $\mathrm{Im}(W)$ of the acoustic signal W received when the resonator was evacuated

Figure 6.1: The shell resonance; the amplitude and phase of the acoustic signal received when the resonator is evacuated.

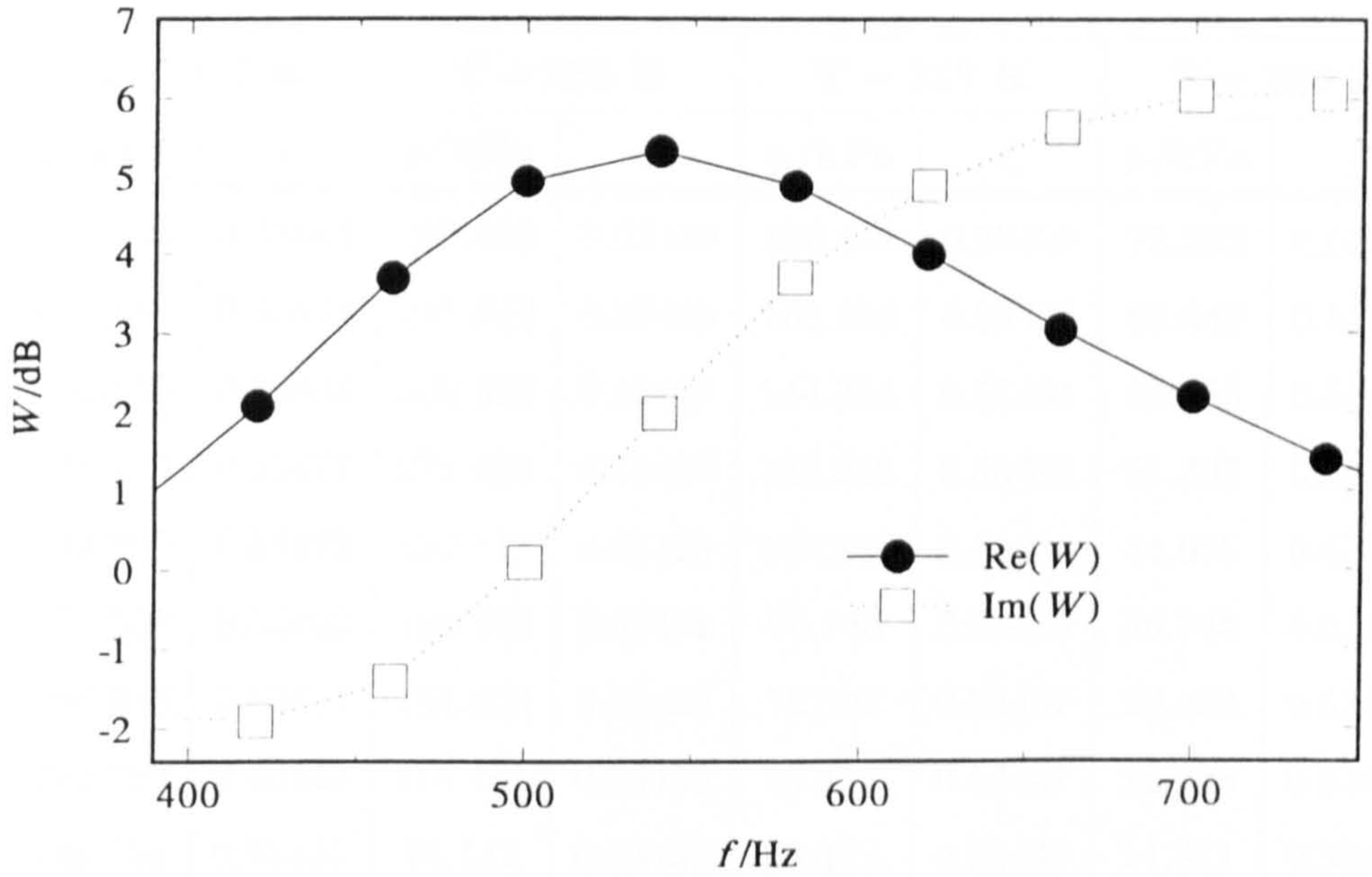

are shown in figure (6.1). The extent to which it perturbed the lower order modes and exactly which modes it influenced was not known. Initially, only the $(0,2,1)$, $(0,3,1)$ and $(0,4,1)$ modes were rejected from the analysis. This decision was based on the fact that when these modes were removed, the values of u/b determined for the other modes, $(0,5,1)$, $(0,7,1)$, $(0,8,1)$, and $(0,9,1)$, could be made to agree to the expected level (of around 20 ppm) by varying the radius ratio $\zeta = a/b$. The results are given in table (6.1).

The resulting values of ζ were fitted using weighted non linear regression analysis where the most significant terms were selected from a bank of terms which included p^n and T^n where $n = -2, -1, 0, 1, 2, 3$ and the all of the cross terms $p^m T^q$ where $m, q = -2, -1, 1$ and 2. Although only terms significant at a probability of 0.99 were selected many different functional forms described the data equally well and showed different behaviour when plotted. From table (6.1) it can be seen that ζ first decreases with pressure and then increases and that the turning point varies with temperature. This behaviour was best described by a five term fit

$$\begin{aligned}\zeta(T,p) = \quad & (0.534403 \pm 0.000006) - (2.0 \pm 0.1) \times 10^{-7} p^2 - (3.4 \pm 0.4) \times 10^{-12} p^3 \\ & + (7.8 \pm 0.5) \times 10^{-11} T p^2 - (8 \pm 1) \times 10^{-12} T^2 p,\end{aligned} \tag{6.14}$$

Table 6.1: Values of the radius ratio ζ determined from the agreement of the $(0,5,1)$, $(0,7,1)$, $(0,8,1)$ and $(0,9,1)$ modes.

T = 317 K		T = 282 K		T = 253 K		T = 230 K	
p/kPa	ζ	p/kPa	ζ	p/kPa	ζ	p/kPa	ζ
739.228	0.53501	388.029	0.53429	180.441	0.53429	73.292	0.53431
666.917	0.53488	347.612	0.53425	162.156	0.53431	65.649	0.53435
592.655	0.53484	309.926	0.53427	144.354	0.53431	58.555	0.53436
518.779	0.53477	271.458	0.53427	126.228	0.53433	51.303	0.53437
443.390	0.53472	232.117	0.53429	108.230	0.53434	44.085	0.53439
370.508	0.53462	193.295	0.53431	90.146	0.53436	36.745	0.53441
296.936	0.53454	154.809	0.53433	72.192	0.53437	29.493	0.53441
222.789	0.53443	116.101	0.53435	54.114	0.53437	22.203	0.53441
148.554	0.53435	76.142	0.53438	36.122	0.53439	14.871	0.53441
74.030	0.53436	38.572	0.53439	18.093	0.53440	7.600	0.53439
39.210	0.53439	22.241	0.53442	11.055	0.53437	4.032	0.53439

which had a standard deviation of 2×10^{-5} which is about 40 ppm in ζ, so the fit could not accommodate the calculated values to within the estimated accuracy. The fit $\zeta(T,p)$ and the calculated values of ζ given in table (6.1) are shown in figure (6.2). The differing pressure dependence of ζ at the different temperatures and the increase in ζ at high pressures were unexpected. The observed trend could possibly have been due to the end plates having an effect at the higher pressures. The cylindrical walls of the resonator have approximately the same thickness so the upwards force exerted on the end plates under pressure would have a greater effect on the larger outer cylinder preventing it from expanding as much as the inner cylinder is compressed resulting in an increase in ζ. The fact that the turning point in p decreases with increasing temperature could possibly have been due to the Young's modulus for aluminium decreasing at higher temperature. There is no way of checking this hypothesis however as the behaviour of an annular shell has not been determined in the literature. It is unlikely that effects of this nature would become important over the moderate range of temperatures and pressures used in this work, a more likely explanation is that the shell resonance at 500 Hz

Figure 6.2: The experimentally determined radius ratio's ζ and the fit given by equation (6.13).

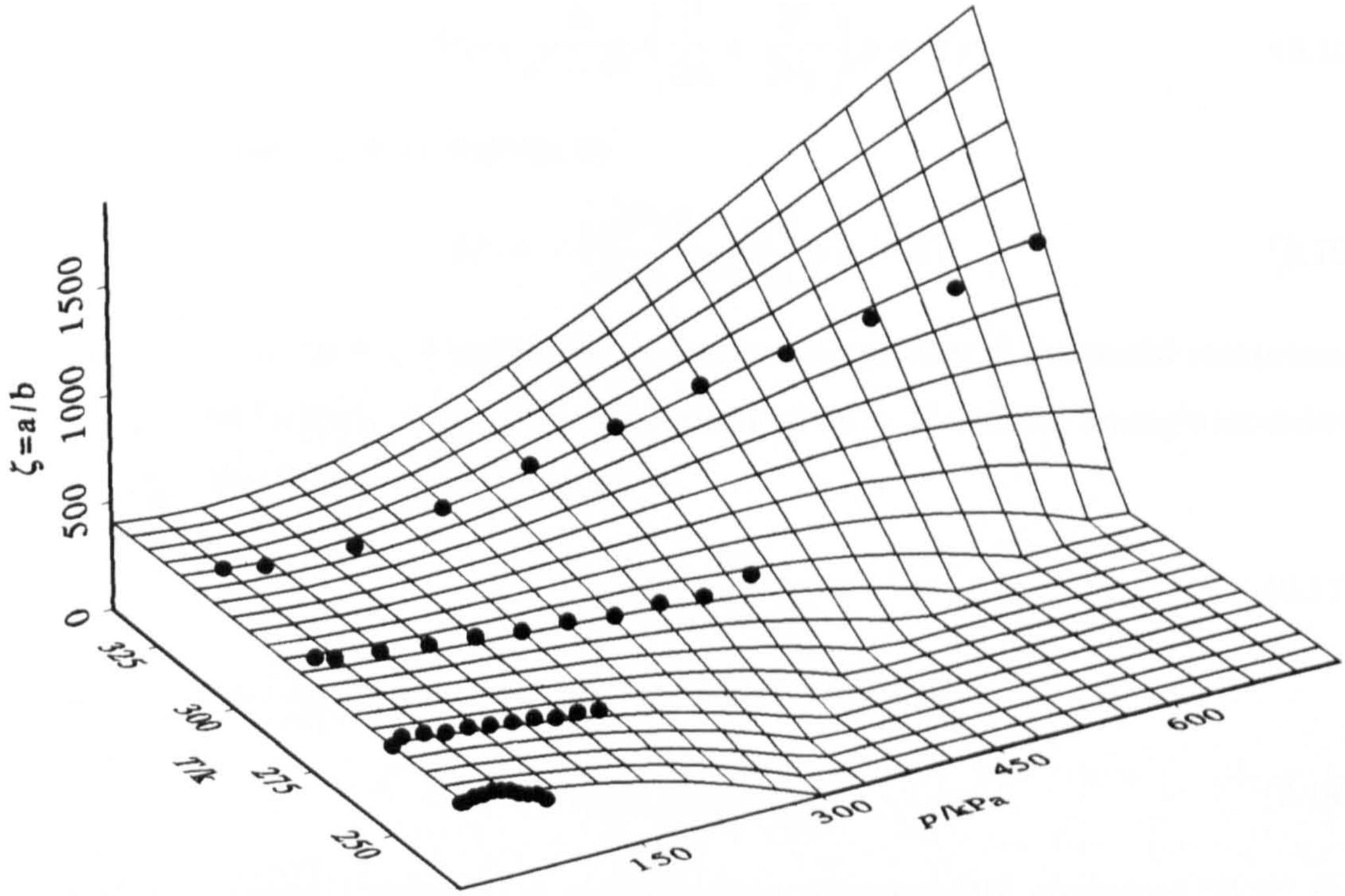

is still affecting the measurements despite the removal of the $(0, 2, 1)$, $(0, 3, 1)$ and $(0, 4, 1)$ modes. The magnitude of the shell correction increases with pressure and could easily be large enough to cause the observed trends in ζ. Similar levels of agreement in u/b were observed over the whole of the experimental T and p ranges whereas better agreement would be expected at high pressures if the shell motion had no effect because the corrections due to the transport properties become smaller. Thus a method of testing which of the $(0, 5, 1)$ and $(0, 7, 1)$ to $(0, 9, 1)$ modes were affected by the motion of the walls was needed and, in addition, the fact that the calculated values of ζ could not be fitted using non linear regression analysis to within the experimental accuracy also needed to be resolved.

Available in the literature[9] are expressions describing the changes in inner and outer radii of a cylindrical shell subject to pressure. If the outer cylindrical wall of the resonator has inner radius b and outer radius c, the inner cylindrical wall of the resonator has inner radius d and outer radius a and p is the internal pressure, the change δb in b is given by

$$\delta b = \frac{b}{c^2 - b^2}\left(\frac{c^2}{2\mu} + \frac{b^2}{2\kappa_T}\right)p = Yp, \tag{6.15}$$

and the change δa in a is given by

$$\delta a = -\left[\frac{ad^2\,(2-\sigma)}{(a^2-d^2)\,E}\right]p = -Xp. \tag{6.16}$$

Here, σ, E, κ_T, and μ describe the mechanical properties of the metal comprising the cylindrical shells. Poisson's ratio is denoted by σ, E denotes Young's modulus, μ is the torsional modulus defined by

$$\mu = \frac{E}{2(1+\sigma)}, \tag{6.17}$$

and κ_T is the reciprocal of the bulk modulus defined by

$$\kappa_T = \frac{E}{3\,(1-2\sigma)}. \tag{6.18}$$

Poisson's ratio was taken as $\sigma = 0.345$ from reference [10] quoted at 20 °C for aluminium, it is unlikely to vary much with temperature because it is the ratio of the lateral contraction per unit breadth divided by the longitudinal extension per unit length. Values of Young's modulus, E were calculated by fitting the values at different temperatures for aluminium given in reference [11], resulting in the expression

$$E/\mathrm{GPa} = 68.237 + 6.729\times10^{-2}\,(T/\mathrm{K}) - 1.94\times10^{-4}\,(T/\mathrm{K})^2\,. \tag{6.19}$$

At a given pressure, $\zeta = a/b$ is given by

$$\begin{aligned}\frac{a}{b} &= \frac{a_0 - Xp}{b_0 + Yp} = \frac{(a_0 - Xp)}{b_0}\left[1 - \frac{Yp}{b_0}\right]^{-1} \\ &\approx \frac{a_0}{b_0} - \left(\frac{X}{b_0} + \frac{Ya_0}{b_0^2}\right)p + Op^2 + \cdots,\end{aligned} \tag{6.20}$$

where $a_0/b_0 = \zeta_0$ indicates the limiting value as $p \to 0$, and the term in p^2 is less than a part in 10^7 of ζ at the maximum experimental pressure of 800 kPa. At 800 kPa the term in p is only 167 ppm of ζ_0. This change is important at the level

Figure 6.3: All experimentally determined values of the radius ratio ζ up to 400 kPa.

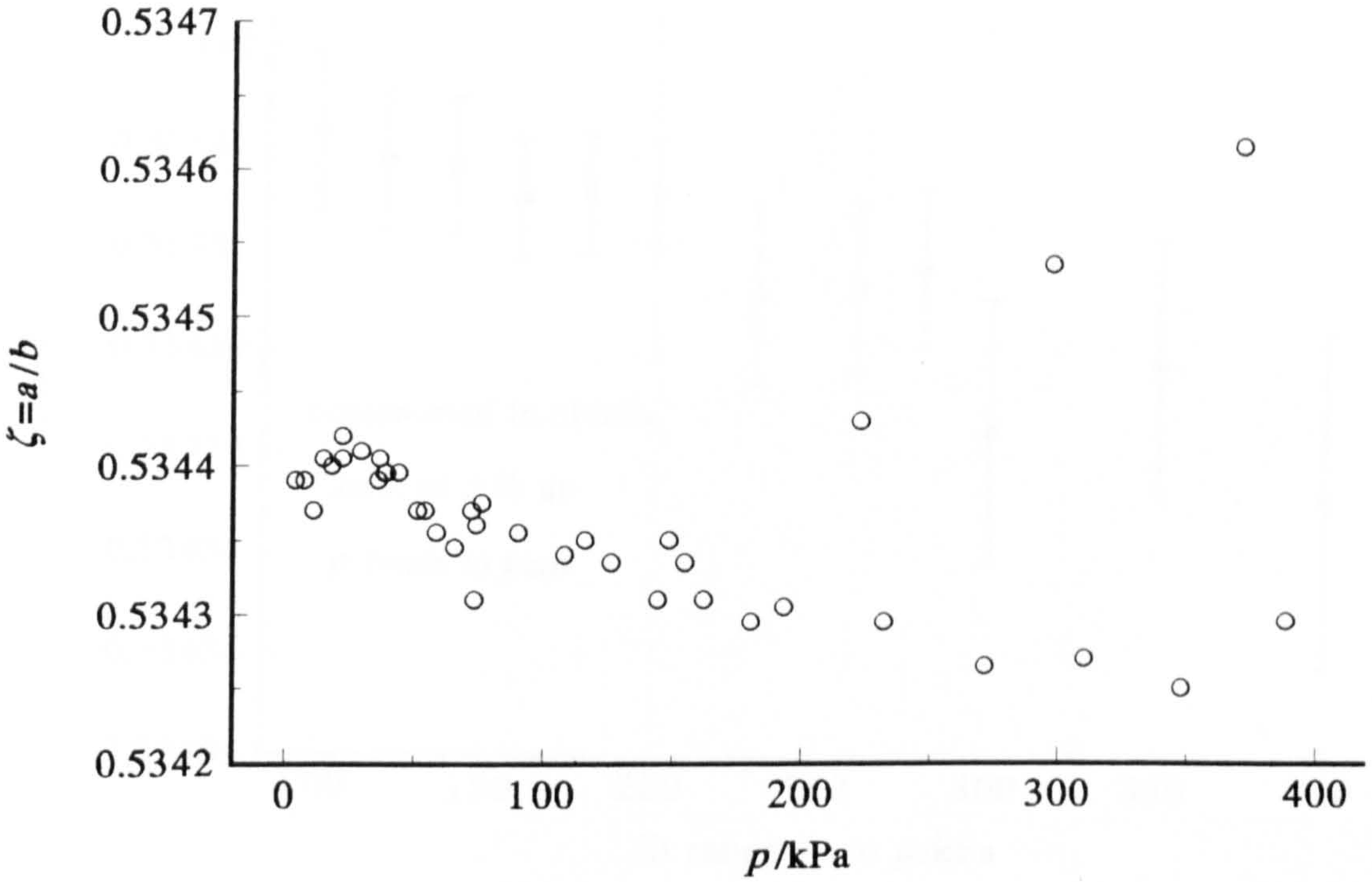

of the accuracy of the experimental results, but as it is small, any errors in the nominal radii of the cylindrical walls or in the elastic constants used for aluminium will result in negligible errors in calculating the slope of ζ with pressure at a given temperature. It must be noted at this point that the limiting value of ζ_0 was not yet known, but the values of a/b at all temperatures should converge as $p \to 0$ because the inner and outer walls are made of the same aluminium alloy and thus have the same expansivity.

The values of ζ at the four experimental temperatures up to 400 kPa are all plotted in figure (6.3) which shows that the values of ζ determined from the initial analysis do converge as expected at low pressure. At low pressures the effects due to the coupling of gas and shell motion become insignificant. Since the theory predicts that ζ has a linear dependence on pressure, linear fits to the experimental values were calculated as the pressure range was systematically truncated. The results are shown in figure (6.4). The linear fit representing the results below 200 kPa was chosen because it had the smallest standard deviation and from figure (6.3) it can be seen that no curvature in ζ is observed below this pressure. Additionally, figure (6.4) shows that further truncation of the pressure

Figure 6.4: Average values of ζ_0 together with standard deviations determined from the linear fits of ζ over progressively truncated pressure ranges.

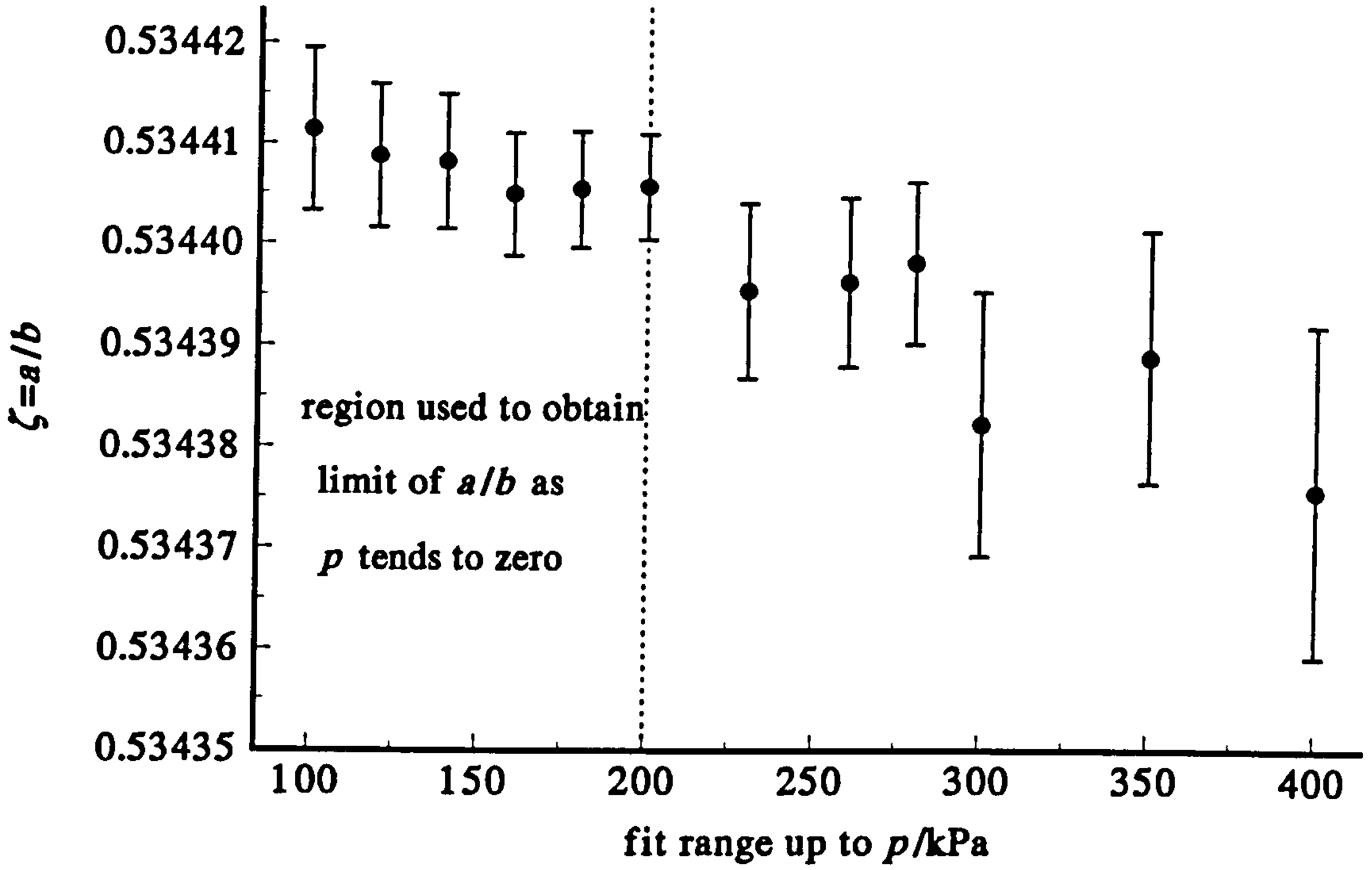

range caused no significant change in ζ_0. The limiting value ζ_0 as $p \to 0$ is therefore given by

$$\zeta_0 = \frac{a_0}{b_0} = 0.534405_4 \pm 0.000005_3, \tag{6.21}$$

where the standard deviation of the coefficient corresponds to an uncertainty of 10 ppm of ζ_0. This limits the accuracy to which the eigenvalues, χ_{mn} and subsequently the speeds of sound, u may be calculated to a level of 10 ppm.

It was still necessary to decide whether the calculated values of ζ using the intercept of the determined values and the pressure dependence as calculated from elastic theory represented the behaviour of the annular shell under pressure to an accuracy sufficient for the experiment. In addition, the resonance modes affected by the shell resonance still needed to be identified as values for u/b were required to calculate the value of the outer radius b given the 'known' speed of sound in propene. Figures (6.5) to (6.8) show the deviations of the calculated values of u/b from the average value $\langle u/b \rangle$ determined from the $(0,7,1)$, $(0,8,1)$ and $(0,9,1)$ modes for the four isotherms. The fractional deviations from $\langle u/b \rangle$ of all the modes are shown so that agreement to the expected level of accuracy of 20 ppm determined by the error in ζ and calculation of the known correction terms

Figure 6.5: Fractional deviations of the calculated values of u/b from the average value $\langle u/b \rangle$ determined for the $(0, 7, 1)$, $(0, 8, 1)$ and $(0, 9, 1)$ modes for the isotherm at 230 K in propene.

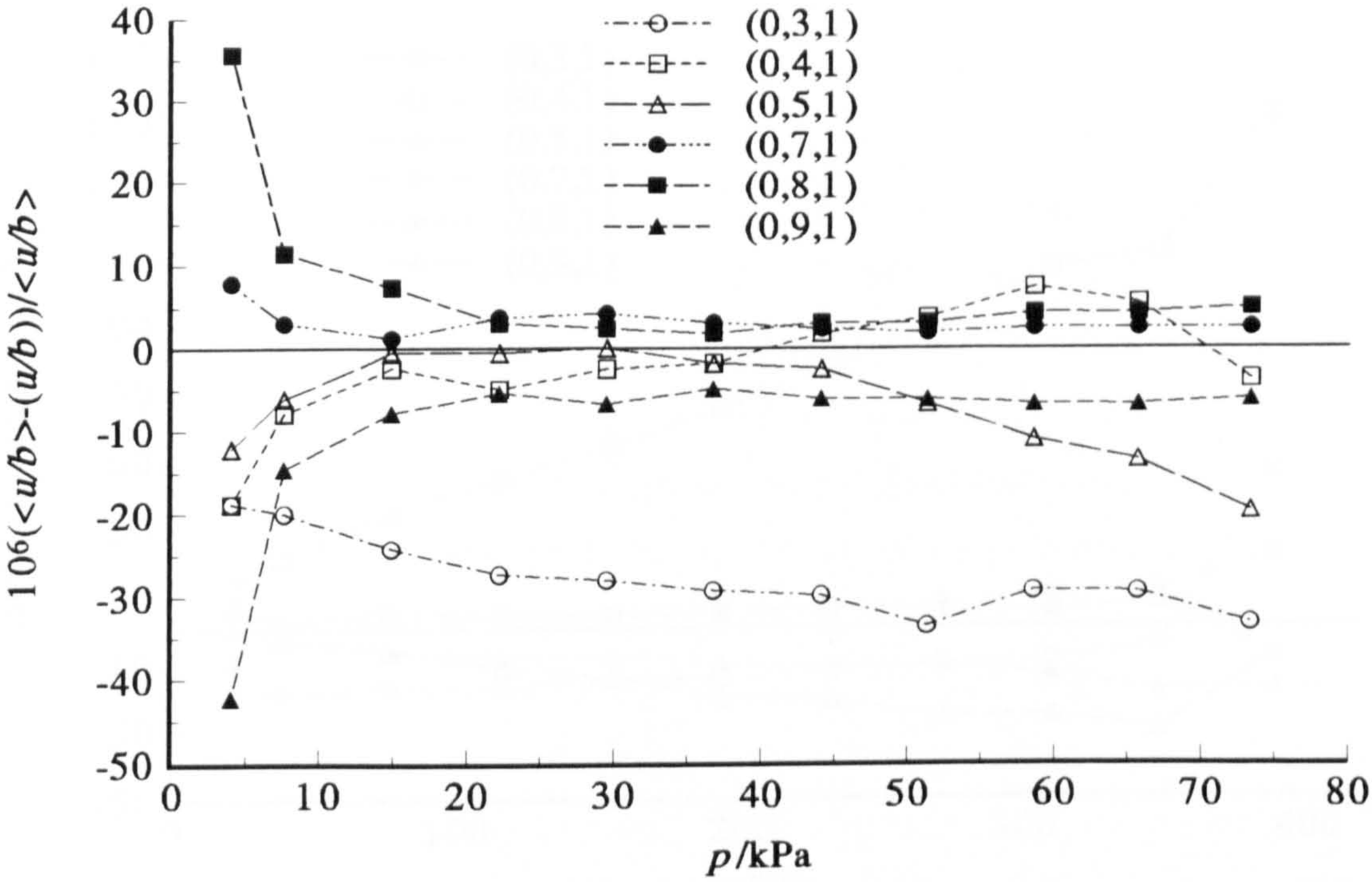

Figure 6.6: Fractional deviations of the calculated values of u/b from the average value $\langle u/b \rangle$ determined for the $(0, 7, 1)$, $(0, 8, 1)$ and $(0, 9, 1)$ modes for the isotherm at 253 K in propene.

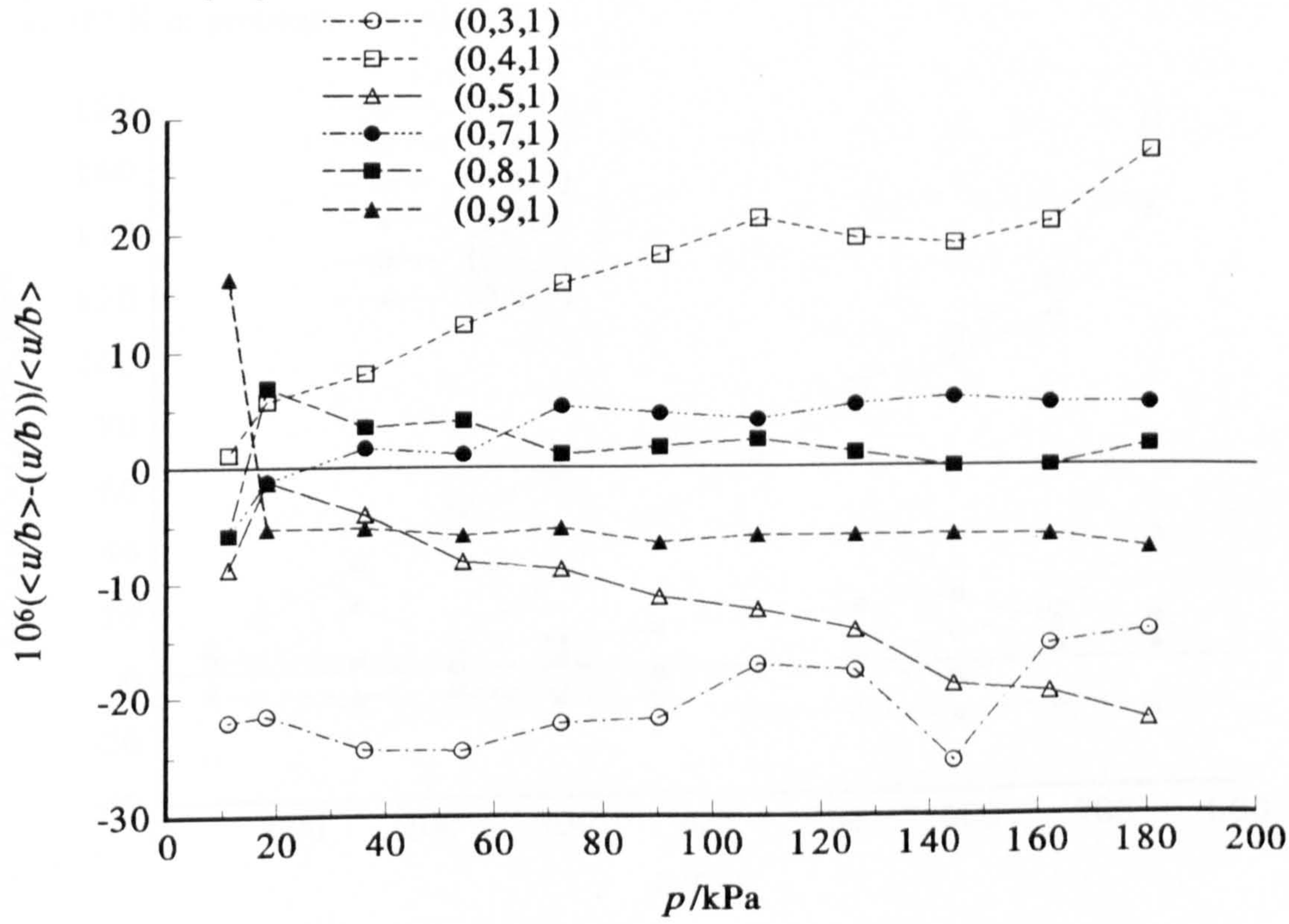

Figure 6.7: Fractional deviations of the calculated values of u/b from the average value $\langle u/b \rangle$ determined for the $(0, 7, 1)$, $(0, 8, 1)$ and $(0, 9, 1)$ modes for the isotherm at 282 K in propene.

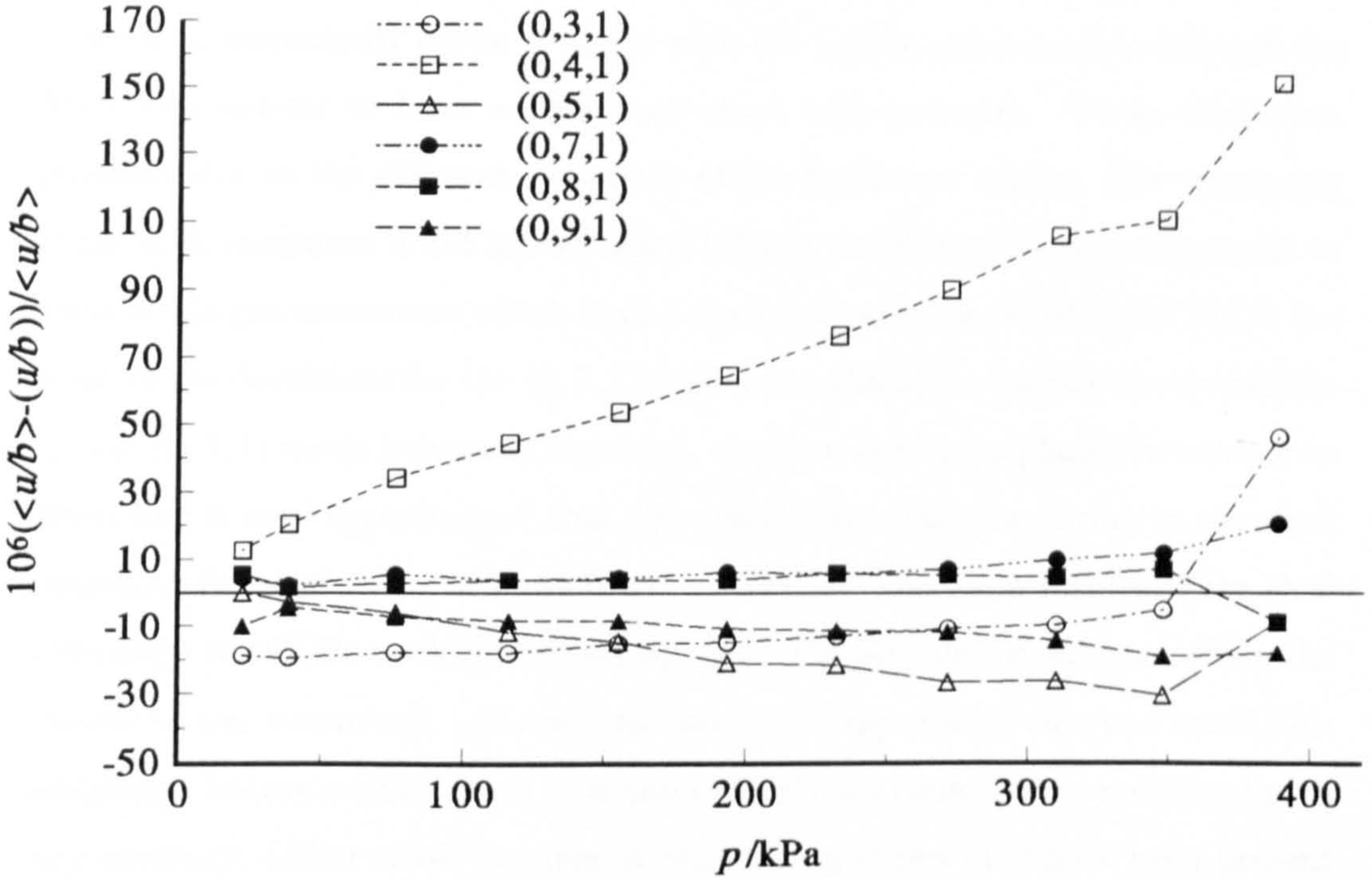

Figure 6.8: Fractional deviations of the calculated values of u/b from the average value $\langle u/b \rangle$ determined for the $(0, 7, 1)$, $(0, 8, 1)$ and $(0, 9, 1)$ modes for the isotherm at 317 K in propene.

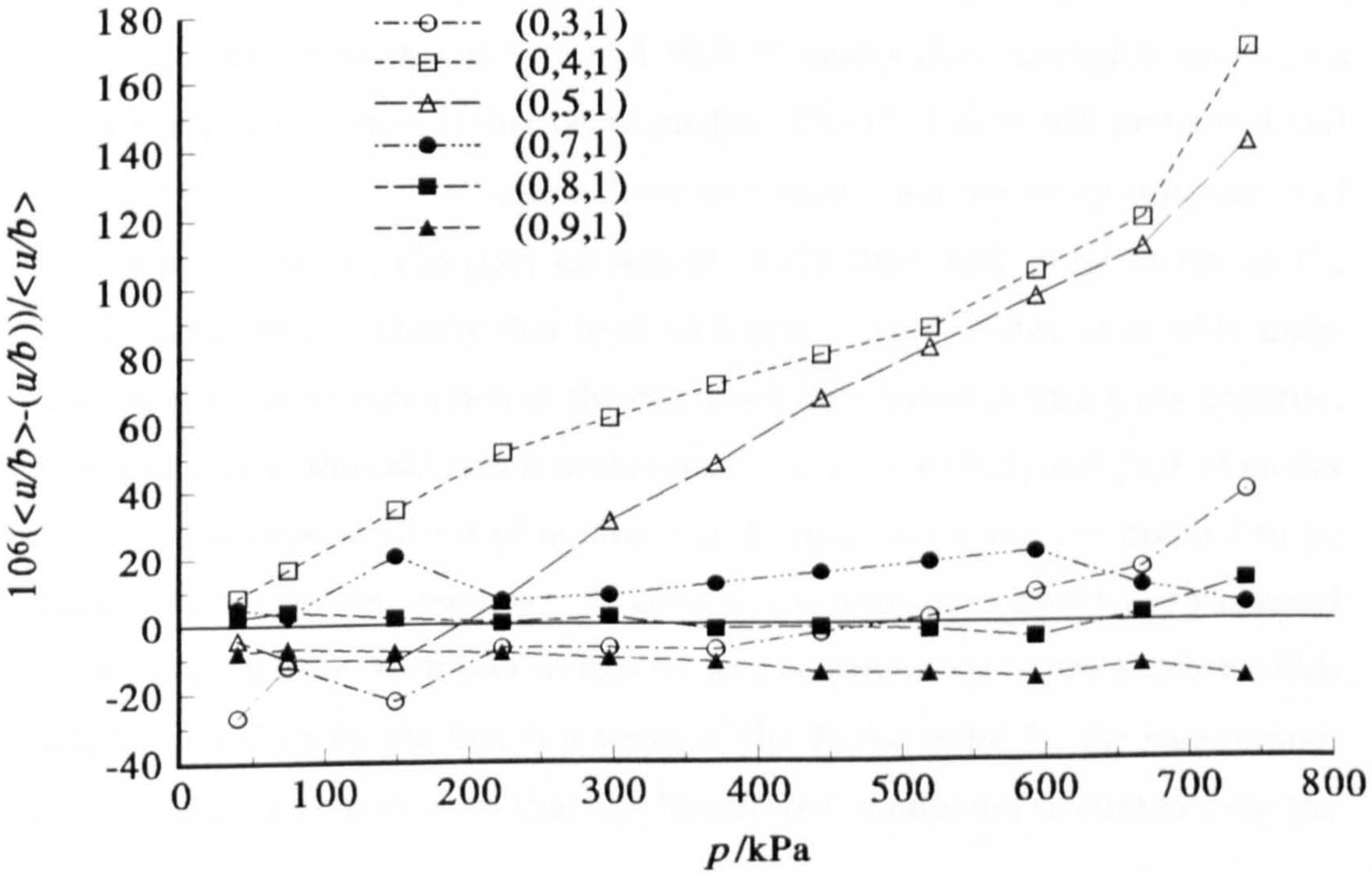

may easily be detected. The $(0,2,1)$ mode has been omitted as the deviations are an order of magnitude larger and will be discussed separately. Figure (6.8) clearly shows the deviations from $\langle u/b \rangle$ for the $(0,4,1)$ and $(0,5,1)$ modes increasing as expected as the pressure increases for the isotherm at 317 K. The $(0,3,1)$ mode however, unexpectedly seems to agree with the higher order modes although the deviations appear to have a significant slope with pressure. These effects are probably due to the different symmetry of the resonance modes. The symmetry of the shell resonance is not known but it is likely it will couple more effectively to some of the gas resonances which have a similar symmetry. At 253 and 282 K the slope of the deviations for the $(0,5,1)$ modes has changed sign but the deviations for the $(0,4,1)$ mode behave as expected. Again a definite explanation cannot be given but it may hypothesised that the change in behaviour is due to the shell resonance being made up of more than one feature. The main feature of the shell resonance at 500 Hz could be picked up using the impedance analyser when the resonator was evacuated, but even the measured response to this was small. An additional feature could be seen at around 750 Hz but could not be measured with any accuracy. Other small features at higher frequencies may have been present and may have caused different resonance modes to be pulled in different directions as the temperature was changed. This occurs because the gas resonances move relative to the shell resonance components because the change in frequency with temperature is governed by different effects. At 230 K the pressure range is limited to 80 kPa and now the $(0,4,1)$ and $(0,5,1)$ modes show negligible deviations from $\langle u/b \rangle$ of the three higher order modes. The $(0,3,1)$ is still perturbed and it may be that it has now moved closer to a small high frequency component of the shell resonance. The poor agreement of the three high order modes at the lowest pressure is probably due to it no longer being possible to reliably make the boundary layer correction to the resonance frequencies at such a low pressure. Along all four of the calibration isotherms the $(0,7,1)$, $(0,8,1)$ and $(0,9,1)$ modes agree to the expected level of accuracy of 20 ppm and hence are deemed to be unaffected by the shell resonance. In general, gas resonances need to be separated by at least ten times their half-widths to have contributions to one another which may be described by the first two terms of the Taylor series for the background. It is probably no coincidence that the 'unaffected' modes are separated from the

Figure 6.9: Variation of the fractional deviations with frequency of the calculated values of u/b for the $(0,2,1)$ mode from the average value $\langle u/b \rangle$ determined for the $(0,7,1)$, $(0,8,1)$ and $(0,9,1)$ modes.

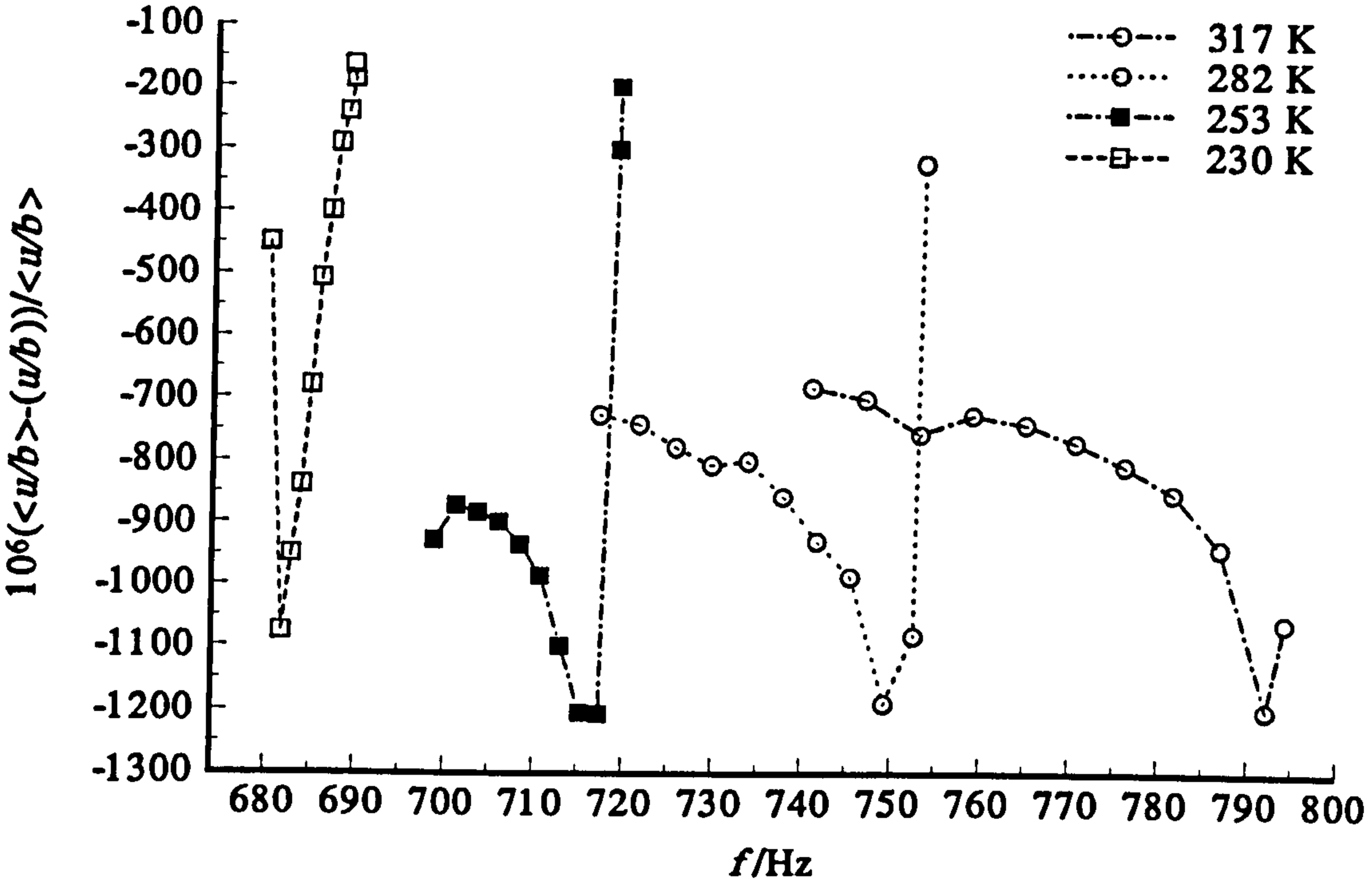

shell resonance by at least ten times its half-width of 150 Hz. More importantly the agreement of the $(0,7,1)$, $(0,8,1)$ and $(0,9,1)$ modes indicates that the model of the response of the resonator under pressure (at least with respect to the radius ratio ζ) based on the elastic theory of two concentric cylinders is adequate and may be used to calculate values of ζ for isotherms carried out on test gases.

The deviations of the $(0,2,1)$ mode from $\langle u/b \rangle$ of the three high order modes for all the isotherms have been plotted against frequency in figure (6.9). For each isotherm the deviations pass through a minimum at a particular frequency that represents the maximum deviation. As mentioned above, the shell resonance investigated at 300 K appeared to have a second feature at around 750 Hz. A possible explanation for the behaviour of the $(0,2,1)$ mode is that by chance it passes through this feature at every temperature. The maximum deviation would then be a measure of the position of this component of the shell resonance. Each isotherm may probe a different portion of it as the shell and gas resonances move

Figure 6.10: Variation of the fractional deviations with pressure of the calculated values of u/b for the $(0,2,1)$ mode from the average value $\langle u/b \rangle$ determined for the $(0,7,1)$, $(0,8,1)$ and $(0,9,1)$ modes.

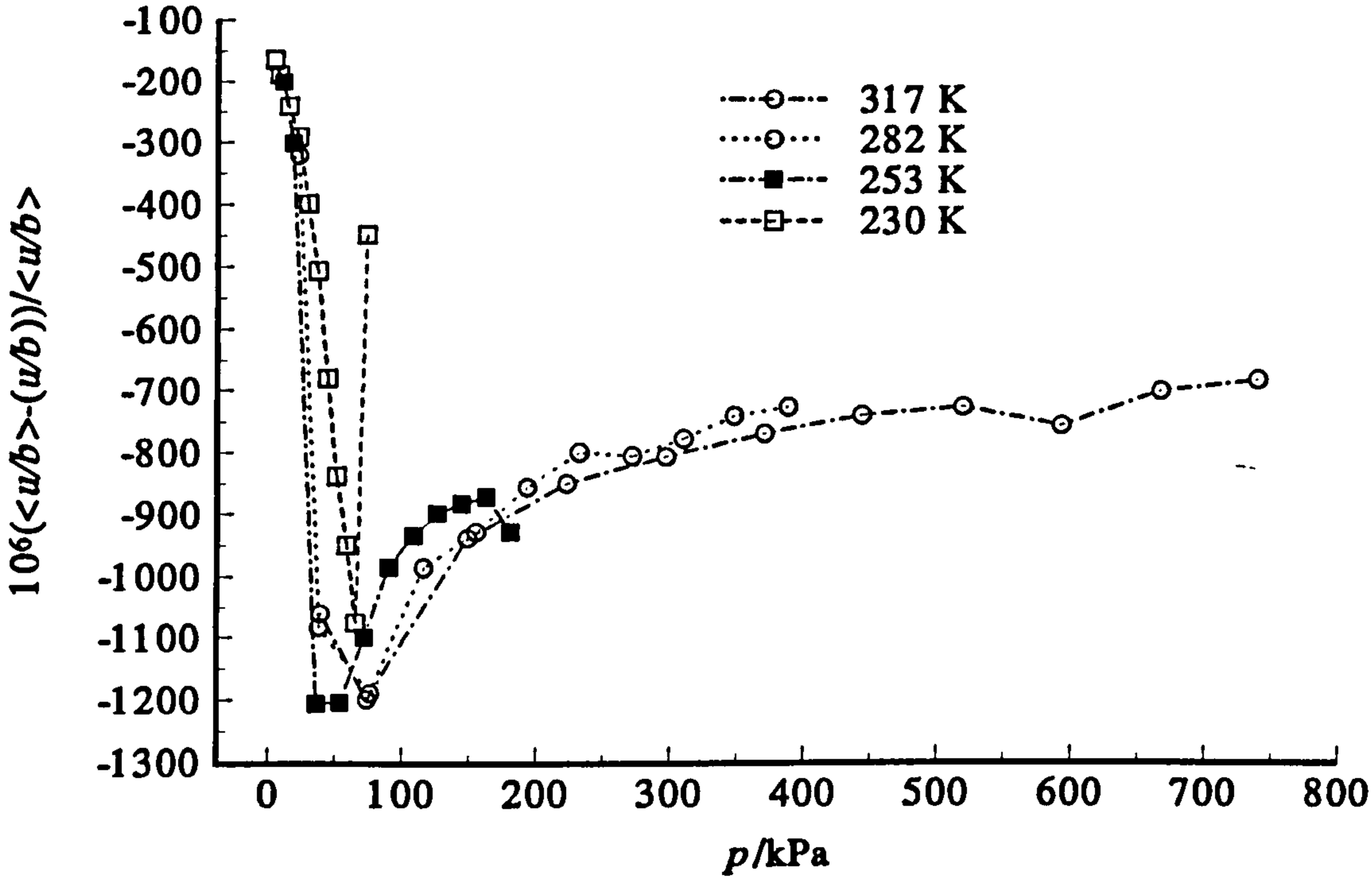

relative to one another. The speed of sound in any medium is given by

$$u^2 = \frac{1}{\rho \kappa_S} = \frac{\gamma}{\rho \kappa_T} \tag{6.22}$$

where κ_T is the reciprocal of the bulk modulus defined by equation (6.18). The speed of sound in the aluminium shell was calculated using the value of the density and heat capacity of Al from reference [10], the elastic properties as described previously and the linear expansivity taken from reference [12]. The speed of sound was found to decrease with temperature so the effect seen with the $(0,2,1)$ mode is not due to a component of the shell resonance.

Another possibility is that the $(0,2,1)$ mode is adversely affected by a geometric imperfection in the resonator. When the deviation of this mode from the mean of the higher order modes is plotted against pressure in figure (6.10) it is very striking that the deviations at all temperatures agree and are a function of pressure. It may be that there is a geometric perturbation to the resonator that affects the $(0,2,1)$ mode most severely due to the number of turning points of the wavefunction. All azimuthal modes are two fold degenerate, where the two com-

ponents correspond to $+|m|$ and $-|m|$, and have m turning points as θ is swept from 0 through to 2π. Eccentricity in the radii of both cylinders for example may cause one component to be shifted to a different extent to the other for the $(0,2,1)$ mode resulting in a shift in the resonance frequency. For the higher order modes that have a greater number of turning points the shifts may tend to average out for the two components of the resonance, or the geometric perturbation may have a functional form such that it does not perturb these modes. If the perturbation to the resonator geometry changes with pressure, it could cause the $(0,2,1)$ mode to be shifted in a way indicated by figure (6.10). For example one side of the resonator may be more firmly bolted than the other so that the changes in the radii with pressure are asymmetric. If the $(0,2,1)$ mode is affected in this way for all the test gases where the frequencies are very different, then the observed form of the deviations for this mode is probably due to geometric changes.

6.4. Determination of the outer radius b.

The eigenvalues χ_{mn} were calculated for each mode at each state point along the isotherms using the accepted values of the radius ratio $\zeta = a/b$ described above. These combined with the corrected resonance frequency values f_N gave values of $u(T,p)/b(T,p)$. An outer radius of 140 mm was used for the calculation of the boundary layer correction terms. This assumption lead to errors in the corrected resonance frequencies and thus the calculated values of u/b that were always smaller than 10 ppm. Values for the speed of sound, u in propene were needed to calculate the outer radius b of the resonator.

6.4.1. Determination of the speed of sound in propene

The propene data that was used to analyse the calibration measurements in the annular resonator is of the form of series expansions in the pressure p describing the speed of sound $u(T,p)/a(T,p \rightarrow 0)$ at eight different temperatures from 220 to 350 K. The limiting value of the radius, $a\,(T,p \rightarrow 0)$ of the spherical resonator in which the measurements were carried out is known to better than 2 ppm[13]. As the temperatures of the two sets of measurements are different, the coefficients were fitted using non linear regression analysis to allow them to be evaluated at

Figure 6.11: Coefficient A_0 in equation (6.22) as function of temperature for propene.

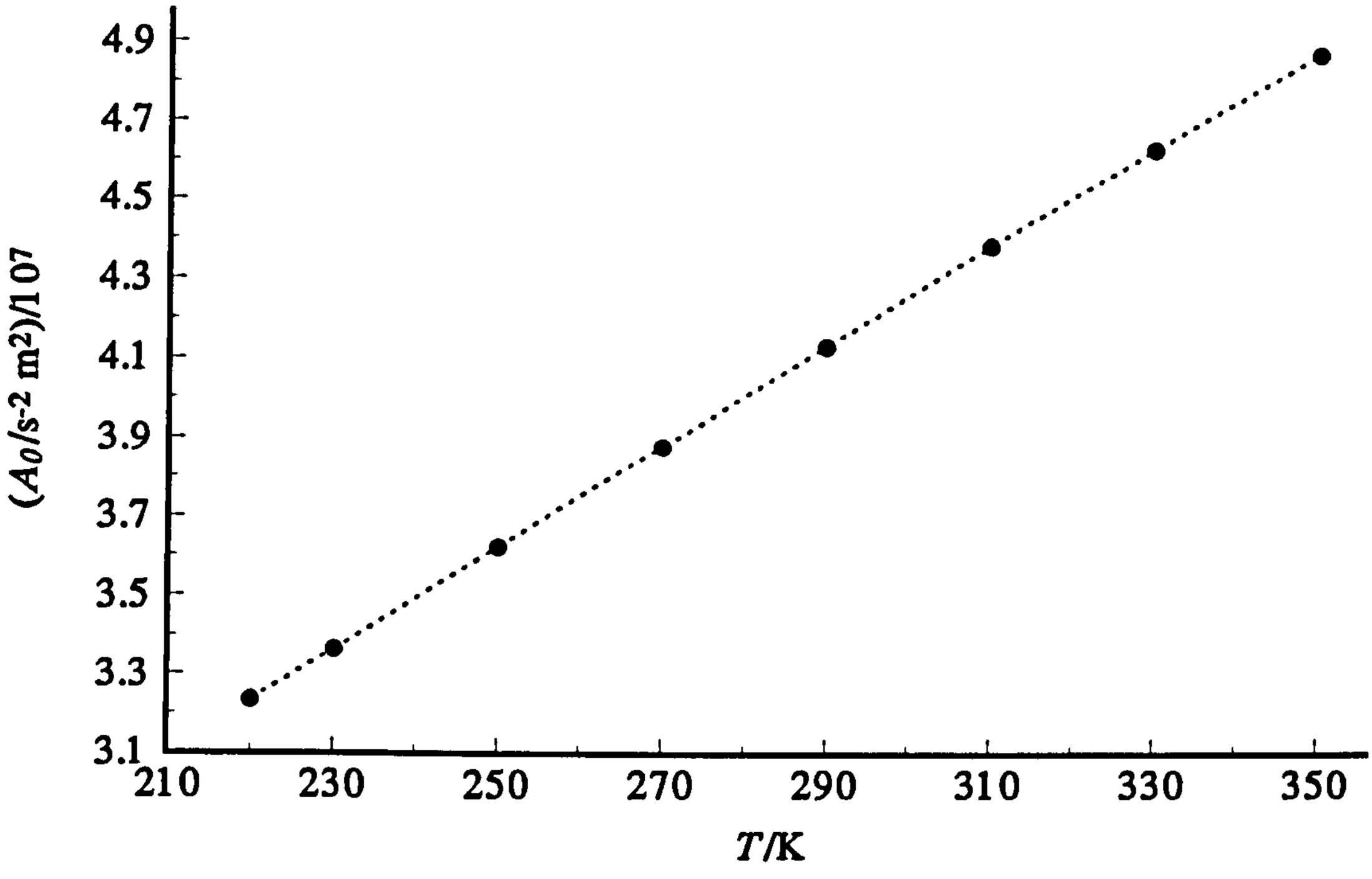

the experimental temperatures used with the annular resonator. In order to do this the speed of sound data for propene from the spherical resonator was forced to four term polynomial fits

$$u^2 = A_0 + A_1 p + A_2 p^2 + A_3 p^3, \tag{6.23}$$

at every temperature despite the very different pressure ranges. In equation (6.23) the speed of sound u is in $\mathrm{m \cdot s^{-1}}$ and the pressure p in Pa. The coefficients and their standard deviations where applicable, are shown in figures (6.11) to (6.14). The values of the first two coefficients could all be fitted to within their standard deviations and different functional forms gave essentially identical values for the calculated speed of sound. The third and fourth coefficients could not be adequately fitted due to the large standard deviations at the lower temperatures. The large standard deviations were due to forcing the data from small pressure ranges to four term fits where they were not justified. Above 250 K four term fits were necessary to fit the data (with the exception of 270 K) and it was possible to fit the values of the third and fourth coefficients at 250, 290, 310, 330 and 350 K to within their standard deviations. The data at 270 K was omitted

Figure 6.12: Coefficient A_1 in equation (6.22) as function of temperature for propene.

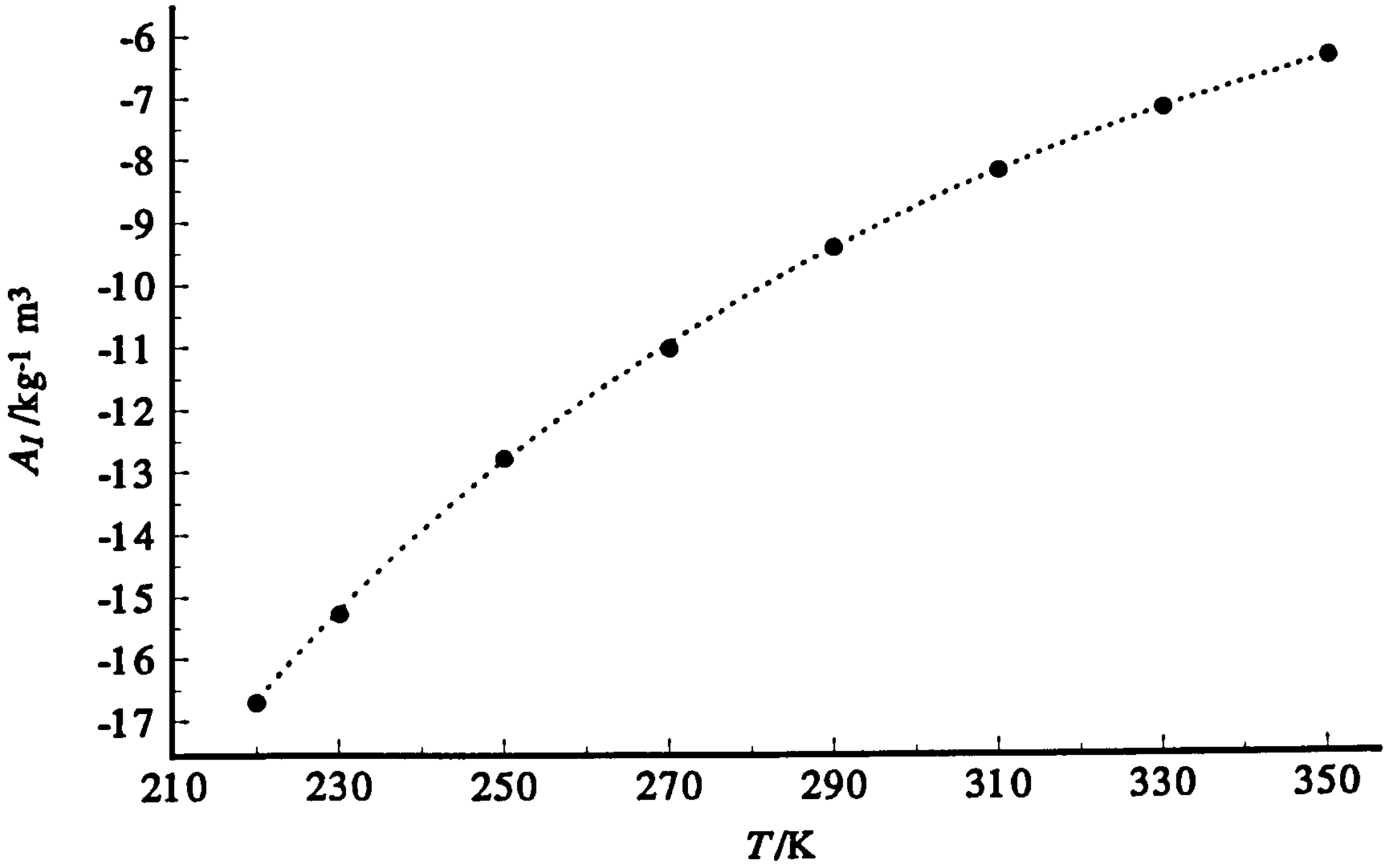

Figure 6.13: Coefficient A_2 in equation (6.22) as function of temperature for propene.

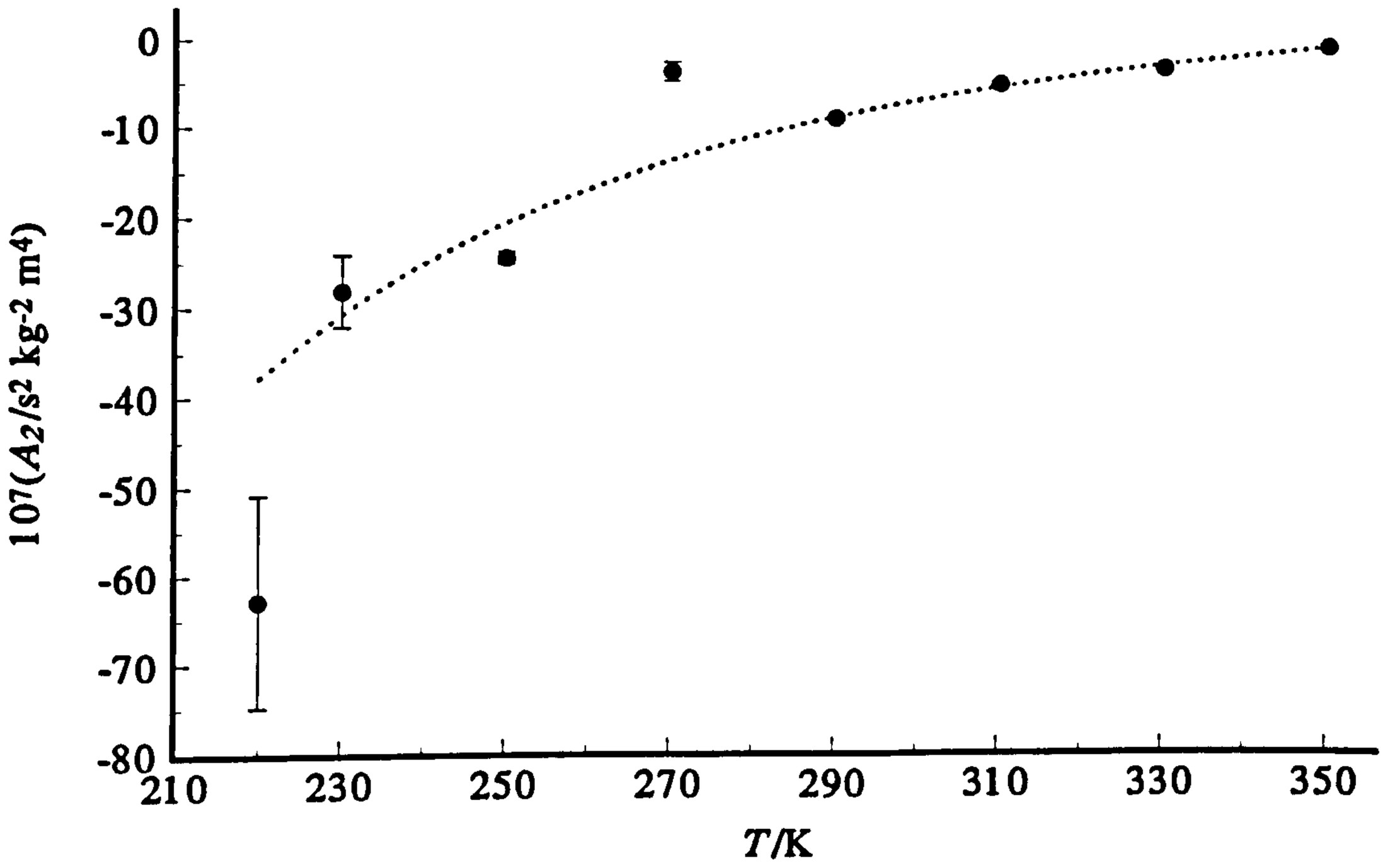

Figure 6.14: Coefficient A_3 in equation (6.22) as function of temperature for propene.

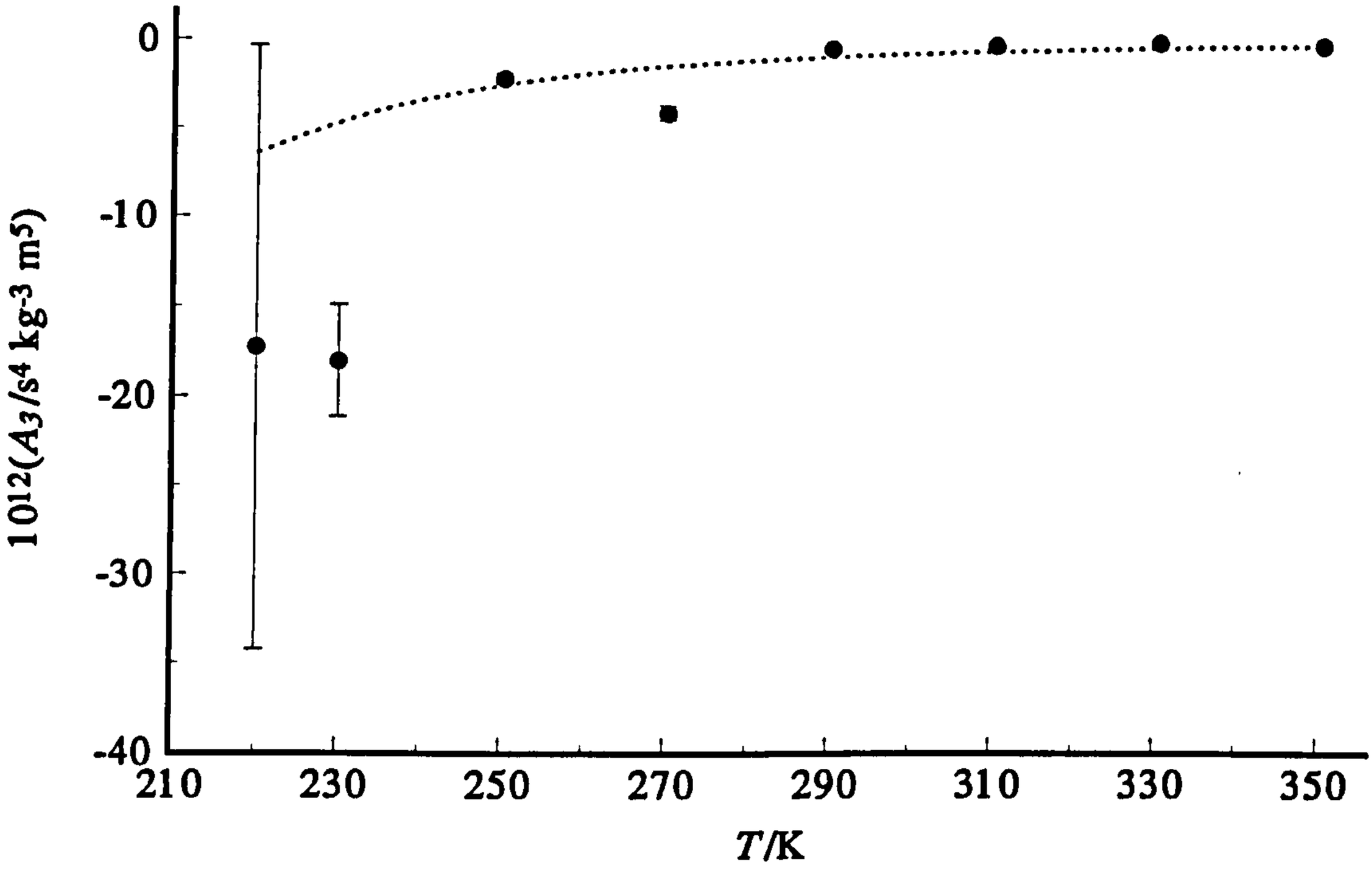

from the analysis because the set of measurements taken in the sphere at this temperature had a much reduced pressure range due to a leak in the system. This procedure allowed the speed of sound in propene to be calculated at pressures up to 800 kPa over the temperature range 250 to 350 K with an accuracy of better than 15 ppm. The average value of $\langle b \rangle$ was extracted from the frequencies of the $(0,7,1)$, $(0,8,1)$ and $(0,9,1)$ modes at each pressure along the isotherms at 253, 282 and 317 K. Combining all the errors from the correction terms, the assumption about the geometry, and the error in the calculated value of u leads to an estimated accuracy of the values of $\langle b \rangle$ of better than 30 ppm. The speed of sound at 230 K was calculated using values for the first two coefficients as used for the higher temperature isotherms. At 230 K, there were isotherms carried out in the sphere and annulus in propene at almost identical temperatures. The isotherm in the sphere had an average temperature of 230.094 K and that in the annulus of 229.895 K and hence the values for the third and fourth coefficients could be used without modification. Worst case extrapolation of these two coefficients to account for the temperature difference of 0.199 K resulted in a sound speed that was different by 12 ppm at the maximum pressure of 70 kPa. The magnitude of

the error introduced is probably only of the order of 2 ppm.

Values of $\langle u(T,p)/b(T,p)\rangle$ for the (0,7,1) to (0,9,1) azimuthal modes of the annular resonator were used to calculate $\langle b\rangle$ at each state point. Global fitting of these data to a function of both temperature and pressure using weighted non linear regression analysis as described for the fitting of ζ was attempted. The temperature dependence was accurately described but the small residual pressure variation could not be fitted unambiguously leading to significantly different estimates of b. For the isotherm at 317 K the calculated shift in b calculated over the same pressure range as the isotherm is 108 ppm in b and the observed shift was 72 ppm. The agreement between the values is encouraging given that the estimated accuracy of b is of the order of 30 ppm. The shift in b with temperature over the experimental range is approximately 3000 ppm so it is unsurprising that the pressure dependence could not be resolved.

Two different methods for solving this problem were attempted. Firstly, the values of the average speed of sound $\langle u(T,p)/b(T,p)\rangle$ along each isotherm were fitted to extract $\langle u(T,p\rightarrow 0)/b(T,p\rightarrow 0)\rangle$ at each of the four calibration temperatures and the limiting values of b determined. This method does not solve the problem of determining the pressure dependence of the outer radius, and additionally, due to the small number of data points the four values of $b(T,p\rightarrow 0)$ could not be fitted unambiguously to a function of temperature. Three different functional forms gave similar standard deviations for the fit but resulted in values of b that differed by up to 100 ppm at the maximum temperature of 339 K, which is outside the estimation of the accuracy of the experimental values.

In the second method, the value of $\langle u(T,p)/b(T,p)\rangle$ at each state point was corrected back to $\langle u(T,p)/b(T,p\rightarrow 0)\rangle$ using the compliance, $(1/b)\,(\partial b/\partial p)$ calculated using the model for the change in geometry of the resonator based on elastic theory. This gave eleven estimates of $b(T,p\rightarrow 0)$ at each calibration temperature increasing the degrees of freedom in the fitting procedure. The level of agreement between the values also gives a measure of how well the elastic model describes the data. If the deviations were within the expected bounds of around 30 ppm, then the elastic theory model could be used with confidence for the remainder of

Figure 6.15: The deviations δb_0 from equation (6.23) of the limiting values b_0 cac-ulated from fitting b at each pressure and those calculated using the compliance.

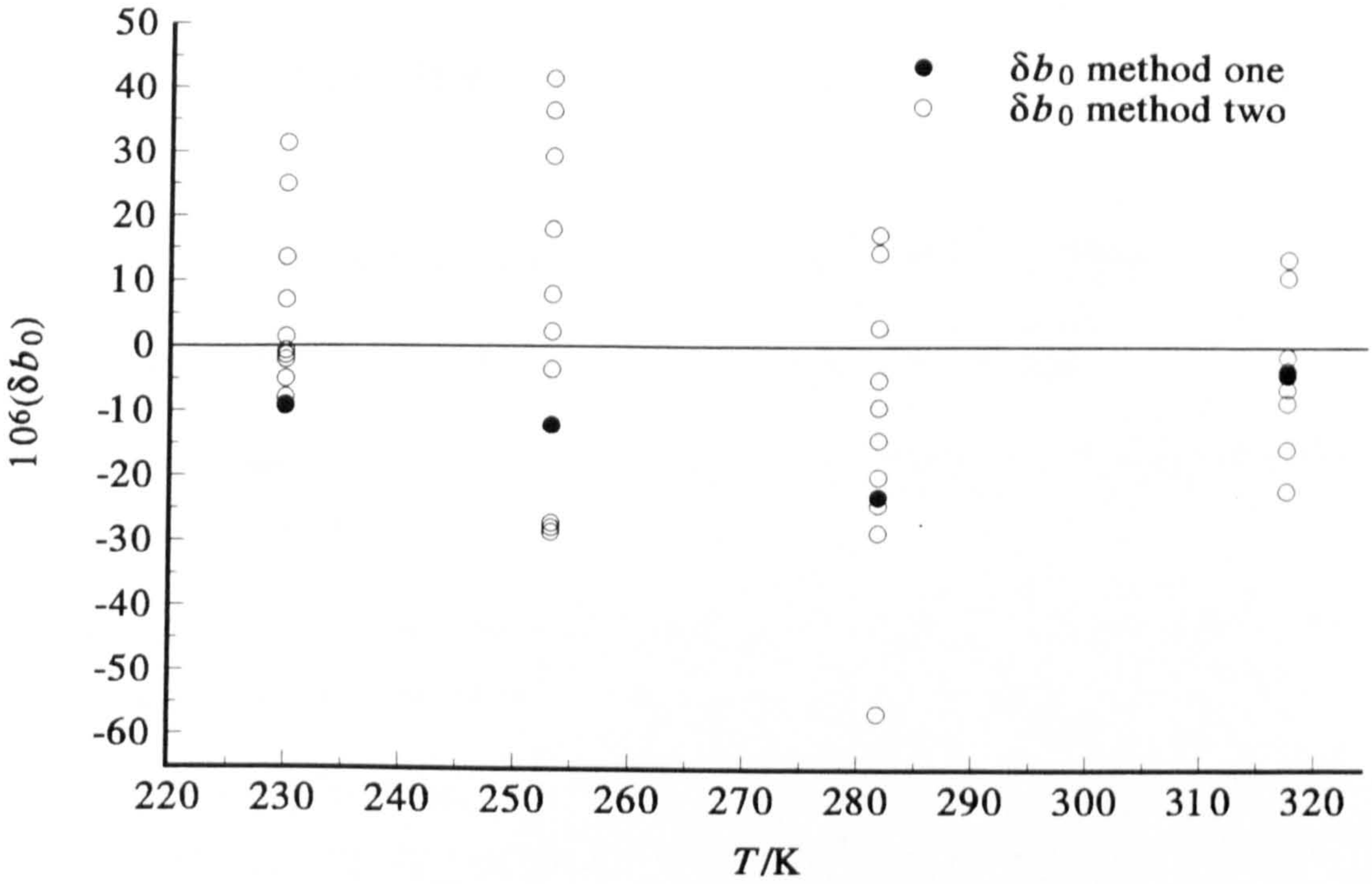

this work. Weighted non linear regression analysis gave

$$b(T, p \to 0)/\mathrm{mm} = b_{0,\mathrm{fit}} = (140.5598 \pm 0.0027) - \frac{(46826 \pm 172)}{(T/\mathrm{K})^2}, \qquad (6.24)$$

with a standard deviation of b equal to 0.0034 mm. This corresponds to 25 ppm in b. The deviations $\delta b_0 = (b_0 - b_{0,\mathrm{fit}})/b_{0,\mathrm{fit}}$ from this equation are shown in figure (6.15), where the excellent agreement of the four values of $b\,(T, p \to 0)$ determined previously with this fit of better than 10 ppm may be seen. The deviations from equation (6.24) are generally of the order of the estimated accuracy of ±30 ppm. The fact that the spread of the data does not vary particularly with temperature, where very different pressure ranges were used, indicates that the elastic model used to determine the pressure dependence of the geometry represents the data adequately. Hence equation (6.24) was used in the analysis of the experimental data discussed in the following chapters.

BIBLIOGRAPHY

[1] Bailey C, Buxton A J and Ewing M B. Unpublished work 1992.

[2] Mehl J B and Moldover M R. *J. Chem. Phys.* 1982, **77**, 455.

[3] Vasserman A A and Litovchenko V V. *Viniti.* 1976, 2226. Deposited Document (Russian).

[4] Parkinson C, Mukhopadhyay P and Gray P. *J. Chem. Soc. Faraday Transactions 1.* 1972, **28**, 1077.

[5] Vargaftik N B. *Tables of the Thermophysical Properties of Liquids and Gases in Normal and Dissociated states.* (Wiley: London, 1975).

[6] Reid R C, Prausnitz J M and Poling B E. *The Properties of Gases and Liquids* Fourth Edition. (McGraw Hill: New York, 1986).

[7] Trusler J P M. Ph.D Thesis, University of London 1984.

[8] Trusler J P M. *Physical Acoustics and Metrology of Fluids.* (Adam Hilger: Worcester, 1991).

[9] Lamb H. *Statics: Including Hydrostatics and the Elements of the Theory of Elasticity.* (Cambridge University Press: Cambridge 1943).

[10] *Kaye & Laby Tables of Physical and Chemical Constants Sixteenth Edition.* Editors:Noyes J G, Asher J, Jones O C and Philips G F. (Longman: Essex, 1995).

[11] Ledbetter H M. *Cryogenics.* 1982, **22**, 653.

[12] Kroeger F R and Swenson C A. *J. Appl. Phys.* 1977, **48**, 853.

[13] Boyes S J. Ph.D Thesis, University of London 1988.

7. ANALYSIS OF ACOUSTIC MEASUREMENTS

7.1. Introduction

This chapter describes the self consistent method of analysis developed to allow the determination of not only the heat capacity and the second virial coefficient for the gas or gas mixture under investigation, but which also provides estimates of the transport properties from an analysis of the half-widths of the resonance modes. The shear and bulk viscosities and the thermal conductivity of a gas are often not available in the literature, or the data do not cover the relevant temperature or pressure ranges. This problem is particularly acute if a gas mixture is under study because the transport properties of the pure components are not strictly additive and the number of systems studied is small.

7.2. Measurements

Eight isotherms were studied in each of the test gases. The same temperatures namely 220, 241, 253, 267, 282, 299, 317 and 339 K were used in every case. The second virial coefficient B varies as an approximate function of $(1/T)$, so the temperatures were chosen to be equally spaced in this variable, in order to weight the data to the lower temperatures where greater variation occurred.

The pressures chosen along each isotherm did not follow the standard pattern used for the calibration measurements. At each temperature, eleven low pressure measurements were taken at 10 kPa intervals from 110 kPa down to 10 kPa and a final measurement was taken at around 5 kPa. However, as the second acoustic virial coefficient β_a varies with temperature these results do not represent investigation of the same extent of the speed of sound variation at every temperature. An additional four equally spaced measurements at higher pressures were added.

At the maximum temperature of 339 K the maximum pressure was chosen as the limiting pressure of the apparatus of 1 MPa or 0.6 times the vapour pressure. The maximum pressure for each of the other 7 temperatures was chosen such that for every isotherm $\beta_a(T)\rho_{MAX}$ gave a constant value. The value of β_a at each temperature was estimated from fits of literature values of B to the square well potential, using equation (1.15), and values for γ^{pg} determined also from published data.

The decision to weight the measurements in favour of the low pressure measurements was based on the unknown size of the perturbation due to motion of the shell walls. As the perturbation is greatest at high pressures it was decided to take enough low pressure data to enable a full analysis even if all the high pressure data had to be rejected. The data at every temperature represents the same fractional change in u^2, so that the same order of polynomial fit should be expected in every case. If higher order terms are required at some temperatures, this fact will immediately point out a source of unknown variation in the results.

The resonance frequencies f and half-widths g were measured for the four azimuthal modes $(0,2,1)$ to $(0,5,1)$, and the three azimuthal modes $(0,7,1)$ to $(0,9,1)$ for the three test gases SF_6, CHF_3 and $\{0.85CH_4+0.15C_2H_6\}$. The lowest order $(0,1,1)$ azimuthal mode was not measured because in some of the test gases used it fell below the cut off frequency of the band pass amplifier of 300 Hz. The 6th order $(0,6,1)$ azimuthal mode was also omitted from the measurements as it lay too close to the $(0,2,1)$ mixed mode for the resonance fitting algorithm described in chapter 5 to extract f and g accurately.

7.3. Calculation of the Corrected Speed of Sound

(u/b) is proportional to the ratio of the corrected resonance frequencies to the eigenvalue χ_{mn} which depends on the cavity geometry. The relevant geometric parameters were discussed in chapter 6. The fractional error in the eigenvalue is of the order of 1×10^{-5}. The resonance frequencies have to be corrected to account for the shear and thermal boundary perturbations, the effects of holes in the resonator wall, and absorption in the bulk of the gas. As for the calibration measurements the effects of imperfect accommodation at the wall is neglected because the two

effects cannot be resolved and are small compared to the errors introduced due to uncertainties in the transport properties. Modes that are adversely affected by motion of the shell wall also need to be removed from the analysis. Estimation of the perturbations require values for γ^{pg} and B for the calculation of γ, and of ρ and c_p that are used to calculate the shear δ_s, and thermal δ_t, penetration lengths which in turn require values of the shear viscosity η and thermal conductivity κ. These are needed to determine the magnitude of the corrections due to the boundary layers and the holes in the wall as well as the classical contribution to the bulk perturbation. In addition, the bulk viscosity η_b is required to calculate the contribution of thermal relaxation to the bulk effects. The equations for the perturbations due to the boundary layers and due to absorption in the bulk of the gas are given in chapter 2 and for the holes in the shell wall in chapter 4.

Initial estimates of γ^{pg}, B, η and κ (which may be estimated from η and γ^{pg}) were obtained from the literature and were used to calculate the contribution g_o to the resonance half-widths due to holes in the wall of the resonator. The experimental half-widths g were corrected to account for the holes in the wall and the remainder $(g - g_o)$ were used to provide estimates for the transport properties κ_0, η_0, and $\eta_{b,0}$ as well as their density dependencies $(\partial\kappa/\partial\rho)$, $(\partial\eta/\partial\rho)$ and $(\partial\eta_b/\partial\rho)$. This procedure is explained in greater detail in a later section of this chapter. The resonance frequencies f were then corrected for holes in the resonator wall, boundary layer perturbations and bulk effects. The values of (u/b) at each of the experimental pressures along the isotherm were analysed to obtain better estimates for γ^{pg} and B as described later in the chapter. The analysis was then repeated using the improved estimates for the transport properties extracted from the half-width analysis and the new γ^{pg} and B to provide better estimates of the contribution to the resonance half-width due to the effect of holes, and the remainder re-analsyed to provide more accurate estimates for the transport properties. These were then used in combination with the new γ^{pg} and B to obtain better estimates of the corrections to the resonance frequencies. The resonance frequencies corrected in the second iteration of the analysis routine are used to provide the final estimates of γ^{pg} and B, further iterations were shown to change the estimates by less than their standard deviations. The transport properties obtained from the second iteration were also taken as the final estimates because

the correction due to the holes in the wall is small compared to full width of the resonance and the values do not even change significantly on the second iteration. The values were updated more for completeness than accuracy.

It has been mentioned above that literature values for some of the gas properties were utilised in the initial iteration of the analytical method. Use of the estimates speeds up the analysis procedure as it reduces the number of iterations required. Usually when no literature results are available only one more iteration is required to reach a self consistent solution for the transport properties and γ^{pg} and B. A very important part of the analysis technique not yet discussed is the removal of data that may cause systematic errors in the results. Inclusion of modes with half-widths which have been perturbed by the shell resonance or other unknown loss mechanisms will lead to systematically large estimates of the transport properties, which in turn will lead to erroneous corrections to the resonance frequencies. The corrections are not linear in temperature thus leading to errors in the limiting slope of the results from which the second acoustic virial coefficient β_a is determined. Consequently in the analysis of the resonance half-widths, modes that showed a pressure dependence different to the majority were removed. The identification of such modes is relatively easy as the analysis program plots the reduced excess half-widths $\Delta g/f$ for each mode at every pressure. The excess half-width Δg is the experimental half-width minus all the calculated contributions to it based on the values of the transport properties extracted from the regression analysis. Pressures for which the excess half-widths showed greater scatter than the majority of the results were also removed from the analysis. This tended to occur at the lowest pressure where the half-width is greatest and thus the excess half-width is more sensitive to the transport properties. In addition at low pressures the experimental half-widths are more likely to be in error due to the influence of nearby modes.

Once a satisfactory half-width analysis had been achieved, the calculated corrected resonance frequencies were used to determine the sound speed at each of the pressures along the isotherm and, as no correction could be applied for the effect of the shell resonance, affected modes had to be removed. Thus modes which did not agree to the expected level (determined by the errors associated with the estimates of the transport properties) were removed from the analysis.

In general the same level of agreement could achieved for the full pressure range. It would be expected that the agreement at the higher pressures would be better due to the smaller bulk and boundary layer corrections, but it is at high pressure that the modes are most severely affected by the shell correction. Due to the frequency of the shell resonance, it was possible that it was perturbing all the modes in the high pressure regime for some of the test gases but, as the extent of the perturbation was unknown, the high pressure results were initially left in the analysis and modes that did not agree were discarded. For a set of data the modes in error were not always easy to identify as the results were scattered. However, as the shell resonance was expected to perturb the lower order modes with which it overlaps to a larger degree, higher order modes that agreed were preferentially retained in the analysis where a coincident agreement between some lower order modes also occurred. However, as all the modes may be affected, it was also necessary to scrutinise the remaining data carefully when the regression to extract γ^{pg} and β_a was performed. The methodology used to remove pressures still in error at this stage is discussed in a later section of this chapter. The decision to remove data is to some extent subjective, but it was attempted to perform the analysis in a rigorous manner designed at each stage to weed out data that would cause systematic errors in the final results. Obviously however, despite all efforts, the results may in some way be affected by systematic errors that would not exist for a system in which an unknown loss mechanism such as the shell resonance does not exist.

7.4. Analysis of the Half-widths to Determine the Transport Properties

The half-widths were fitted using a regression routine in which the different density dependence of the contributions due to the thermal and shear boundary layers and the bulk to the half-widths allows the loss mechanisms to be resolved. Originally, a least-squares type of analysis was attempted in which the thermal conductivity κ, the shear viscosity η and the bulk viscosity η_b were all free variables. This method, however, did not always reach a stable solution. Unfortunately, the thermal and shear boundary layer contributions to the half-width have the same

density dependence so the approach relied on the small difference in the ratios of the thermal to shear effects for each resonance mode to separate the variables. The differences were obviously not significant enough to support this type of analysis, but the situation could have been improved by the choice of a different set of modes for study in which the ratios of the thermal to shear effects differ to a greater extent. For example, radial modes have far greater thermal losses compared to azimuthal modes which suffer large shear losses. Extraction of the transport properties of the gas under study was not the primary objective of this work and the choice of modes was determined by those that were still resolved at low pressures where the bulk contribution is very large. Due to the specific design of the resonator these were the low order low frequency azimuthal modes that minimise the bulk term. The ratio of the thermal to shear losses for these modes varies less than 10 % for the set of modes $(0,2,1)$ to $(0,9,1)$. When the thermal conductivity is taken to be a function of the viscosity, the half-widths may be analysed unambiguously to extract coefficients related to the shear viscosity and its density dependence (from which the thermal conductivity may be estimated), and the bulk viscosity and its density dependence. Three different expressions were used to connect the shear viscosity to the thermal conductivity, they were the Euken relation, the modified Euken expression and the Stiel-Thodos relation[1]. It was expected that the expression that most accurately describes the relation between the shear viscosity and the thermal conductivity would give a half-width fit with a lower standard deviation than the others. However, all three gave very similar results and resulted in heat capacities and second virial coefficients that agreed to well within their standard deviations. For the azimuthal modes used, the ratio of the thermal to shear effects does not vary much between the modes. Consequently the partitioning of the thermal and shear effects is not critical at the level to which empirical relations such as those used can describe the transport properties. This issue is specifically investigated for CHF_3. For the other two test gases the Steil-Thodos relation was used because for other polyatomic gases this has been found to describe the dependency of the thermal conductivity on the shear viscosity most accurately. The Steil-Thodos expression has in general been found to describe thermal conductivities to within 2 % when reliable values of the shear viscosity and specific heat capacity are used[1]. Obviously, use of a relation

which does not describe the dependency of the thermal conductivity on the shear viscosity to within a few per cent would result in systematic errors in the heat capacities and second virial coefficients extracted from the sound speeds.

If the thermal conductivity κ is written as

$$\kappa = D\eta, \tag{7.1}$$

then the sum of the contributions to the half-width G may be written as

$$\begin{aligned} G = g - g_o = \; & g_h + g_s + g_b \\ = \; & \left[\sqrt{\pi f}\left(\left\{(\gamma-1)\sqrt{\frac{D}{c_p}}\sqrt{\frac{\eta}{\rho}}\right\}H + \sqrt{\frac{\eta}{\rho}}S\right)\right] \\ & + \left\{\frac{\pi f^2}{u^2}\left[\frac{4}{3}\frac{\eta}{\rho} + (\gamma-1)\frac{D}{c_p}\frac{\eta}{\rho} + \frac{\eta_b}{\rho}\right]\right\}. \end{aligned} \tag{7.2}$$

by summing equations (2.88), (2.89) and equation (2.52) in which the absorption coefficient α is given by equation (2.33). Equation (7.2) may not be fitted using a regression routine because many of the terms have the same density dependence. In equation (7.2), H and S are the integral parts of the expression for the contributions to the resonance half-widths given by

$$\begin{aligned} H = \; & \frac{1}{2V\Lambda_N^0}\left\{\left[\frac{bL}{\varepsilon}\left(\zeta R_m^2(\chi_{mn}\zeta) + R_m^2(\chi_{mn})\right)\right]\right. \\ & + \left(b^2 R_m^2(\chi_{mn})\left[1 - \left(\frac{m}{\chi_{mn}}\right)^2\right]\right. \\ & \left.\left. - (\zeta b)^2 R_m^2(\chi_{mn}\zeta)\left[1 - \left(\frac{m}{\chi_{mn}\zeta}\right)^2\right]\right)\right\}, \end{aligned} \tag{7.3}$$

and

$$\begin{aligned} S = \; & \frac{1}{\left[(l\pi/L)^2 + (\chi_{mn}/b)^2\right]2V\Lambda_N^0}\left\{\left[\frac{bL}{\varepsilon}\left(\left\{(l\pi/L)^2 + (m/b\zeta)^2\right\}\zeta R_m^2(\chi_{mn}\zeta)\right.\right.\right. \\ & \left.\left.\left. + \left\{(l\pi/L)^2 + (m/b)^2\right\}R_m^2(\chi_{mn})\right)\right] \\ & + \left[(\chi_{mn}/b)^2\left(b^2 R_m^2(\chi_{mn})\left[1 - \left(\frac{m}{\chi_{mn}}\right)^2\right]\right.\right. \\ & \left.\left.\left. - (\zeta b)^2 R_m^2(\chi_{mn}\zeta)\left[1 - \left(\frac{m}{\chi_{mn}\zeta}\right)^2\right]\right)\right]\right\}. \end{aligned} \tag{7.4}$$

which depend on the geometry of the annular cavity. In equations (7.3) and (7.4) Λ_N^0 is given by equation (2.75). In the analysis the shear η and bulk η_b viscosities

were described by

$$\eta = \eta_0 + \eta_1 \rho, \tag{7.5}$$

and

$$\eta_b = \eta_{b,0} + \eta_{b,1} \rho \tag{7.6}$$

where η_0 is limiting value of the shear viscosity as the density ρ tends to zero and η_1 describes a linear density dependence $\eta_1 = \partial\eta_0/\partial\rho$, $\eta_{b,0}$ is the limiting value of the bulk viscosity as the density tends to zero and $\eta_{b,1} = \partial\eta_{b,0}/\partial\rho$ again describes a linear density dependence. The assumption was made that the shear and bulk viscosities could be described adequately by these linear equations over the experimental density range. This was important in the calculation of $(\eta/\rho)^{\frac{1}{2}}$, which becomes

$$\begin{aligned} \left(\frac{\eta}{\rho}\right)^{\frac{1}{2}} &= \left(\frac{\eta_0 + \eta_1\rho}{\rho}\right)^{\frac{1}{2}} \\ &= \left(\frac{\eta_0}{\rho}\right)^{\frac{1}{2}} \left(1 + \frac{\eta_1\rho}{\eta_0}\right)^{\frac{1}{2}} \\ &\simeq \left(\frac{\eta_0}{\rho}\right)^{\frac{1}{2}} + \frac{\eta_1}{2}\left(\frac{\rho}{\eta_0}\right)^{\frac{1}{2}}, \end{aligned} \tag{7.7}$$

using the binomial approximation correct to the second term. In order to fit the quantity G, equation (7.2) was written as

$$G = \frac{XW}{\rho} + YW + \eta_0^{\frac{1}{2}} \frac{Z}{\rho^{\frac{1}{2}}} + \frac{\eta_1}{2\eta_0^{\frac{1}{2}}} Z\rho^{\frac{1}{2}}, \tag{7.8}$$

using equations (7.5) to (7.7) . W, X, Y and Z in equation (7.8) are given by

$$W = \frac{\pi f^2}{u^2}, \tag{7.9}$$

$$X = \frac{4}{3}\eta_0 + \frac{D}{c_p}(\gamma - 1)\eta_0 + \eta_{b,0}, \tag{7.10}$$

$$Y = \frac{4}{3}\eta_1 + \frac{D}{c_p}(\gamma - 1)\eta_1 + \eta_{b,1}, \tag{7.11}$$

and

$$Z = \sqrt{\pi f}\left(\left\{\sqrt{\frac{D}{c_p}}(\gamma - 1)\right\} H + S\right). \tag{7.12}$$

In equations (7.9) and (7.12), f is the corrected resonance frequency and u is the sound speed correct to the second acoustic virial coefficient. Because the corrected resonance frequencies depend on the transport properties which in turn depend on the values of B, β_a, and C_p^{pg}, via the calculation of u and f, and γ and

C in equations (7.10) to (7.12), the importance of the iterative procedure for the analysis of the results is highlighted.

The value of D in equations (7.1) to (7.12) depends on which relation is being used to relate the thermal conductivity to the shear viscosity. The limiting value of the thermal conductivity as the density ρ tends to zero κ_0 is simply given by $\kappa_0 = D\eta_0$, and its associated linear density dependence by $\kappa_1 = D\eta_1$. For the Steil-Thodos relation $D^{[1]}$ is given by

$$D = \frac{1}{M}\left(1.15C_V + 2.03R\right), \tag{7.13}$$

for the Euken relation by

$$D = \frac{1}{M}\left(1.00C_V + 2.25R\right), \tag{7.14}$$

and for the modified Euken relation by

$$D = \frac{1}{M}\left(1.32C_V + 1.77R\right), \tag{7.15}$$

where M is the molar mass of the gas, C_V is the molar isochoric heat capacity and R is the gas constant.

Using equations (2.32) and (7.6), estimates of the limiting value of the vibrational time constants as the density tends to zero $\tau_{\mathrm{vib},0}\rho$, at a density of 1 kg m^{-3} were obtained from

$$\tau_{\mathrm{vib},0}\rho = \frac{\eta_{\mathrm{b},0}}{(\gamma - 1)\, u^2 \Delta}, \tag{7.16}$$

and the associated density dependence $\partial\left(\tau_{\mathrm{vib},0}\rho\right)/\partial\rho$ from

$$\partial\left(\tau_{\mathrm{vib},0}\rho\right)/\partial\rho = \frac{\eta_{\mathrm{b},1}}{(\gamma - 1)\, u^2 \Delta}. \tag{7.17}$$

In the two equations above γ, u and $\Delta = C_{\mathrm{vib}}/C_p$ are calculated for a density of 1 kg·m^{-3} using the values of B determined from the sound speed analysis.

A check on the completeness of the acoustic model is possible by comparing the experimental and calculated half-widths. If the model were complete and the transport properties exact, then the excess half-widths Δg would be zero. The analysis method described here results in excess half-widths scattered around zero but some unknown loss mechanisms may have been absorbed by some of the coefficients or their density dependencies. This may result in the estimated corrections to the resonance frequencies that are erroneously large. However,

unknown loss mechanisms generally result in a perturbation to the resonance frequency, which to a first approximation would be expected to be of the same order of magnitude as the contribution to the resonance half-width. Consequently, such effects are likely to be partially self compensating and unfortunately cannot be quantified.

7.5. Extracting β_a and C_p^{pg} from the Experimental Data

The experimental quantity extracted from the data is $(u/b)^2$, so the results were fitted using either

$$\left(\frac{u}{b}\right)^2 = \frac{A_0}{b^2} + \left(\frac{A_1}{b^2}\right)p + \left(\frac{A_2}{b^2}\right)p^2 + \cdots \tag{7.18}$$

or its density explicit equivalent

$$\left(\frac{u}{b}\right)^2 = \frac{A_0}{b^2}\left\{1 + \beta_a\rho_n + \gamma_a\rho_n^2 + \cdots\right\} \tag{7.19}$$

where γ^{pg} and the relationship between the coefficients of equations (7.18) and (7.19) are given in chapter 1. The (p, V_m, T) virial coefficients B and C are related to the acoustic virial coefficients through second order differential equations. These equations were also given in chapter 1. For most of the experimental data only two term fits were statistically significant so that a full set of results for the third acoustic virial coefficient was not obtained. It is a disadvantage that either equation must be truncated to represent the experimental results as this leads to systematic errors in the values of the coefficients depending on the order of the final equation. These systematic differences may be estimated however, and, if the differences between the coefficients determined with a truncated pressure range and fewer terms in the equation differ significantly from those determined using the full pressure range it is likely that part of the set of data is in error. The product $\beta_a(T)\,\rho_{MAX}$ was chosen to be a constant for all the isotherms so that all the estimates of β_a and A_0 suffer from comparable systematic errors because the same order of polynomial should be used at each experimental temperature.

For absolute measurements of the speed of sound u, the radius b of the cavity is required. The method by which this was determined from calibration measurements was described in chapter 6. Once the radius has been determined, perfect

gas heat capacities can be determined from A_0. From the second and third acoustic virial coefficients, estimates of the of the second and third (p, V_m, T) virial coefficients can be made.

The accuracy of the acoustic virial coefficients are determined primarily by errors in u^2 and p. Although the uncertainty in C_p^{pg}/R includes contributions from T and b in addition to those from (A_0/b^2), these only contribute about 0.001 fractionally which may be small compared with those arising from the presence of impurities. For example, with measurements on propene an impurity $x(H_2O) = 1 \times 10^{-4}$ would contribute about 0.02 fractionally to C_p^{pg}/R while $x(\text{air}) = 1 \times 10^{-4}$ would contribute about 0.01 fractionally. The perfect gas heat capacities determined for each substance were used to obtain smoothing equations constructed from a combination of negative and positive powers in T using an adaptive regression algorithm. All the terms selected had a statistical significance greater than 0.99 and the data were weighted by the normalised inverse of their variance.

7.6. Determination of the Virial coefficient, B

In order to determine the second virial coefficient B from the experimental data, it is necessary to solve the differential equation (1.15). Bruch[2] demonstrated a numerical method of integration of this equation with specified boundary conditions for ^{4}He, and Mehl and Moldover[3] also analysed their precise measurements in ethene in this way. This method however favours the use of at least one initial condition at the lowest experimental temperature[2],[3]. It is at the lowest temperatures that conventional measurements are least reliable, and the requirement for literature data defeats the purpose of exploiting acoustic measurements independently. If β_a were known accurately over a wide temperature range, the results may be inverted[4] to provide both B and a spherically symmetric intermolecular pair potential energy function U, without recourse to (p, V_m, T) measurements. Reliable estimates of the second virial coefficient may be obtained using semi empirical methods[5]-[7] for solving equation (1.15) based on explicit assumptions about the functional form of the intermolecular potential energy function. In this method, no explicit account is taken of the integration constants required for the

Figure 7.1: The square well potential as a function of intermolecular separation r.

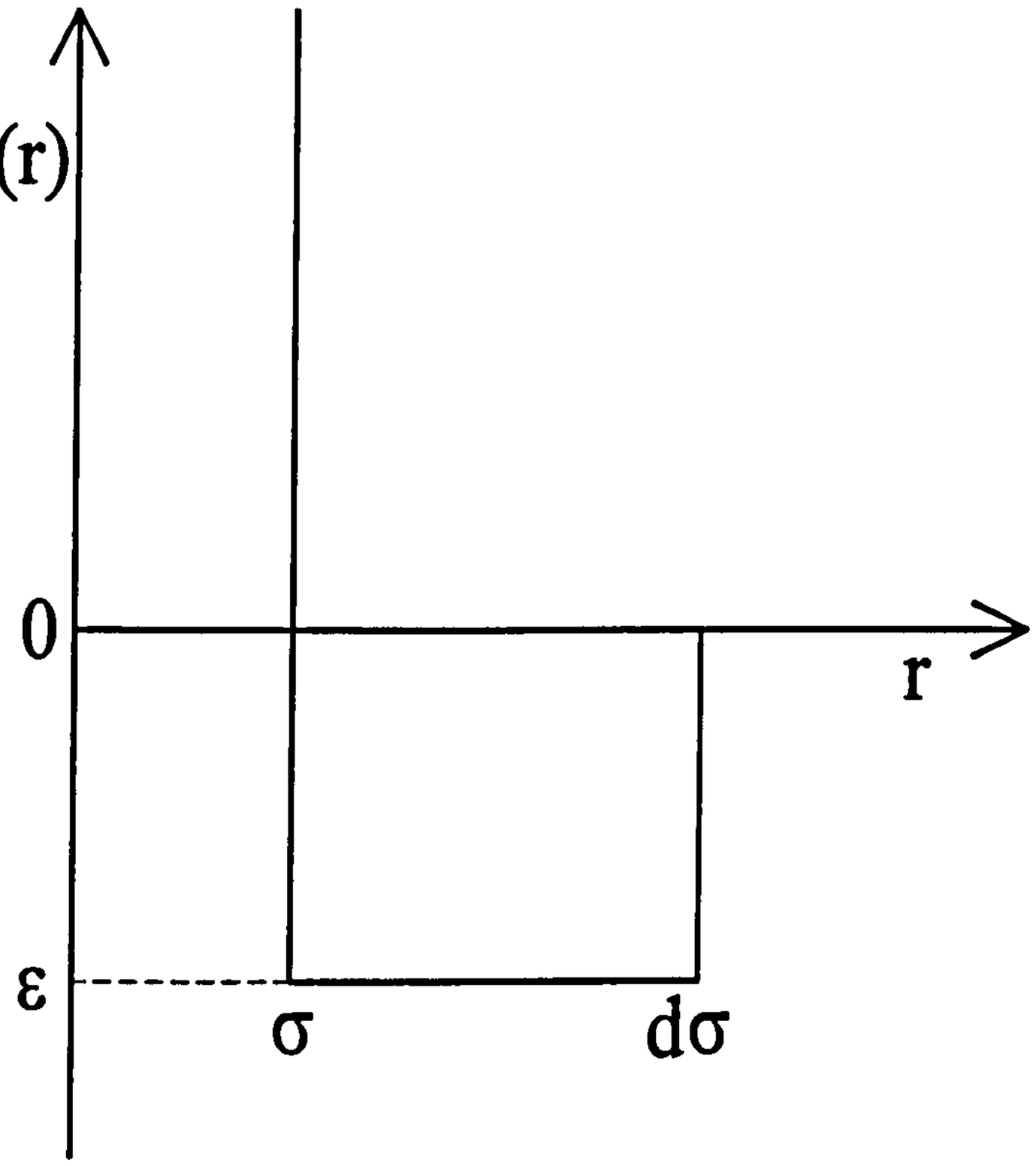

general solution. However, Boyd and Mountain[8] argue that it does implicitly account for the homogeneous solution. In the absence of reliable initial conditions or results of sufficient accuracy over a wide temperature range, this approach was used. Many functional forms for the potential energy function U may be used but as it is known that B is relatively insensitive to the detailed shape of the function, simple models which may only be crude approximations to the true function are sufficient to accurately represent B and its derivatives. Since B is related to the intermolecular potential, U by the integral equation (1.13), the assumption of a functional form for U implicitly imposes a functional form on B providing a route to the solution of the differential equation.

If the simplest square-well intermolecular potential energy function

$$\left.\begin{aligned} U(r) &= \infty, \quad (r < \sigma), \\ U(r) &= \varepsilon, \quad (\sigma \leq r \leq d\sigma), \\ U(r) &= 0, \quad (r > d\sigma), \end{aligned}\right\} \tag{7.20}$$

where r is the intermolecular separation, and the parameters ε, σ, and d are shown

in figure (7.1) is assumed, then B may be shown to be given by

$$\begin{aligned} B(T) &= \left(\frac{2\pi L\sigma^3}{3}\right)\left[d^3-(d^3-1)\exp\left(\frac{\varepsilon}{kT}\right)\right] \\ &= a+b\exp\left(\frac{c}{T}\right) \end{aligned} \tag{7.21}$$

where L is the Avogadro constant and k is the Boltzmann constant. Combination of equations (1.15) and (7.21) yields

$$\begin{aligned} \beta_a = \; & 2a+2b\left[1-\left(\frac{c}{T}\right)(\gamma^{pg}-1)\right. \\ & \left.+\left\{\frac{(\gamma^{pg}-1)^2}{2\gamma^{pg}}\right\}\left(\frac{c}{T}\right)\left\{2+\left(\frac{c}{T}\right)\right\}\right]\exp\left(\frac{c}{T}\right), \end{aligned} \tag{7.22}$$

for which a self consistent solution of the parameters a, b, and c can be determined by non-linear regression analysis with experimental values of β_a and C_p^{pg}. The errors introduced by imposing a functional form on B are difficult to assess, but in previous work the values determined from different functional forms have been shown to agree to within their standard deviations.

A similar approach may be adopted for the estimation of the third virial coefficient C if a full set of γ_a values is available. However there are additional uncertainties because the reliability of representing third virial coefficients by this method is less well understood. The third virial coefficient depends on three body interactions and the intermolecular potential energy function is a pair potential. This procedure was not attempted in this work as many of the data sets could be described by two term fits once high pressure data perturbed by the shell resonance had been removed hence a full set of third acoustic virial coefficients was not available.

BIBLIOGRAPHY

[1] Reid R C, Prausnitz J M and Poling B E. *The Properties of Gases and Liquids* Fourth Edition. (McGraw Hill: New York, 1986).

[2] Bruch L W. *Phys. Rev.* 1969, **178**, 303.

[3] Mehl J B and Moldover M R. *Proc. Eighth Symp. on Thermophysical Prop.* Sengers J V: Editor. (*Am. Soc. Mech. Eng.:* New York, 1982).

[4] Ewing M B. *Mol. Phys.* 1987, **60**, 681.

[5] Goodwin A R H. Ph.D Thesis, University of London 1988.

[6] Ewing M B, Goodwin A R H, McGlashan M L and Trusler J P M. *J. Chem. Thermodyn.* 1987, **19**, 721.

[7] Ewing M B and Trusler J P M. *J. Chem. Phys.* 1989, **90**, 1106.

[8] Boyd M E and Mountain R D. *Phys. Rev. A.* 1970, **2**, 2164.

8. EXPERIMENTAL RESULTS

8.1. Introduction

The results obtained for the three experimental systems are presented here. Mean sound speeds calculated from the experimental resonance frequencies are documented for each gas as well as the acoustic virial coefficients determined from their analysis. The perfect gas heat capacities and second virial coefficients, extracted as described in chapter 7, are reported here and compared with literature sources. The transport properties determined from the analysis of the resonance half-widths are also discussed and compared with available literature values.

SF_6 is the experimental system that is most severely affected by the shell resonance as the measured resonance modes in this gas are at low frequencies. This leads to a substantial degree of overlap between them and the shell resonance. In the discussion of the analysis of SF_6 particular attention is paid to the procedure by which affected modes were identified and removed. The effect of fitting the data to a pressure or density series is also considered. The density series often converges faster[1],[4], so any systematic errors arising from truncating the series may be investigated.

For the binary mixture of methane and ethane, which is expected to be the least affected by the shell resonance, the experimental second virial coefficients are used to estimate the cross virial coefficients and interaction virial coefficients which are compared with published results. The possibility of fractionation occurring as the pressure is reduced along an isotherm and the resulting change in composition affecting the results is commented on with respect to other work[1]. The vibrational relaxation times determined from this work are compared to those for the pure components and with published data.

In the analysis of CHF_3 the effect of analysing the half-widths using the Euken, modified Euken and Stiel-Thodos relations is examined. The systematic

differences in the values of the thermal conductivity and shear viscosity obtained are discussed with reference to literature data. An important conclusion from this study was that the method of analysis did not cause significant systematic changes in the vibrational relaxation times or in the acoustic virial coefficients that were extracted from sound speeds corrected using the transport properties calculated in the half-width analysis.

8.2. Sulfur Hexafluoride

Eight isotherms were studied for SF_6 at temperatures between 230 and 340 K. Firstly the experimental half-widths were analysed to provide estimates for the thermal conductivity, shear viscosity and vibrational relaxation time using literature data for the heat capacity, second virial coefficient, second acoustic virial coefficient and transport properties. Shear viscosities were taken from accurate measurements by Wakeham *et al.*[2] while values for the thermal conductivities were estimated using the Stiel-Thodos expression because this approach has been shown to give good agreement with experimentally determined values[3]. The accuracy of these initial data was not of particular importance as the self consistent iterative procedure described in chapter 7 was used to analyse the results and the literature values merely speed up the analysis by reducing the number of iterations required to two. The heat capacity was estimated using a correlation based on experimental results[3], and the second virial coefficients were those recommended in reference [17]. The resonance frequencies were then analysed to provide better estimates of the heat capacity and virial coefficients. The half-width fitting was then repeated and the final values for the shear viscosity, thermal conductivity and vibrational relaxation time obtained. These values were used in the final analysis of the resonance frequencies to give the perfect gas heat capacity and second acoustic virial coefficient. The experimental values over the whole of the temperature range were fitted to a square-well potential to provide the final estimate of the second virial coefficient. In the analysis of the half-width data for SF_6, the Stiel-Thodos expression was used to relate the thermal conductivity and shear viscosity. As mentioned above it has been observed to give good agreement with experimental data and the effects of using alternative expressions is discussed

Table 8.1: Resonance modes rejected at each experimental temperature in the half-width analysis for SF_6.

T/K	Modes Rejected
230	(0,2,1) (0,3,1) (0,4,1)
241	(0,2,1) (0,3,1) (0,4,1) (0,8,1)
253	(0,2,1) (0,3,1) (0,4,1) (0,9,1)
267	(0,2,1) (0,3,1) (0,4,1) (0,8,1)
282	(0,2,1) (0,3,1) (0,4,1) (0,8,1)
299	(0,2,1) (0,4,1) (0,7,1) (0,8,1)
317	(0,2,1) (0,4,1) (0,7,1)
339	(0,2,1) (0,4,1) (0,8,1)

with reference to CHF_3.

At each pressure along the isotherm the resonance frequencies of the seven azimuthal modes (0,2,1), (0,3,1), (0,4,1), (0,5,1), (0,7,1), (0,8,1) and (0,9,1) were measured. The expected level of agreement of the sound speeds and half-widths is limited by the accuracy with which the geometry of the cavity is known. As discussed in chapter 6 this limits the accuracy to about the level of 20 ppm. Resonance modes that were discrepant by significantly more than 20 ppm in both the analysis of the half-widths and the sound speeds were rejected from the analysis.

8.2.1. Half-width Fitting

Table (8.1) shows the resonance modes rejected from the seven measured modes for the half-width analysis. The shell resonance is at around 500 Hz with a half-width g of around 150 Hz (see chapter 6). At $10g$ from the centre frequency the shell resonance will be reduced to 10 % of its maximum amplitude assuming it has a Lorentzian lineshape. At this amplitude it is still likely to affect the results implying that all the measurements in SF_6 will be perturbed to some degree as all the experimental frequencies lie in the range 0 to 2000 Hz. The (0,2,1) mode at approximately 400 Hz and the (0,3,1) mode at approximately 600 Hz will be affected most severely as they are closest to the shell resonance. The effect on the

resonance half-widths will not be as great as on the resonance frequencies but may still cause systematic errors in the derived transport properties if affected modes are not identified and removed. As expected in general it is the low order modes which were removed from the analysis. The $(0,2,1)$ and $(0,4,1)$ modes were discarded at all eight temperatures and the $(0,3,1)$ mode was rejected from the five isotherms at lower temperatures. At any given temperature is was also necessary to remove one of the higher-order modes. The reason for this is not known but a variety of effects may be significant. As explained in chapter 6 the exact shape of the shell resonance was not probed so the perturbation may not follow the expected trend in frequency described by the expression (2.104) given in chapter 2 and, consequently shell motion may also affect the higher-order modes. In addition the effect of imperfect geometry is unknown. This may be complicated by the different filling pressures used for each isotherm and the thermal cycling of the resonator which may have given rise to distortions in its shape that were unique for each isotherm causing different resonance modes to be perturbed at each temperature. Perturbations due to the shell resonance will become less important at low pressures whereas the effect of geometric perturbations on the half-widths is unknown. Combinations of these effects may give rise to complicated trends in the excess half-widths which cannot be resolved; particularly in view of the changes that may occur in the geometric perturbation as the pressure is reduced along an isotherm. For every isotherm the data at the lowest pressure was discarded because under these conditions the accuracy of the large half-widths were limited not by the geometry of the resonator but by the fitting procedure, described in chapter 5, to extract them from the primary acoustic response. Figures (8.1), (8.2) and (8.3) show the fractional excess half-widths $\Delta g/f$ ($\Delta g = g_{\mathrm{exp}} - g_{\mathrm{calc}}$) for the low temperature isotherm at 230 K, at an intermediate temperature of 282 K, and at the highest experimental temperature of 339 K. The large symbols represent data selected for the analysis and the small symbols represent data rejected from the analysis. At every temperature, the $(0,2,1)$ mode shows fractional excess half-widths of up to 1000 ppm which is an order of magnitude greater than for the other modes and is plotted separately; obviously the $(0,2,1)$ mode must be removed from the analysis. From figures (8.1), (8.2) and (8.3) it may be seen that the agreement between the fractional excess half-widths of the selected modes is

Figure 8.1: Fractional excess half-widths $\Delta g/f$ for the isotherm at 230 K in SF_6.

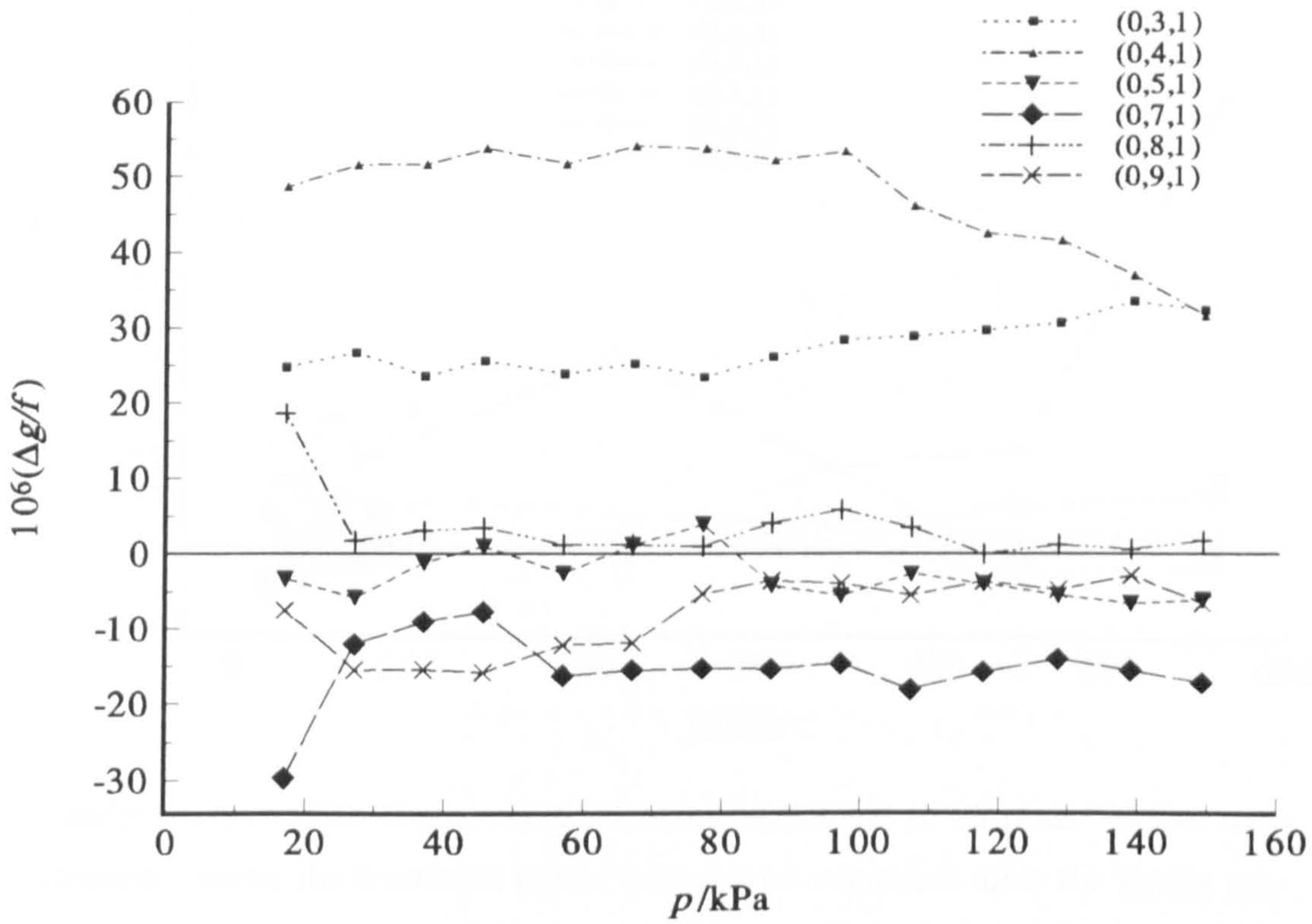

Figure 8.2: Fractional excess half-widths $\Delta g/f$ for the isotherm at 282 K in SF_6.

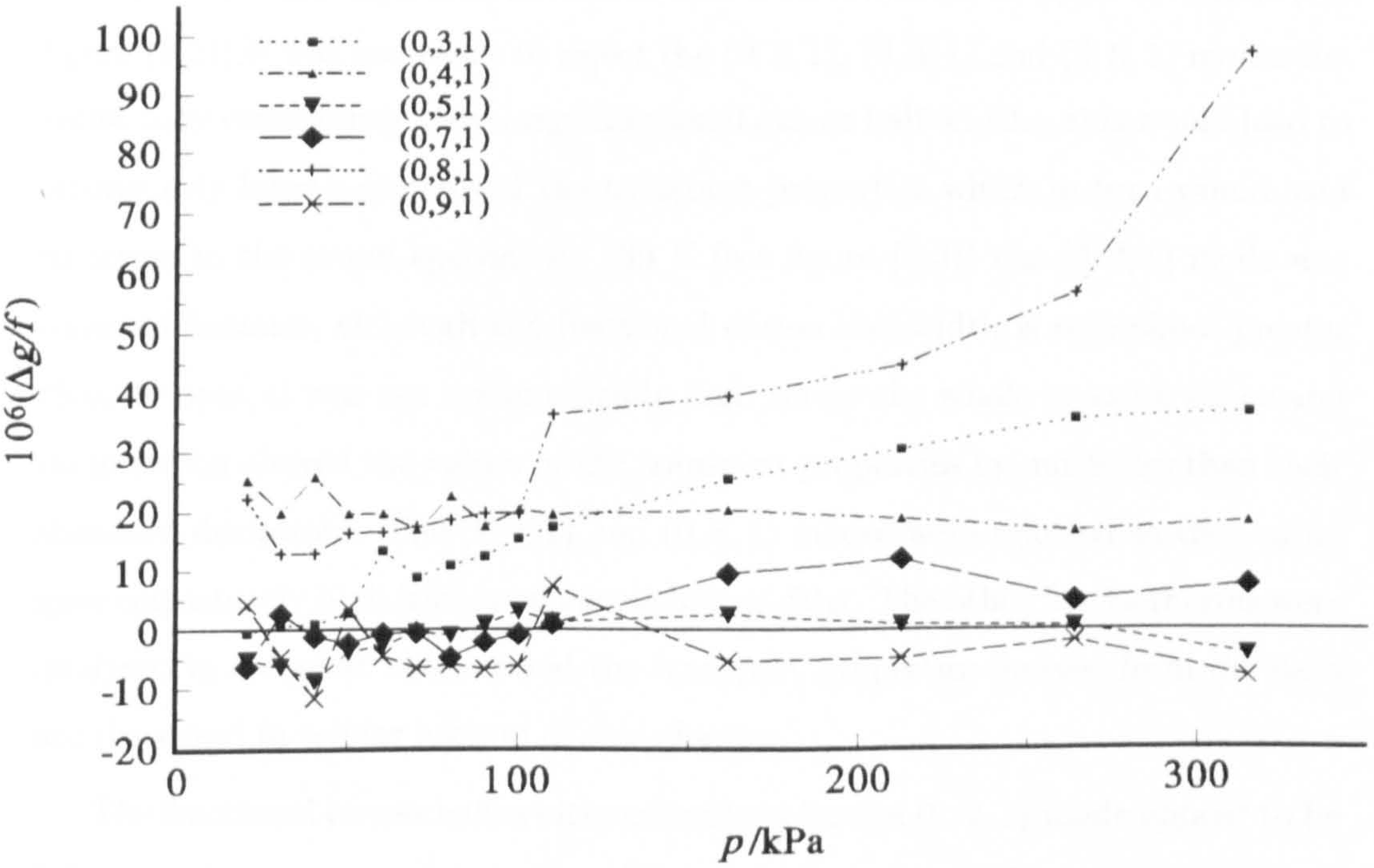

Figure 8.3: Fractional excess half-widths $\Delta g/f$ for the isotherm at 339 K in SF_6.

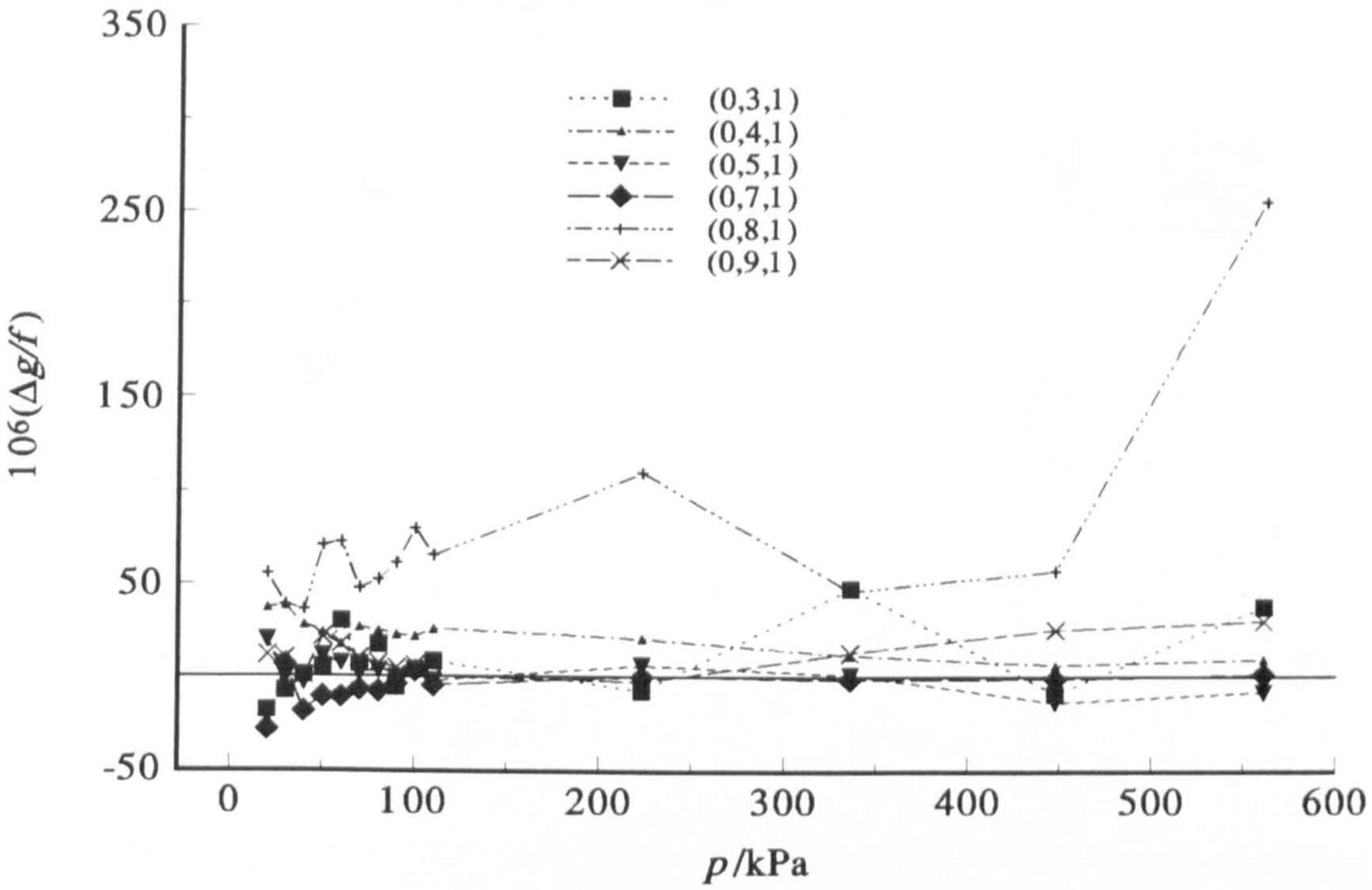

nearly always within the predicted limiting agreement of 20 ppm. Modes were discarded when the fractional excess half-widths calculated after the fitting procedure were systematically large and outside the expected level of agreement of 20 ppm. At 230 K (see figure (8.1)) the $(0, 3, 1)$ and $(0, 4, 1)$ modes were removed for this reason having fractional excess half-widths around 40 ppm. At 282 K (see figure (8.2)) it was necessary to reject the $(0, 3, 1)$, $(0, 4, 1)$ and $(0, 8, 1)$ modes because they consistently gave large fractional excess half-widths; this would lead to erroneously large estimates of the transport properties which in turn would lead to errors in the sound speeds. At 339 K (see figure (8.3)) the $(0, 3, 1)$ mode was retained because, although the fractional excess half-width is sometimes greater than 20 ppm, it was not systematically high across the whole pressure range and its inclusion altered the values of the transport properties by much less than their standard deviations. The $(0, 4, 1)$ and $(0, 8, 1)$ modes were rejected as they again gave consistently high fractional excess half-widths. The other five isotherms were analysed in a similar manner and the transport properties derived from the data are discussed in a later section of this chapter.

The fractional excess half-widths calculated for the $(0, 2, 1)$ mode appear to be following the same trend over the whole of the experimental temperature range.

Figure 8.4: Fractional excess half-widths $\Delta g/f$ for the $(0,2,1)$ mode for the isotherms at 230 K, 282 K and 339 K in SF_6.

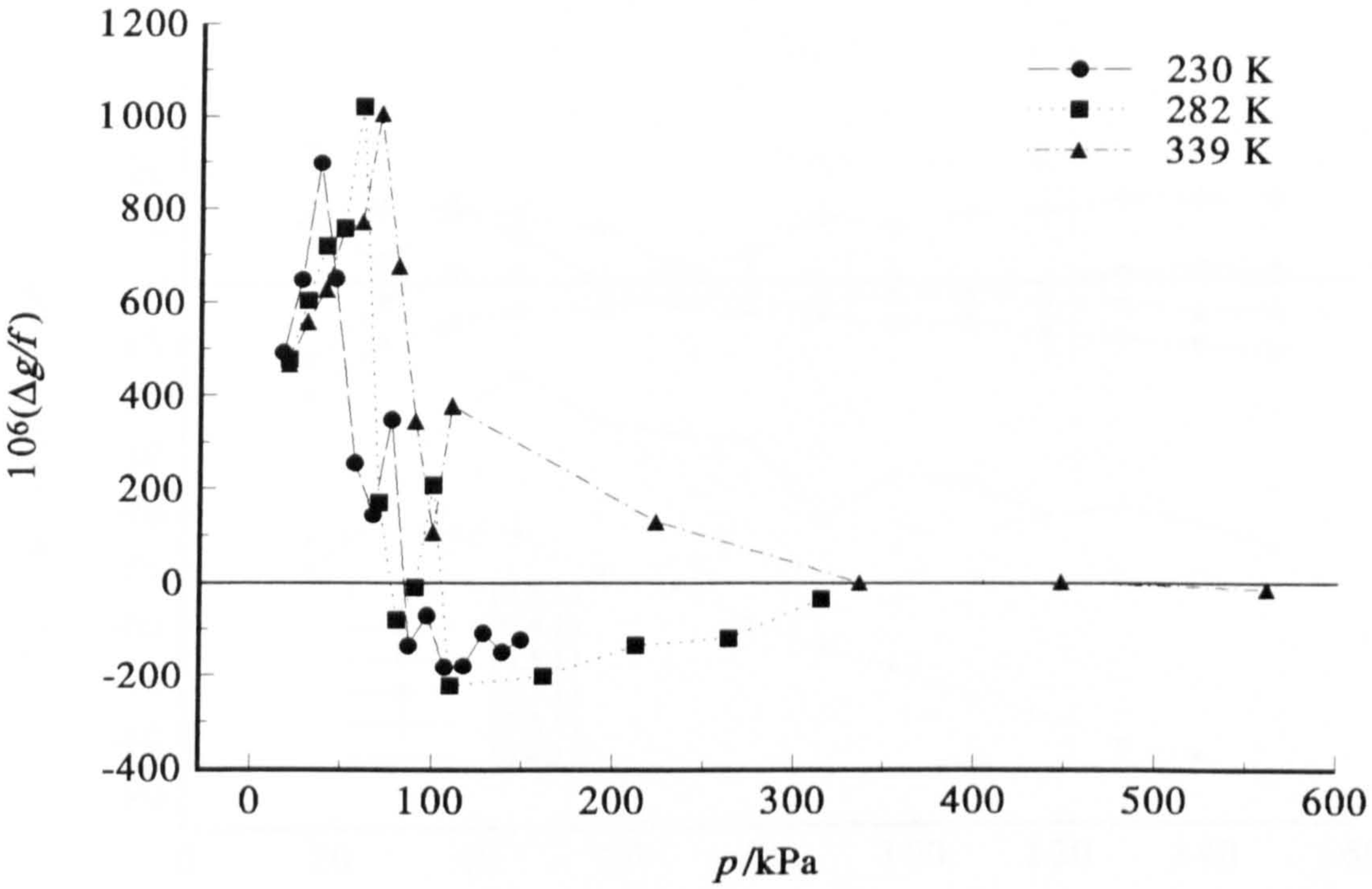

The data for the three isotherms is plotted in figure (8.4) which shows a maximum around 50 kPa and a minimum around 100 kPa. This will be discussed in more detail in the next section.

8.2.2. Mode Selection for the Sound Speed Analysis

The ratio of the angular frequency to the eigenvalue for each mode gives u/b where u is the speed of sound and b the radius of the resonator. It is this experimental quantity that should agree for the different modes at each pressure to nearly the limiting value of 20 ppm. The agreement for SF_6 will be less good than for propene because it is known that the shell resonance will be affecting the modes measured in SF_6. The shell resonance has a greater effect on the mode frequencies than the half-widths and the difficulties are expected to increase at higher pressures.

Figures (8.5), (8.6) and (8.7) show the fractional deviations of the u/b values for each mode from the average $\langle u/b \rangle$ calculated for the modes selected. Data is presented for the lowest temperature isotherm at 230 K, at an intermediate temperature of 282 K, and the highest experimental temperature of 339 K. The large symbols represent data selected for the analysis and small symbols data

Figure 8.5: Fractional deviations of the calculated values of u/b from the average value $\langle u/b \rangle$ determined for the selected modes for the isotherm at 230 K in SF_6.

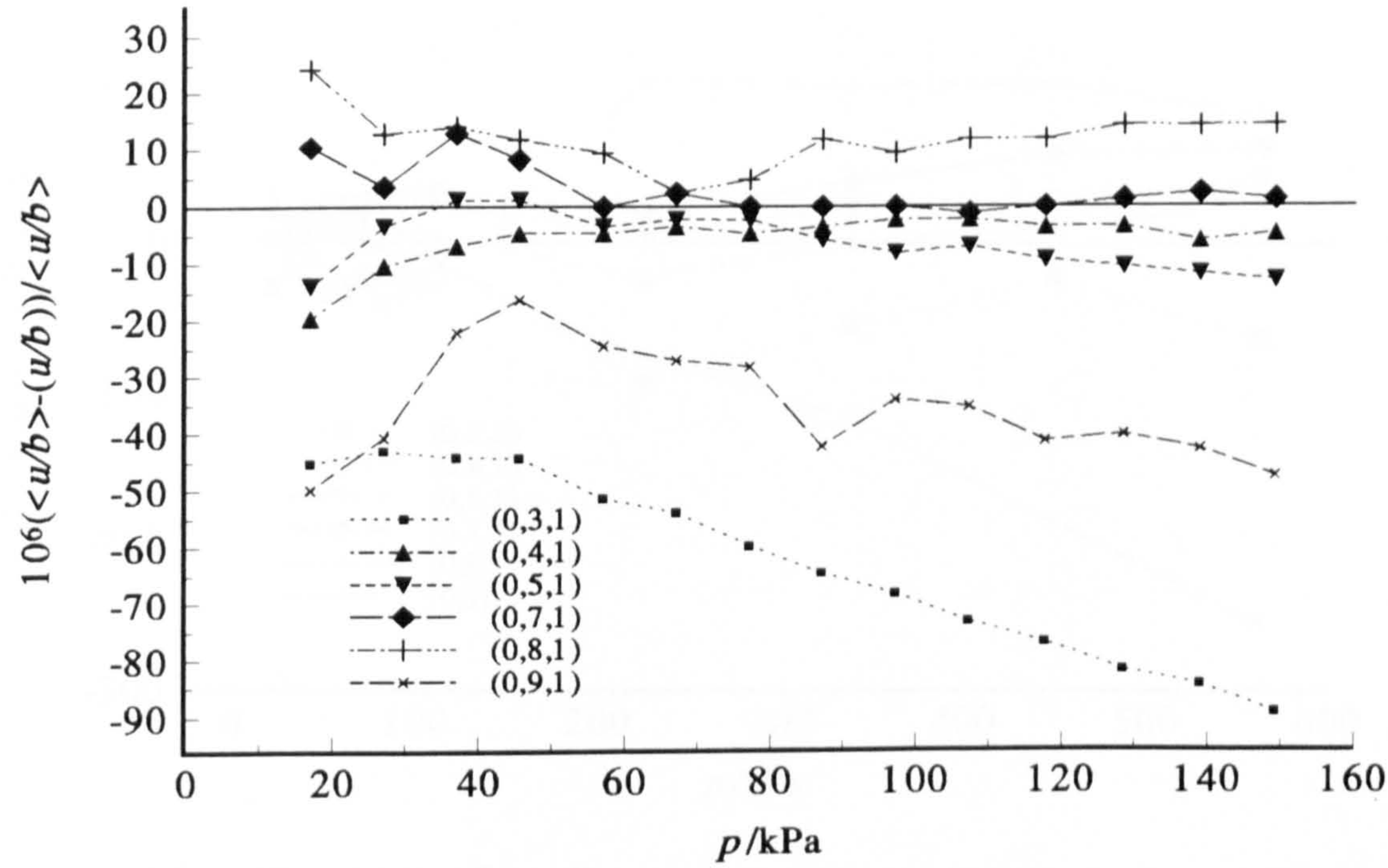

Figure 8.6: Fractional deviations of the calculated values of u/b from the average value $\langle u/b \rangle$ determined for the selected modes for the isotherm at 282 K in SF_6.

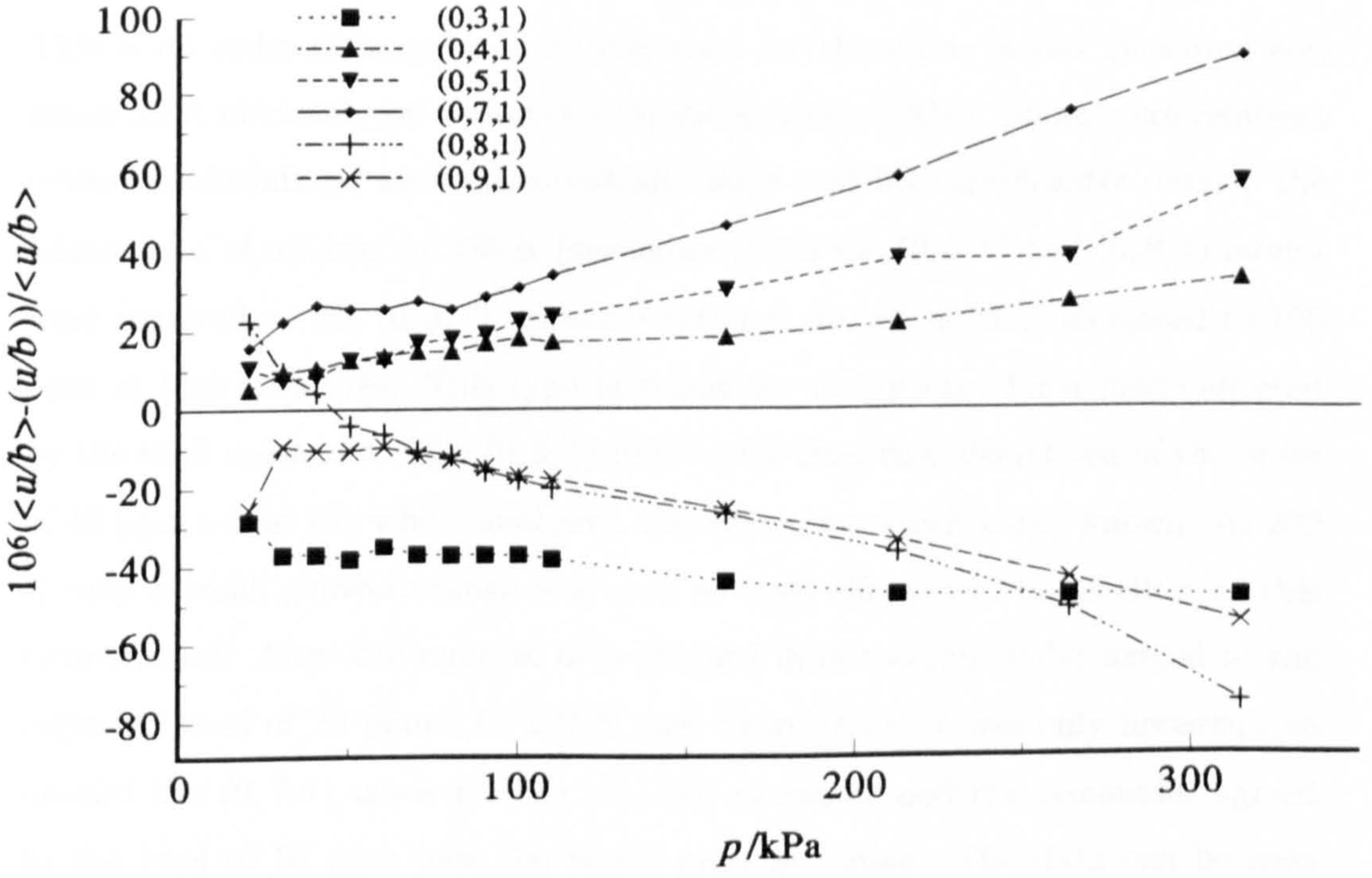

Figure 8.7: Fractional deviations of the calculated values of u/b from the average value $\langle u/b \rangle$ determined for the selected modes for the isotherm at 339 K in SF_6.

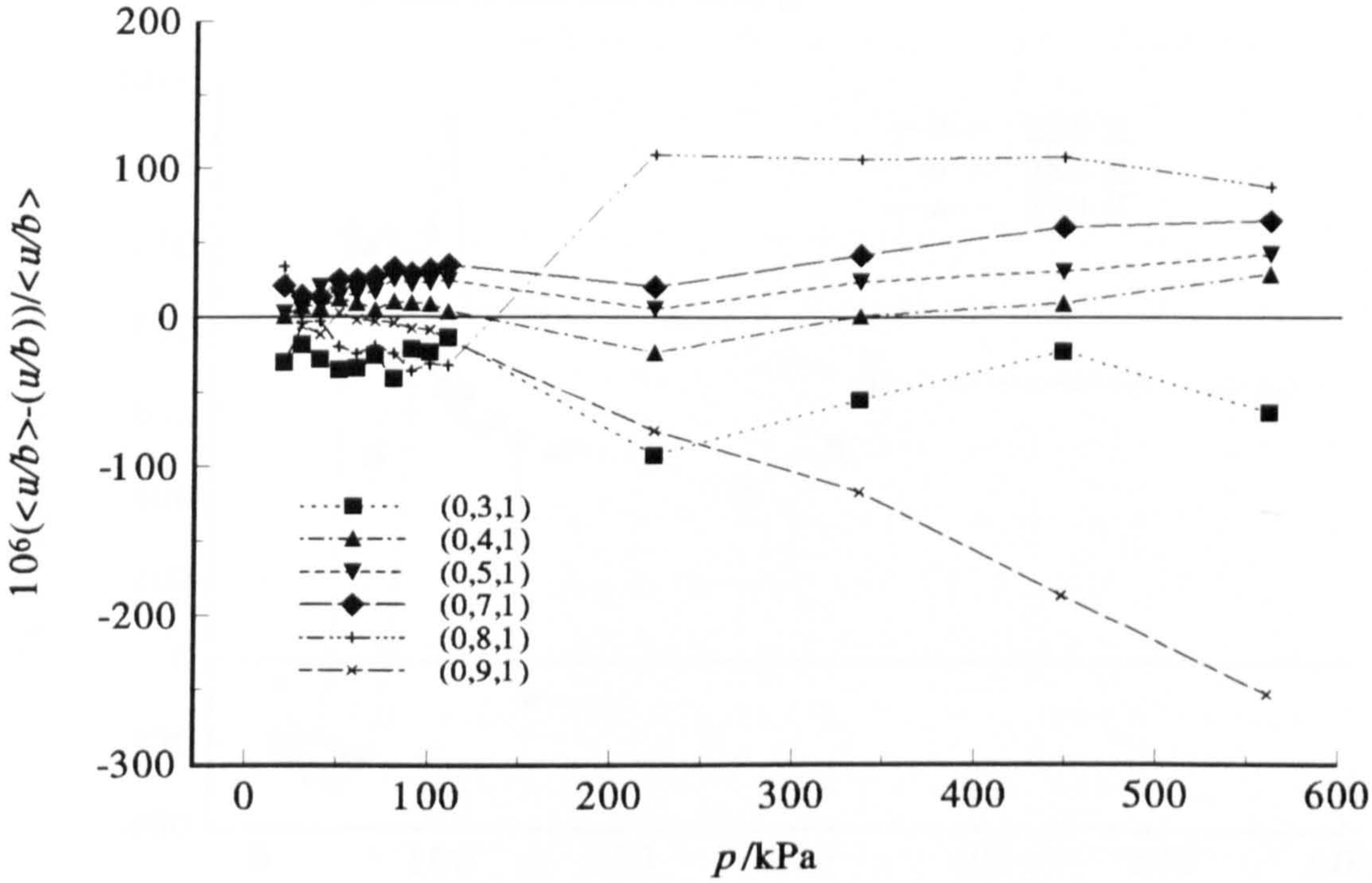

rejected from the analysis. From figures (8.5), (8.6) and (8.7) it may be seen that agreement between the speeds of sound for the modes retained in the analysis is generally about the level of 50 ppm. At every temperature, the $(0, 2, 1)$ mode shows perturbations to u/b of the order of 1000 ppm and is plotted separately. This is an order of magnitude greater than for the other modes measured and again must obviously be removed from the analysis. Other modes were removed when the deviations were systematically large and lay significantly outside the selected set of modes. At 230 K (see figure (8.5)) the $(0, 3, 1)$ and $(0, 9, 1)$ modes were removed as the $(0, 3, 1)$ showed fractional deviations that increased to 100 ppm at high pressures. This type of behaviour is expected for a mode affected by the shell resonance. The $(0, 9, 1)$ mode gave fractional deviations of the order of 40 ppm across the whole isotherm, the reason for which is not known. At 230 K only a small pressure range was used so shell effects will be smallest at this temperature. After the removal of perturbed data the remainder agreed to the expected level of 20 ppm. At 282 K (see figure (8.6)) it was only necessary to discard the $(0, 7, 1)$ mode for the top four pressures and the remainder agreed to the level of 50 ppm over the whole pressure range. The data can be seen

Figure 8.8: Fractional deviations of the calculated values of u/b for the $(0,2,1)$ mode from the average value $\langle u/b \rangle$ determined for the selected modes for the isotherms at 230 K, 282 K and 339 K in SF_6.

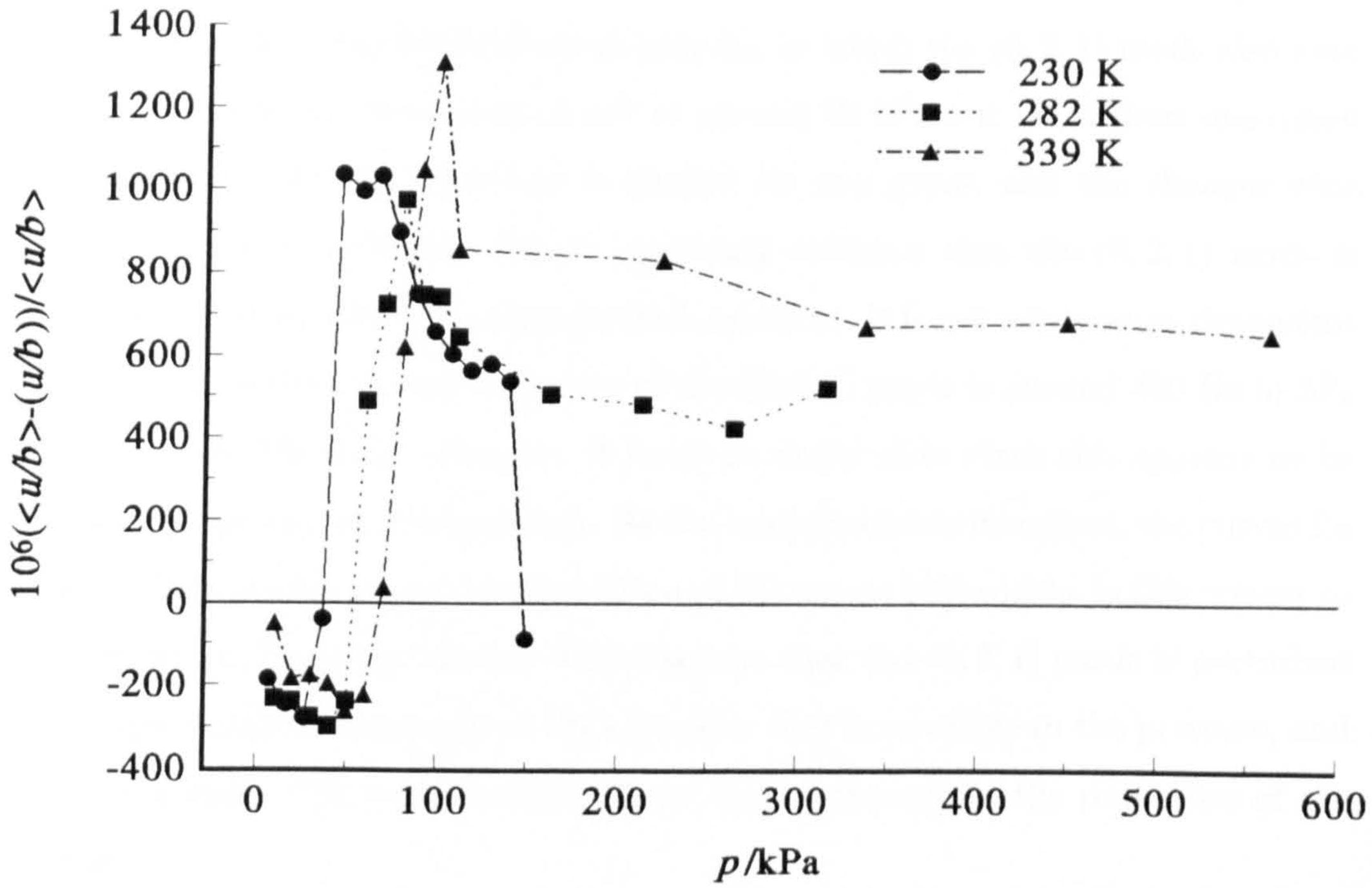

to converge at low pressures as the influence of the shell resonance is reduced. There may be a case for removing the $(0,3,1)$ mode because at low pressures it is systematically lower than the others but it was included because removing it made little difference to the transport properties obtained, which agreed to within their standard deviations. It is this type of subjective decision that can lead to small systematic errors in the analysis. At 339 K (see figure (8.7)) the $(0,8,1)$ and $(0,9,1)$ modes were rejected for the top four pressures where they significantly diverge from the majority of the data. The agreement of the remaining modes for the four high pressure measurements above 110 kPa is only 60 ppm due to the increased influence of the shell resonance. The limiting level of agreement of 20 ppm may be seen to be too stringent a test for the agreement of the speed of sound data for SF_6 where the shell resonance perturbs the modes. The other five isotherms were analysed in a similar manner and the speed analysis used to extract the acoustic virial coefficients is discussed in the next section.

The deviations of u/b for the $(0,2,1)$ mode are plotted in figure (8.8) and, as for the half-widths, there is agreement over the whole of the experimental

temperature range. The deviations have a minimum at around 50 kPa and a maximum at around 100 kPa. This is the opposite of the effect on the half-widths but the extrema occur at the same pressures providing evidence that the same perturbation is giving rise to these observations. The behaviour also agrees in some ways with the observations in propene in which the $(0, 2, 1)$ mode also gave a minimum in the deviations of u/b at around 50 kPa but no obvious maximum at 100 kPa. As the behaviour is similar for two gases, and the changes with pressure are so dramatic, this is important evidence that the $(0, 2, 1)$ mode is perturbed by an effect that changes with pressure. It is not a frequency dependent perturbation because the frequency of the $(0, 2, 1)$ mode is around 400 Hz in SF_6 and around 700 Hz in propene. It must be noted that there also appears to be some dependency on temperature. As the temperature is increased, the curves for the u/b deviations in propene and SF_6 and the excess half-widths in SF_6 appear to be shifted to higher pressures. This suggests that the $(0, 2, 1)$ mode is perturbed by a geometric deformation of the resonator that is sensitive to the pressure, and that the shift with temperature may be due to changes in the properties of the shell.

8.2.3. Sound Speed Analysis

The sound speeds along each isotherm were fitted to polynomials in pressure and density as described in chapter 7 to obtain C_p^{pg} and β_{a}. The relation between the coefficients of the two series is given in chapter 1. As discussed in chapter 7, the data was weighted to low pressures where the shell resonance has only a small effect and only four high pressure points were taken for each temperature so that the fractional change in the sound speed is constant for each isotherm over the whole of the experimental temperature range. This is clearly seen in figure (8.9) which shows average sound speeds $\langle u \rangle$ along the isotherms at 230, 282 and 339 K. The shell perturbation is directly related to the density and, for the largest pressure at 339 K, the density is 3 times greater than at the highest pressure at 230 K. Thus for the higher-temperature isotherms, the high pressure data has to be carefully examined to check that it is not affected by the shell resonance. The number of terms required in the fit for the full pressure range should be constant at each temperature because the fractional change in

Figure 8.9: Average sound speeds $\langle u \rangle$ determined for the selected modes for the isotherms at 230 K, 282 K and 339 K in SF_6.

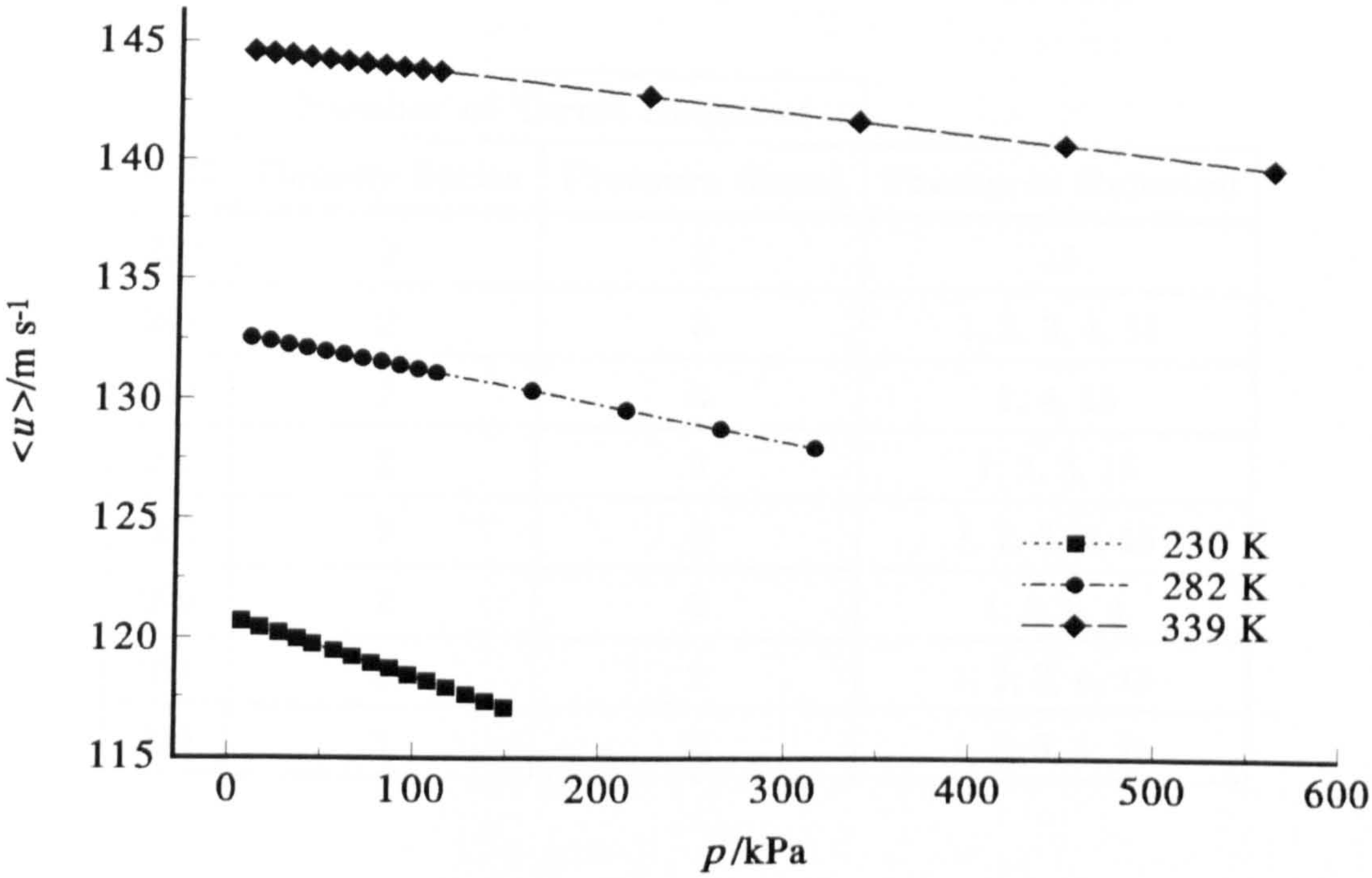

the sound speeds is approximately the same. If a greater number of terms than expected is required to fit the data along an isotherm, then the shell resonance may be causing additional curvature in the data. Such a discontinuity in the slope of the results above the pressure at which shell motion becomes important may be detected by a sharp change in slope of a deviation plot from the fit with the expected number of terms. The fit at the lowest temperature of 230 K where it is likely that the shell is having only a small effect over the whole pressure range of up to 150 kPa gives the number of terms that should be expected at the higher temperatures. Table (8.2) gives the number of terms required for both the pressure series and the density series at each temperature and also indicates which pressures along each isotherm were removed to avoid systematic errors due to the shell resonance. An additional term was included in the fit only when it was significant at a probability of 0.99. Figure (8.10) depicts the fractional deviations of the average speed of sound $\langle u \rangle$ from the values u_{calc} calculated from the two term density series and three term pressure series at 230 K. There are no discontinuities or curvature in the deviation plot, which demonstrates that no additional terms in the series are necessary, that the data is unaffected by the wall

Table 8.2: Number of terms required for the density and pressure series fits to the speed of sound in SF_6 and the data rejected from each isotherm.

	Number of Terms Required		
T/K	**Density Series**	**Pressure Series**	**Pressures Rejected**
230	2	3	15
241	2	3	1, 2, 3, 4, 15
253	2	3	1, 4, 15
267	2	3	1, 2, 3, 15
282	2	2	1, 2, 3, 4, 15
299	2	2	1, 2, 3, 4
317	2	2	1, 2, 3, 4, 15
339	2	2	1, 2, 3, 4, 15

Figure 8.10: Fractional deviations of the average sound speeds $\langle u \rangle$ determined for the selected modes from the calculated values for the isotherm at 230 K in SF_6.

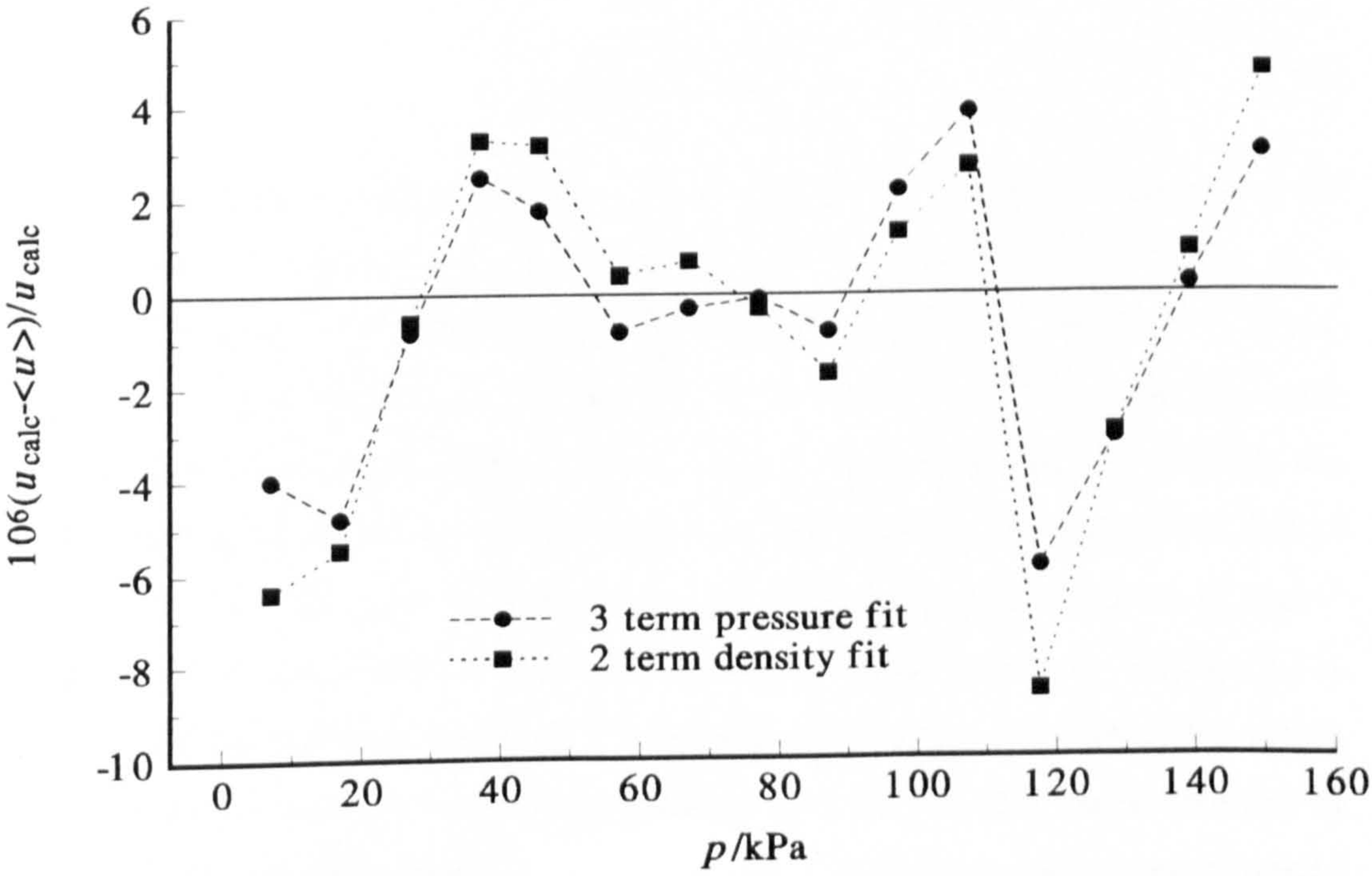

motion, and that all pressures should be retained in the analysis. The three term pressure fit in this case may be seen to model the data slightly better than the two term density series but the difference is not significant. The standard deviations of the calculated sound speeds were estimated from the agreement between the modes, and along the isotherm are of the order of 20 ppm. It is encouraging to see that all the data could be accommodated in the fit to within this level, indeed if a point cannot be fitted to within about three standard deviations, this is again evidence that the data is perturbed. The data at the lowest pressure was removed for every isotherm because the accuracy of the resonance frequencies was limited by the Lorentzian algorithm used to extract them from modes with such large half-widths. It has been found in previous work[1],[4] that the density explicit series tends to converge faster and this was found to be the case for the isotherms at 230, 241, 253, and 267 K where, after removal of pressures affected by the shell resonance, the density series required only two terms to represent the sound speeds adequately whereas the pressure series required three terms. Truncation of the series causes systematic errors in the coefficients and, since these may be estimated, this provides another test that additional terms are not hiding the effects of the shell resonance. For the pressure series in which the coefficients are A_0, A_1 and A_2 the fractional systematic error in β_a caused by truncation of the series from three to two terms may be estimated by

$$\frac{\delta\beta_a}{\beta_a} = \frac{A_2 \langle p \rangle}{A_1}, \tag{8.1}$$

where $\langle p \rangle$ is the average pressure for the isotherm. At 282 K analysis of the full pressure range gave $\beta_a = -519.40$ cm^3·mol^{-1} for the two term fit and $\beta_a = -504.78$ cm^3·mol^{-1} for the three term fit, a change of about 15 cm^3·mol^{-1}. Equation (8.1) limits the expected change to 5 cm^3·mol^{-1} indicating that the data is affected by the shell motion. When the top four pressures are removed the regression gives $\beta_a = -502.29$ cm^3·mol^{-1} for the two term fit and $\beta_a = -507.13$ cm^3·mol^{-1} for the three term fit, a change of about the expected 5 cm^3·mol^{-1} showing that the perturbed data had been successfully removed. Figure (8.11) shows the fractional deviations of the average speed of sound $\langle u \rangle$ from the values u_{calc} calculated from the two term pressure and density fits finally selected in which the highest four pressures were removed. The rejected high-pressure points

Figure 8.11: Fractional deviations of the average sound speeds $\langle u \rangle$ determined for the selected modes from the calculated values for the isotherm at 282 K in SF_6.

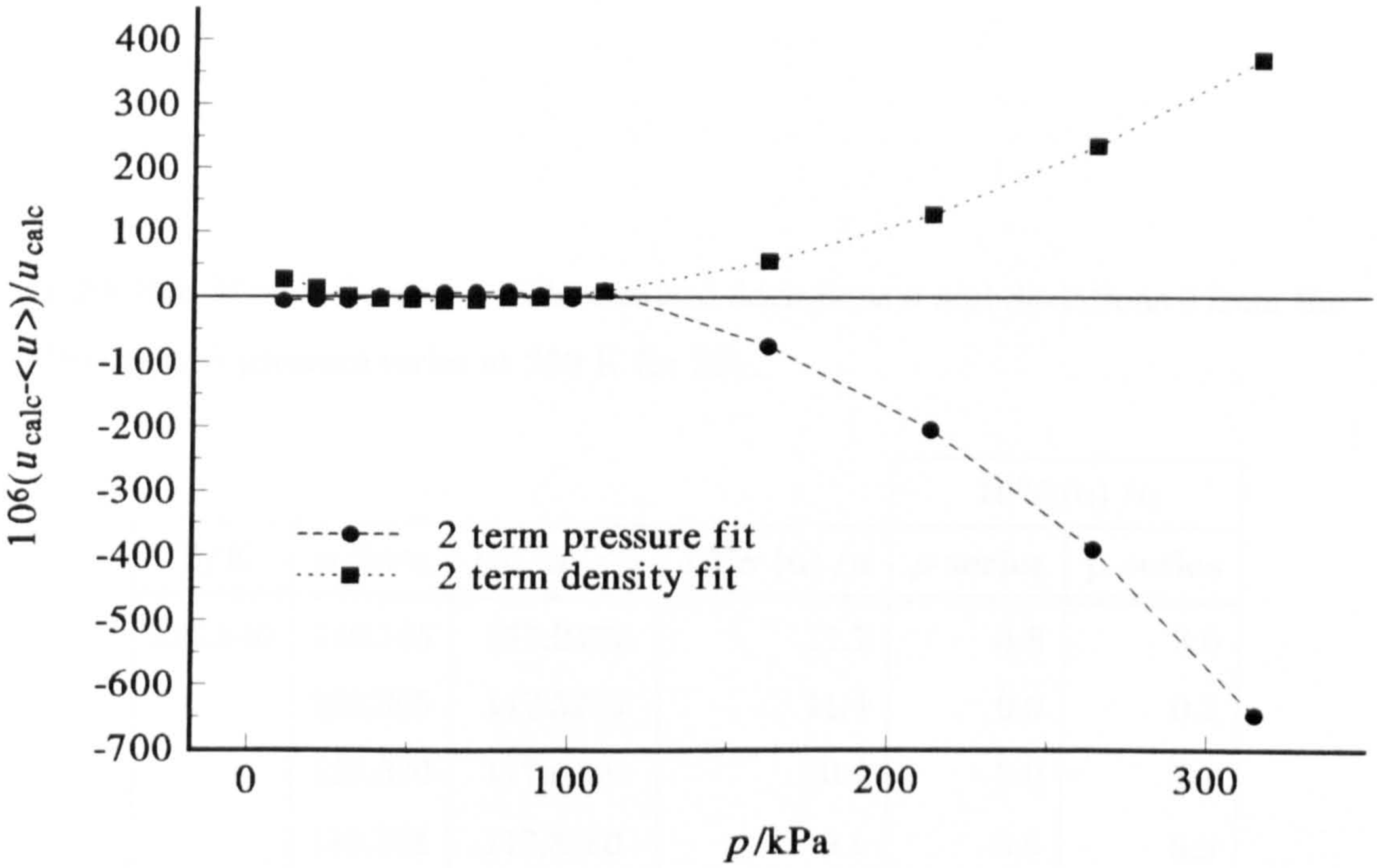

can be seen to deviate significantly from the fit and could not be fitted to within a few standard deviations with the expected number of terms; two terms for the density series and three for the pressure series. Figure (8.12) displays the fractional sound speed deviations at 339 K for the finally selected two-term pressure and density series in which the four highest pressures were discarded. Similarly to 282 K these rejected data show large deviations from the fit whereas the rest of the data may easily be fitted within the typical standard deviations of 20 ppm. The other five isotherms were analysed using the same procedure and the results are listed in tables (8.3) to (8.10) which give the mean quantity $\langle u \rangle$, together with the standard deviation σ of the mean at a given state point and the deviation $\delta = u_{calc} - \langle u \rangle$ of the mean from the equation of best fit, for both the density and pressure series. In tables (8.3) to (8.10) (a) indicates a state point removed from the analysis.

8.2.4. Transport Properties

The transport properties derived from the analysis of the resonance half-widths in SF_6 are presented in this section and compared with published data. The

Table 8.3: Mean values of u with standard deviations σ and deviations δ from the density and pressure series at 230 K for SF_6.

				$10^6\delta\,(u)/u$	
T/K	**p/kPa**	$\langle u\rangle$/m·s^{-1}	$10^6\sigma\,(u)/u$	**ρ series**	**p series**
229.840	149.125	117.0471	11.7	4.8	3.0
	138.865	117.3226	11.4	0.9	0.2
	128.320	117.6036	10.4	-3.0	3.1
	117.561	117.8880	9.1	-8.6	5.9
	107.119	118.1633	7.7	2.7	3.9
	97.075	118.4249	7.4	1.3	2.2
	86.997	118.6852	7.7	-1.7	-0.8
	77.027	118.9412	3.9	-0.3	-0.1
	66.966	119.1974	3.1	0.7	-0.3
	56.986	119.4497	6.3	0.4	-0.8
	45.512	119.7378	10.8	3.2	1.8
	36.930	119.9515	15.1	3.3	2.5
	26.989	120.1969	10.0	-0.6	-0.8
	16.989	120.4417	21.0	-5.5	-4.8
	7.008	120.6848	14.3	(a)	(a)

Table 8.4: Mean values of u with standard deviations σ and deviations δ from the density and pressure series at 241 K for SF_6.

				$10^6\delta\,(u)\,/u$	
T/K	**p/kPa**	$\langle u\rangle$/m·s^{-1}	$10^6\sigma\,(u)\,/u$	**ρ series**	**p series**
240.449	176.568	119.3800	22.6	(a)	(a)
	159.623	119.7962	21.0	(a)	(a)
	142.132	120.2147	16.1	(a)	(a)
	124.327	120.6305	7.7	(a)	(a)
	105.446	121.0218	14.3	5.1	0.3
	95.887	121.2405	12.4	1.8	0.5
	85.903	121.4674	10.0	-3.0	-1.9
	76.452	121.6816	9.8	-1.1	1.4
	66.752	121.8996	9.3	-3.1	0.0
	55.670	122.1473	9.9	-2.8	0.2
	46.854	122.3430	8.3	-3.9	-1.8
	37.075	122.5593	8.2	-0.1	0.1
	27.980	122.7596	15.8	5.3	3.2
	18.966	122.9559	16.3	2.2	-2.5
	10.027	123.1467	78.0	(a)	(a)

Table 8.5: Mean values of u with standard deviations σ and deviations δ from the density and pressure series at 253 K for SF_6.

				$10^6\delta\,(\mathbf{u})\,/\mathbf{u}$	
T/K	**p/kPa**	$\langle\mathbf{u}\rangle/\mathbf{m{\cdot}s^{-1}}$	$10^6\sigma\,(\mathbf{u})\,/\mathbf{u}$	ρ **series**	**p series**
253.157	198.713	122.3675	10.0	(a)	(a)
	175.355	122.8508	7.0	10.9	3.9
	153.028	123.3076	9.0	-9.2	-9.7
	130.459	123.7638	5.1	(a)	(a)
	99.414	124.3889	14.7	4.4	8.5
	89.911	124.5764	14.1	0.1	4.2
	79.960	124.7721	13.2	-0.9	2.0
	69.972	124.9671	12.0	-5.4	-3.2
	60.011	125.1611	11.0	-4.9	-3.5
	49.991	125.3552	8.4	-4.2	-4.3
	40.009	125.5475	9.7	-3.7	-4.8
	30.016	125.7395	9.9	1.1	-1.6
	20.008	125.9314	21.9	10.3	6.1
	10.022	126.1229	14.4	(a)	(a)

Table 8.6: Mean values of u with standard deviations σ and deviations δ from the density and pressure series at 267 K for SF_6.

				$10^6\delta\,(u)/u$	
T/K	**p/kPa**	$\langle u \rangle$/m·s^{-1}	$10^6\sigma\,(u)/u$	**ρ series**	**p series**
266.626	256.672	124.9563	27.5	(a)	(a)
	220.182	125.6164	27.8	(a)	0.4
	183.469	126.2717	29.1	(a)	-0.1
	147.001	126.9131	24.4	13.1	-1.9
	110.344	127.5495	18.6	0.5	2.7
	100.352	127.7210	16.9	-3.9	0.5
	90.369	127.8918	17.1	-5.7	0.0
	80.360	128.0622	13.9	-8.6	-2.0
	70.377	128.2320	11.4	-6.6	-0.4
	60.364	128.4014	11.8	-4.6	0.0
	50.389	128.5694	9.9	-3.4	-1.2
	39.082	128.7594	7.7	1.9	0.4
	30.084	128.9103	10.2	9.3	4.3
	20.308	129.0720	16.9	5.6	-4.0
	10.476	129.2337	61.7	(a)	(a)

Table 8.7: Mean values of u with standard deviations σ and deviations δ from the density and pressure series at 282 K for SF_6.

				$10^6\delta\,(u)/u$	
T/K	**p/kPa**	$\langle u\rangle$/m·s^{-1}	$10^6\sigma\,(u)/u$	**ρ series**	**p series**
281.913	314.920	127.9859	68.5	(a)	(a)
	263.821	128.7835	54.0	(a)	(a)
	212.651	129.5689	45.0	(a)	(a)
	161.619	130.3404	36.6	(a)	(a)
	110.263	131.1045	28.9	8.7	-9.6
	100.248	131.2522	27.7	3.2	-2.9
	90.332	131.3979	25.8	-1.9	1.1
	80.325	131.5452	23.9	-1.2	7.9
	70.296	131.6914	24.1	-6.5	5.7
	60.319	131.8369	22.1	-6.8	5.2
	50.307	131.9827	22.5	-5.1	3.8
	40.347	132.1271	21.8	-4.1	-1.2
	30.355	132.2718	20.9	0.4	-5.7
	20.364	132.4171	21.5	13.4	-4.5
	10.338	132.5624	98.4	(a)	(a)

Table 8.8: Mean values of u with standard deviations σ and deviations δ from the density and pressure series at 299 K for SF_6.

				$10^6\delta\,(u)\,/u$	
T/K	**p/kPa**	$\langle u \rangle$/m·s^{-1}	$10^6\sigma\,(u)\,/u$	**ρ series**	**p series**
298.474	353.658	131.8209	80.1	(a)	(a)
	292.800	132.6227	68.2	(a)	(a)
	231.776	133.4153	56.5	(a)	(a)
	170.716	134.1981	33.2	(a)	(a)
	110.299	134.9630	26.2	12.4	-2.3
	100.404	135.0869	25.5	6.1	0.6
	90.375	135.2121	24.1	0.3	1.6
	80.413	135.3365	22.8	-2.8	3.4
	70.342	135.4617	21.8	-6.5	2.5
	60.405	135.5850	19.5	-9.8	0.0
	50.417	135.7086	17.4	-11.6	-3.3
	40.419	135.8327	17.3	-8.3	-3.4
	30.438	135.9564	19.0	-3.8	-4.3
	20.442	136.0805	24.0	5.8	-2.2
	10.453	136.2006	172.3	(a)	(a)

Table 8.9: Mean values of u with standard deviations σ and deviations δ from the density and pressure series at 317 K for SF_6.

				$10^6\delta\,(u)\,/u$	
T/K	**p/kPa**	$\langle u \rangle$/m·s^{-1}	$10^6\sigma\,(u)\,/u$	**ρ series**	**p series**
317.347	396.321	136.0401	100.5	(a)	(a)
	324.590	136.8320	51.6	(a)	(a)
	252.274	137.6175	51.0	(a)	(a)
	181.494	138.3756	42.1	(a)	(a)
	110.050	139.1317	24.0	6.6	-1.7
	100.065	139.2369	22.5	2.5	-0.3
	89.981	139.3432	22.1	1.0	2.5
	80.044	139.4475	20.8	-2.5	1.6
	70.068	139.5520	16.3	-4.9	0.6
	60.150	139.6556	15.3	-7.6	-2.1
	50.202	139.7601	15.2	-4.1	0.0
	40.307	139.8653	15.1	-2.8	-1.4
	30.255	139.9687	17.2	1.5	-1.2
	20.284	140.0734	27.6	10.3	2.1
	10.352	140.1799	99.1	(a)	(a)

Table 8.10: Mean values of u with standard deviations σ and deviations δ from the density and pressure series at 339 K for SF_6.

				$10^6\delta\,(u)\,/u$	
T/K	**p/kPa**	$\langle u\rangle$/m·s^{-1}	$10^6\sigma\,(u)\,/u$	**ρ series**	**p series**
338.987	560.806	139.7202	127.8	(a)	(a)
	447.522	140.7475	102.0	(a)	(a)
	336.004	141.7479	78.1	(a)	(a)
	223.120	142.7477	73.1	(a)	(a)
	110.220	143.7382	25.8	7.5	2.3
	100.248	143.8252	25.4	4.7	3.0
	90.230	143.9121	25.5	-1.2	-0.3
	80.373	143.9981	28.8	-2.1	0.6
	70.240	144.0855	20.5	-8.3	-4.8
	60.252	144.1727	23.4	-6.1	-2.5
	50.298	144.2593	22.8	-4.6	-2.0
	40.268	144.3467	17.8	-1.1	-0.2
	30.155	144.4347	11.8	2.8	1.0
	20.343	144.5203	26.4	9.7	4.4
	10.373	144.6004	144.2	(a)	(a)

Figure 8.12: Fractional deviations of the average sound speeds $\langle u \rangle$ determined for the selected modes from the calculated values for the isotherm at 339 K in SF_6.

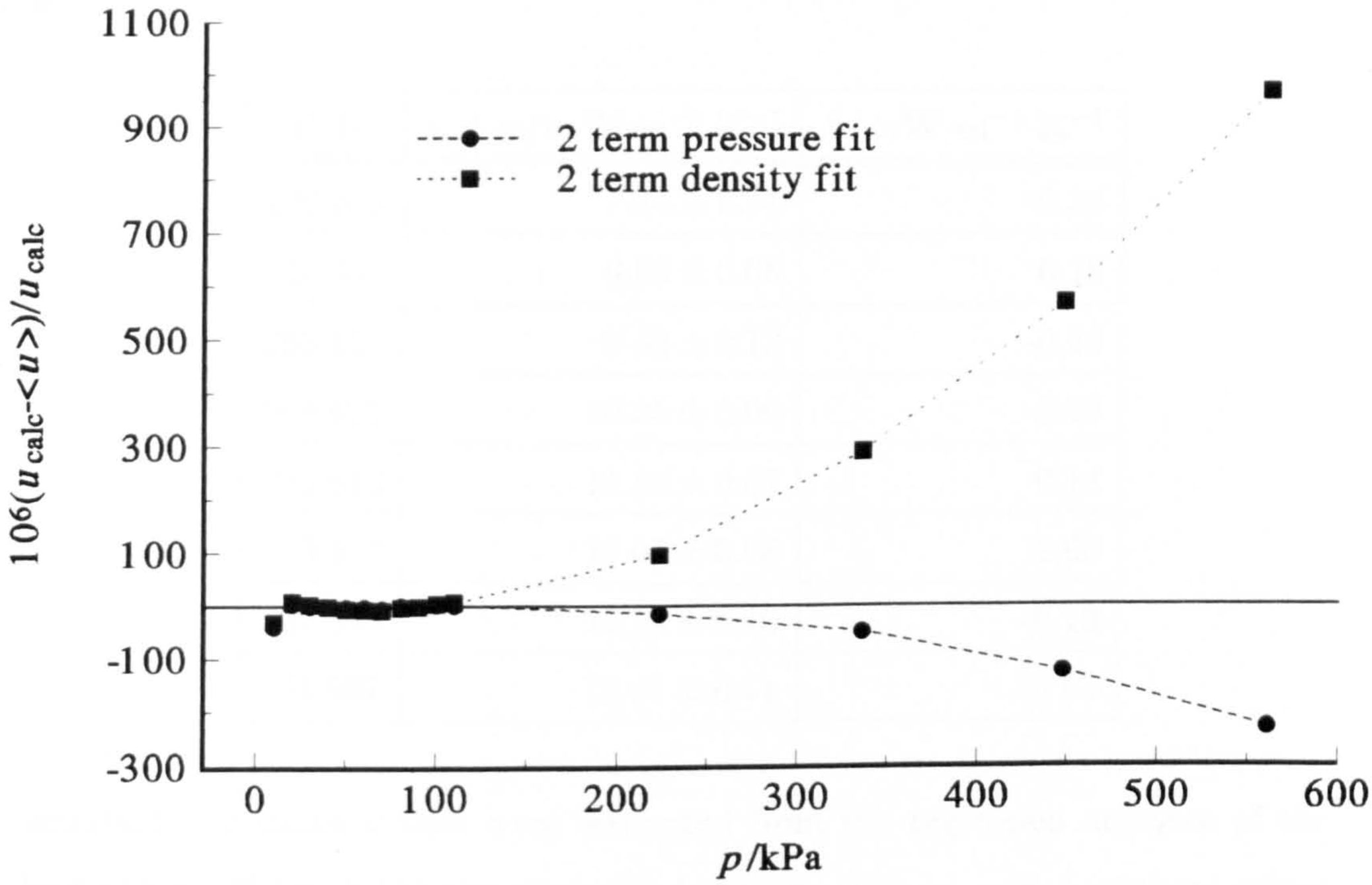

transport properties are the limiting values as the density tends to zero but the subscripts have been dropped for clarity.

Thermal Conductivity Results

The thermal conductivity and its density dependence were determined at each experimental temperature. Both quantities were fitted using weighted non-linear regression analysis in which the most significant terms were selected from a bank of terms T^n, where $n = -4, -3, \cdots +4$. For the thermal conductivity, κ this gave

$$\kappa/\mathrm{mW \cdot m^{-1} \cdot K^{-1}} = 0.16947 \times 10^{-3} T^2 - 0.277 \times 10^{-9} T^4, \qquad (8.2)$$

with a standard deviation of 0.24 $\mathrm{mW \cdot m^{-1} \cdot K^{-1}}$. The density dependence of the thermal conductivity $(\partial\kappa/\partial\rho)$ was not found to have a significant temperature dependence over the experimental range and the weighted mean value is

$$(\partial\kappa/\partial\rho)\,/\mathrm{mW \cdot m^2 \cdot K^{-1} \cdot kg^{-1}} = 0.32 \qquad (8.3)$$

which has a standard deviation of 0.04 $\mathrm{mW \cdot m^2 \cdot K^{-1} \cdot kg^{-1}}$. Table (8.11) gives the experimentally determined values of the thermal conductivity κ along with their

Table 8.11: Values of the thermal conductivity κ, its standard deviation σ and deviation δ from the smoothing equation at each experimental temperature in SF_6.

T/K	$\kappa \pm \sigma$/mW·m^{-1}·K^{-1}	δ/mW·m^{-1}·K^{-1}
229.840	7.84 ± 0.11	-0.34
240.449	9.06 ± 0.06	0.19
253.157	9.48 ± 0.12	-0.24
266.625	10.35 ± 0.09	-0.30
281.613	11.84 ± 0.07	0.14
299.477	13.05 ± 0.08	0.08
317.346	14.13 ± 0.10	-0.13
338.987	15.83 ± 0.11	0.01

standard deviations σ that were estimated from the regression analyses of the half-widths. Table (8.11) also gives the deviations $\delta = \kappa_{\text{exp}} - \kappa_{\text{calc}}$ of these values from equation (8.2). Table (8.12) gives the experimentally determined values of the initial density dependence of the thermal conductivity $(\partial\kappa/\partial\rho)$ along with their standard deviations σ as well as the deviations $\delta = (\partial\kappa/\partial\rho)_{\text{exp}} - (\partial\kappa/\partial\rho)_{\text{calc}}$ of these values from equation (8.3). Figures (8.13) and (8.14) show the deviations δ from equations (8.2) and (8.3), and it is encouraging that all the data may be fitted to within three standard deviations.

Figure (8.15) shows the nearly linear dependence of the thermal conductivity with temperature over the experimental range and the agreement with literature results. Reference [5] gives a corresponding states analysis based on experimental data. This experimental data is limited to temperatures above 298 K and it can be seen that above this temperature the results from this work show good agreement. Below 298 K the experimental results deviate systematically from the extrapolation of the corresponding states correlation of Uribe *et al.*[5]. The result of Hermans and co-workers[6] and Plank[7] are significantly high compared to this work but there is excellent agreement with the most recent literature determination of Tanaka *et al.*[8] of better than 1 % over the overlapping temperature range.

Table 8.12: Values of the initial density dependence of the thermal conductivity $(\partial\kappa/\partial\rho)$, its standard deviation σ and deviation δ from the smoothing equation at each experimental temperature in SF_6.

$\mathbf{T/K}$	$(\partial\boldsymbol{\kappa}/\partial\boldsymbol{\rho}) \pm \boldsymbol{\sigma}/\mathbf{mW{\cdot}m^2{\cdot}K^{-1}{\cdot}kg^{-1}}$	$\boldsymbol{\delta}/\mathbf{mW{\cdot}m^2{\cdot}K^{-1}{\cdot}kg^{-1}}$
229.840	0.33 ± 0.02	0.01
240.449	0.28 ± 0.01	-0.04
253.157	0.36 ± 0.02	0.04
266.625	0.36 ± 0.02	0.04
281.613	0.31 ± 0.01	-0.01
299.477	0.33 ± 0.02	0.01
317.346	0.38 ± 0.02	0.06
338.987	0.38 ± 0.02	0.06

Figure 8.13: Deviations δ of the thermal conductivity κ of SF_6 from equation (8.2).

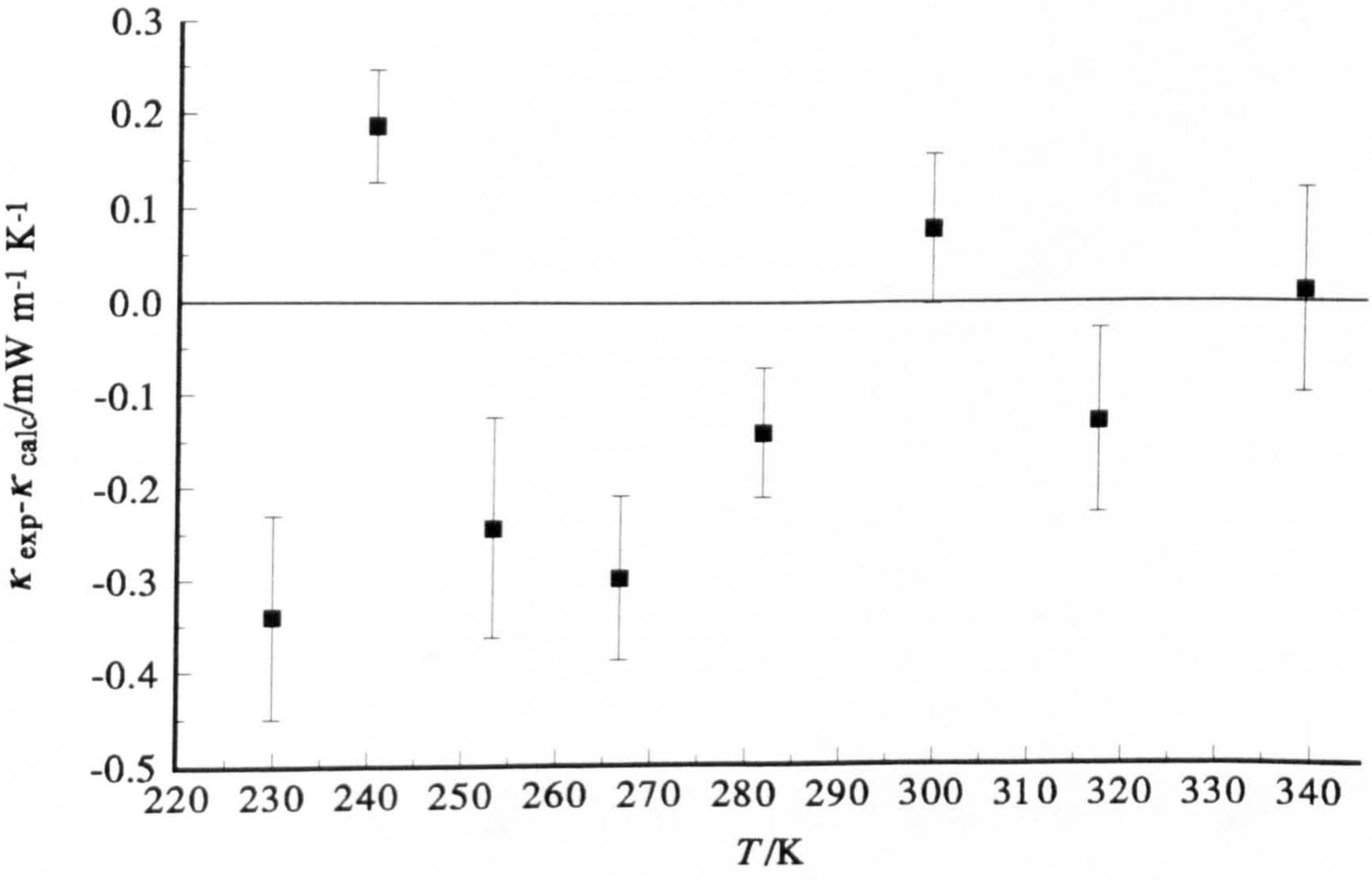

Figure 8.14: Deviations δ of the initial density dependence of the thermal conductivity $(\partial\kappa/\partial\rho)$ of SF_6 from equation (8.3).

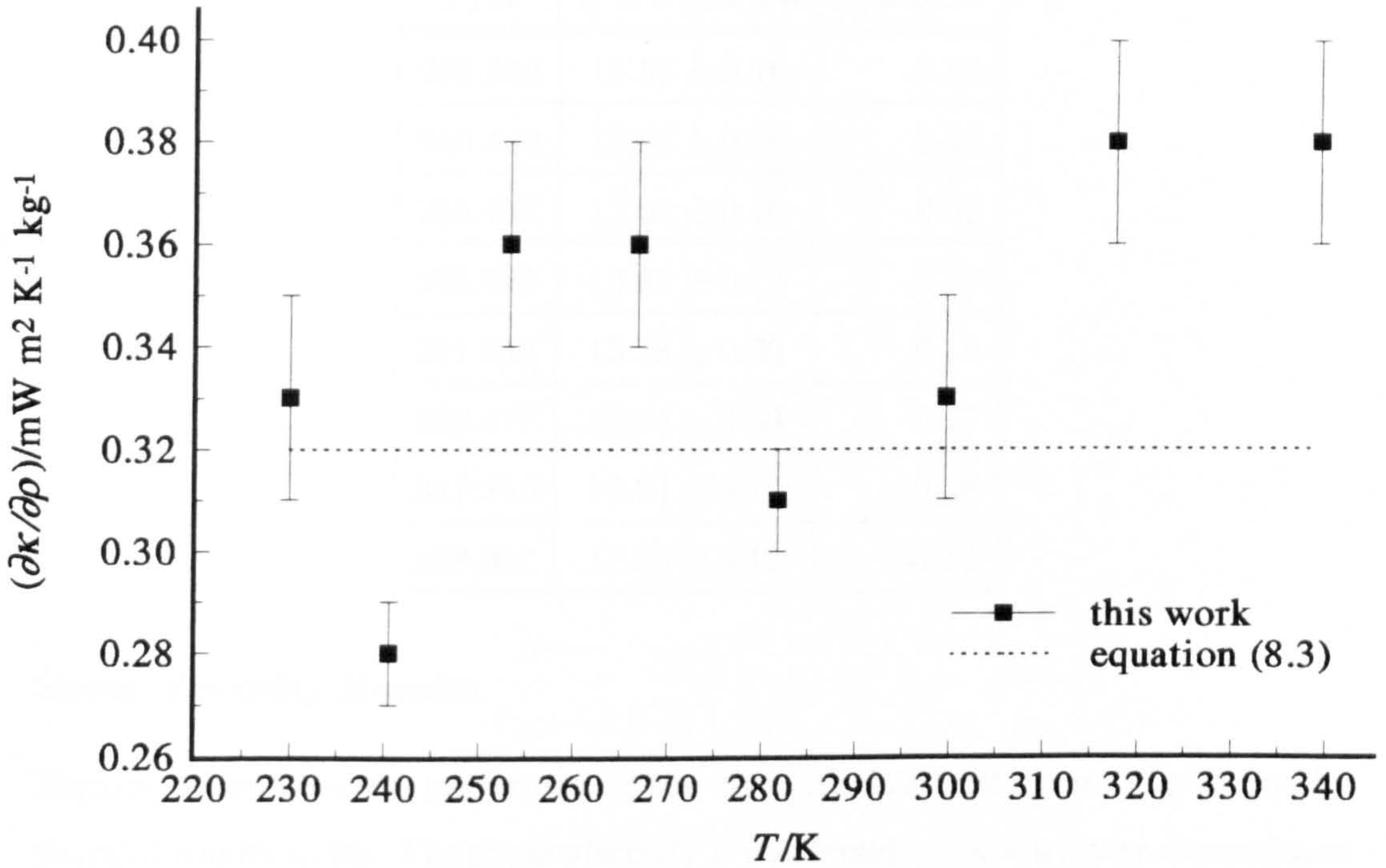

Figure 8.15: Comparison of the thermal conductivity κ of SF_6 determined in this work with published values.

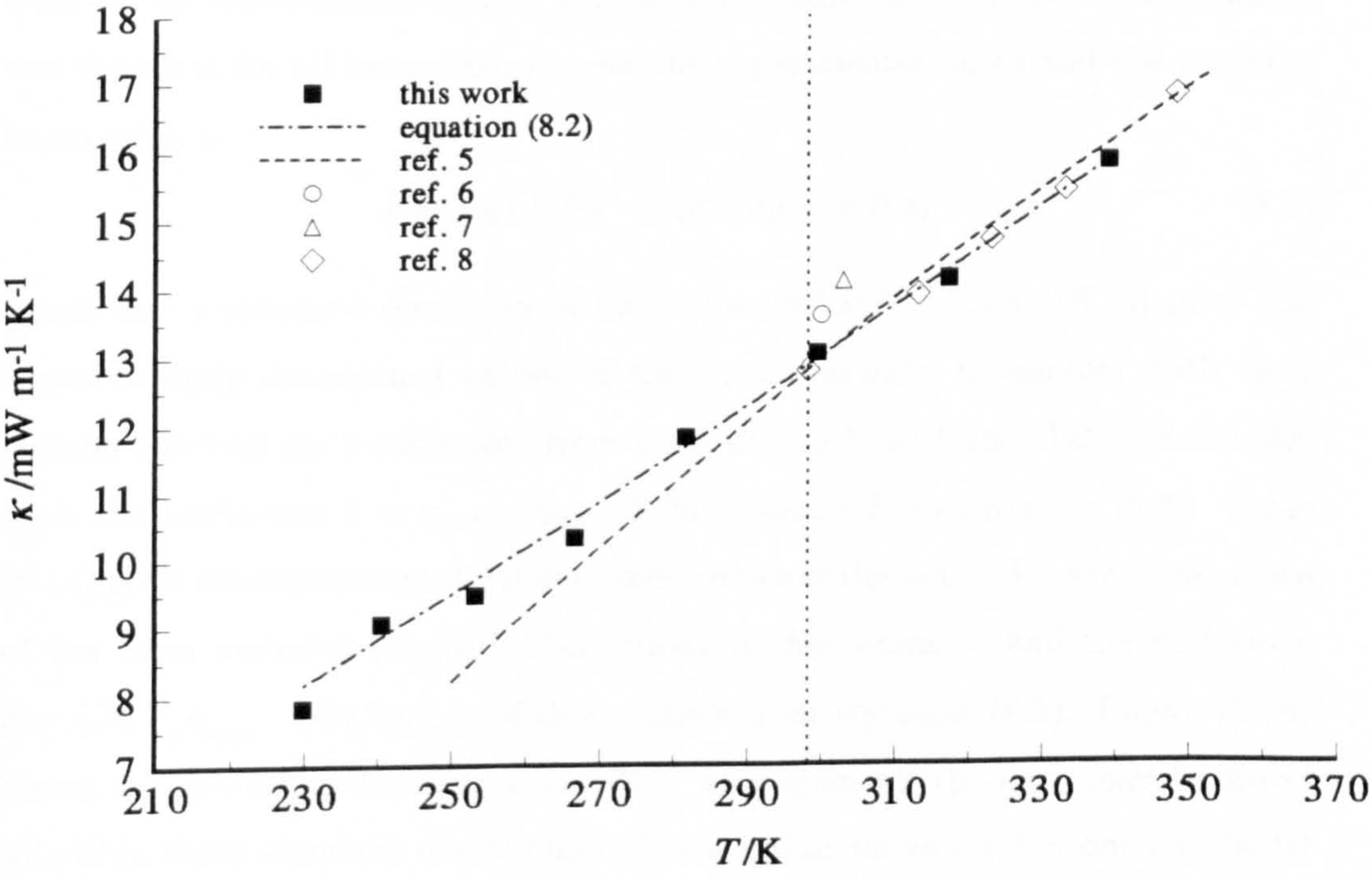

Table 8.13: Values of the shear viscosity η, its standard deviation σ and deviation δ from the smoothing equation at each experimental temperature in SF_6.

T/K	$\eta \pm \sigma/\mu$**Pa·s**	δ/μ**Pa·s**
229.840	11.55 ± 0.16	-0.63
240.449	12.93 ± 0.08	0.19
253.157	13.04 ± 0.16	-0.38
266.625	13.81 ± 0.12	-0.32
281.613	15.18 ± 0.09	0.25
299.477	16.04 ± 0.09	0.17
317.346	16.64 ± 0.12	-0.18
338.987	17.85 ± 0.12	-0.12

Shear Viscosity Results

Regression analysis was performed on the viscosity data in the same way as for the thermal conductivity. The shear viscosity η was found to have a linear dependence on temperature over the experimental range and may be represented by

$$\eta/\mu\text{Pa} \cdot \text{s} = 0.053T \tag{8.4}$$

with a standard deviation of 0.34 μPa · s. The density dependence of the viscosity was the same for all temperatures over the experimental range and the weighted mean value is

$$(\partial\eta/\partial\rho)\,/\mu\text{Pa} \cdot \text{s} \cdot \text{m}^3 \cdot \text{kg}^{-1} = 0.42 \tag{8.5}$$

which has a standard deviation of 0.05 μPa·s·m^3·kg^{-1}. Table (8.13) gives the experimentally determined values of the shear viscosity η together with their standard deviations σ estimated from the half-width analyses. Table (8.13) also gives the deviations $\delta = \eta_{\text{exp}} - \eta_{\text{calc}}$ of these values from equation (8.4). Table (8.14) gives the experimentally determined values of the initial density dependence of the shear viscosity $(\partial\eta/\partial\rho)$, their standard deviations σ, and the deviations $\delta = (\partial\eta/\partial\rho)_{\text{exp}} - (\partial\eta/\partial\rho)_{\text{calc}}$ of these values from equation (8.5). Figure (8.16) shows the deviations from equation (8.4) and again all the data may be fitted to within three standard deviations indicating that no values fall outside the 99

Table 8.14: Values of the initial density dependence of the shear viscosity $(\partial\eta/\partial\rho)$, its standard deviation σ and deviation δ from the smoothing equation at each experimental temperature in SF_6.

T/K	$(\partial\eta/\partial\rho) \pm \sigma/\mu$**Pa·s·m^3·kg^{-1}**	δ/μ**Pa·s·m^3·kg^{-1}**
229.840	0.48 ± 0.03	0.06
240.449	0.40 ± 0.02	-0.02
253.157	0.50 ± 0.03	0.08
266.625	0.48 ± 0.02	0.06
281.613	0.40 ± 0.01	-0.02
299.477	0.40 ± 0.02	-0.02
317.346	0.45 ± 0.02	0.03
338.987	0.43 ± 0.03	0.01

Figure 8.16: Deviations δ of the shear viscosity η of SF_6 from equation (8.4).

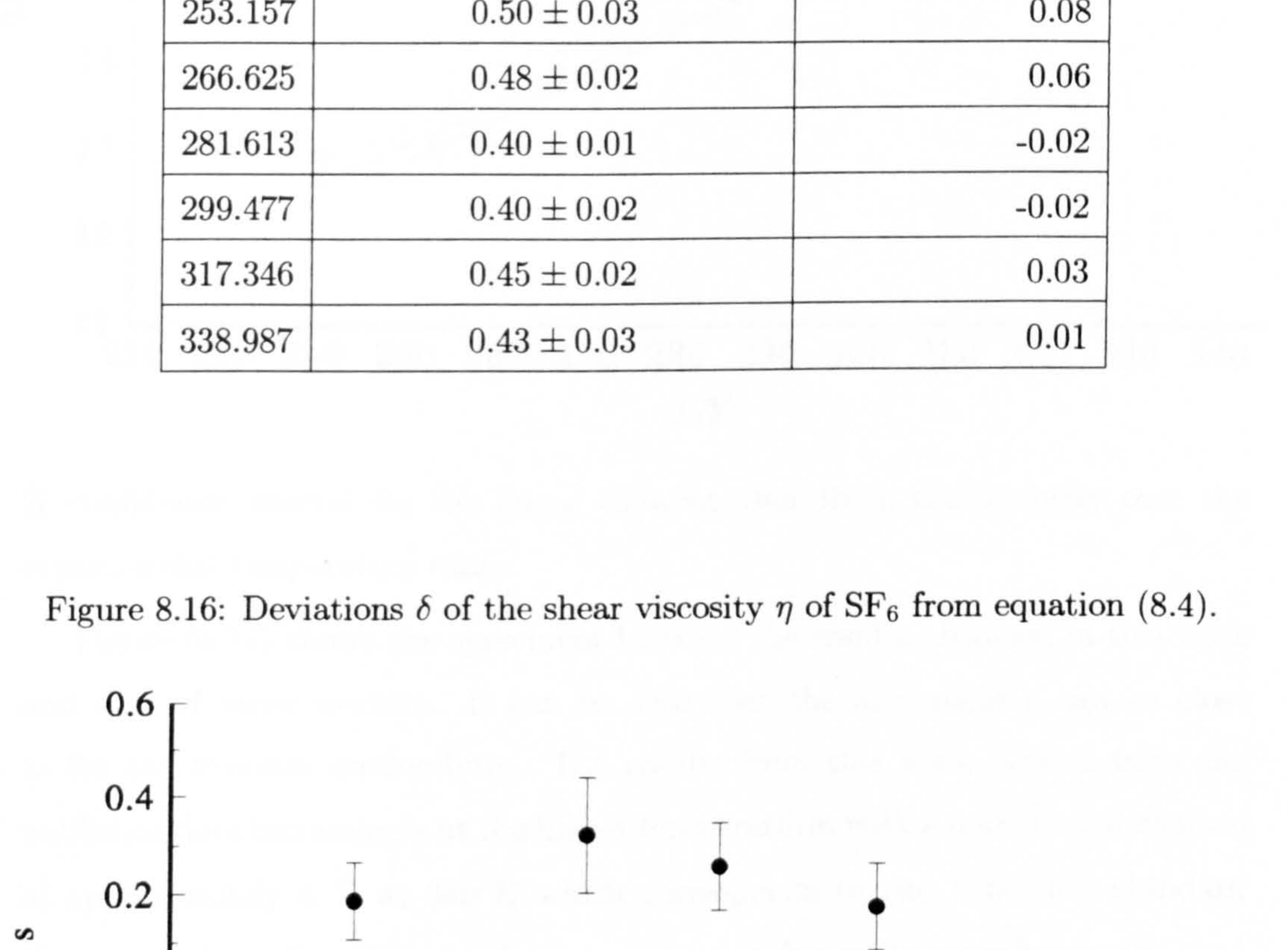

Figure 8.17: Comparison of the shear viscosity η of SF_6 determined in this work with published values.

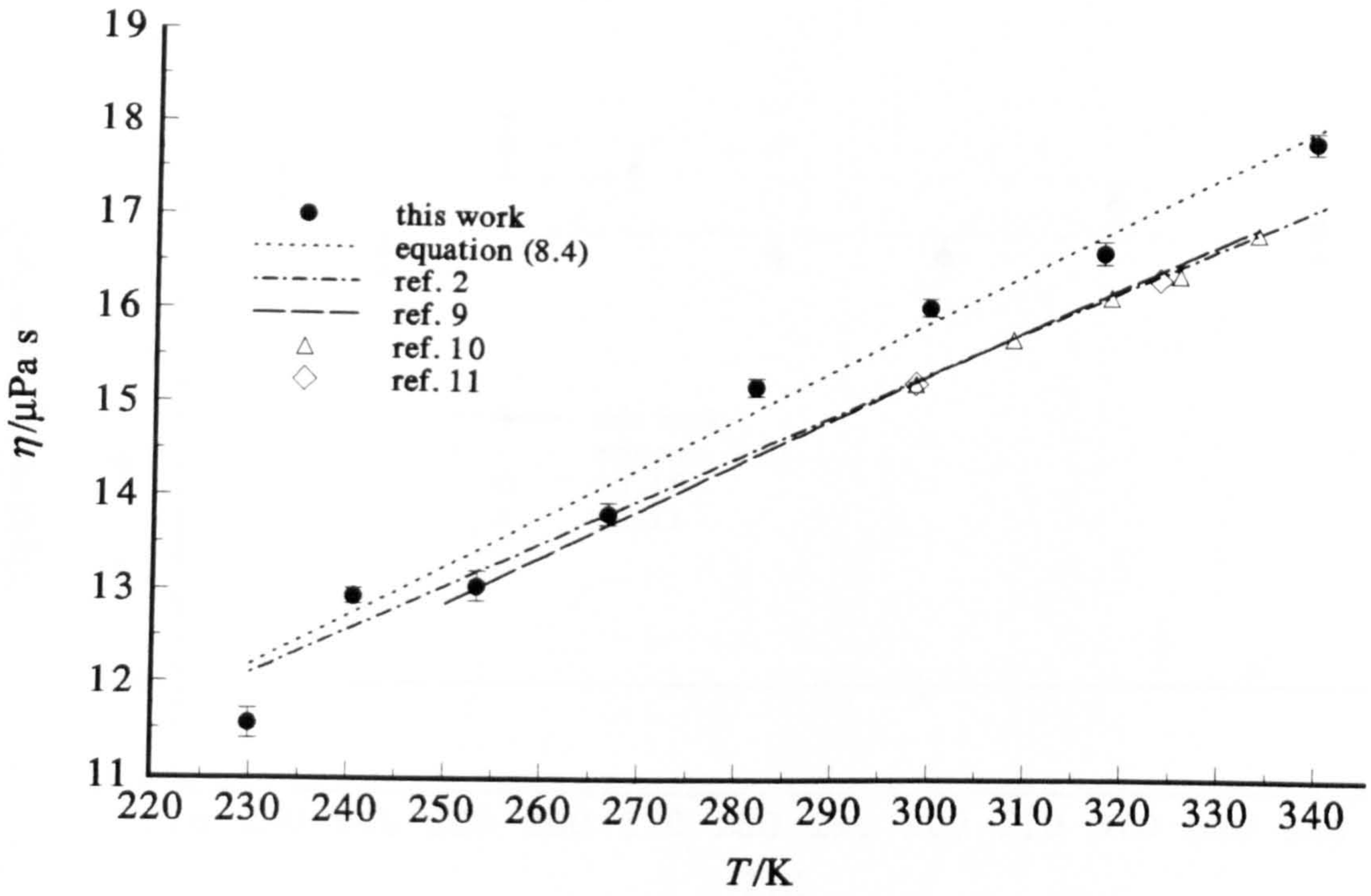

% confidence interval for the linear equation describing the viscosity over the experimental temperature range.

Figure (8.17) shows the agreement between the results obtained in this work and that of other workers. It can be seen that the agreement is not as close as for the thermal conductivity. The results from this work deviate from the published data increasingly at the higher temperatures with a maximum deviation of approximately 5 % at 340 K which corresponds to two times the standard deviation of the fit. This level of agreement is favorable considering the very different systematic errors inherent in an analysis of this kind. The importance of the transport properties derived in this work lies in the ability to analyse the speed of sound data without recourse to published data and not in their absolute accuracy. The results from this work are larger and this may be partly due to the Stiel-Thodos relation used to correlate the values of the thermal conductivity and viscosity. In addition, any unidentified loss mechanisms in the resonator or the inclusion of modes affected even slightly by the shell resonance will give rise to overestimates of the transport properties and the results from this work should be treated with caution. The literature results all agree to better than

Figure 8.18: Deviations δ of the initial density dependence of the shear viscosity $(\partial\eta/\partial\rho)$ of SF_6 from equation (8.5).

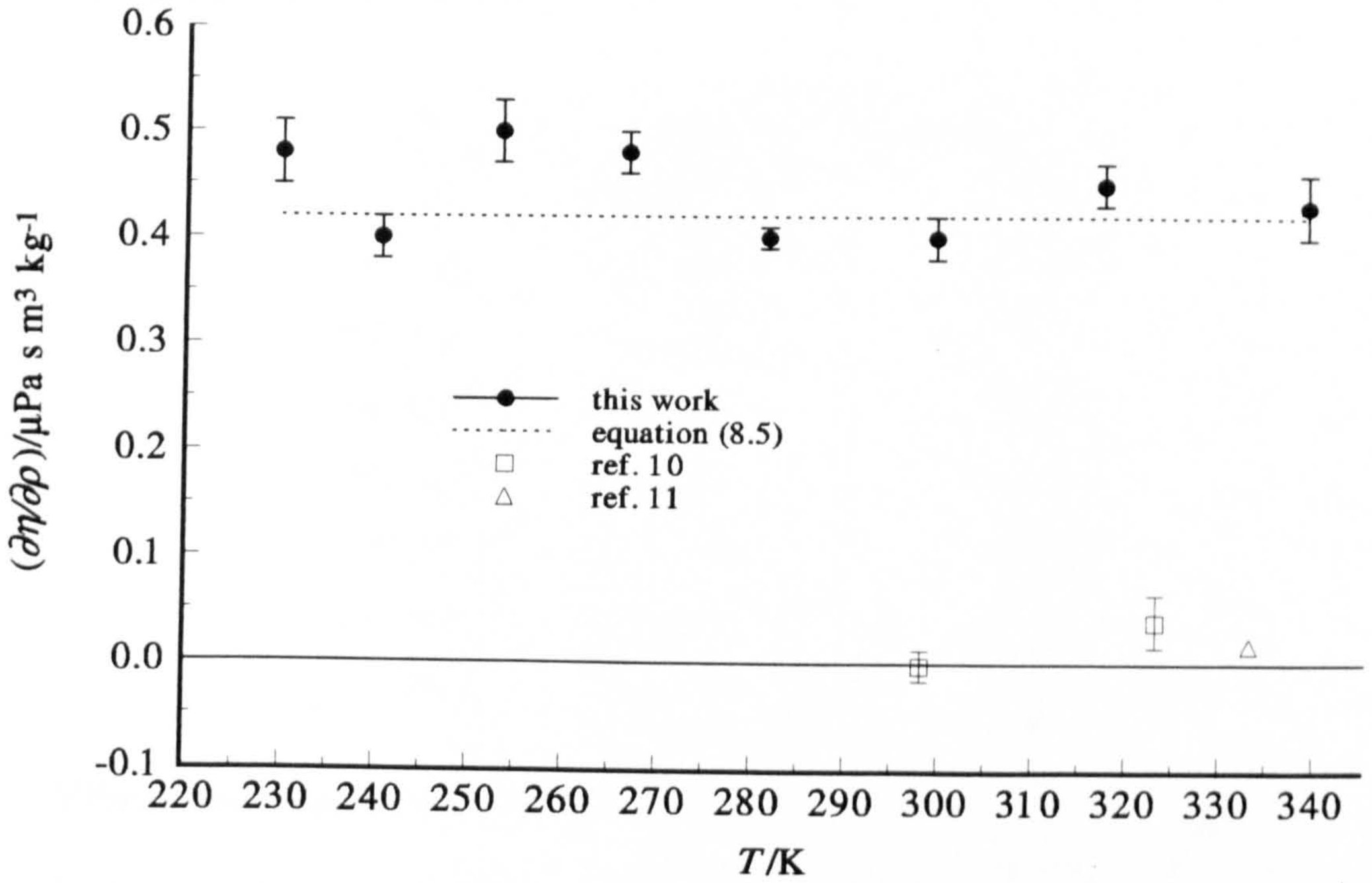

2 % over the range 230 to 340 K. References [2] and [9] represent corresponding states correlations of experimental data by Wakeham *et al.* and Mason *et al.* respectively. Both sets of authors used the same primary data and give essentially identical results above 300 K. The experimental data of Hoogland *et al.*[10] using a capillary-flow viscometer and that of Vogel *et al.*[11] using an oscillating disk viscometer show remarkable agreement for measurements produced using different experimental techniques leading to the conclusion that the results presented here are in error by up to 5 %.

Figure (8.18) shows the initial density dependence of the viscosity determined in this work and that of other workers[10],[11]. The results from this work are an order of magnitude greater than the published results and this is probably due to the density dependent term absorbing the effect of the shell resonance which increases with density. The density dependence of the thermal conductivity given in the previous section is also likely to be in error by an order of magnitude and no importance should be attributed to the initial density dependencies of the transport properties.

Table 8.15: Values of the vibrational relaxation time $\tau\rho$ at a density of 1 kg·m^3, its standard deviation σ and deviation δ from the smoothing equation at each experimental temperature in SF_6.

T/K	$\boldsymbol{\tau\rho \pm \sigma/\mu s \cdot kg \cdot m^{-3}}$	$\boldsymbol{\delta/\mu s \cdot kg \cdot m^{-3}}$
229.840	6.55 ± 0.06	-0.09
240.449	5.97 ± 0.03	-0.06
253.157	5.68 ± 0.06	0.12
266.625	5.16 ± 0.04	0.04
281.613	4.65 ± 0.03	-0.04
299.477	4.24 ± 0.03	0.00
317.346	3.90 ± 0.03	0.06
338.987	3.36 ± 0.04	-0.08

Vibrational Relaxation Times

Vibrational relaxation makes an important contribution to the losses in sulfur hexafluoride. In order to account for this and to correct the observed frequencies for dispersion, estimates of the vibrational relaxation times at each experimental temperature were required. The estimates presented here were determined by separating out the different density dependencies of the known loss mechanisms that contribute to the resonance half-widths. Values of $\tau\rho$ at a density of 1 kg·m^3 and their associated standard deviations σ are given in table (8.15). The values may be represented by

$$\tau\rho/\mu s \cdot kg \cdot m^{-3} = \frac{0.508 \times 10^6}{T^2} - \frac{0.384 \times 10^8}{T^3} \tag{8.6}$$

over the experimental temperature range with a standard deviation of 0.08 μs·kg·m^{-3}. Table (8.15) also gives the deviations $\delta = (\tau\rho)_{exp} - (\tau\rho)_{calc}$ of the experimental results from equation (8.6) and it may be seen from figure (8.19) that all the experimental data could be fitted to within two standard deviations. The only literature value[12] for the vibration relaxation time is shown in figure (8.20) in which the vibrational relaxation time at a density of 1 kg·m^3 is plotted as a function of temperature. The literature result determined using interferrometric techniques is of the same magnitude as the data presented here and the agree-

Figure 8.19: Deviations δ of the vibrational relaxation times $\tau\rho$ of SF_6 at a density of 1 kg·m^3 from equation (8.6).

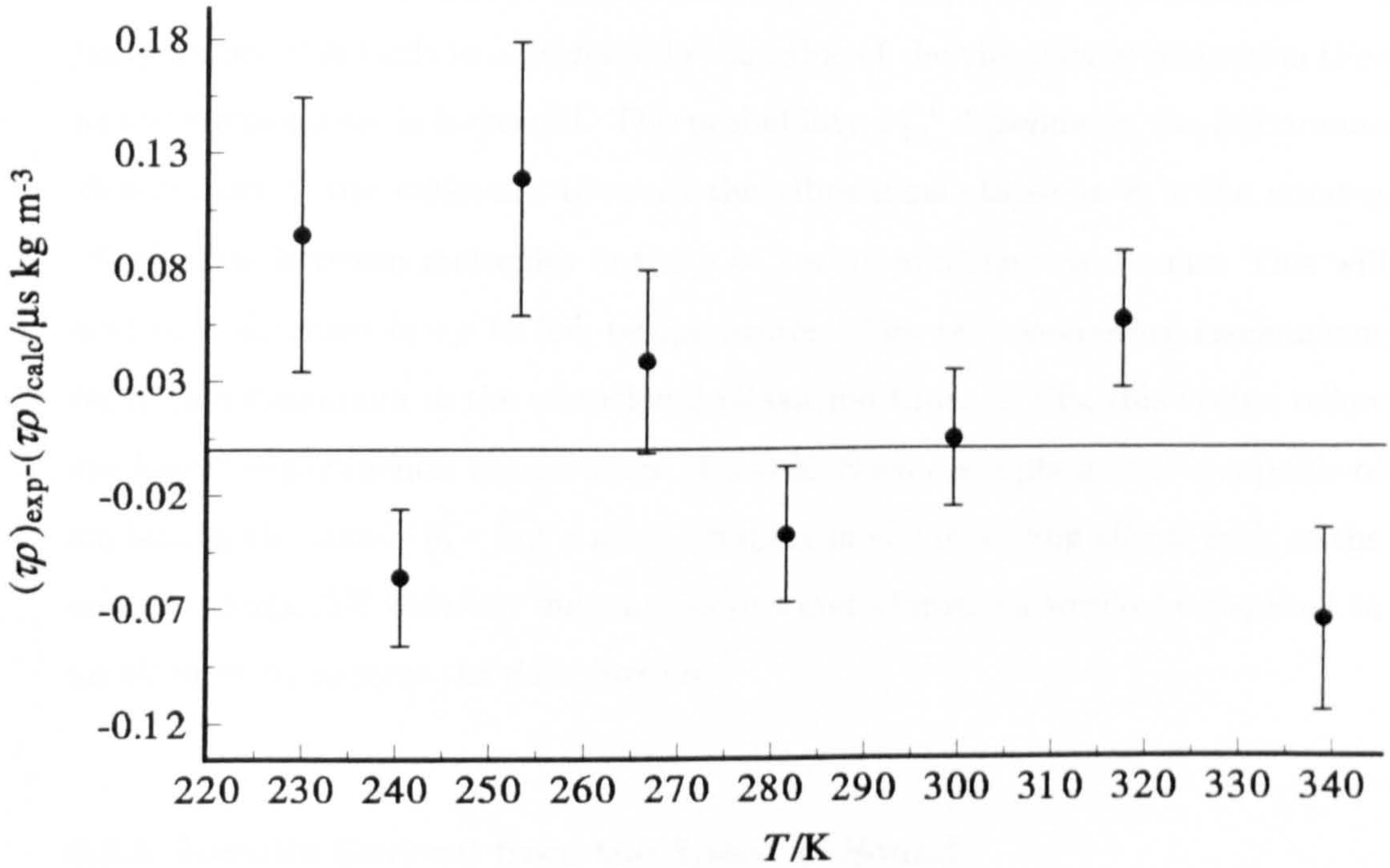

Figure 8.20: Comparison of the vibrational relaxation times $\tau\rho$ of SF_6 at a density of 1 kg·m^3 determined in this work with published values.

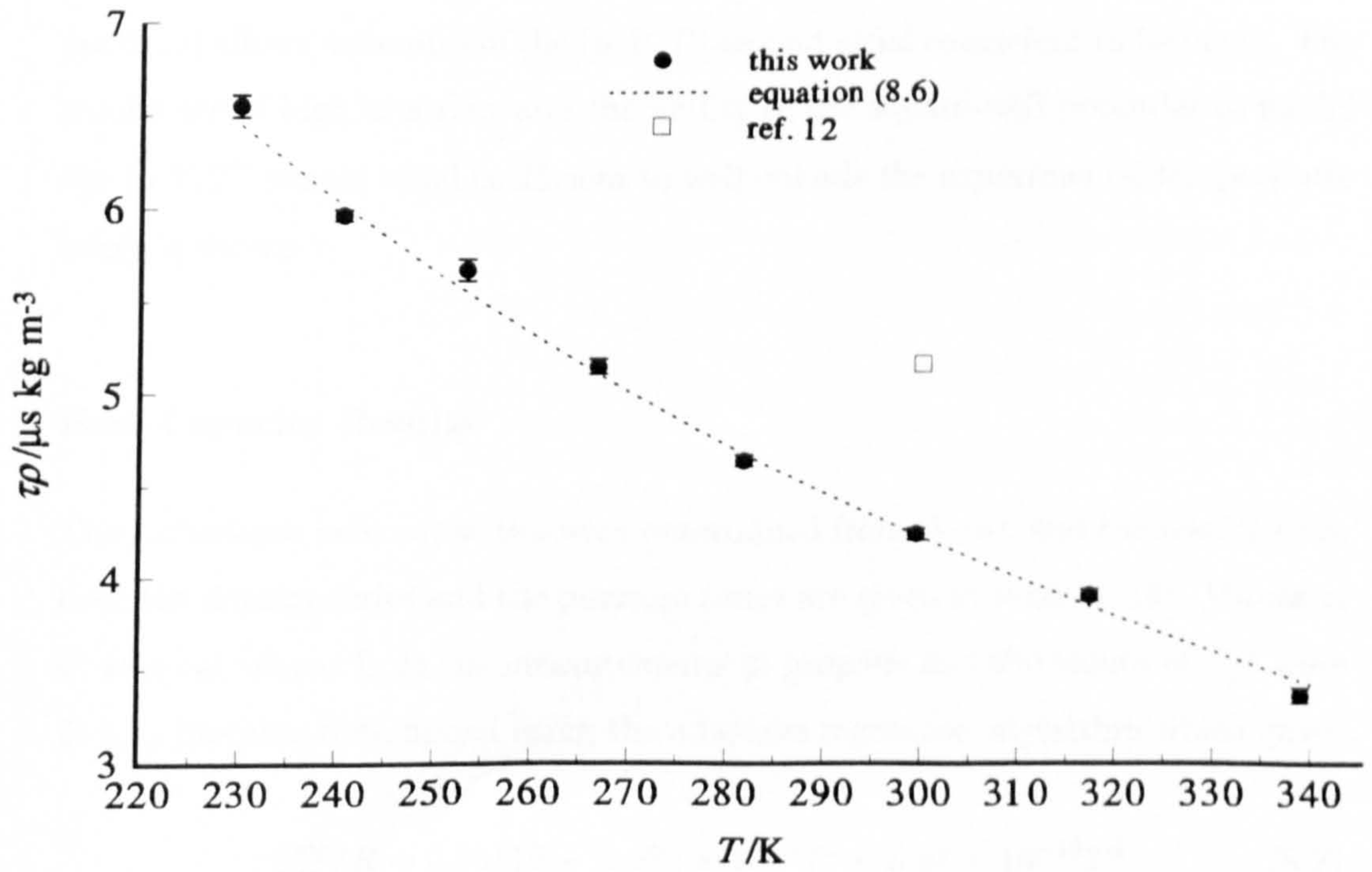

ment is not bad considering the very different experimental methods. The results show the expected temperature dependence[13] which depends on the ratio of the number of collisions $Z_{10} = P_{10}^{-1}$ required for a molecule in the $\nu = 1$ state to deactivate, and the gas kinetic collision rate Z. $\tau = Z_{10}/Z$ and as Z increases with temperature this leads to a decrease in the value of the vibrational relaxation time as the temperature is increased. The probability P_{10}^{-1} depends on the Boltzmann distribution of the molecules between the vibrational states as it is the number of collisions between molecules in the $\nu = 1$ state and the $\nu = 0$ state. This will lead to a decrease in $\tau\rho$ at low temperatures. The two competing mechanisms result in a maximum in the vibrational relaxation time. In SF_6 this occurs below the lowest experimental temperature of 230 K. Such a simple model is capable of explaining the trends in τ but a more complex model including effects such as the energy change ΔE between the translations and vibrations would be required in an attempt to analyse the data further.

8.2.5. Results Derived from the Speed of Sound

Values of the perfect gas heat capacity and second acoustic virial coefficient were determined by analysis of the speed of sound data along each isotherm in terms of a density or pressure series. Combination of these results with a square-well potential allows estimates of the (p, V, T) second virial coefficient to be made. The results are of high accuracy and the ability of the square-well potential to model the (p, V, T) second virial coefficient to well outside the experimental temperature range is shown.

Heat Capacity Results

The perfect-gas heat capacities were determined from A_0/b^2, and the results from both the density series and the pressure series are given in table (8.16). Values of b^2 were calculated from the measurements in propene and the values of C_p^{pg} were fit to a function determined using the adaptive regression algorithm which gave

$$C_p^{\mathrm{pg}}/R = 0.0541T - 0.583 \times 10^{-4}T^2 + 0.85 \times 10^{-10}T^4 \qquad (8.7)$$

Table 8.16: Perfect-gas heat capacities C_p^{pg} derived from the density and pressure series, estimated standard deviations σ, and deviations Δ from the smoothing equations for SF_6.

	Density series		**Pressure series**	
T/K	$\mathbf{C_p^{pg}/R \pm \sigma}$	$\boldsymbol{\Delta}$	$\mathbf{C_p^{pg}/R \pm \sigma}$	$\boldsymbol{\Delta}$
229.840	9.5980 ± 0.0009	-0.0056	9.5987 ± 0.0014	-0.0032
240.449	9.9413 ± 0.0014	0.0071	9.9392 ± 0.0029	0.0073
253.157	10.3450 ± 0.0013	0.0232	10.3436 ± 0.0024	0.0267
266.625	10.6828 ± 0.0020	-0.0408	10.6786 ± 0.0034	-0.0375
281.613	11.1504 ± 0.0033	-0.0110	11.1389 ± 0.0033	-0.0136
299.477	11.6581 ± 0.0039	-0.0149	11.6508 ± 0.0037	-0.0141
317.346	12.1990 ± 0.0043	0.0223	12.1927 ± 0.0032	0.0212
338.987	12.7771 ± 0.0043	-0.0042	12.7726 ± 0.0042	-0.0069

with a standard deviation of 0.025 R for the values determined using the density series, and

$$C_p^{\mathrm{pg}}/R = 3.54 + 0.0274T - \frac{0.66 \times 10^9}{T^4} \tag{8.8}$$

with a standard deviation of 0.025 R for the values determined using the pressure series. Table (8.16) also gives the deviations $\Delta = \left(C_p^{\mathrm{pg}}/R\right)_{\mathrm{exp}} - \left(C_p^{\mathrm{pg}}/R\right)_{\mathrm{calc}}$ from equations (8.7) and (8.8). Figure (8.21) depicts the deviations Δ of the experimental results from equations (8.7) and (8.8) which may be seen to be very similar for both methods. The data cannot always be fitted to within a small multiple of the standard deviation indicating that there are unknown errors in the analysis but no datum can be singled out as particularly in error. Comparison with published data is by means of figure (8.22) which gives equation (8.8) and values calculated from spectroscopic information as deviations from equation (8.7). The pressure fit results are essentially identical to those of the density fit and the values calculated from spectroscopic information and those based on an correlation of experimental values deviate from those in this work by up to 0.25 R. The set of spectroscopic values a) were calculated using the vibrational frequencies from the infra-red spectrum of Gaunt[14] and the Raman spectrum of Yost *et al.*[15] assuming that SF_6 is an harmonic oscillator. The set of spectroscopic values b)

Figure 8.21: Deviations Δ of the perfect gas heat capacities C_p^{pg} of SF_6 determined from the density and pressure series from equations (8.7) and (8.8).

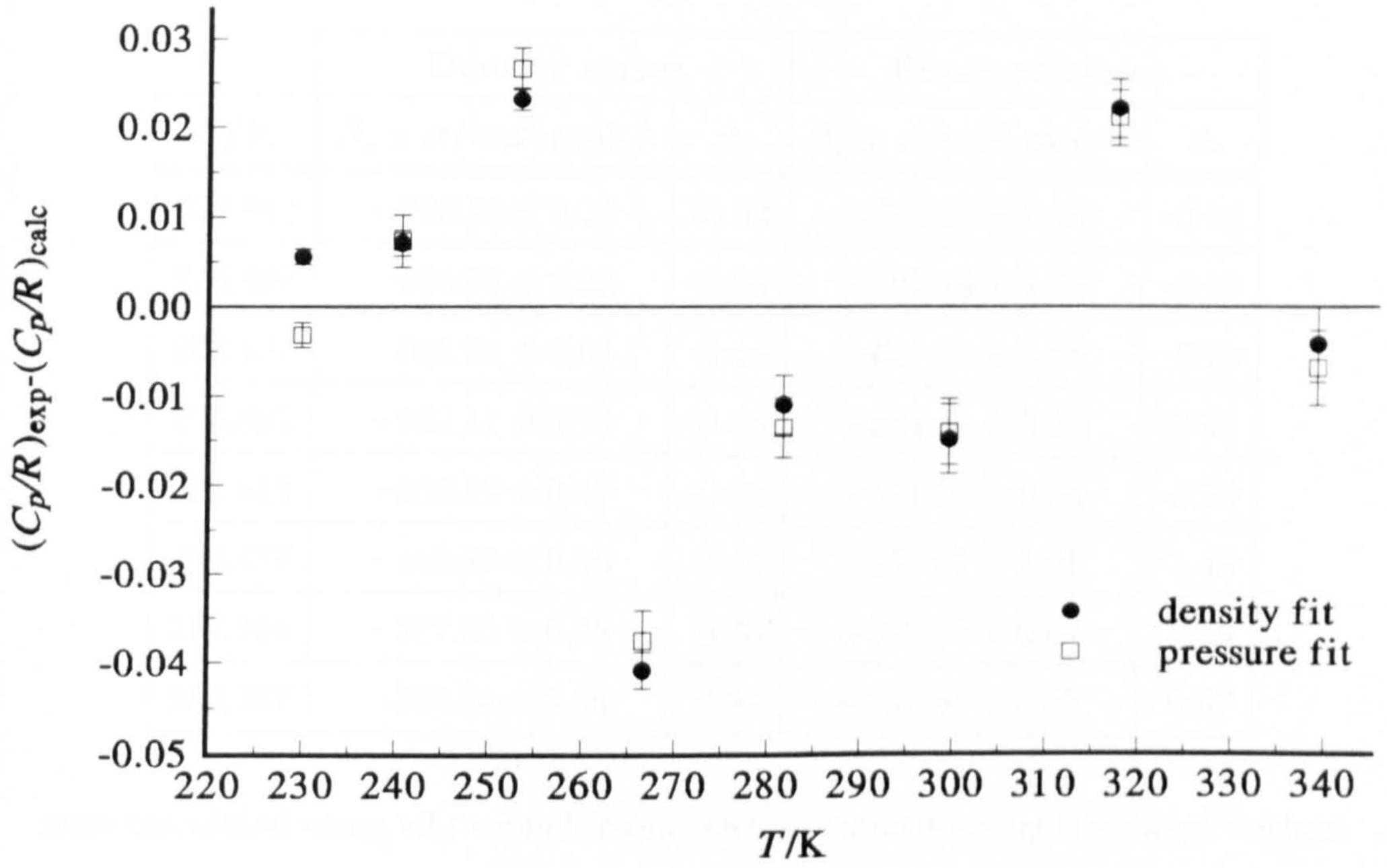

Figure 8.22: Comparison of the perfect gas heat capacities C_p^{pg} of SF_6 determined in this work with published values.

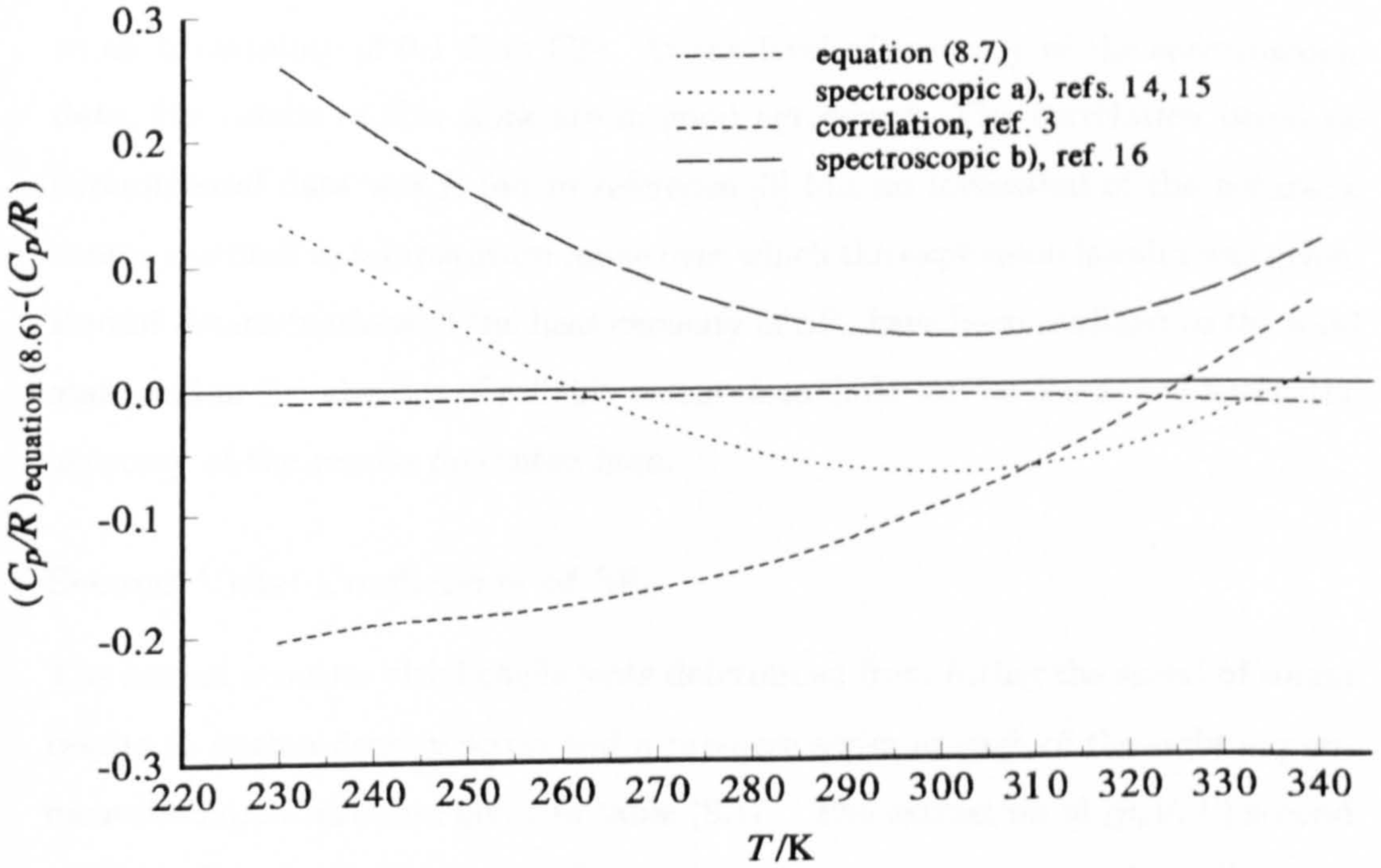

Table 8.17: Values of the second acoustic virial coefficient β_a from the density and pressure series, estimated standard deviations σ, and deviations Δ from the square well potential for SF_6.

	Density series		**Pressure series**	
T/K	$\beta_a \pm \sigma$/cm^3·mol^{-1}	**Δ**	$\beta_a \pm \sigma$/cm^3·mol^{-1}	**Δ**
229.840	-763.92 ± 0.11	-0.02	-763.03 ± 0.48	-0.98
240.449	-696.76 ± 0.22	0.03	-698.49 ± 1.18	-0.59
253.157	-626.61 ± 0.61	0.44	-627.25 ± 0.66	3.26
266.625	-562.11 ± 0.26	0.36	-564.84 ± 0.48	2.43
281.613	-502.29 ± 0.47	-0.32	-511.26 ± 0.54	-3.99
299.477	-443.87 ± 0.56	-3.45	-450.07 ± 1.01	-4.49
317.346	-387.86 ± 0.45	0.75	-392.50 ± 0.44	0.49
338.987	-334.34 ± 0.56	0.94	-337.54 ± 0.55	0.67

were calculated using vibrational frequencies recommended by Herzberg[16] where the lowest wavenumber band is assigned as 361 cm^{-1}, 17 wavenumbers higher than the other authors. This band is both Raman and infra-red inactive and is assigned using combination bands. As it is the lowest wavenumber band and is also triply degenerate it has the largest contribution to the heat capacity leading to an uncertainty of 0.1 R in C_p^{pg}. At the level of accuracy of the spectroscopic data, the results of this work are in good agreement. The correlation based on experimental data was found in reference [3] but no indication of the accuracy, source material or temperature range over which the expression is valid was given. Recent determinations of the heat capacity of SF_6 have been confined to the solid state and in the absence of reliable recent data little can be concluded about the accuracy of the results presented here.

Second Virial Coefficients of SF_6

The second acoustic virial coefficients determined from fitting the speed of sound results to both a density series and a pressure series at each of the eight experimental temperatures are given in table (8.17). The extraction of (p, V, T) second virial coefficients was by means of regression analysis using the square-well poten-

Figure 8.23: Deviations Δ of the second acoustic virial coefficients β_{a} of SF_6 determined from the density and pressure series from equations (8.9) and (8.10) with equation (1.15).

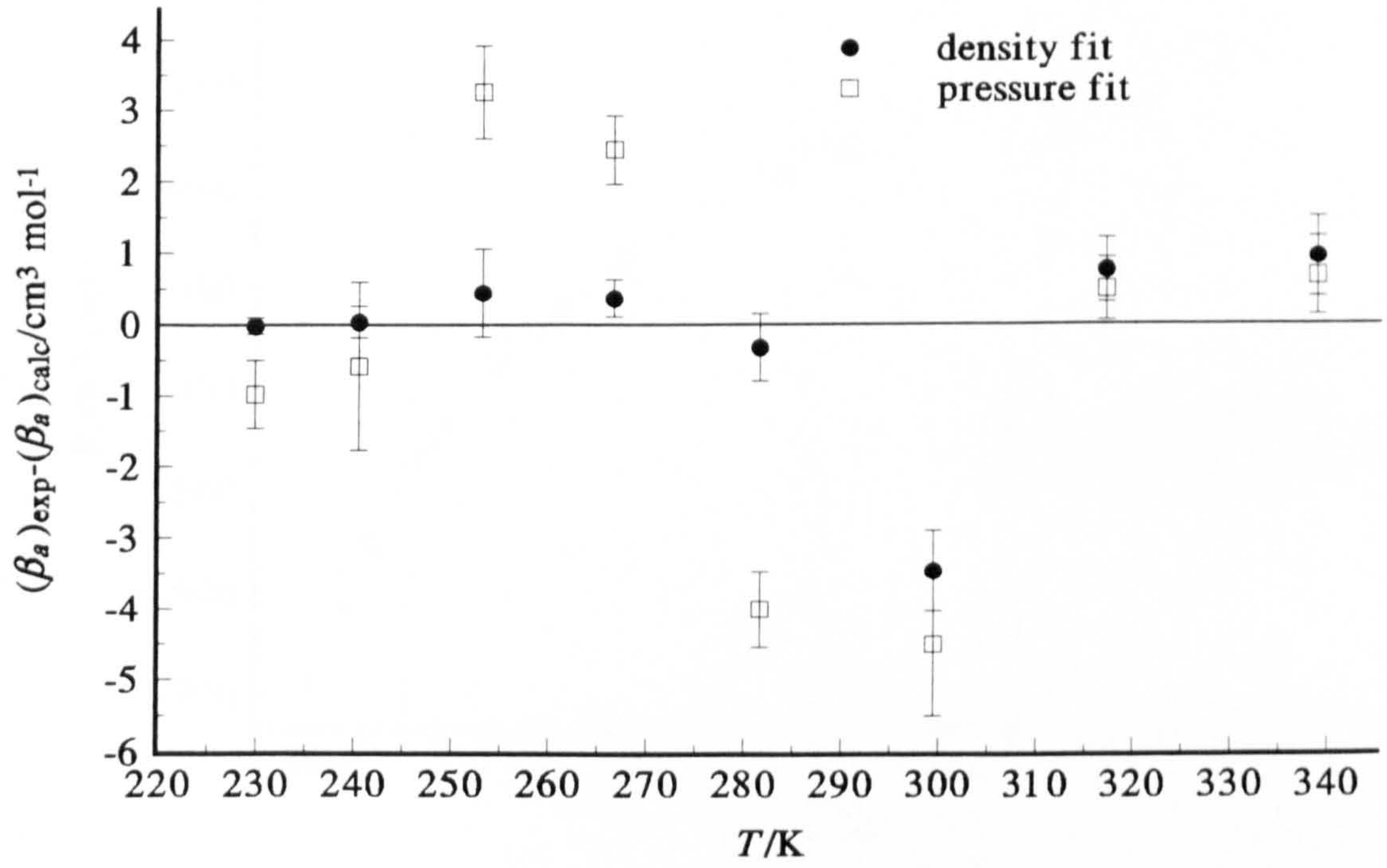

tial and equation (1.15). The experimental determinations of C_p^{pg} were used in conjunction with the acoustic second virial coefficients β_{a}. Weighted non-linear analysis of the experimental β_{a} with γ^{pg} and the square-well function yielded

$$B/\mathrm{cm}^3 \cdot \mathrm{mol}^{-1} = 298 - 194.9 \exp\left(320\ \mathrm{K}/T\right) \tag{8.9}$$

which fit the results from the density series with a weighted standard deviation of 0.7 $\mathrm{cm}^3 \cdot \mathrm{mol}^{-1}$, and

$$B/\mathrm{cm}^3 \cdot \mathrm{mol}^{-1} = 447 - 312 \exp\left(250\ \mathrm{K}/T\right) \tag{8.10}$$

which fit the results from the pressure series with a weighted standard deviation of 3.0 $\mathrm{cm}^3 \cdot \mathrm{mol}^{-1}$. In figure (8.23) the experimental β_{a} are shown as deviations $\Delta = (\beta_{\mathrm{a}})_{\mathrm{exp}} - (\beta_{\mathrm{a}})_{\mathrm{calc}}$ from equations (8.9) and (8.10) with equation (1.15). These deviations Δ are also given in table (8.17). With the exclusion of the datum at 299 K, the experimental values are fit to within a few multiples of their standard deviations and exclusion of this point altered the values of B by much less than their standard deviation and leads to a misleading estimate of the accuracy of the

Figure 8.24: Comparison of the second virial coefficients B of SF_6 determined from the density and pressure series and those recommended in reference [17].

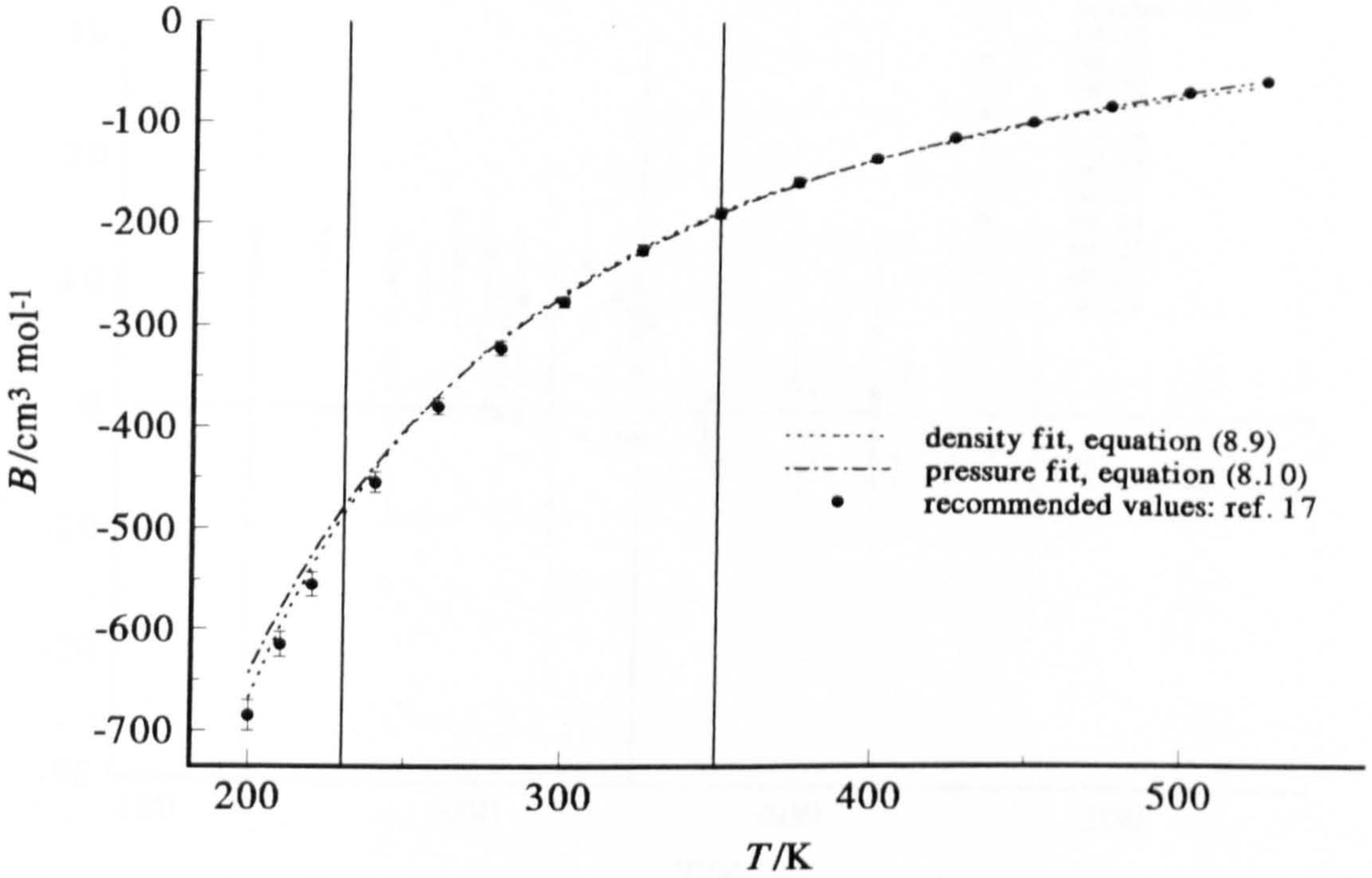

results. The results from the pressure series can be seen to have larger standard deviations and in general show more scatter from the fit which has a correspondingly higher standard deviation. These observations are due to the use of either two or three term fits of the speed of sound results which have differing systematic errors. In comparison the density fits only supported two terms leading to the inclusion of similar systematic errors in each case giving a more consistent data set. For the β_a results from the density series it was easy to judge the exponential term that best represented the data whereas for the noisy β_a results from the pressure series the difference was minimal for many different exponents. Due these factors, for the remaining two systems only the density fits of the speed of sound have been employed leading to consistent data which may be analysed easily. It must be remembered however that this does lead to similar systematic errors in all the resulting values of β_a due to truncation of the series.

Figure (8.24) shows the variation of the (p, V, T) second virial coefficient B with temperature. The agreement between the solutions for the density and pressure series is excellent over the experimental temperature range of 230 to 340 K and at every temperature in this range the results agree with those recommended

Figure 8.25: Deviations ΔB of the second virial coefficients B of SF_6 from equation (8.9).

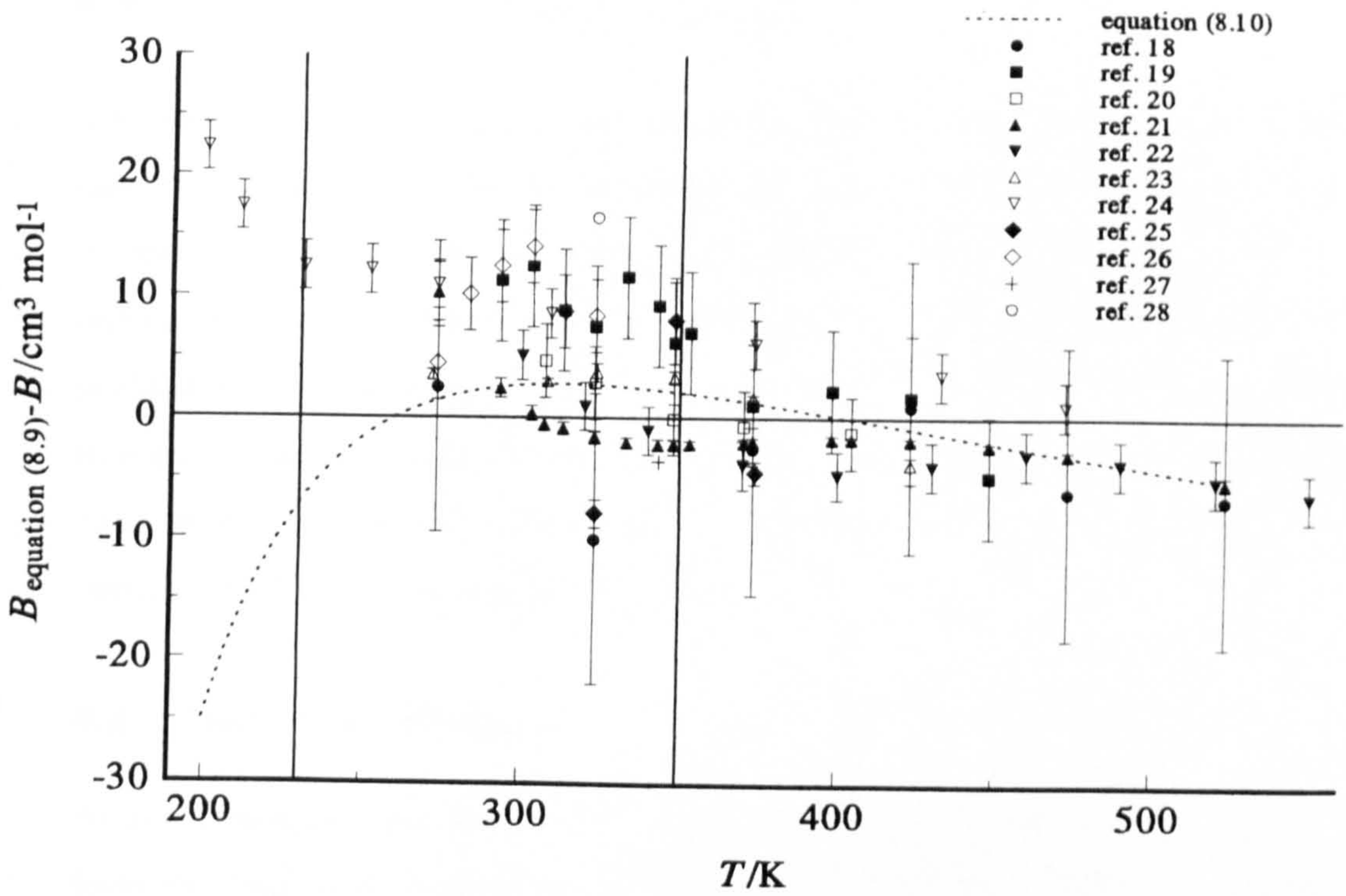

in reference [17] to within their estimated error. Below 230 K the results from the density series agree well with the recommended values but the results from the pressure series can be seen to deviate by up to 40 $cm^3 \cdot mol^{-1}$. At temperatures above 340 K both equations show excellent agreement with the recommended values to well above the experimental temperature range. Figure (8.25) shows all the available literature data[18]-[28] as deviations $\Delta B = B_{\text{equation (8.9)}} - B$ from equation (8.9) and it is immediately apparent that the agreement with other workers is excellent even well outside the experimental temperature range. In general the results agree with those determined using classical (p, V, T) methods to within a few multiples of the estimated errors. In particular the precise measurements of Rosenthal *et al.*[21] differ from (8.9) by less than 5 $cm^3 \cdot mol^{-1}$ in the range 270 to 470 K. At temperatures below 250 K where there is only one published set of results equation (8.9) is likely to give the most accurate predictions of B as classical methods suffer from systematic errors due to adsorption at low reduced temperatures. This work again illustrates the precision with which virial coefficients may be estimated using acoustic techniques, and in particular the accuracy that may be achieved for gases such as SF_6 in which there is severe dispersion,

which is minimised using an annular resonator.

8.3. $\{(1-x)\,CH_4 + xC_2H_6\}\,; x = 0.15$

The methane-ethane mixture was studied at eight at temperatures between 230 and 340 K. The experimentally determined frequencies were corrected as outlined in chapter 2. The transport properties and virial coefficients required in the various correction terms were determined using the iterative procedure discussed in chapter 7. As no literature data were available, a third iteration was performed to reach a stable solution for all the variables. In the analysis of the half-width data for the mixture, the Stiel-Thodos expression was again used to relate the thermal conductivity and shear viscosity.

8.3.1. Half-width Fitting

At every temperature the $(0,2,1)$, $(0,3,1)$ and $(0,4,1)$ modes were discarded from the half-width analysis as they showed consistent discrepancies from the remaining four modes of greater than 20 ppm. The lowest pressure point was also removed at each temperature due to the very large half-widths compromising the accuracy of the results. The fractional excess halfwidths $\Delta g/f$ for a typical isotherm at 253 K are shown in figure (8.26). The small symbols represent data rejected from the analysis; the $(0,3,1)$ mode was rejected as the fractional excess half-width increases to a value of 50 ppm, and the $(0,4,1)$ mode was removed as the fractional excess half-width was consistently high by about 45 ppm for the whole isotherm. The $(0,2,1)$ mode was also discarded from the half-width analysis and the fractional excess half-widths $\Delta g/f$ for this mode as well as its fractional deviations from the mean speed of sound $\langle u/b \rangle$ calculated from the selected modes are plotted in figure (8.27). The behaviour of the $(0,2,1)$ mode in the mixture is similar to that in propene and SF_6. The fractional excess half-width is again high at low pressures going through a maximum then subsequently decreasing. The value at the highest pressure does not follow this trend and appears to be in error. The fractional deviation in u is again around -200 ppm at pressures below 70 kPa and again becomes large and positive at higher pressures. A maxima is not seen in this plot but the pressure at which it occurs may have been missed,

Figure 8.26: Fractional excess half-widths $\Delta g/f$ for the isotherm at 253 K in the mixture.

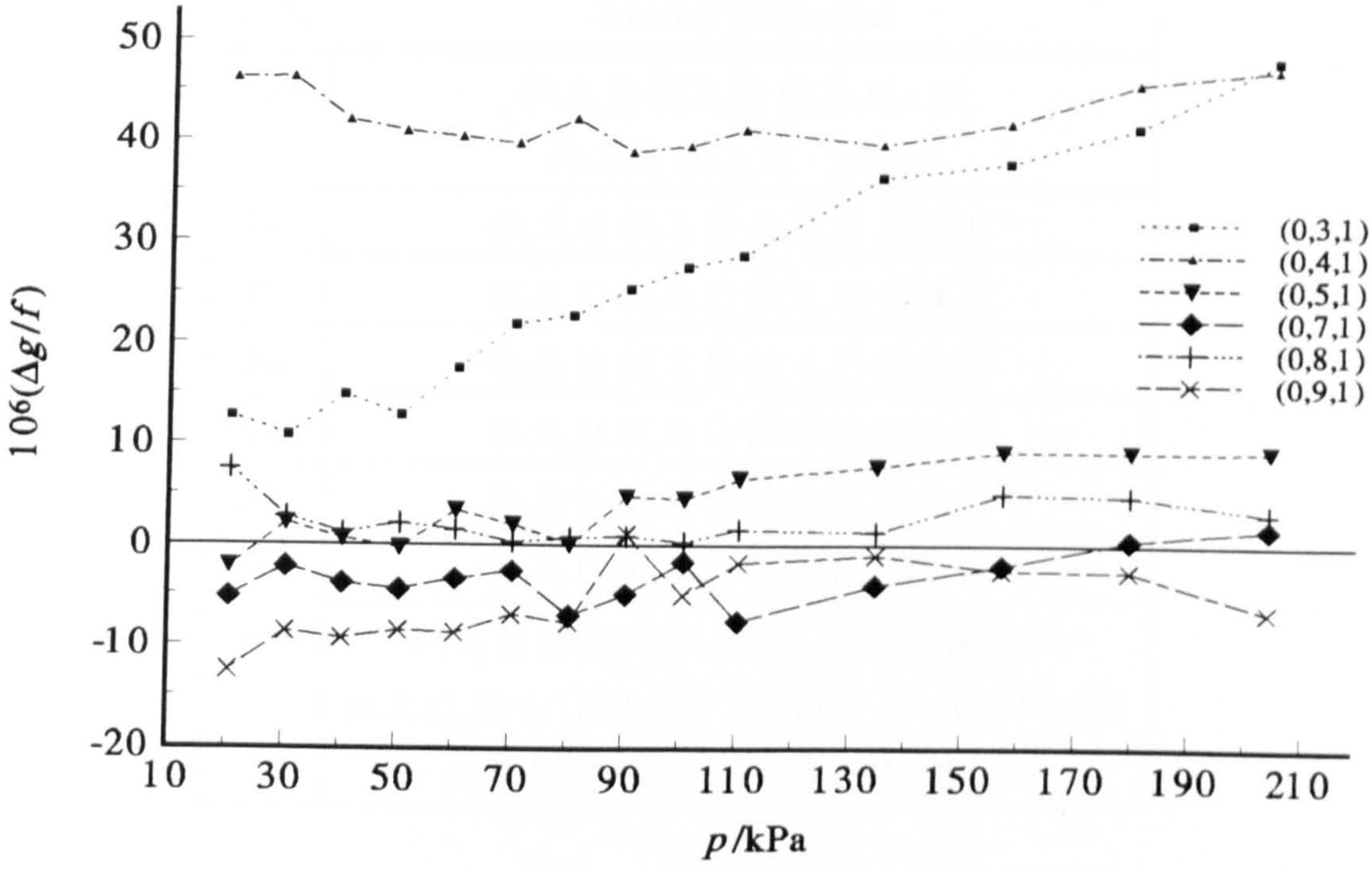

Figure 8.27: Fractional deviations of the calculated values of u/b for the $(0, 2, 1)$ mode from the average value $\langle u/b \rangle$ and fractional excess half-widths $\Delta g/f$ for the $(0, 2, 1)$ mode for the isotherm at 253 K in the mixture.

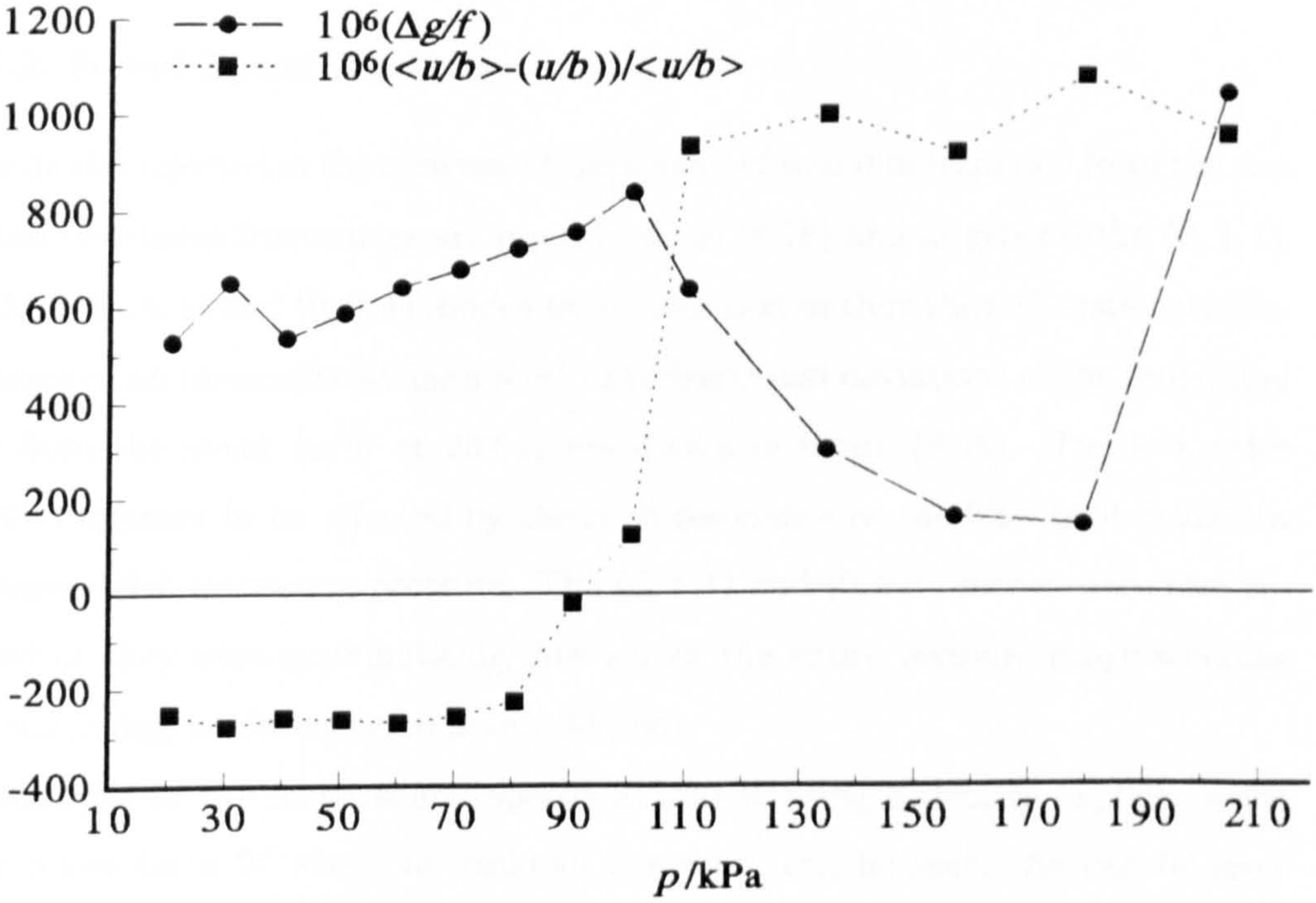

Table 8.18: Resonance modes rejected at each experimental temperature in the sound speed analysis for the mixture.

T/K	**Modes Rejected**
230	$(0,2,1)$ $(0,3,1)$ $(0,9,1)$: p1 $(0,2,1)$ $(0,3,1)$: p2-p15
241	$(0,2,1)$ $(0,3,1)$ $(0,4,1)$ $(0,9,1)$
253	$(0,2,1)$ $(0,3,1)$ $(0,4,1)$ $(0,9,1)$
267	$(0,2,1)$ $(0,3,1)$ $(0,4,1)$ $(0,9,1)$
282	$(0,2,1)$ $(0,3,1)$ $(0,4,1)$ $(0,9,1)$
299	$(0,2,1)$ $(0,3,1)$ $(0,4,1)$ $(0,9,1)$
317	$(0,2,1)$ $(0,3,1)$ $(0,4,1)$ $(0,9,1)$
339	$(0,2,1)$ $(0,3,1)$ $(0,9,1)$: p1, p2, p8, p13 $(0,2,1)$ $(0,3,1)$ $(0,4,1)$ $(0,9,1)$: p3-p6, p14, p15 $(0,2,1)$ $(0,3,1)$ $(0,4,1)$: p7, p9-p12

and the deviations do not show a clear minimum at 50 kPa. Despite these small differences which are likely to be due to the choice of modes retained in the analysis, the similarities in the behaviour again indicate a geometric perturbation which severely affects the $(0,2,1)$ mode.

8.3.2. Sound Speed Analysis

The modes rejected in the analysis of the speeds of sound determined from the corrected resonance frequencies are given in table (8.18) and in general the $(0,2,1)$, $(0,3,1)$, $(0,4,1)$ and $(0,9,1)$ modes were discarded as they showed systematic deviations of an unacceptably high level. The fractional deviations of the individual u/b from the mean $\langle u/b \rangle$ at 253 K are shown in figure (8.28). The low order $(0,3,1)$ appears to be affected by the shell resonance as the fractional deviation increases with increasing pressure. The $(0,4,1)$ and $(0,9,1)$ modes were also rejected as they were systematically low across the entire pressure range whereas the remaining modes agree to about 20 ppm.

Analysis of the mean sound speeds at 230 K using a density explicit series gave a two term fit where no residual curvature can be seen. As can be seen

Figure 8.28: Fractional deviations of the calculated values of u/b from the average value $\langle u/b \rangle$ determined for the selected modes for the isotherm at 253 K in the mixture.

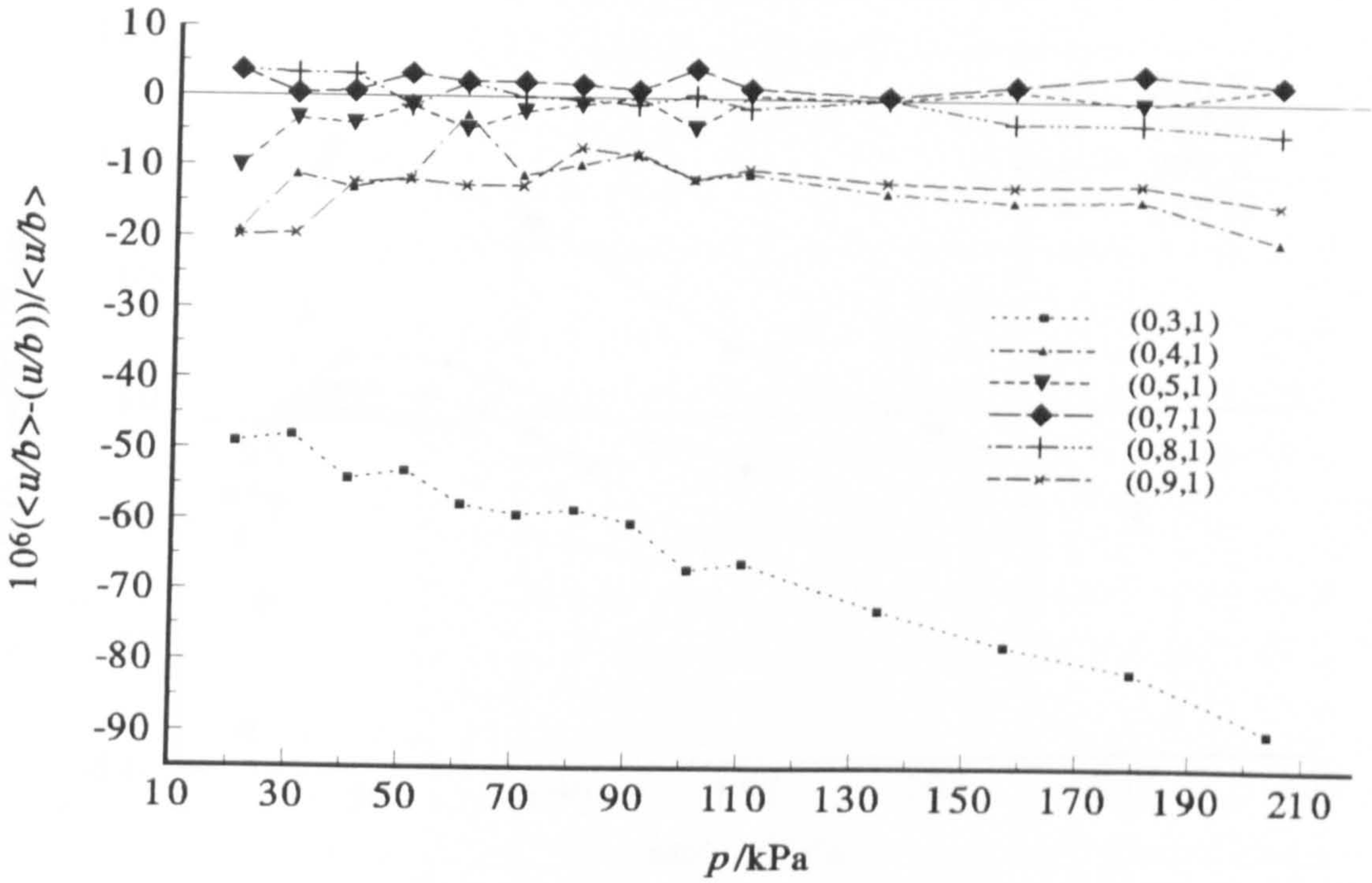

Figure 8.29: Fractional deviations of the average sound speeds $\langle u \rangle$ determined for the selected modes from the calculated values for the isotherm at 230 K in the mixture.

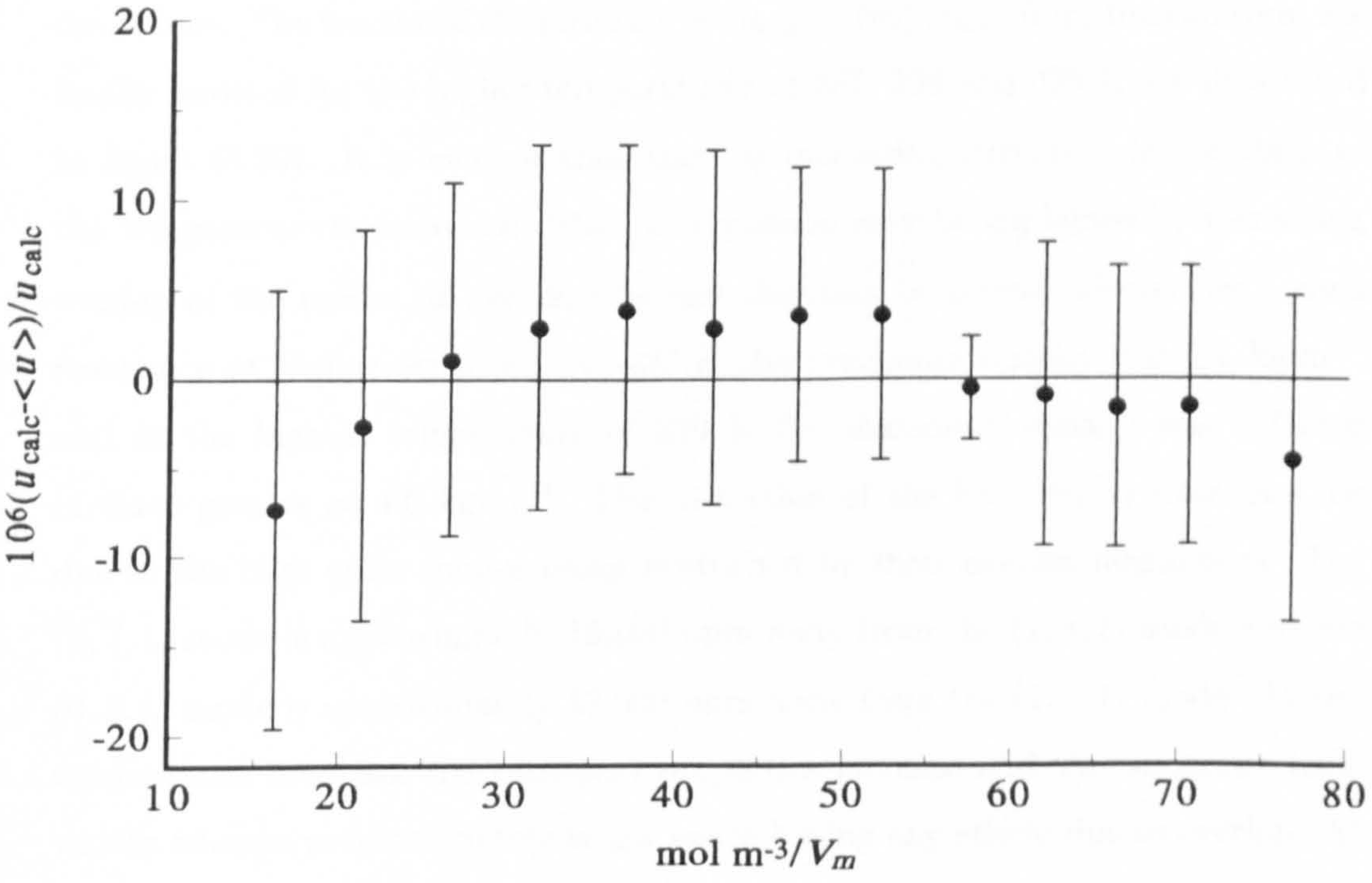

Figure 8.30: Fractional deviations of the average sound speeds $\langle u \rangle$ determined for the selected modes from the calculated values for the isotherms at 267 K, 299 K and 339 K in the mixture.

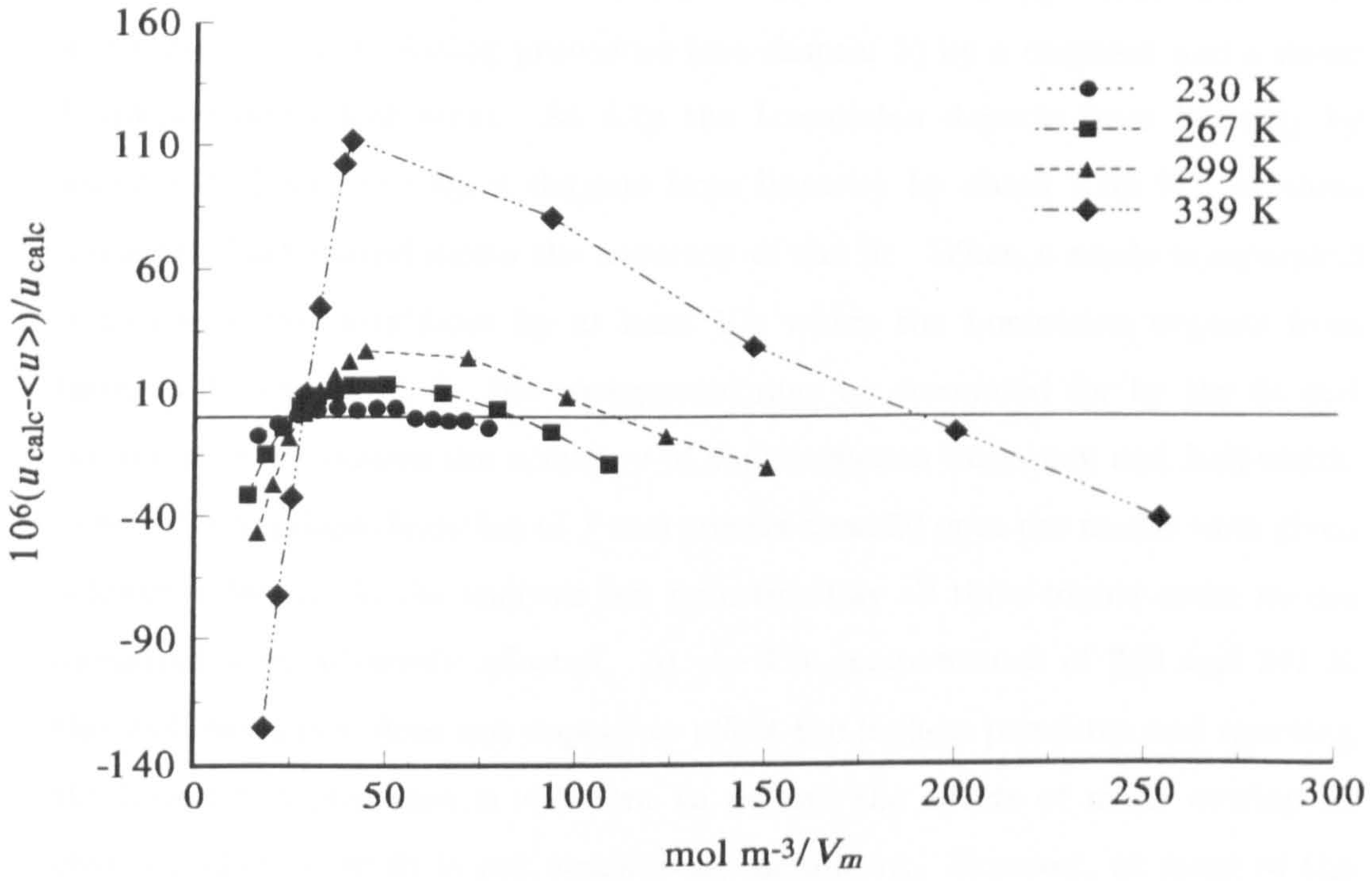

in figure (8.29) which shows the fractional deviations $\delta = (u_{\text{calc}} - \langle u \rangle)/u_{\text{calc}}$ of the mean speeds of sound $\langle u \rangle$ from the values u_{calc} calculated from the two term density series, all the data are easily accommodated to within their standard deviations. The fractional deviations $\delta = (u_{\text{calc}} - \langle u \rangle)/u_{\text{calc}}$ from the two term fits finally selected for the higher temperatures of 267, 299 and 339 K are illustrated in figure (8.30). It is evident that there is increasing curvature in the data as the temperature is increased. This phenomenon may be explained by increasing overlap of the modes at low density and the data becoming affected by a shell resonance at higher densities. At 230 K the maximum density was 1.4 kg·m^{-3} and at the highest temperature of 339 K the maximum density was a factor of three greater at 4.6 kg·m^{-3}. The distortion of the low density data may be due to the high order modes being perturbed by their nearest neighbours. The $(0, 7, 1)$ mode is approximately 15,000 ppm away from the $(1, 3, 1)$ mode and the $(0, 8, 1)$ mode is approximately 13,000 ppm away from the $(1, 5, 1)$ mode. As the temperature increases the transport properties increase and the resonance half-widths become proportionately larger exacerbating any effects due to overlap. At

the lowest pressure of about 10 kPa the $(0,8,1)$ mode is separated by $6.6g$ from the $(1,5,1)$ mode at 230 K and by only $4.7g$ at 339 K. At $4.7g$ the amplitude of the mode has decreased to 21 % of its maximum amplitude whereas by $6.6g$ it has decreased to 15 %. The contributions due to nearby modes modes are accounted for in the fitting procedure (see chapter 5) by a constant and a linear frequency dependent term. At $4.7g$ the Lorentzian departs from linearity by about 0.2 % and at $6.6g$ it departs from linearity by about 0.05 %. At these levels the background limits the accuracy of the fit. When a mode is separated from its nearest neighbour by at least $10g$ where the Lorentzian departs from linearity by only 0.01 %, the background may be accounted for by the fit and no longer compromises the accuracy of the resonance frequency and half-width. When the standard deviation of f was greater than 20 ppm the modes were given a lower weighting in the analysis but unfortunately all three higher order modes measured were adversely affected. At the low temperatures of 230 and 241 K the shell resonance does not appear to affect the highest pressures and rejecting the lowest two pressures is sufficient to remove the effects of mode overlap so that a higher order fit is not statistically significant. However, at some of the intermediate temperatures such as 267 K and 299 K shown in figure (8.30) the curvature may be fitted by an additional third term resulting in a statistically significant reduction in the standard deviation of the fit. The higher order fit was rejected as the curvature of the data should be approximately constant over the whole of the experimental temperature range because the fractional change in the sound speed is about the same. At the highest temperatures of 317 and 339 K the combined effects can no longer be accommodated by an extra term in the series as the change in slope of the data is so severe. In addition, the second acoustic virial coefficients β_a from the higher order fits when significant could not be fitted to the square well potential to within a few standard deviations whereas the set of results from the two term fits are internally consistent. The values from the three term fits are systematically less negative and differ by more than the truncation in the series would predict. It was not possible to eliminate the effects due to the shell resonance and mode overlap as they affected too much of the data at the higher temperatures but the low pressure points severely in error were removed. At 230 K the lowest two pressures were removed and by 339 K the lowest four

Table 8.19: Mean values of u with standard deviations σ and deviations δ from the density series at 230 K for the mixture.

T/K	p/kPa	$\langle u \rangle$/m·s^{-1}	$10^6\sigma(u)/u$	$10^6\delta(u)/u$
229.890	145.531	368.6545	9.2	-4.5
	133.933	368.7889	7.8	-1.5
	125.789	368.8825	7.9	-1.6
	117.751	368.9750	8.5	-0.9
	109.297	369.0720	2.9	-0.5
	99.223	369.1888	8.1	3.6
	89.827	369.2962	8.2	3.6
	80.160	369.4063	9.9	2.9
	70.287	369.5192	9.2	3.9
	60.537	369.6299	10.2	2.9
	50.646	369.7417	9.9	1.1
	40.719	369.8530	11.0	-2.6
	30.904	369.9626	12.3	-7.3
	20.942	370.0714	14.3	(a)
	10.988	370.1655	15.0	(a)

pressures were discarded. These effects are likely to compromise the accuracy of the high temperature data but up to 299 K they were less than 50 ppm of the average sound speed and even at 339 K were of the order of 100 ppm which is only five times the expected level of agreement. Tables (8.19) to (8.26) list the mean speeds of sound $\langle u \rangle$, the standard deviations of the mean σ and the deviations $\delta = u_{\mathrm{calc}} - \langle u \rangle$ of mean from the finally adopted two term smoothing equations. In tables (8.19) to (8.26) (a) indicates a state point removed from the analysis.

8.3.3. Transport Properties

Analysis of the half-widths yielded estimates of the vibrational relaxation time as $\tau\rho$, the shear viscosity η and its initial density dependence $(\partial\eta/\partial\rho)$, as well as the thermal conductivity κ and its initial density dependence $(\partial\kappa/\partial\rho)$.

Table 8.20: Mean values of u with standard deviations σ and deviations δ from the density series at 241 K for the mixture.

T/K	p/kPa	$\langle u \rangle$/m·s^{-1}	$10^6\sigma(u)/u$	$10^6\delta(u)/u$
240.956	172.389	376.9979	4.0	-9.4
	156.701	377.1544	3.9	-5.9
	142.184	377.2991	3.5	-2.0
	127.239	377.4479	3.5	2.2
	109.236	377.6268	2.6	7.2
	99.513	377.7221	2.0	7.1
	89.527	377.8200	1.3	7.0
	79.616	377.9171	4.0	7.1
	69.944	378.0110	2.9	5.3
	59.994	378.1079	2.5	4.3
	50.079	378.2026	3.7	-0.9
	40.180	378.2968	3.6	-6.9
	30.219	378.3907	5.5	-15.2
	20.279	378.4793	8.7	(a)
	10.335	378.5560	28.9	(a)

Table 8.21: Mean values of u with standard deviations σ and deviations δ from the density series at 253 K for the mixture.

T/K	p/kPa	$\langle u \rangle$/m·s^{-1}	$10^6\sigma(u)/u$	$10^6\delta(u)/u$
253.155	203.901	385.8902	4.0	-3.6
	179.372	386.1002	3.7	-1.2
	156.927	386.2910	3.0	-1.4
	134.538	386.4811	0.2	-0.7
	110.217	386.6888	1.3	4.0
	100.512	386.7703	4.2	2.8
	90.394	386.8562	1.2	4.1
	80.422	386.9405	1.6	4.7
	70.380	387.0238	2.1	1.6
	60.363	387.1078	3.9	0.7
	50.423	387.1915	2.7	1.1
	40.417	387.2733	3.7	-4.7
	30.458	387.3557	3.2	-7.4
	20.485	387.4333	8.6	(a)
	10.337	387.5074	16.0	(a)

Table 8.22: Mean values of u with standard deviations σ and deviations δ from the density series at 267 K for the mixture.

T/K	p/kPa	$\langle u \rangle$/m·s^{-1}	$10^6\sigma(u)/u$	$10^6\delta(u)/u$
266.647	238.265	395.3631	2.9	-19.2
	205.201	395.5984	2.5	-6.1
	174.161	395.8176	1.6	3.2
	142.607	396.0386	0.7	9.7
	109.959	396.2654	0.8	13.2
	99.986	396.3340	1.2	13.0
	90.103	396.4021	2.7	12.9
	80.063	396.4702	3.2	10.7
	70.064	396.5382	2.5	8.7
	60.098	396.6050	2.9	4.6
	50.116	396.6700	3.9	-4.3
	40.106	396.7344	3.1	-14.9
	30.117	396.7963	5.9	-31.3
	20.121	396.8527	9.1	(a)
	10.120	396.8832	27.7	(a)

Table 8.23: Mean values of u with standard deviations σ and deviations δ from the density series at 282 K for the mixture.

T/K	p/kPa	$\langle u \rangle$/m·s^{-1}	$10^6\sigma(u)/u$	$10^6\delta(u)/u$
281.693	318.874	405.2693	9.0	-2.9
	266.344	405.5828	6.9	-3.8
	215.173	405.8884	5.3	-1.4
	163.230	406.4147	3.2	(a)
	110.471	406.5119	0.8	7.5
	100.499	406.5709	0.4	7.8
	90.462	406.6297	2.0	7.1
	80.181	406.6903	2.3	7.1
	70.432	406.7460	1.8	3.1
	60.468	406.8041	3.3	2.0
	50.537	406.8612	0.9	-1.2
	40.520	406.9169	0.2	-8.8
	30.523	406.9724	5.8	-16.5
	20.546	407.0229	12.1	(a)
	10.588	407.0608	44.4	(a)

Table 8.24: Mean values of u with standard deviations σ and deviations δ from the density series at 299 K for the mixture.

T/K	p/kPa	$\langle u \rangle$/m·s^{-1}	$10^6\sigma(u)/u$	$10^6\delta(u)/u$
298.517	369.462	416.1750	7.8	-20.7
	303.813	416.4916	6.4	-8.0
	239.702	416.8011	4.9	7.9
	176.209	417.1066	3.2	23.9
	109.646	417.4199	2.0	26.7
	99.353	417.4664	1.4	22.6
	89.865	417.5084	0.5	16.9
	79.977	417.5521	1.8	10.9
	69.974	417.5949	3.1	1.6
	60.087	417.6370	2.2	-8.1
	50.043	417.6759	4.3	-27.2
	40.111	417.7142	2.5	-46.5
	30.124	417.7518	5.6	(a)
	20.175	417.7786	13.6	(a)
	10.186	417.7867	31.2	(a)

Table 8.25: Mean values of u with standard deviations σ and deviations δ from the density series at 317 K for the mixture.

T/K	p/kPa	$\langle u \rangle$/m·s^{-1}	$10^6\sigma(u)/u$	$10^6\delta(u)/u$
317.454	498.102	427.6123	13.0	-46.5
	403.920	427.9686	10.0	-12.3
	306.040	428.3384	6.9	25.8
	208.466	428.7040	4.0	60.5
	107.912	429.0654	0.4	64.0
	98.640	429.0925	0.9	50.2
	88.906	429.1208	0.9	35.1
	79.244	429.1493	1.7	21.2
	69.442	429.1751	2.9	-0.1
	59.674	429.1998	2.9	-23.6
	49.766	429.2159	8.9	-68.3
	39.911	429.2348	6.7	-106.1
	30.026	429.2484	9.8	(a)
	20.279	429.2458	14.9	(a)
	10.580	429.1998	34.1	(a)

Table 8.26: Mean values of u with standard deviations σ and deviations δ from the density series at 339 K for the mixture.

T/K	p/kPa	$\langle u \rangle$/m·s^{-1}	$10^6\sigma(u)/u$	$10^6\delta(u)/u$
338.994	707.654	439.9889	18.3	-41.3
	558.765	440.4013	15.1	-6.3
	409.958	440.8113	8.9	28.4
	260.841	441.2275	2.8	80.2
	110.630	441.6356	1.0	111.6
	110.644	441.6315	3.2	102.3
	90.623	441.6583	2.5	44.5
	80.612	441.6691	8.0	9.5
	70.628	441.6766	3.2	-32.5
	60.645	441.6851	2.2	-72.3
	50.647	441.6878	2.2	-125.3
	40.654	441.6683	8.0	(a)
	30.660	441.6531	12.7	(a)
	20.679	441.6100	15.7	(a)
	10.689	441.5137	41.3	(a)

Table 8.27: Values of the vibrational relaxation time $\tau\rho$ at a density of 1 kg·m^3, its standard deviation σ and deviation δ from the smoothing equation at each experimental temperature in the mixture.

T/K	$\tau\rho \pm \sigma$/ns·kg·m^{-3}	δ/ns·kg·m^{-3}
229.890	18.7 ± 7.6	2.6
240.956	23.5 ± 5.0	1.5
253.155	22.6 ± 3.3	-3.9
266.647	30.9 ± 3.0	1.3
281.693	33.7 ± 2.5	2.3
298.517	30.5 ± 1.8	-1.1
317.454	30.2 ± 2.1	0.1
338.994	26.4 ± 3.4	0.3

Vibrational Relaxation Time

Table (8.27) gives the experimentally determined values of the vibrational relaxation time at a density of 1 kg $\cdot$ m^{-3} their standard deviations σ and deviations $\delta = (\tau\rho)_{\text{exp}} - (\tau\rho)_{\text{calc}}$ from the smoothing equation

$$\tau\rho/\mu\text{s} \cdot \text{kg} \cdot \text{m}^{-3} = 0.0630 - 0.214 \times 10^{-11} T^4 - \frac{0.114 \times 10^9}{T^4} \qquad (8.11)$$

which fit the results over the experimental temperature range with a standard deviation of 0.0025 μs $\cdot$ kg $\cdot$ m^{-3}. Figure (8.31) shows that all the results may be fitted to within one standard deviation and that the vibrational relaxation time for the mixture has a maximum at about 290 K. The results of Boyes[1] are also plotted in figure (8.31) and the results at 250, 275 and 300 K agree with this work to within their combined standard deviations. The result of Boyes at 350 K appears to be in error and in general the data from reference [1] shows less curvature than the results from this work. The overall level of agreement is very encouraging considering that the pressure ranges used, the resonator geometry and the method of extracting the vibrational relaxation time were all different.

Comparing the values of $\tau\rho$ determined for the mixture with those determined for pure methane[1],[4], it is evident that ethane is an efficient catalyst for the equilibration of translational energy throughout all the available degrees of freedom.

Figure 8.31: Comparison of the vibrational relaxation times $\tau\rho$ of the mixture at a density of 1 kg·m^3 determined in this work with published values.

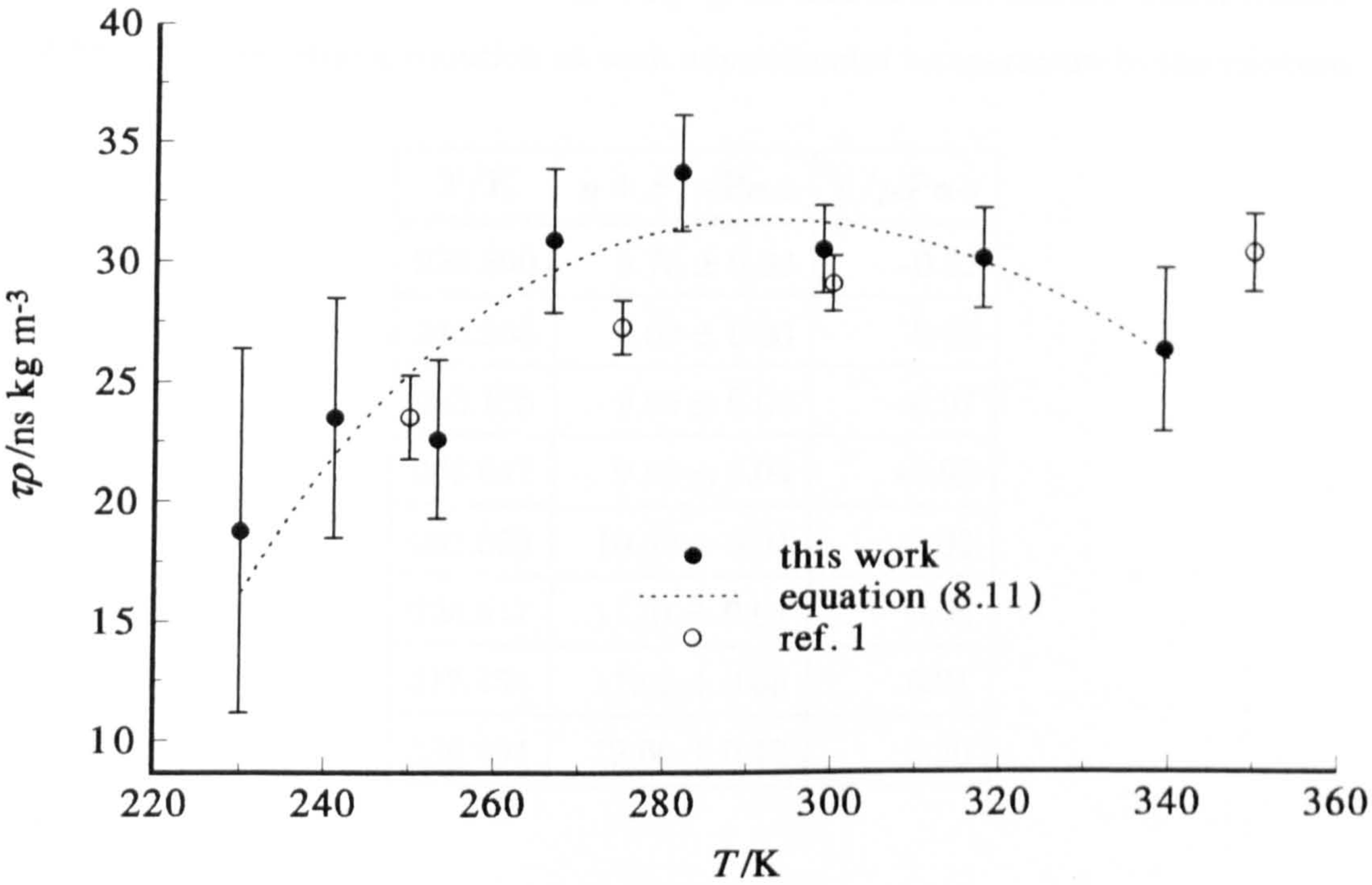

The time constant for the process is decreased by a factor of 30 at 350 K and by a factor of 100 at 250 K.

Shear Viscosity and Thermal Conductivity

The shear viscosity and thermal conductivity data extracted from the half-width fitting and used to correct the observed resonance frequencies for the thermal and viscous boundary layers are given in tables (8.28), (8.29), (8.30) and (8.31). The results, their standard deviations σ and deviations $\delta(x) = x_{\text{exp}} - x_{\text{calc}}$ from the smoothing equations given below are quoted. In every case the smoothing equations (8.12) to (8.15) determined using the adaptive regression algorithm fitted all the experimental data to within two standard deviations. The shear viscosity η may be represented over the experimental temperature range by

$$\eta/\mu\text{Pa}\cdot\text{s} = 0.0363T + \frac{0.12\times10^{10}}{T^4}, \tag{8.12}$$

with a standard deviation of 0.09 μPa · s. The density dependence of the viscosity $(\partial\eta/\partial\rho)$ was found to be constant over the experimental temperature range and

Table 8.28: Values of the shear viscosity η, its standard deviation σ and deviation δ from the smoothing equation at each experimental temperature in the mixture.

T/K	$\eta \pm \sigma/\mu$Pa·s	δ/μPa·s
229.890	8.75 ± 0.06	-0.02
240.956	9.09 ± 0.05	0.00
253.155	9.55 ± 0.04	0.07
266.647	9.89 ± 0.04	-0.02
281.693	10.33 ± 0.04	-0.09
298.517	11.01 ± 0.04	0.02
317.454	11.63 ± 0.05	-0.01
338.994	12.60 ± 0.10	0.20

Table 8.29: Values of the initial density dependence of the shear viscosity $(\partial\eta/\partial\rho)$, its standard deviation σ and deviation δ from the smoothing equation at each experimental temperature in the mixture.

T/K	$(\partial\eta/\partial\rho) \pm\sigma/\mu$Pa·s·m^3·kg^{-1}	δ/μPa·s·m^3·kg^{-1}
229.890	0.94 ± 0.09	0.08
240.956	0.89 ± 0.07	0.02
253.155	0.82 ± 0.05	-0.05
266.647	0.88 ± 0.06	0.01
281.693	0.90 ± 0.05	0.04
298.517	0.82 ± 0.05	-0.05
317.454	0.89 ± 0.06	0.03
338.994	0.90 ± 0.11	0.03

Table 8.30: Values of the thermal conductivity κ, its standard deviation σ and deviation δ from the smoothing equation at each experimental temperature in the mixture.

T/K	$\kappa \pm \sigma$/mW·m^{-1}·K^{-1}	δ/mW·m^{-1}·K^{-1}
229.880	23.40 ± 0.18	-0.11
240.956	24.48 ± 0.14	0.09
253.155	26.00 ± 0.11	0.21
266.647	27.16 ± 0.12	-0.06
281.693	28.77 ± 0.12	-0.20
298.517	31.20 ± 0.11	0.13
317.454	33.68 ± 0.15	-0.10
338.994	37.44 ± 0.31	0.09

the weighted mean value is

$$(\partial\eta/\partial\rho)\,/\mu\mathrm{Pa}\cdot\mathrm{s}\cdot\mathrm{m}^3\cdot\mathrm{kg}^{-1} = 0.87, \tag{8.13}$$

which has a standard deviation of 0.04 μPa·s·m^3·kg^{-1}. The thermal conductivity and its initial density dependence were also fitted to smoothing equations using the adaptive regression routine. For the thermal conductivity, κ this gave

$$\kappa/\mathrm{mW}\cdot\mathrm{m}^{-1}\cdot\mathrm{K}^{-1} = 0.01203T - 0.875\times10^{-6}T^3 + 0.232\times10^{-8}T^4, \tag{8.14}$$

with a standard deviation of 0.16 mW·m^{-1}·K^{-1}. The density dependence of the thermal conductivity $(\partial\kappa/\partial\rho)$ was again found to be constant over the experimental temperature range and the weighted mean value is

$$(\partial\kappa/\partial\rho)\,/\mathrm{mW}\cdot\mathrm{m}^2\cdot\mathrm{K}^{-1}\cdot\mathrm{kg}^{-1} = 2.41, \tag{8.15}$$

which has a standard deviation of 0.15 mW·m^2·K^{-1}·kg^{-1}.

Because no literature results for the shear viscosity of the mixture at this composition exist, estimates for the mixture were made using the method of Wilke[29] and values for the pure components. The estimation method of Wilke is a simplification of the kinetic theory approach for gaseous mixtures in which second order effects are neglected. It is applicable to mixtures of non-polar polyatomic

Table 8.31: Values of the initial density dependence of the thermal conductivity $(\partial\kappa/\partial\rho)$, its standard deviation σ and deviation δ from the smoothing equation at each experimental temperature in the mixture.

T/K	$(\partial\kappa/\partial\rho) \pm\sigma$/mW·m^2·K^{-1}·kg^{-1}	δ/mW·m^2·K^{-1}·kg^{-1}
229.890	2.52 ± 0.25	0.11
240.956	2.40 ± 0.19	-0.01
253.155	2.23 ± 0.14	-0.18
266.647	2.41 ± 0.16	0.00
281.693	2.51 ± 0.14	0.10
298.517	2.31 ± 0.14	-0.10
317.454	2.58 ± 0.18	0.17
338.994	2.67 ± 0.33	0.26

gases in which the molecular weights of the components are similar. Wilke compared values with data on 17 binary mixtures and reported an average deviation of less than 1 %. For a binary mixture the expression for the shear viscosity of the mixture η_{mix} reduces to

$$\eta_{\text{mix}} = \frac{y_1\eta_1}{y_1 + y_2\phi_{12}} + \frac{y_1\eta_1}{y_1 + y_2\phi_{12}}, \tag{8.16}$$

in which η_1, η_2 are the pure component viscosities and y_1, y_2 are the mole fractions. The interaction parameters ϕ_{12} and ϕ_{21} for the gas mixture viscosity are given by

$$\phi_{12} = \frac{\left[1 + (\eta_1/\eta_2)^{\frac{1}{2}} (M_2/M_1)^{\frac{1}{4}}\right]^2}{\{8\,[1 + (M_1/M_2)]\}^{\frac{1}{2}}}, \tag{8.17}$$

and

$$\phi_{21} = \phi_{12}\frac{\eta_2}{\eta_1}\frac{M_1}{M_2}, \tag{8.18}$$

in which M_1, M_2 are the molar masses of the pure components. Values of the low pressure shear viscosity of methane were taken from reference [30] and fitted to a smoothing equation using the adaptive regression algorithm. Smoothed values for the limiting low pressure viscosity of ethane were taken from reference [31] and the mixture viscosities calculated from equations (8.16) to (8.18) are plotted in figure (8.32) together with the experimental results. The results of this work are seen

Figure 8.32: Comparison of the shear viscosity η of the mixture determined in this work with values determined using published results for the pure components and the estimation method of Wilke.

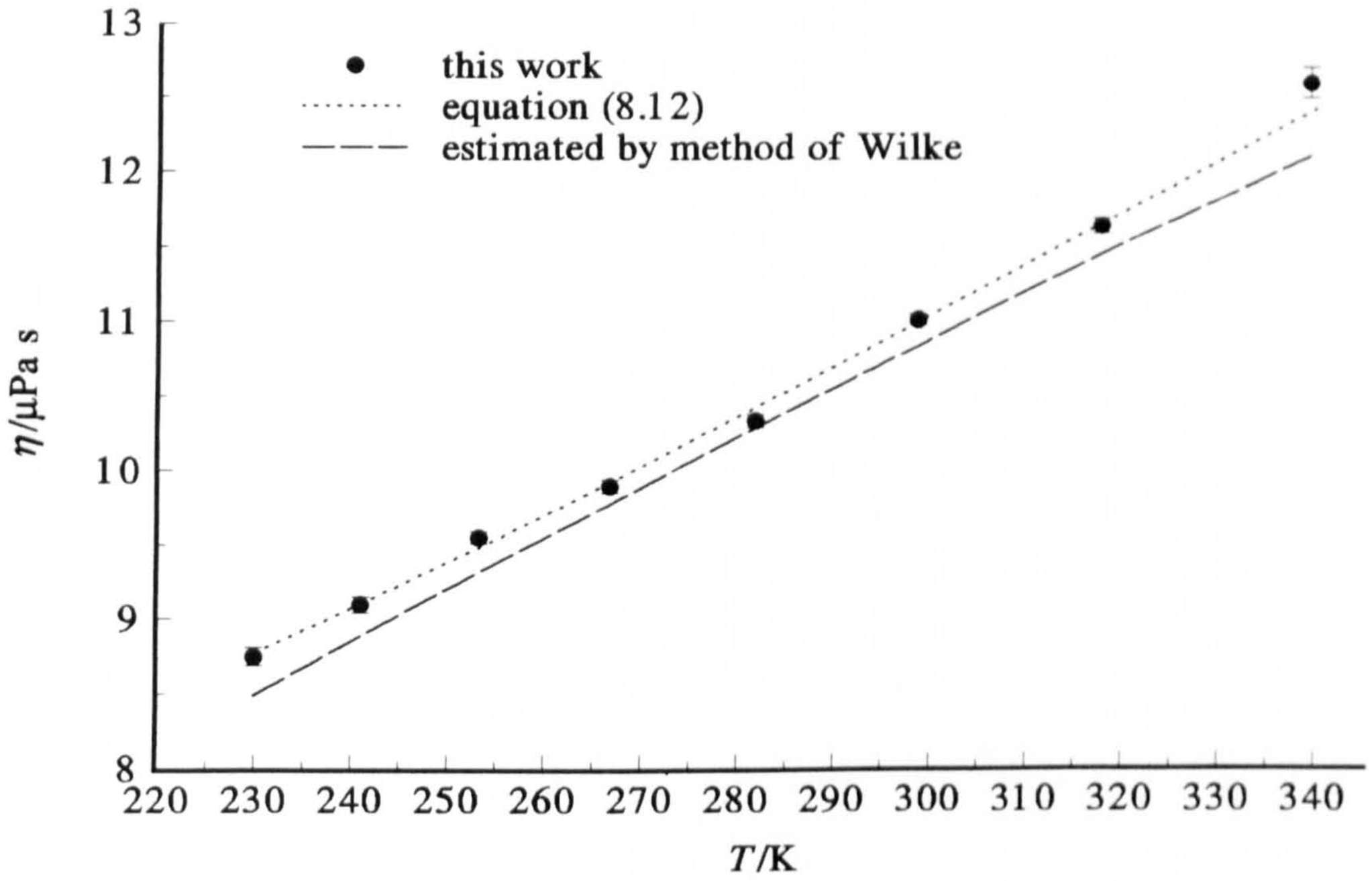

to deviate from the estimated values by up to 4 % and are systematically high as was the case for sulfur hexafluoride. The pure component data is accurate to 1 % and the estimation method introduces additional uncertainty of the order of 1 %. At this level the agreement is relatively good but unknown loss mechanisms in the resonator and imposing the Stiel-Thodos relation between the shear viscosity and the thermal conductivity are likely to lead to systematic errors that cannot be evaluated. As for sulfur hexafluoride the results for the shear viscosity and thermal conductivity derived from this work should be treated with caution.

No thermal conductivity results were available for the methane-ethane mixture at the mole fractions used in this work so values were again estimated from the thermal conductivities of the pure components. The Mason and Saxena[32] modification to the Wassiljewa equation was used which for a binary mixture reduces to equations (8.16) to (8.18) in which η_{mix}, η_1 and η_2 are replaced by κ_{mix}, κ_1 and κ_2. Values of the low pressure thermal conductivity for methane were taken from the work of Johnston *et al.*[33] and were fitted to a smoothing equation. Smoothed values for the limiting low pressure thermal conductivity

Figure 8.33: Comparison of the thermal conductivity κ of the mixture determined in this work with values determined using published results for the pure components and the estimation method of Mason and Saxena.

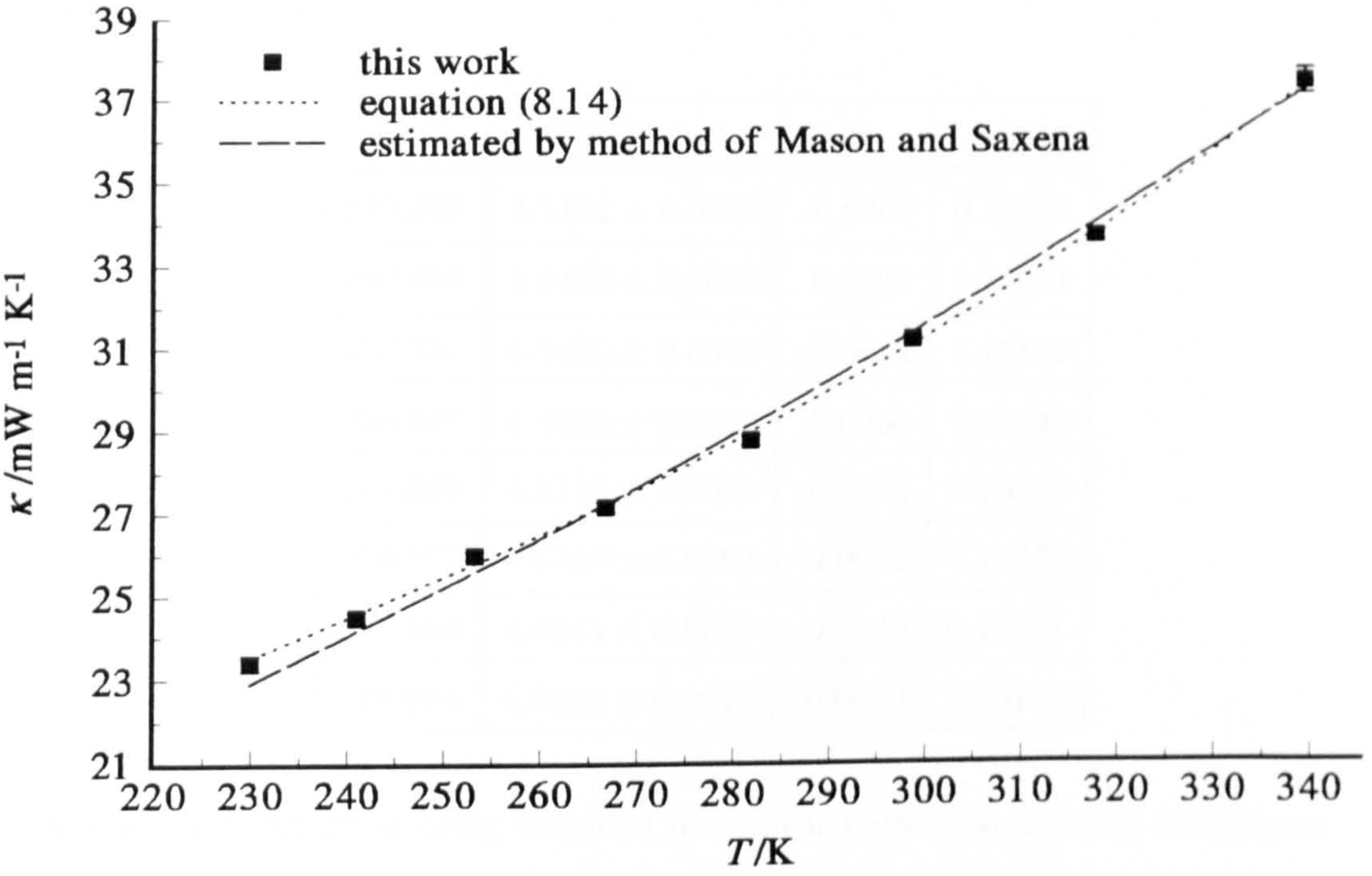

of ethane were again taken from reference [31]. The estimates of the thermal conductivity of the mixture are plotted in figure (8.33) together with the experimentally determined results. The excellent agreement of better than 2 % across the whole of the experimental temperature range may be coincidental as the pure component data is only accurate to about this level and the estimation method may lead to additional uncertainty of up to 4 %[3]. As for sulfur hexafluoride, the thermal conductivity results derived from the absorption coefficient for the speed of sound together with the Stiel-Thodos relation agree with literature data to better than 2 % giving confidence in this method of determining the thermal conductivity.

8.3.4. Results Derived from the Speed of Sound

Perfect-gas heat capacities for the mixture were determined from the constant term in the density series fits to the speed of sound data and are presented in table (8.32) along with their standard deviations σ and deviations $\Delta = C_p^{\mathrm{pg}}/R\,(\mathrm{exp}) - C_p^{\mathrm{pg}}/R\,(\mathrm{calc})$ from the smoothing equation, (8.19). The values of C_p^{pg} were fit to

Table 8.32: Perfect-gas heat capacities C_p^{pg} derived from the density and pressure series, estimated standard deviations σ, and deviations Δ from the smoothing equations for the mixture. Estimated values of the final mole fraction of ethane x in the mixture.

T/K	$\mathbf{C_p^{pg}/R \pm \sigma}$	**Δ**	**x**
229.890	4.3121 ± 0.0002	-0.0001	0.15296
240.956	4.3450 ± 0.0002	0.0005	0.15231
253.155	4.3860 ± 0.0002	-0.0014	0.15157
266.647	4.4465 ± 0.0003	0.0030	0.15143
281.693	4.5156 ± 0.0002	-0.0005	0.15082
298.517	4.6105 ± 0.0004	0.0005	0.15073
317.454	4.7341 ± 0.0010	0.0020	0.15101
338.994	4.8895 ± 0.0012	-0.0030	0.15143

a function determined using weighted non-linear regression analysis which gave

$$C_p^{pg}/R = 3.935 + 0.239 \times 10^{-7} T^3 + \frac{0.11 \times 10^7}{T^3} \tag{8.19}$$

with a standard deviation of 0.002 R.

Figure (8.34) depicts the deviations $\Delta\left(C_p^{pg}/R\right) = \left(C_p^{pg}/R\right) - \left(C_p^{pg}/R\right)_{\text{equation (8.19)}}$ of the experimental results and available literature data[1],[34] from equation (8.19). The experimental data cannot always be fitted to within a small multiple of the standard deviation indicating that there are unknown errors in the analysis but no datum can be singled out as particularly in error. The results from this work agree well with those of Peek[34] except for his data at 250 and 275 K which were rejected from his final analysis. The results of this work and those of Peek can be seen to deviate significantly from the results of Boyes[1] which are likely to be in error due to precondensation. At the highest pressures used by Boyes the partial pressure of ethane exceeded the vapour pressure of ethane at some of the experimental temperatures leading to a liquid film of ethane on the inner surface of the resonator. As the pressure was reduced this caused methane to be preferentially removed from the mixture resulting in a mole fraction that differed significantly from the manufacturers certified value of 0.1500. The results from

Figure 8.34: Comparison of the perfect gas heat capacities C_p^{pg} of the mixture determined in this work with published values.

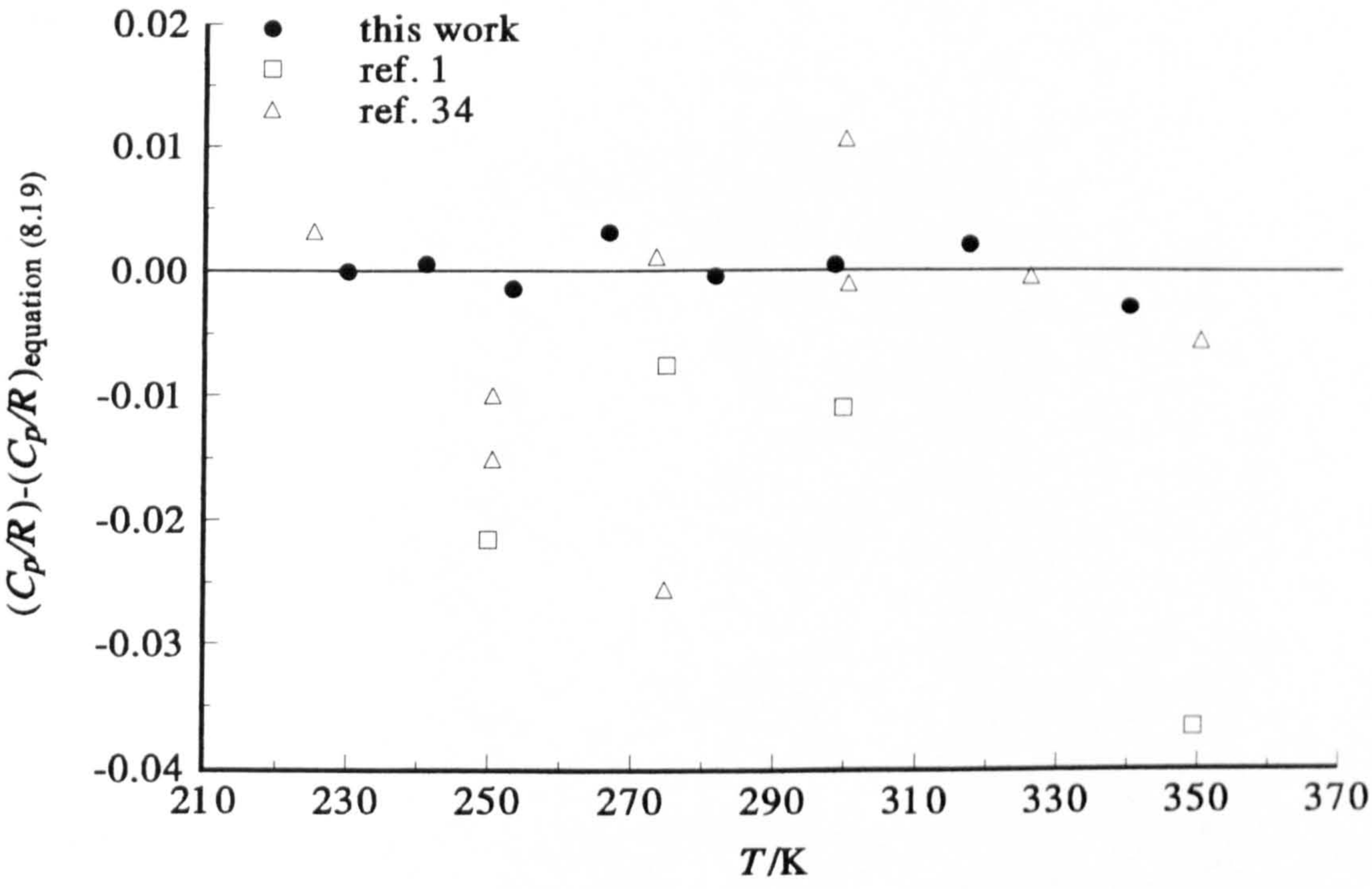

this work will affected by fractionation to a lesser degree as it is expected to occur as the pressure is reduced. The lighter methane molecules will be preferentially pumped away despite the very low pumping speeds used to try and minimise this effect. The systematic change in the mole fraction x can be monitored since it is possible to estimate x from the zero-pressure limit of the speed of sound. Values of x determined for the eight isotherms are given in table (8.32) and were determined from A_0 assuming that

$$\gamma_{\mathrm{mix}}^{\mathrm{pg}} = \frac{(1-x)\, C_p^{\mathrm{pg}}(\mathrm{CH_4}) + x C_p^{\mathrm{pg}}(\mathrm{C_2H_6})}{(1-x)\, C_V^{\mathrm{pg}}(\mathrm{CH_4}) + x C_V^{\mathrm{pg}}(\mathrm{C_2H_6})}, \tag{8.20}$$

and

$$M_{\mathrm{mix}} = (1-x)\, M_{\mathrm{CH_4}} + x M_{\mathrm{C_2H_4}}.$$

The perfect-gas heat capacities of the pure components were taken from reference [1] for ethane and reference [35] for methane. The deviations of x from the manufacturers certified value never exceed 0.003 which is less than the deviations observed by both Boyes and Peek.

The second acoustic virial coefficients β_{a} determined from the second terms of the density series fits of the speed of sound data at the eight experimental

Table 8.33: Values of the second acoustic virial coefficient $\beta_{\mathrm{a,mix}}$ from the density series, estimated standard deviations σ, and deviations Δ from the square well potential for the mixture.

T/K	$\boldsymbol{\beta_{\mathrm{a,mix}} \pm \sigma / \mathrm{cm}^3 \cdot \mathrm{mol}^{-1}}$	**Δ**
229.890	-116.48 ± 0.12	-0.44
240.956	-102.58 ± 0.11	0.59
253.155	-90.78 ± 0.06	-0.12
266.647	-76.29 ± 0.16	2.34
281.693	-67.33 ± 0.07	-0.49
298.517	-55.24 ± 0.18	0.25
317.454	-43.67 ± 0.31	0.87
338.994	-33.26 ± 0.28	0.60

temperatures are given in table (8.33) together with their standard deviations σ. The second (p, V, T) virial coefficients B_{mix} were extracted by means of a weighted regression analysis using the square-well potential in conjunction with the experimental β_{a} and C_p^{pg}. This yielded

$$B_{\mathrm{mix}}/\mathrm{cm}^3 \cdot \mathrm{mol}^{-1} = 252 - 193.5 \exp\left(140\ \mathrm{K}/T\right), \tag{8.21}$$

with a standard deviation of 0.8 $\mathrm{cm}^3 \cdot \mathrm{mol}^{-1}$. With the exception of the datum at 267 K the data were fitted to within a few multiples of their standard deviations. Removal of this point did not significantly alter the fit and the deviations $\Delta = (\beta_{\mathrm{a}})_{\mathrm{exp}} - (\beta_{\mathrm{a}})_{\mathrm{calc}}$ of the experimental data from equation (8.21) with equation (1.15) are also given in table (8.33).

Table (8.34) gives the cross virial coefficients B_{12} and interaction virial coefficients δ_{12} for the mixture derived from the relations

$$\delta_{12} = 2B_{12} - (B_{11} + B_{22}), \tag{8.22}$$

and

$$B_{\mathrm{mix}} = (1-x)\, B_{11} + x\,(1-x)\,\delta_{12} + x B_{22}, \tag{8.23}$$

where B_{NN} are the virial coefficients for the pure components $\mathrm{N} = 1, 2$ which were taken from reference [1]. Unweighted analysis of the cross virial coefficients B_{12}

Table 8.34: Values of the cross virial coefficient B_{12} and the interaction virial coefficient δ_{12} for the mixture.

T/K	$\mathbf{B_{12}/cm^3 \cdot mol^{-1}}$	$\boldsymbol{\delta_{12}}$
229.890	-153.62	88.05
240.956	-140.19	77.89
253.155	-126.94	69.07
266.647	-113.88	61.51
281.693	-100.97	55.13
298.517	-88.27	49.87
317.454	-75.77	45.65
338.994	-63.45	42.39

using the square well potential gave

$$B_{12}/\mathrm{cm}^3 \cdot \mathrm{mol}^{-1} = 774.67 - 675.74 \exp\left(73\ \mathrm{K}/T\right), \tag{8.24}$$

with a standard deviation of 0.01 $cm^3 \cdot mol^{-1}$. The results from this work, equation (8.24) and available literature data[1],[34]-[40] are plotted in figure (8.35). In general the agreement with the literature data is very good. The low temperature data of Hoover *et al.*[38] deviates from equation (8.24) by about 17 $cm^3 \cdot mol^{-1}$ which is accordance with previous studies. The previous determinations are plotted as deviations $\Delta B_{12} = (B_{12})_{\text{equation (8.24)}} - (B_{12})$ from equation (8.24) in figure (8.36) and the excellent agreement of generally better than 5 $cm^3 \cdot mol^{-1}$ can be clearly seen. The high temperature data of Dantzler *et al.*[39] shows systematic deviations from the results presented here but the two highest temperature points are outside the temperature range covered in this work. The level of agreement between all the data with the exception of that given in references [38] and [39] is remarkable considering that extracting B_{12} requires a knowledge of the second virial coefficients for the pure components, and it is likely that different authors use different values of B_{11} and B_{22}.

The interaction virial coefficients δ_{12} given in table (8.34) are plotted in figure (8.37) together with the results of Boyes and Peek. At temperatures below 300 K the results from this work are in excellent agreement with the previous determina-

Figure 8.35: Comparison of the second cross virial coefficients B_{12} of the mixture determined from the density series with published results.

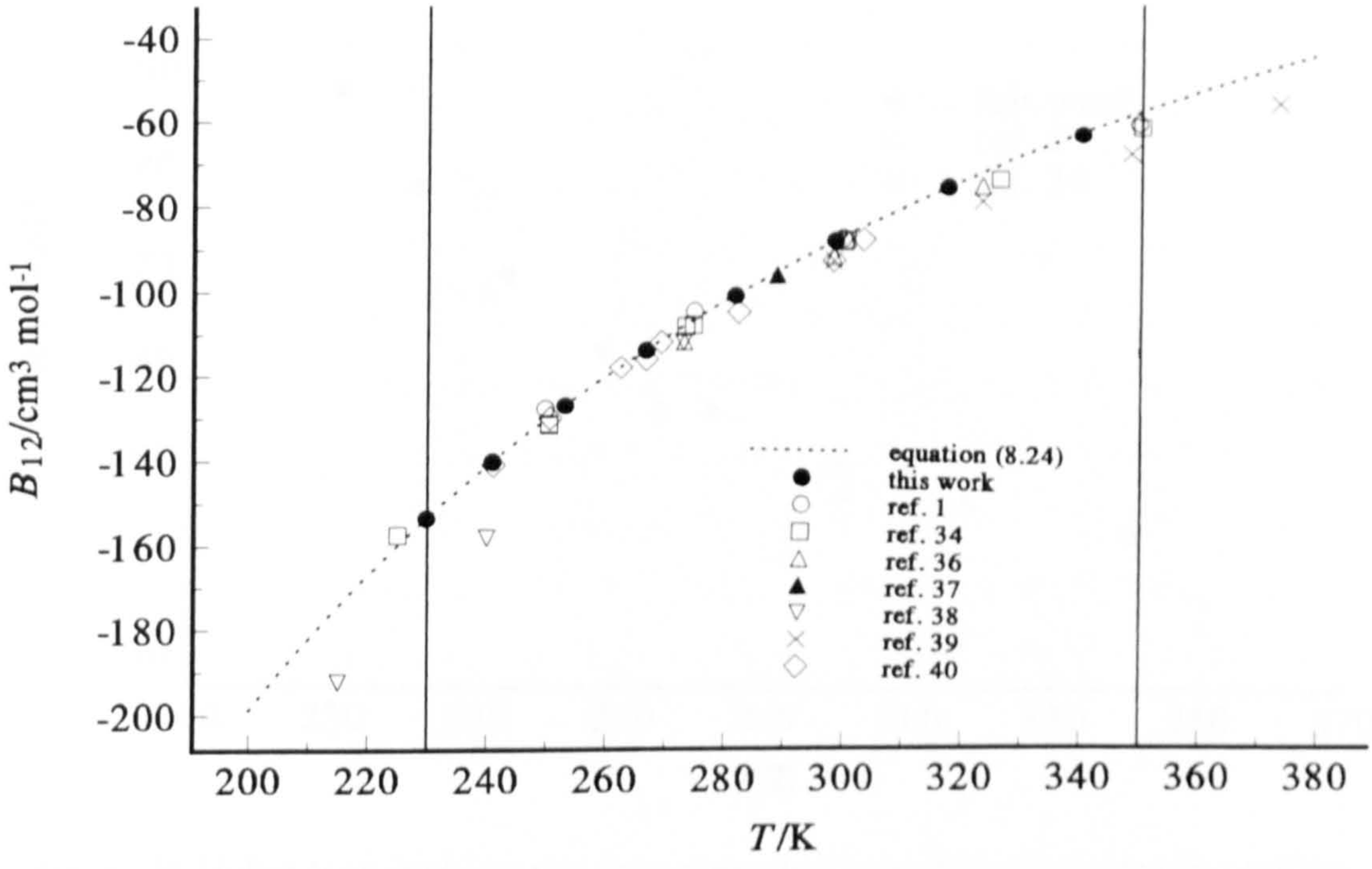

Figure 8.36: Deviations ΔB_{12} of the second cross virial coefficients of the mixture from equation (8.24).

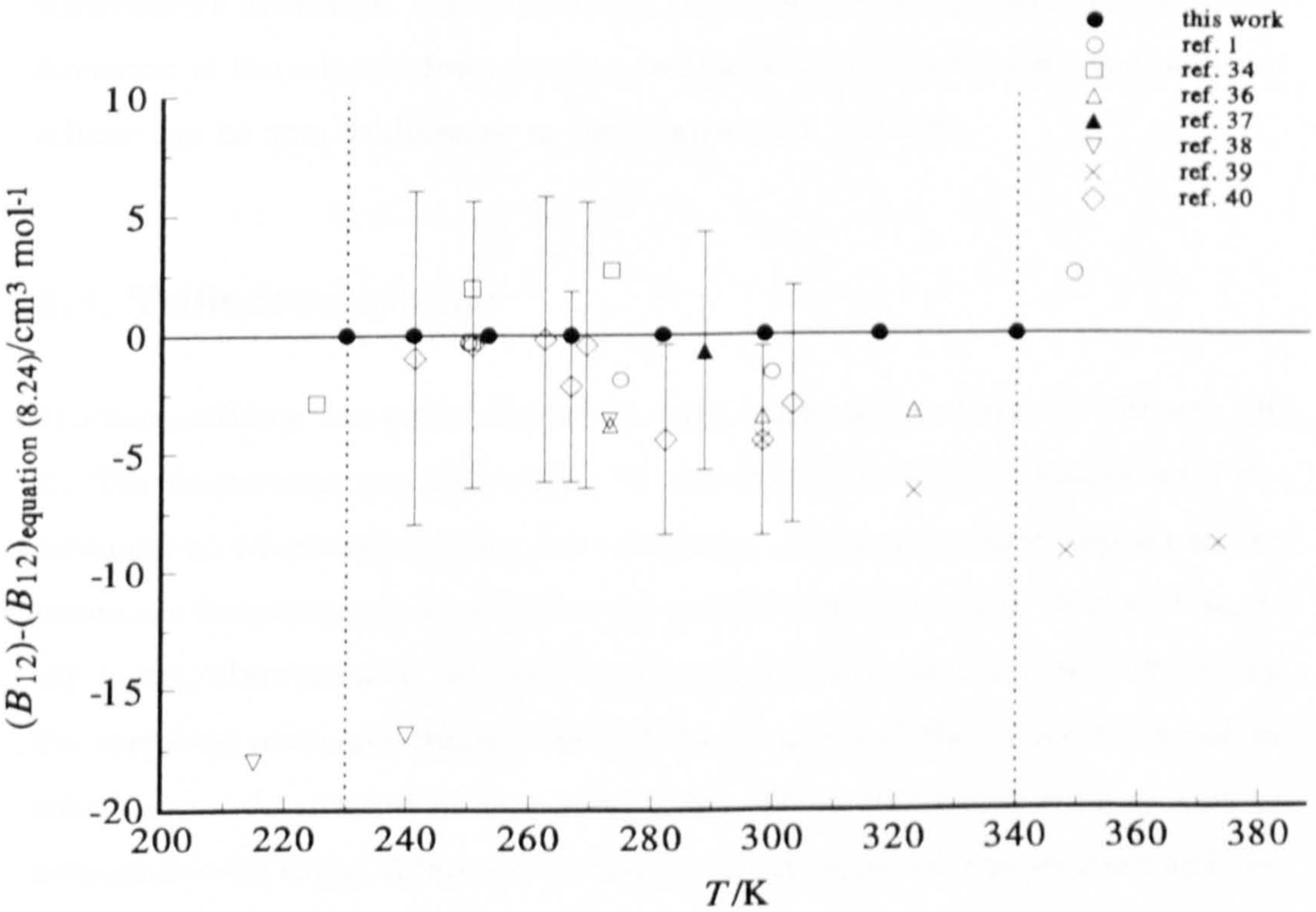

Figure 8.37: Comparison of the second interaction virial coefficients δ_{12} of the mixture determined from the density series with published results.

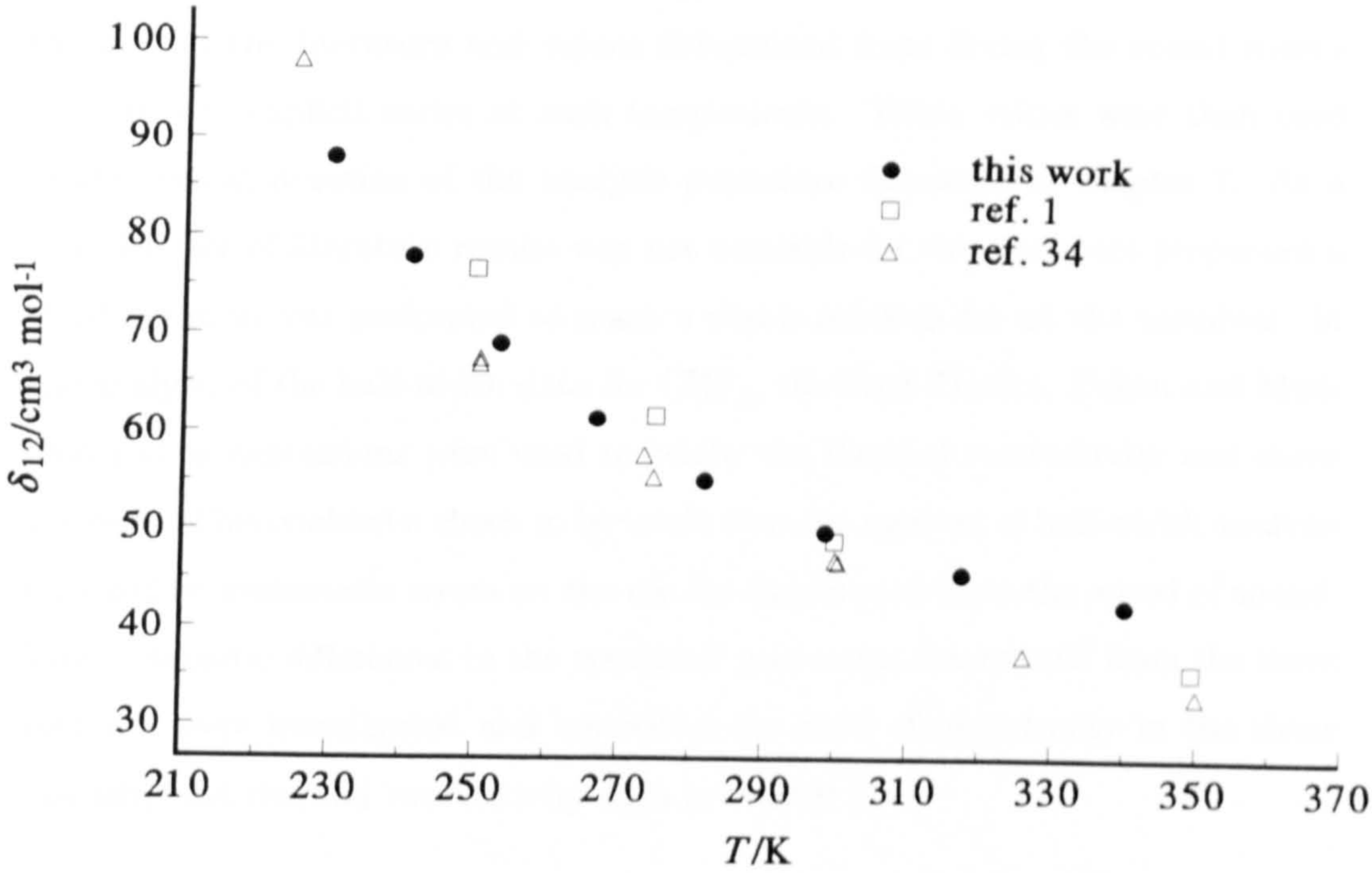

tions. At higher temperatures the data presented here show a systematic positive deviation. This may be due to the additional curvature of the speed of sound data due to the shell resonance and mode overlap that adversely affected the high temperature isotherms. The interaction virial coefficient represents the degree of deviation of the mixture from ideality and the interactions between methane and ethane can be seen to decrease as the temperature increases.

8.4. Trifluoromethane

Trifluoromethane was again studied at eight temperatures between 230 and 340 K. The frequencies and half-widths of the $(0, 2, 1)$ to $(0, 9, 1)$ modes were determined at 15 pressures along each isotherm. Corrections were applied to the resonance frequencies to account for the effects of the shear and thermal boundary layers, absorption in the bulk of the gas and holes in the shell wall. Using the corrected resonance frequencies and the geometry of the cavity, the speed of sound u was determined at each state point. Small corrections were applied to account for the slight differences between the experimental temperature and the

stated temperature for each isotherm. The transport properties required in the various correction terms were determined from an analysis of the resonance half-widths. Initial estimates of the heat capacity and second virial coefficients were taken from the literature and values determined from fitting the sound speeds to a density explicit series at each temperature. These values were then used in the second iteration of the analysis procedure discussed in chapter 7. As a complete set of literature results was not available for the transport properties a third iteration was performed to reach a stable solution for all the variables. In the analysis of the half-width data for CHF_3, the Stiel-Thodos, Euken and Modified Euken expressions were used to relate the thermal conductivity and shear viscosity. This enabled a check to be made that the method of half-width analysis imposed no systematic errors on the results determined from the speed of sound. The systematic differences in the transport properties determined from the three methods were investigated and quantified the level of uncertainty in the shear viscosity and thermal conductivity data presented here.

8.4.1. Half-width Fitting

In CHF_3 only the three highest frequency resonance modes were above 2000 Hz and therefore unaffected by the shell resonance. The lower order modes may all be affected to some degree and modes that gave fractional excess halfwidths $\Delta g/f = (g_{\text{exp}} - g_{\text{calc}})/f$ of significantly greater than 20 ppm were discarded from the analysis. As for the other gases the $(0,2,1)$ mode was always significantly perturbed and is discussed separately. The highest frequency $(0,7,1)$, $(0,8,1)$ and $(0,9,1)$ modes were retained at every temperature. Surprisingly the lower frequency $(0,3,1)$ and $(0,5,1)$ modes were found in some cases to be unperturbed whereas the $(0,4,1)$ showed significant deviations from the higher order modes over the whole of the temperature range. The selection of the lower order modes at each state point was determined by their observed agreement with the higher frequency modes which it was expected would be unperturbed by the shell resonance. The modes rejected from the analysis are given in table (8.35). The lowest pressure point was also removed at each temperature due to the very large half-widths which again compromised the accuracy of the results. The fractional excess half-widths $\Delta g/f$ for a typical isotherm at 317 K are shown in figure (8.38).

Table 8.35: Resonance modes rejected at each experimental temperature in the half-width analysis for CHF_3.

T/K	Modes Rejected
230	(0, 2, 1) (0, 4, 1)
241	(0, 2, 1) (0, 5, 1) (0, 8, 1) : p1-p9 (0, 2, 1) (0, 3, 1) : p9-p15
253	(0, 2, 1) (0, 3, 1) (0, 4, 1) (0, 5, 1) : p1-p4 (0, 2, 1) (0, 4, 1) : p5-p15
267	(0, 2, 1) (0, 3, 1) (0, 4, 1) (0, 5, 1) : p1-p4 (0, 2, 1) (0, 4, 1) : p5-p15
282	(0, 2, 1) (0, 3, 1) (0, 4, 1) (0, 5, 1) : p1-p4 (0, 2, 1) (0, 4, 1) (0, 5, 1) : p5-p10 (0, 2, 1) (0, 4, 1) : p11-p15
299	(0, 2, 1) (0, 4, 1)
317	(0, 2, 1) (0, 4, 1)
339	(0, 2, 1) (0, 4, 1) : p1-p5, p9-p15 (0, 2, 1) (0, 4, 1) (0, 5, 1) : p6-p8

Figure 8.38: Fractional excess half-widths $\Delta g/f$ for the isotherm at 317 K in CHF_3.

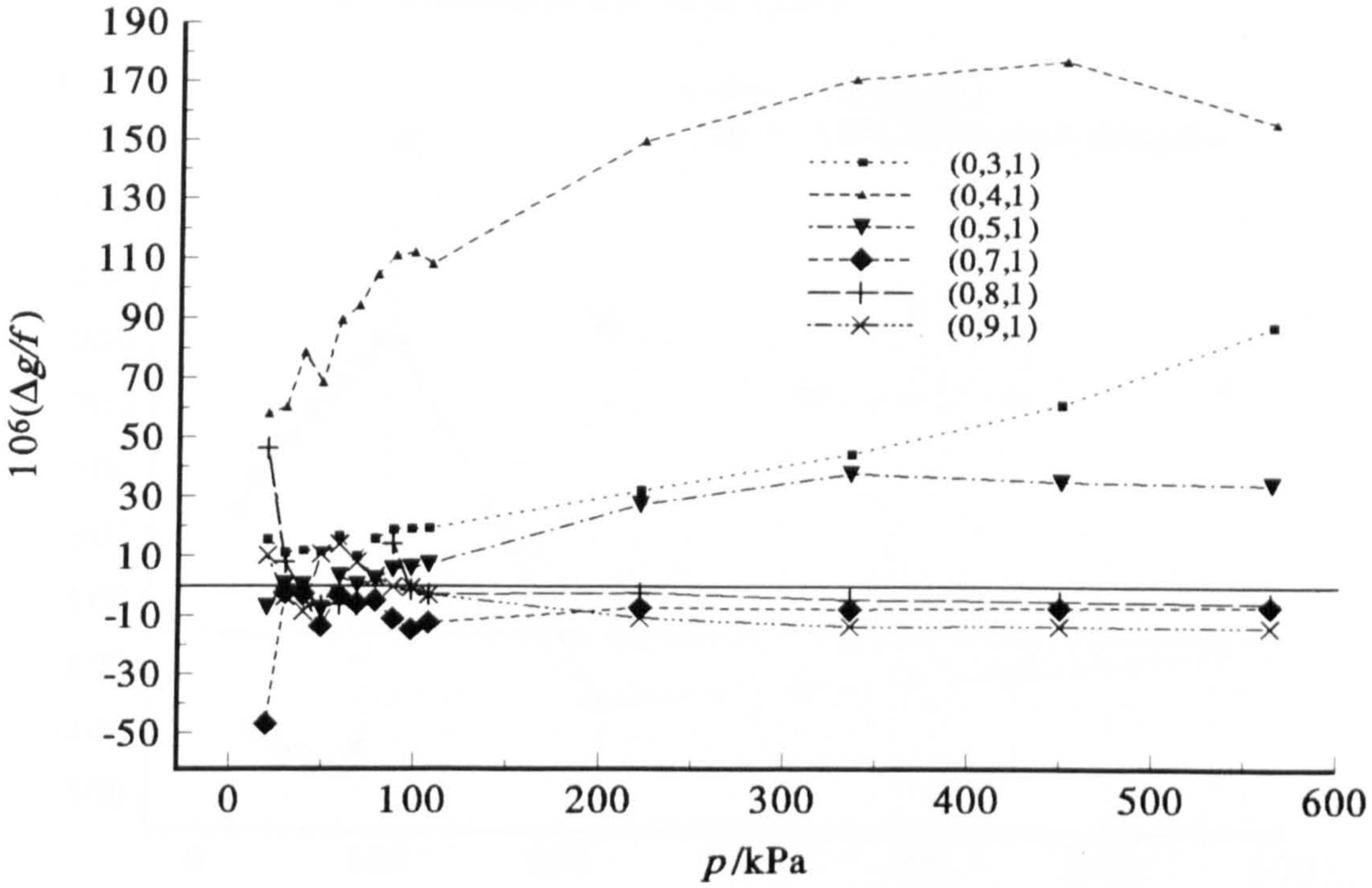

The small symbols represent data rejected from the analysis. The $(0, 3, 1)$ mode was discarded as the factional excess half-width increased to 80 ppm and, even for the ten low pressure measurements it was consistently high by 10 to 15 ppm. The $(0, 4, 1)$ mode was also removed as the fractional excess half-width was greater than 50 ppm for the whole isotherm. The $(0, 5, 1)$ mode was retained in the half-width analysis despite the fractional excess half-width increasing to around 35 ppm as it agreed with the higher order modes for the low pressure measurements. In this region the half-widths are large and determine the values of the transport properties derived from the results. Inclusion of the $(0, 5, 1)$ mode altered the values of the transport properties by much less than their standard deviations.

The behaviour of the $(0, 2, 1)$ was again different from the remaining set of modes. The fractional excess half-widths for this mode and the deviations from the mean speeds of sound $\langle u/b \rangle$ are plotted in figure (8.39). The form of the deviations in CHF_3 is similar to that in the mixture, in propene, and in SF_6. The excess half-width is again high at low pressures going through a maximum before decreasing. The deviation in u is again negative at low pressure and becomes large and positive at higher pressure as in the other gases. A minima may be

Figure 8.39: Fractional deviations of the calculated values of u/b for the $(0, 2, 1)$ mode from the average value $\langle u/b \rangle$ and fractional excess half-widths $\Delta g/f$ for the $(0, 2, 1)$ mode for the isotherm at 317 K in CHF_3.

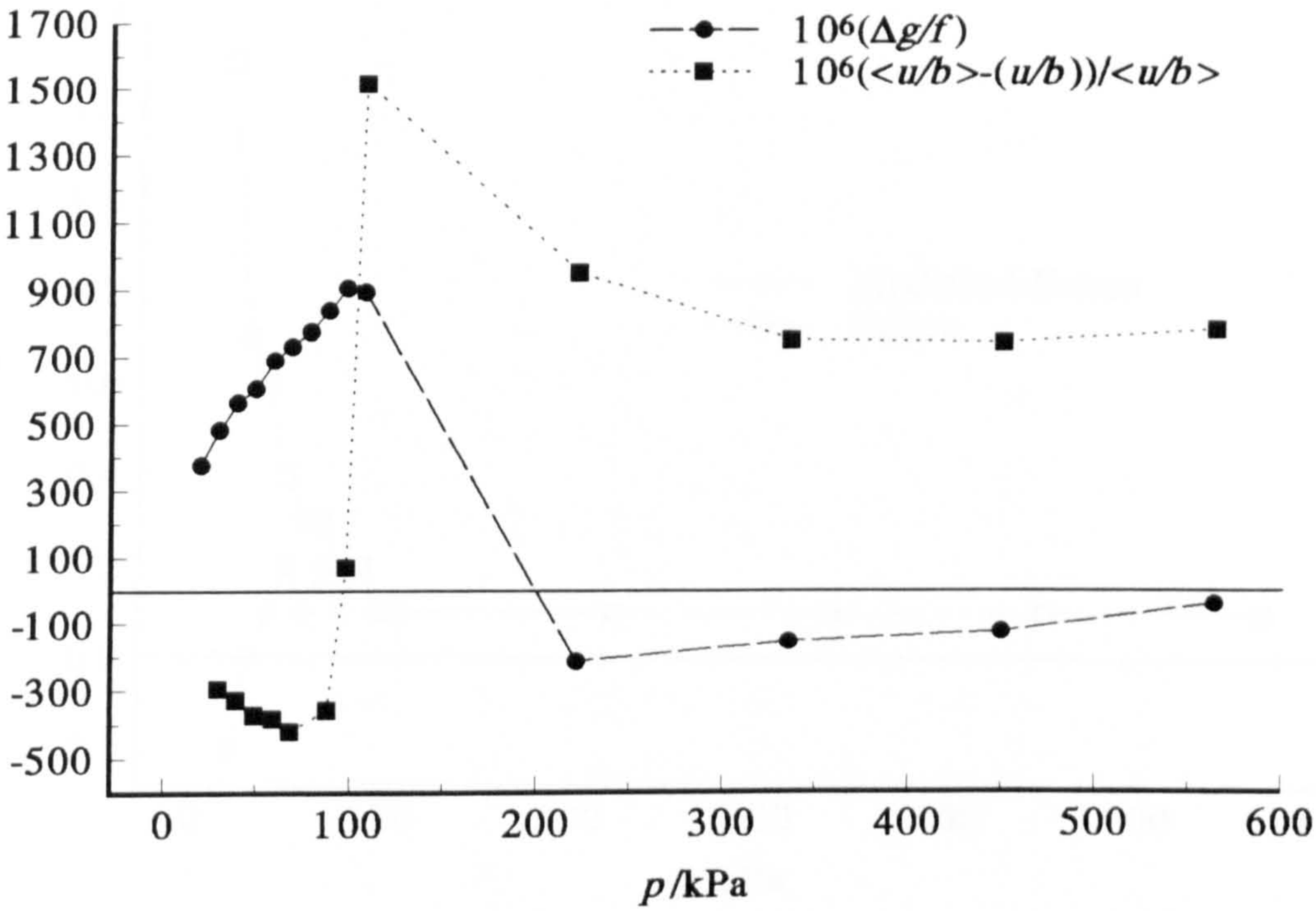

seen below 70 kPa and a maxima occurs at 100 kPa as for SF_6. Despite some small differences which are likely to be due to the choice of modes retained in the analysis, the similarities in the behaviour again indicate a pressure dependent geometric perturbation which severely affects the $(0, 2, 1)$ mode.

The half-width analysis was repeated at each temperature with the same set of modes using the Stiel-Thodos, Euken and Modified Euken expressions to relate the shear viscosity and thermal conductivity. The excess half-widths for each method never differed by more than 2 ppm which is far less than the overall level of accuracy of the experiment which is limited to 20 ppm by the accuracy to which the geometry of the cavity is known. The deviations $\Delta(\Delta g/f) = (\Delta g/f)_{\text{S-T}} - (\Delta g/f)$ of the excess half-widths determined using the Euken and Modified Euken expressions from those determined using the Stiel-Thodos expression are shown in figure (8.40) for the $(0, 9, 1)$ mode at 317 K. If the ratio of thermal to shear losses were constant for all the resonance modes, an arbitrary expression could be used to relate the thermal conductivity and shear viscosity and no useful information could be extracted. For the seven azimuthal modes measured in this work, the

Figure 8.40: Deviations of the fractional excess half-widths $\Delta(\Delta g/f)$ for the Euken and Modified-Euken half-width analysesd from those from the Stiel-Thodos method of half-width analysis for the $(0, 9, 1)$ mode at 317 K in CHF_3.

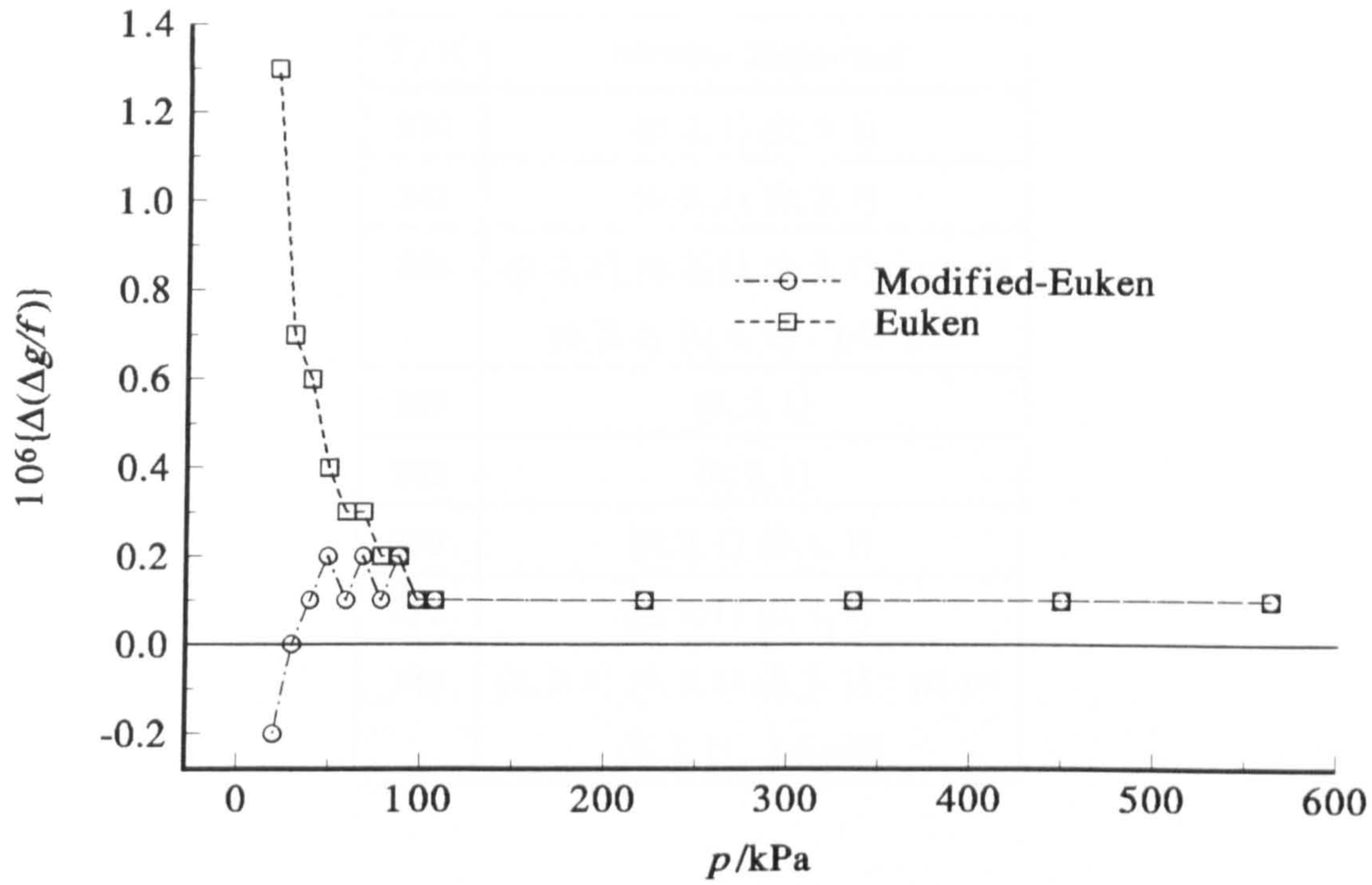

ratio of the thermal to shear losses differs by 10 % between the lowest order $(0, 2, 1)$ mode and highest order $(0, 7, 1)$ mode measured. The three expressions were found to be equally good at describing these losses so the experiment is not sensitive to the method of half-width analysis for the set of modes used. If a different set of modes for which the ratios of thermal to shear losses were very different had been measured, it then may have been possible to resolve the thermal conductivity and shear viscosity without the need for an explicit expression linking the two parameters. For example, radial modes have greater thermal losses in proportion to the shear losses than azimuthal modes.

8.4.2. Sound Speed Analysis

The modes rejected in the analysis of the speeds of sound determined from the corrected resonance frequencies are given in table (8.36) and in general two or three of the lower order $(0, 2, 1)$ to $(0, 5, 1)$ modes were rejected as they showed systematic deviations of an unacceptably high level from the higher order $(0, 7, 1)$ to $(0, 9, 1)$ modes. The deviations of the individual u/b from the mean $\langle u/b \rangle$ at

Table 8.36: Resonance modes rejected at each experimental temperature in the sound speed analysis for CHF_3.

T/K	**Modes Rejected**
230	$(0,2,1)$ $(0,3,1)$
241	$(0,2,1)$ $(0,3,1)$
253	$(0,2,1)$ $(0,3,1)$ $(0,5,1)$: p1-p9 $(0,2,1)$ $(0,4,1)$: p10-p15
267	$(0,2,1)$
282	$(0,2,1)$
299	$(0,2,1)$ $(0,4,1)$
317	$(0,2,1)$ $(0,4,1)$
339	$(0,2,1)$ $(0,4,1)$ $(0,5,1)$: p1-p4 $(0,2,1)$: p5-p15

Figure 8.41: Fractional deviations of the calculated values of u/b from the average value $\langle u/b \rangle$ determined for the selected modes for the isotherm at 317 K in CHF_3.

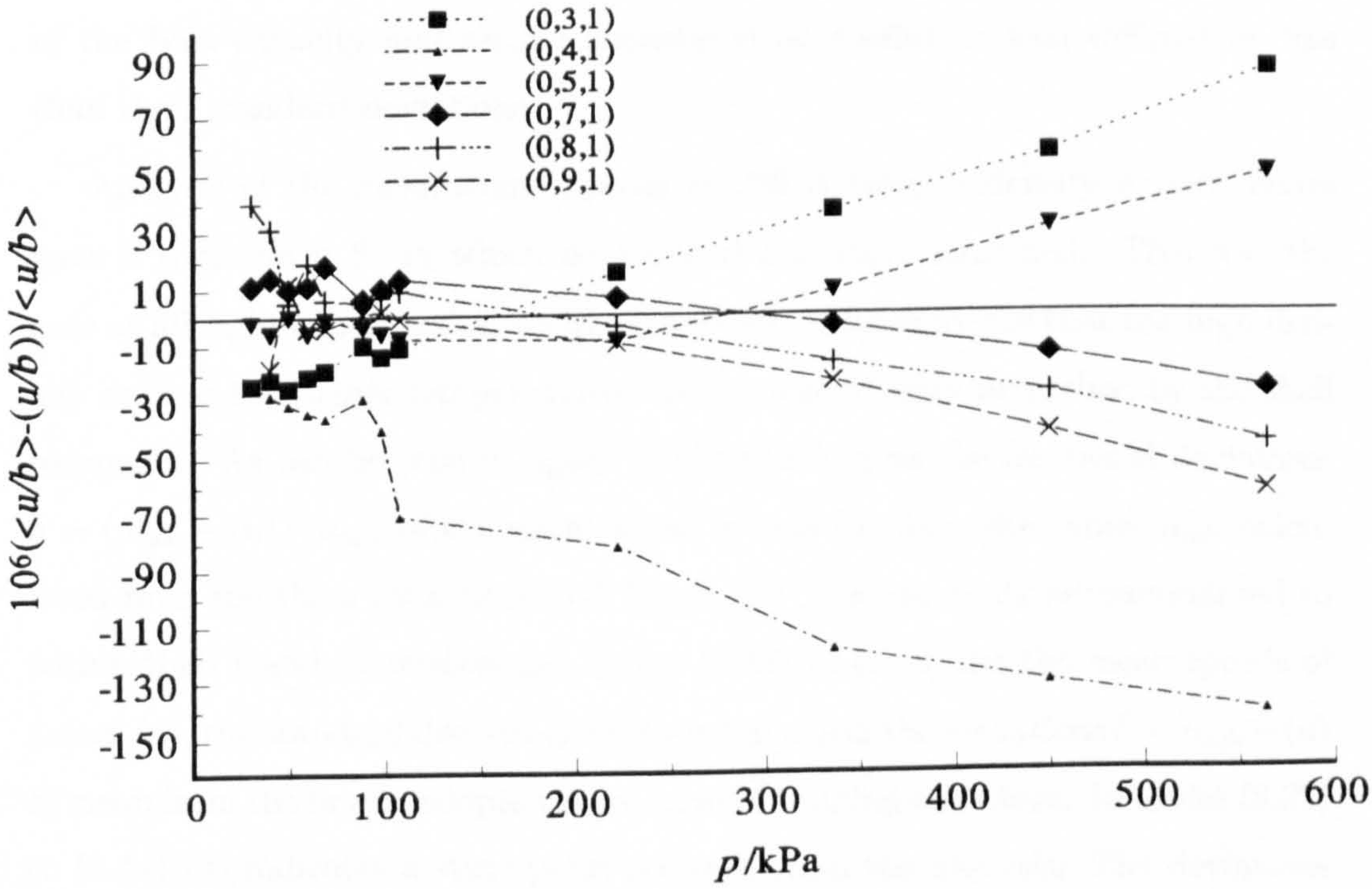

Figure 8.42: Fractional deviations of the average sound speeds $\langle u \rangle$ determined for the selected modes from the calculated values for the isotherm at 317 K in CHF_3.

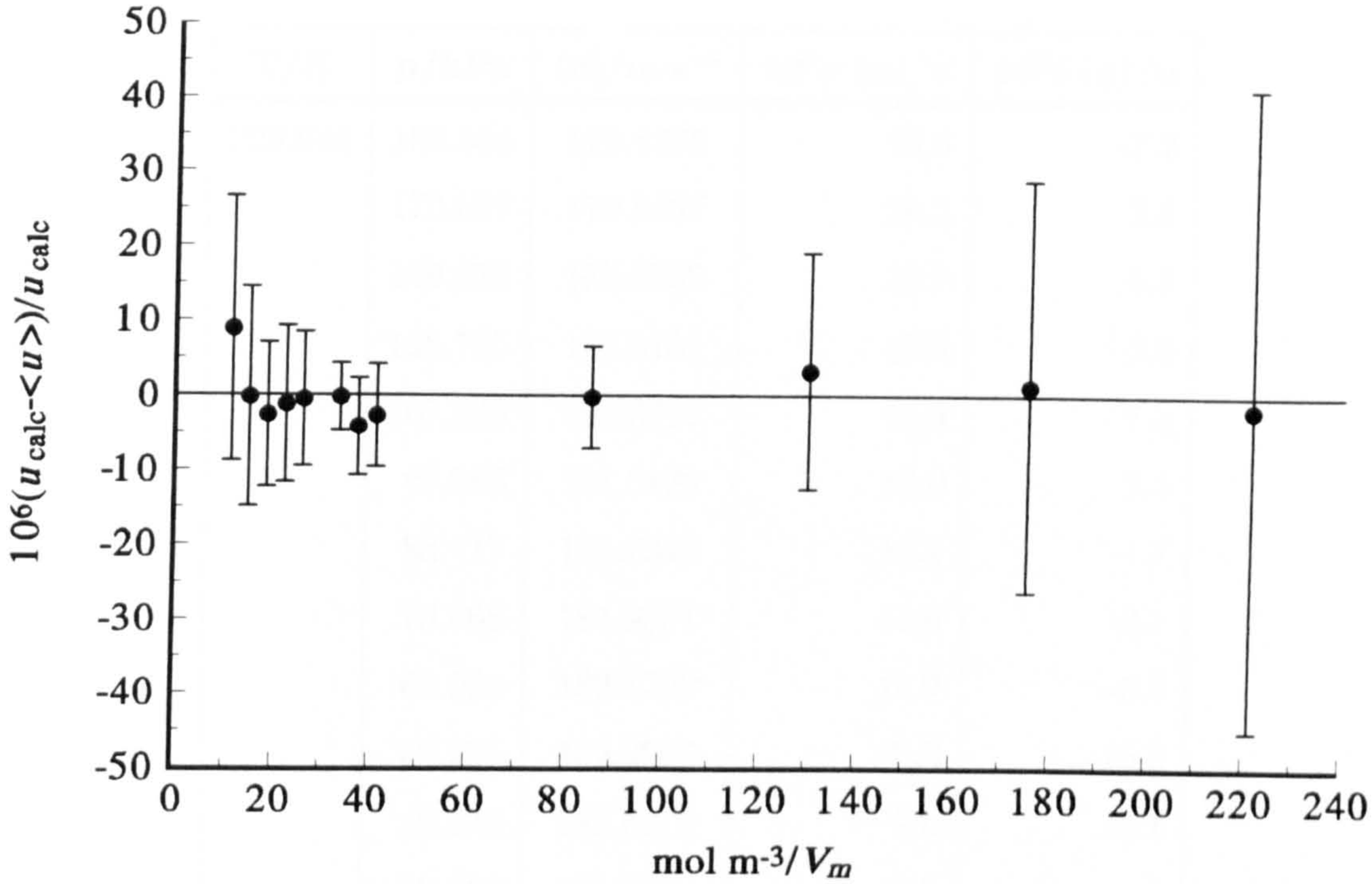

317 K are shown in figure (8.41). The $(0, 4, 1)$ appears to be severely affected by the shell resonance and the deviation increases with increasing pressure. The $(0, 3, 1)$ and $(0, 5, 1)$ modes also appear to be affected by the shell resonance to a lesser degree but were retained in the analysis as their inclusion resulted in values of the heat capacity and second acoustic virial coefficient that differed by less than their standard deviations.

Analysis of the mean sound speeds at 230 K using a density explicit series gave a three term fit in which no residual curvature remained. This was the case at all eight experimental temperatures providing evidence that the high density data at the higher temperatures was not significantly perturbed by the shell resonance. As can be seen in figure (8.42) which gives the fractional deviations $\delta = (u_{\text{calc}} - \langle u \rangle) / u_{\text{calc}}$ of the mean sound speeds $\langle u \rangle$ from the values u_{calc} calculated from the three term fit at 317 K, all the data are easily accommodated to within their standard deviations. Tables (8.37) to (8.44) list the mean speeds of sound $\langle u \rangle$, the standard deviations of the mean σ and the deviations $\delta = u_{\text{calc}} - \langle u \rangle$ of mean from the finally adopted three term smoothing equations. In tables (8.37) to (8.44) (a) indicates a state point removed from the analysis. The deviations

Table 8.37: Mean values of u with standard deviations σ and deviations δ from the density series at 230 K for CHF_3.

T/K	**p/kPa**	$\langle \mathbf{u} \rangle / \mathbf{m \cdot s^{-1}}$	$\mathbf{10^6 \sigma\,(u)\,/u}$	$\mathbf{10^6 \delta\,(u)\,/u}$
229.946	188.534	179.4235	25.6	-7.2
	170.637	179.8437	24.2	2.1
	149.871	180.3269	22.2	5.5
	128.705	180.8151	17.5	3.8
	107.525	181.3010	14.9	7.5
	97.988	181.5176	13.0	2.5
	88.417	181.7343	12.1	-1.7
	78.668	181.9551	11.6	-2.1
	68.991	182.1729	10.9	-5.9
	59.285	182.3906	8.2	-10.3
	49.478	182.6112	9.6	-8.1
	39.613	182.8326	9.2	-4.2
	29.817	183.0551	10.3	18.2
	19.993	183.2815	20.0	(a)
	10.053	183.5320	56.0	(a)

from the smoothing equations were generally less than 10 ppm which represents the limiting accuracy of this experiment given the current knowledge of the geometry of the cavity and the way in which it responds to pressure changes. The data for CHF_3 provided the fewest difficulties in its analysis because the frequencies were sufficiently high that the $(0,7,1)$ to $(0,9,1)$ modes avoided significant perturbation by the shell resonance, and the low pressure data was not significantly compromised by resonance overlap.

8.4.3. Transport Properties

Analysis of the half-widths yielded estimates of the vibrational relaxation time as $\tau\rho$, the shear viscosity η and its initial density dependence $(\partial\eta/\partial\rho)$, as well as the thermal conductivity κ and its initial density dependence $(\partial\kappa/\partial\rho)$. This data was extracted from half-width analyses employing the Stiel-Thodos (S-T), Euken

Table 8.38: Mean values of u with standard deviations σ and deviations δ from the density series at 241 K for CHF_3.

T/K	**p/kPa**	$\langle \mathbf{u} \rangle / \mathbf{m \cdot s^{-1}}$	$\mathbf{10^6 \sigma\,(u)\,/u}$	$\mathbf{10^6 \delta\,(u)\,/u}$
240.971	234.066	182.9855	17.5	14.1
	163.636	183.6325	12.3	(a)
	171.057	184.2628	11.8	29.0
	138.924	184.9039	11.1	15.6
	107.493	185.5277	7.7	-4.5
	97.997	185.7161	8.2	-8.2
	88.434	185.9053	7.6	-13.7
	78.675	186.0991	9.7	-13.3
	68.938	186.2920	9.2	-14.9
	59.193	186.4855	8.1	-13.2
	49.347	186.6836	10.4	4.6
	39.613	186.8813	12.6	32.7
	29.801	187.0884	15.8	(a)
	19.999	187.3155	23.7	(a)
	10.188	187.6142	85.2	(a)

Table 8.39: Mean values of u with standard deviations σ and deviations δ from the density series at 253 K for CHF_3.

T/K	**p/kPa**	$\langle \mathbf{u} \rangle / \mathbf{m \cdot s^{-1}}$	$\mathbf{10^6 \sigma\,(u)\,/u}$	$\mathbf{10^6 \delta\,(u)\,/u}$
253.095	291.322	186.8002	13.5	12.1
	245.295	187.6111	8.8	-7.4
	199.516	188.4104	6.9	-19.2
	153.541	189.2079	5.9	-13.1
	107.204	190.0087	4.2	23.0
	97.534	190.1725	5.4	18.5
	87.841	190.3362	4.0	13.8
	78.209	190.4980	5.1	6.0
	68.472	190.6614	5.5	-0.3
	58.766	190.8234	7.1	-9.5
	48.901	190.9891	6.3	-11.4
	39.204	191.1525	7.9	-8.5
	29.687	191.3128	10.2	-4.1
	20.009	191.4767	24.8	6.8
	10.194	191.6490	81.0	(a)

Table 8.40: Mean values of u with standard deviations σ and deviations δ from the density series at 267 K for CHF_3.

T/K	**p/kPa**	$\langle$**u**$\rangle$/**m·s**$^{-1}$	$\mathbf{10^6\sigma\,(u)\,/u}$	$\mathbf{10^6\delta\,(u)\,/u}$
266.652	365.512	190.9412	41.7	-6.9
	301.272	191.9054	36.0	6.6
	236.355	192.8664	29.2	7.1
	171.828	193.8107	26.1	2.9
	107.494	194.7415	20.4	0.6
	97.733	194.8816	20.6	-0.8
	88.018	195.0205	19.8	-4.6
	78.307	195.1590	19.5	-8.4
	68.561	195.2980	19.9	-10.8
	58.887	195.4350	17.5	-17.3
	49.144	195.5778	17.8	2.6
	39.379	195.7183	17.2	9.8
	29.696	195.8570	18.2	14.9
	19.998	196.0012	27.9	(a)
	10.302	196.1474	91.9	(a)

Table 8.41: Mean values of u with standard deviations σ and deviations δ from the density series at 282 K for CHF_3.

T/K	**p/kPa**	$\langle \mathbf{u} \rangle / \mathbf{m \cdot s^{-1}}$	$\mathbf{10^6 \sigma\,(u)\,/u}$	$\mathbf{10^6 \delta\,(u)\,/u}$
281.503	400.393	196.1018	34.7	-6.4
	326.762	197.0307	28.8	3.5
	253.939	197.9409	36.3	11.7
	180.806	198.8435	26.2	3.7
	107.759	199.7364	21.5	-6.7
	97.788	199.8587	20.0	-2.6
	88.035	199.9771	19.8	-4.0
	78.343	200.0941	17.9	-8.3
	68.675	200.2120	17.8	-6.0
	58.971	200.3291	16.7	-9.0
	49..283	200.4472	19.3	-5.5
	39.586	200.5668	18.2	5.8
	29.855	200.6879	18.7	23.6
	20.207	200.8080	33.0	(a)
	10.440	200.9382	107.3	(a)

Table 8.42: Mean values of u with standard deviations σ and deviations δ from the density series at 299 K for CHF_3.

T/K	**p/kPa**	$\langle \mathbf{u} \rangle / \mathbf{m \cdot s^{-1}}$	$\mathbf{10^6 \sigma\,(u)\,/u}$	$\mathbf{10^6 \delta\,(u)\,/u}$
298.262	457.445	201.4249	17.7	-3.9
	369.264	202.4512	12.7	5.1
	282.745	203.3515	6.0	2.6
	195.463	204.2517	5.3	0.7
	107.261	205.1532	7.7	-3.8
	97.470	205.2529	7.6	-3.9
	87.812	205.3515	7.4	-2.3
	78.123	205.4503	7.7	-0.5
	68.453	205.5481	9.3	-2.8
	58.801	205.6461	10.9	-1.9
	49.080	205.7452	11.9	0.6
	39.292	205.8449	12.0	3.6
	29.691	205.9426	18.6	6.5
	20.008	206.0437	41.1	(a)
	10.332	206.3632	1606.4	(a)

Table 8.43: Mean values of u with standard deviations σ and deviations δ from the density series at 317 K for CHF_3.

T/K	**p/kPa**	$\langle \mathbf{u} \rangle / \mathbf{m \cdot s^{-1}}$	$\mathbf{10^6 \sigma\,(u)\,/u}$	$\mathbf{10^6 \delta\,(u)\,/u}$
317.375	563.612	207.1728	43.3	-1.8
	449.418	208.1570	27.7	1.3
	335.593	209.1317	15.9	3.3
	221.602	210.1003	6.9	-0.2
	107.461	211.0641	6.9	-2.7
	97.782	211.1453	6.5	-4.2
	88.002	211.2284	4.5	-0.2
	78.265	211.3195	93.6	(a)
	68.296	211.3939	9.0	-0.5
	58.935	211.4724	10.5	-1.2
	49.014	211.5554	9.7	-2.6
	39.293	211.6375	14.7	-0.2
	29.643	211.7203	17.7	8.9
	19.806	211.8045	41.0	(a)
	10.022	211.8902	138.6	(a)

Table 8.44: Mean values of u with standard deviations σ and deviations δ from the density series at 339 K for CHF_3.

T/K	**p/kPa**	$\langle \mathbf{u} \rangle / \mathbf{m \cdot s^{-1}}$	$\mathbf{10^6 \sigma\,(u)\,/u}$	$\mathbf{10^6 \delta\,(u)\,/u}$
338.976	801.361	212.7315	29.6	-9.1
	627.788	213.9367	17.4	20.9
	452.794	215.1368	8.9	-15.7
	281.136	216.3261	6.8	15.1
	107.586	217.5147	14.1	-5.7
	97.930	217.5803	10.2	-9.0
	88.198	217.6475	12.6	-7.4
	78.381	217.7158	17.2	-3.1
	68.685	217.7825	18.5	-2.3
	58.898	217.8495	18.3	-3.3
	49.242	217.9168	20.1	1.8
	39.593	217.9839	16.2	5.7
	29.337	218.0564	25.5	15.8
	19.995	218.1245	45.6	(a)
	10.302	218.2062	160.7	(a)

Figure 8.43: Comparison of the shear viscosity η of CHF_3 determined in this work with published values.

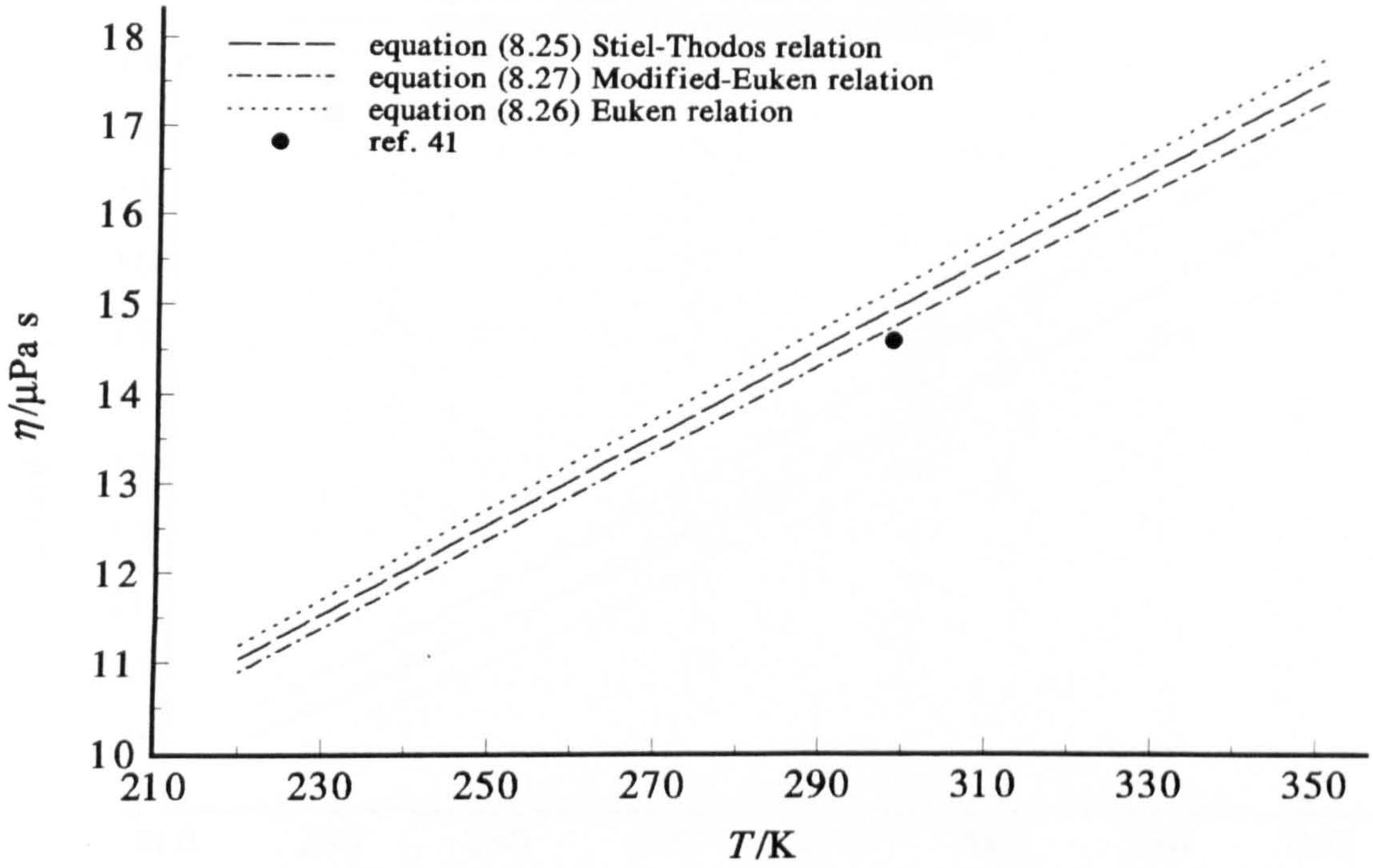

(E-U) and Modified Euken (M-E) expressions.

Shear Viscosity and Thermal Conductivity

The three methods of half-width analysis resulted in values of the thermal conductivity, the shear viscosity and their density dependencies that were systematically different. The smoothing equations for the shear viscosities η (equations (8.25) to (8.27)) and thermal conductivities κ (equations (8.31) to (8.33)) determined using the three methods are plotted in figure (8.43) and (8.44) together with all the literature results[41]-[43]. For both properties the S-T method used for the other two gases gives intermediate values. The shear viscosities determined by the E-U method are systematically higher than the S-T method and the values determined from the M-E method systematically lower. For the thermal conductivity the converse is true. In both cases the proportional deviation of the results for each method remains the same over the whole of the experimental temperature range. The thermal conductivity data from the S-T method is about 5 % lower than that from the M-E method and about 5 % higher than that from the E-U method. The spread of the data gives an indication of the uncertainty associated

Figure 8.44: Comparison of the thermal conductivity κ of CHF_3 determined in this work with published values.

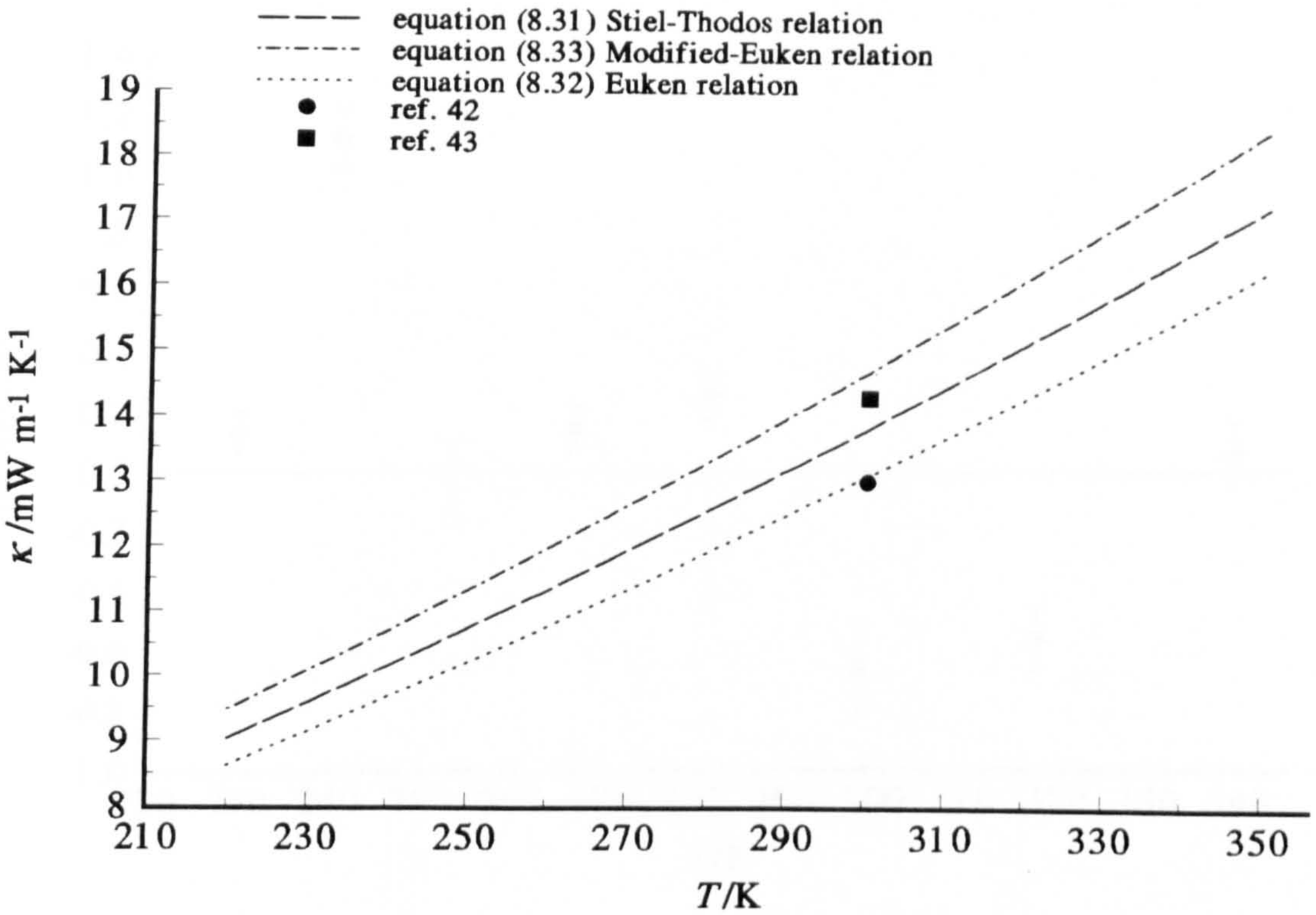

with thermal conductivities determined in this way, which is therefore estimated at 10 %. The shear viscosities that come from a S-T method of analysis are about 2.5 % lower than those from the E-U method and about 2.5 % higher than those from the M-E method giving an uncertainty associated with shear viscosities determined in this way of about 5 %. The level of agreement of the transport property data with published results and estimation techniques has been satisfactory in all three experimental systems given the known uncertainty imposed on the values by the need for an expression relating κ and η. In addition, there may be further systematic errors due to unidentified loss mechanisms operating in the resonator or the inclusion of data affected by the shell resonance. The sole result found in the literature[41] for the shear viscosity of CHF_3 is low compared to the values obtained in this work. It deviates by just over 5 % from the E-U method value, by about 3 % from the S-T method value and by approximately 1 % from the M-E method value. Both published results[42],[43] for the thermal conductivity of CHF_3 at 300 K fall within the span of the results generated by all three methods of half-width analysis.

The shear viscosity values determined using the Stiel-Thodos method $\eta_{\text{S-T}}$ may

Figure 8.45: Deviations δ of the shear viscosity η of CHF_3 extracted using the Steil-Thodos method of half-width analysis from equation (8.25).

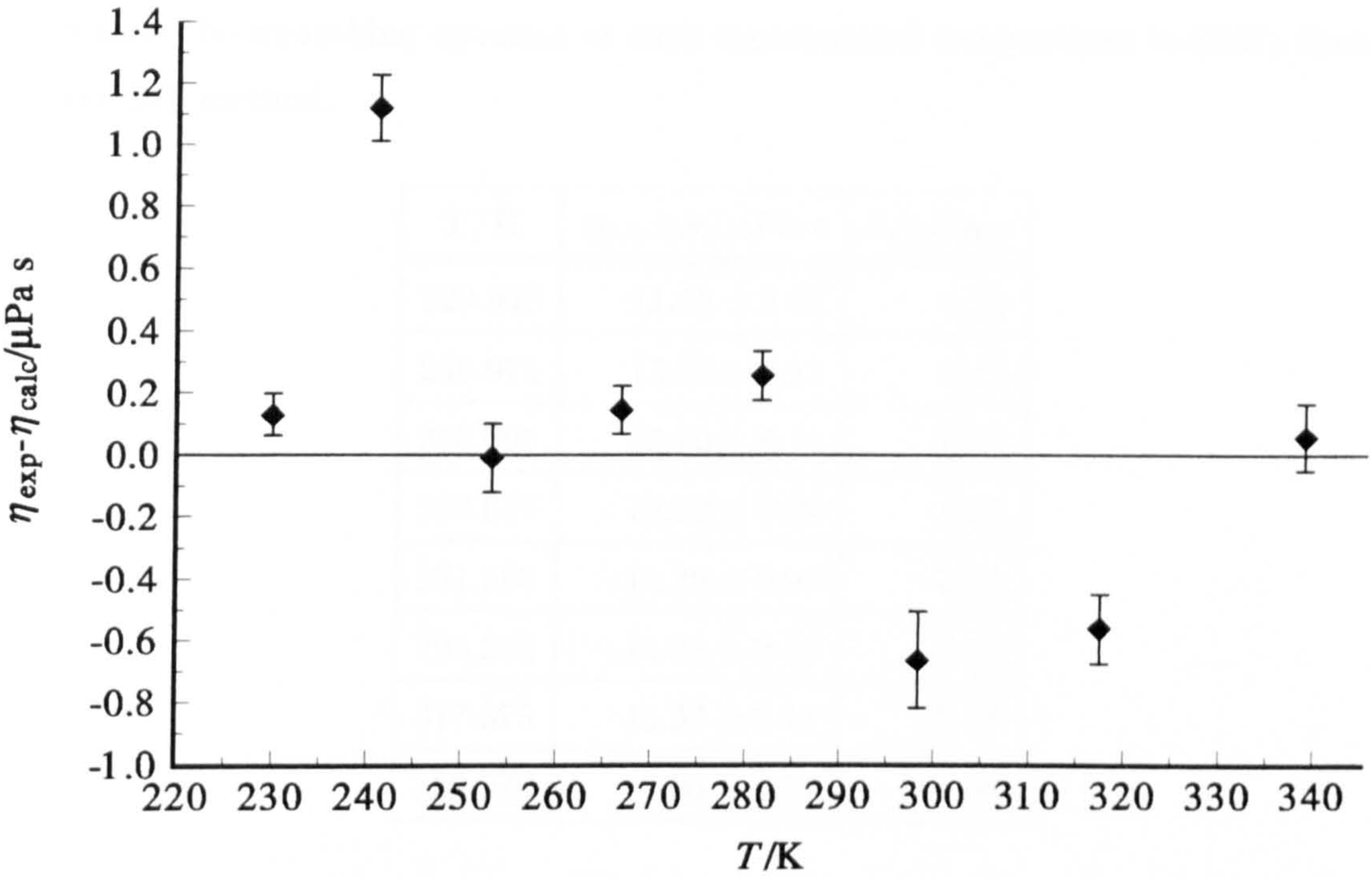

be represented over the experimental temperature range by

$$\eta_{\text{S-T}}/\mu\text{Pa}\cdot\text{s} = 0.0502T, \tag{8.25}$$

with a standard deviation of 0.55 μPa $\cdot$ s. $\eta_{\text{E-U}}$ was fitted to

$$\eta_{\text{E-U}}/\mu\text{Pa}\cdot\text{s} = 0.0509T, \tag{8.26}$$

with a standard deviation of 0.51 μPa $\cdot$ s and $\eta_{\text{M-E}}$ described by

$$\eta_{\text{M-E}}/\mu\text{Pa}\cdot\text{s} = 0.0495T, \tag{8.27}$$

with a standard deviation of 0.49 μPa $\cdot$ s. The same functional form was found for each method and the experimental results, their standard deviations σ and deviations from the smoothing equations $\delta = \eta_{\text{exp}} - \eta_{\text{calc}}$ are given in tables (8.45), (8.46) and (8.47). The deviations are essentially the same for each method and the deviations for the S-T method are shown in figure (8.45). The point at 241 K was rejected in the regression analysis as its exclusion led to a significant reduction in the standard deviation of the fit. All the remaining data were fit to a few multiples of their standard deviations.

Table 8.45: Values of the shear viscosity η, its standard deviation σ and deviation δ from the smoothing equation at each experimental temperature in CHF_3 from the S-T method.

T/K	$\boldsymbol{\eta_{\text{S-T}} \pm \sigma / \mu}$**Pa·s**	$\boldsymbol{\delta / \mu}$**Pa·s**
229.946	11.68 ± 0.07	0.13
240.971	13.22 ± 0.11	1.12
253.095	12.70 ± 0.11	-0.01
266.652	13.53 ± 0.08	0.15
281.503	14.39 ± 0.08	0.26
298.262	14.31 ± 0.16	-0.66
317.375	15.37 ± 0.11	-0.56
338.976	16.96 ± 0.11	-0.06

Table 8.46: Values of the shear viscosity η, its standard deviation σ and deviation δ from the smoothing equation at each experimental temperature in CHF_3 from the E-U method.

T/K	$\boldsymbol{\eta_{\text{E-U}} \pm \sigma / \mu}$**Pa·s**	$\boldsymbol{\delta / \mu}$**Pa·s**
229.946	11.83 ± 0.07	0.12
240.971	13.40 ± 0.11	1.13
253.095	12.87 ± 0.11	-0.02
266.652	13.72 ± 0.08	0.14
281.503	14.59 ± 0.08	0.25
298.262	14.90 ± 0.11	-0.29
317.375	15.58 ± 0.12	-0.58
338.976	17.19 ± 0.11	-0.07

Table 8.47: Values of the shear viscosity η, its standard deviation σ and deviation δ from the smoothing equation at each experimental temperature in CHF_3 from the M-E method.

T/K	$\boldsymbol{\eta_{\text{M-E}} \pm \sigma / \mu}$**Pa·s**	$\boldsymbol{\delta / \mu}$**Pa·s**
229.946	11.51 ± 0.07	0.12
240.971	13.04 ± 0.11	1.10
253.095	12.52 ± 0.11	-0.02
266.652	13.34 ± 0.08	0.13
281.503	14.19 ± 0.08	0.24
298.262	14.49 ± 0.11	-0.28
317.375	15.15 ± 0.12	-0.57
338.976	17.73 ± 0.11	-0.06

The density dependence of the viscosity $(\partial\eta/\partial\rho)$ was found to be independent of temperature over the experimental range for all three methods. The weighted mean values are

$$(\partial\eta/\partial\rho)_{\text{S-T}} / \mu\text{Pa} \cdot \text{s} \cdot \text{m}^3 \cdot \text{kg}^{-1} = 0.49, \tag{8.28}$$

which has a standard deviation of 0.12 μPa·s·m^3·kg^{-1},

$$(\partial\eta/\partial\rho)_{\text{E-U}} / \mu\text{Pa} \cdot \text{s} \cdot \text{m}^3 \cdot \text{kg}^{-1} = 0.50, \tag{8.29}$$

which has a standard deviation of 0.12 μPa·s·m^3·kg^{-1}, and

$$(\partial\eta/\partial\rho)_{\text{M-E}} / \mu\text{Pa} \cdot \text{s} \cdot \text{m}^3 \cdot \text{kg}^{-1} = 0.48, \tag{8.30}$$

which has a standard deviation of 0.12 μPa·s·m^3·kg^{-1}. The value at 241 K was retained in these analyses as its removal had no significant effect on the standard deviation of the fit. The experimental results, their standard deviations σ and deviations from the smoothing equations $\delta = (\partial\eta/\partial\rho)_{\text{exp}} - (\partial\eta/\partial\rho)_{\text{calc}}$ are given in tables (8.48), (8.49) and (8.50).

The thermal conductivity and its initial density dependence were also fitted to smoothing equations using the adaptive regression routine. For the thermal conductivity, κ the resulting expressions were

$$\kappa_{\text{S-T}}/\text{mW} \cdot \text{m}^{-1} \cdot \text{K}^{-1} = 0.0270T + 0.63 \times 10^{-4}T^2, \tag{8.31}$$

Table 8.48: Values of the initial density dependence of the shear viscosity $(\partial\eta/\partial\rho)$, its standard deviation σ and deviation δ from the smoothing equation at each experimental temperature in CHF_3 from the S-T method.

T/K	$(\partial\eta/\partial\rho)_{\text{S-T}} \pm\sigma/\mu\text{Pa·s·m}^3\text{·kg}^{-1}$	$\delta/\mu\text{Pa·s·m}^3\text{·kg}^{-1}$
229.946	0.60 ± 0.03	0.11
240.971	0.62 ± 0.04	0.13
253.095	0.51 ± 0.04	0.02
266.652	0.36 ± 0.03	-0.13
281.503	0.33 ± 0.03	-0.16
298.262	0.50 ± 0.04	0.01
317.375	0.55 ± 0.04	0.06
338.976	0.56 ± 0.03	0.07

Table 8.49: Values of the initial density dependence of the shear viscosity $(\partial\eta/\partial\rho)$, its standard deviation σ and deviation δ from the smoothing equation at each experimental temperature in CHF_3 from the E-U method.

T/K	$(\partial\eta/\partial\rho)_{\text{E-U}} \pm\sigma/\mu\text{Pa·s·m}^3\text{·kg}^{-1}$	$\delta/\mu\text{Pa·s·m}^3\text{·kg}^{-1}$
229.946	0.62 ± 0.03	0.11
240.971	0.63 ± 0.04	0.13
253.095	0.52 ± 0.04	0.02
266.652	0.37 ± 0.03	-0.14
281.503	0.34 ± 0.03	-0.17
298.262	0.51 ± 0.04	0.01
317.375	0.57 ± 0.04	0.06
338.976	0.57 ± 0.03	0.07

Table 8.50: Values of the initial density dependence of the shear viscosity $(\partial\eta/\partial\rho)$, its standard deviation σ and deviation δ from the smoothing equation at each experimental temperature in CHF_3 from the M-E method.

T/K	$(\partial\eta/\partial\rho)_{\text{M-E}} \pm\sigma/\mu\text{Pa·s·m}^3\text{·kg}^{-1}$	$\delta/\mu\text{Pa·s·m}^3\text{·kg}^{-1}$
229.946	0.59 ± 0.03	0.11
240.971	0.60 ± 0.04	0.12
253.095	0.50 ± 0.04	0.02
266.652	0.35 ± 0.03	-0.13
281.503	0.32 ± 0.03	-0.16
298.262	0.49 ± 0.04	0.01
317.375	0.54 ± 0.04	0.06
338.976	0.55 ± 0.03	0.07

with a standard deviation of 0.44 $\text{mW} \cdot \text{m}^{-1}\cdot\text{K}^{-1}$,

$$\kappa_{\text{E-U}}/\text{mW} \cdot \text{m}^{-1} \cdot \text{K}^{-1} = 0.0267T + 0.56 \times 10^{-4}T^2, \tag{8.32}$$

with a standard deviation of 0.38 $\text{mW} \cdot \text{m}^{-1}\cdot\text{K}^{-1}$, and

$$\kappa_{\text{M-E}}/\text{mW} \cdot \text{m}^{-1} \cdot \text{K}^{-1} = 0.0267T + 0.74 \times 10^{-4}T^2, \tag{8.33}$$

with a standard deviation of 0.42 $\text{mW} \cdot \text{m}^{-1}\cdot\text{K}^{-1}$. The experimental results, their standard deviations σ and deviations $\delta = \kappa_{\text{exp}} - \kappa_{\text{calc}}$ from equations (8.31) to (8.33) are given in tables (8.51), (8.52) and (8.53). The deviations are again essentially independent of the method used to analyse the half-widths and the deviations for the Stiel-Thodos method are plotted in figure (8.46). In the regression analysis of the thermal conductivity data the point at 241 K was again removed and the remaining data were fit to better than twice the standard deviation of the fit.

The density dependence of the thermal conductivity $(\partial\kappa/\partial\rho)$ was again found to be constant over the experimental temperature range and the weighted mean values for the three methods are

$$(\partial\kappa/\partial\rho)_{\text{S-T}}/\text{mW} \cdot \text{m}^2 \cdot \text{K}^{-1} \cdot \text{kg}^{-1} = 0.43, \tag{8.34}$$

Figure 8.46: Deviations δ of the thermal conductivity κ of CHF_3 extracted using the Stiel-Thodos method of half-width analysis from equation (8.31).

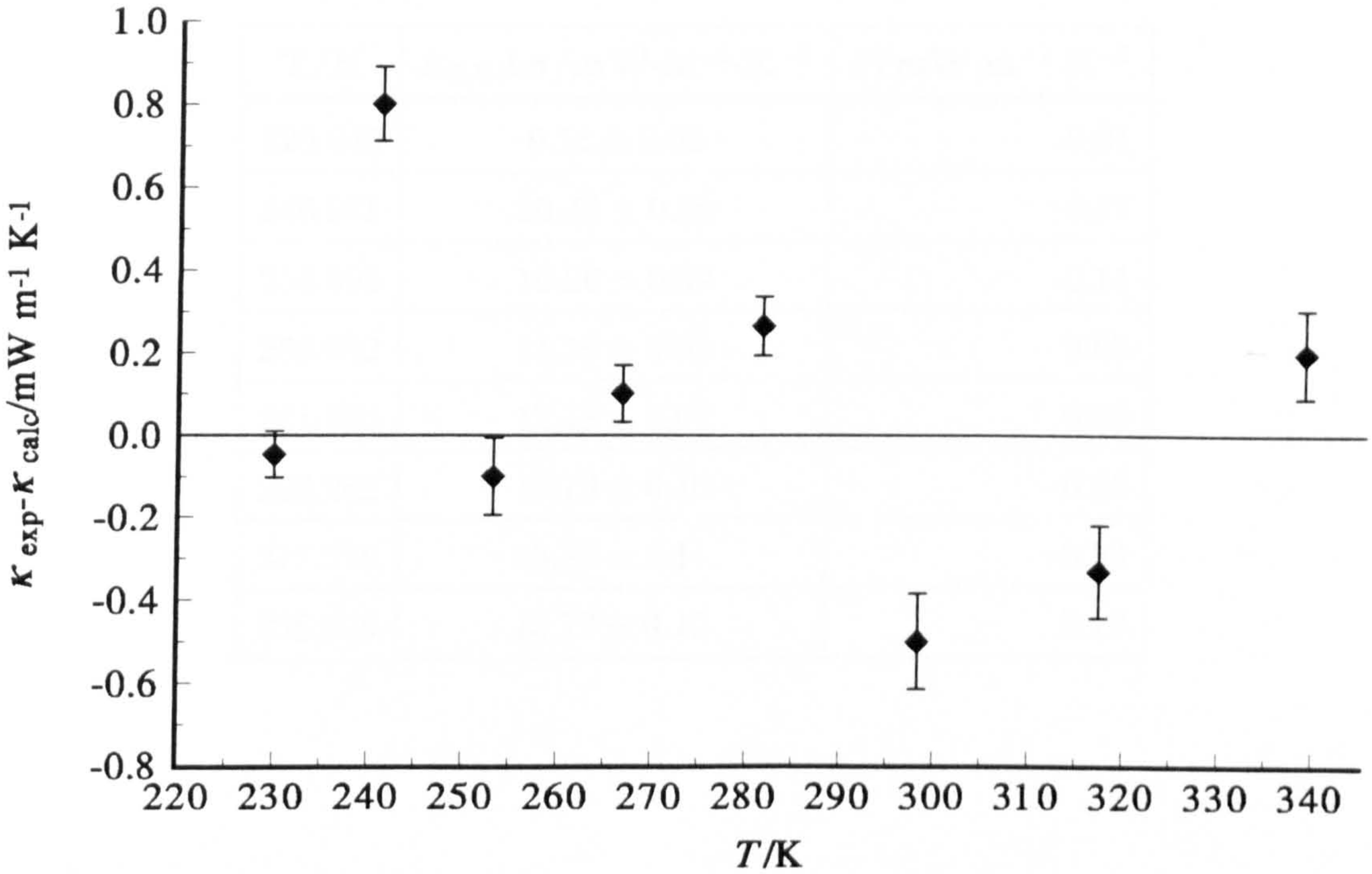

Table 8.51: Values of the thermal conductivity κ, its standard deviation σ and deviation δ from the smoothing equation at each experimental temperature in CHF_3 from the S-T method.

T/K	$\kappa_{\text{S-T}} \pm \sigma$/mW·m^{-1}·K^{-1}	δ/mW·m^{-1}·K^{-1}
229.946	9.57 ± 0.06	-0.05
240.971	11.02 ± 0.09	0.80
253.095	10.80 ± 0.09	-0.10
266.652	11.80 ± 0.07	0.10
281.503	12.87 ± 0.07	0.27
298.262	13.18 ± 0.11	-0.50
317.375	14.64 ± 0.11	-0.33
338.976	16.73 ± 0.11	0.20

Table 8.52: Values of the thermal conductivity κ, its standard deviation σ and deviation δ from the smoothing equation at each experimental temperature in CHF_3 from the E-U method.

T/K	$\boldsymbol{\kappa_{\text{E-U}} \pm \sigma / \text{mW} \cdot \text{m}^{-1} \cdot \text{K}^{-1}}$	$\boldsymbol{\delta / \text{mW} \cdot \text{m}^{-1} \cdot \text{K}^{-1}}$
229.946	9.11 ± 0.05	-0.01
240.971	10.48 ± 0.09	0.77
253.095	10.26 ± 0.09	-0.11
266.652	11.19 ± 0.06	0.05
281.503	12.18 ± 0.07	0.19
298.262	12.79 ± 0.10	-0.20
317.375	13.80 ± 0.11	-0.36
338.976	15.73 ± 0.10	0.19

Table 8.53: Values of the thermal conductivity κ, its standard deviation σ and deviation δ from the smoothing equation at each experimental temperature in CHF_3 from the M-E method.

T/K	$\boldsymbol{\kappa_{\text{M-E}} \pm \sigma / \text{mW} \cdot \text{m}^{-1} \cdot \text{K}^{-1}}$	$\boldsymbol{\delta / \text{mW} \cdot \text{m}^{-1} \cdot \text{K}^{-1}}$
229.946	10.06 ± 0.06	-0.01
240.971	11.60 ± 0.10	0.85
253.095	11.39 ± 0.10	-0.13
266.652	12.46 ± 0.07	0.05
281.503	13.62 ± 0.08	0.21
298.262	14.35 ± 0.11	-0.23
317.375	15.56 ± 0.12	-0.40
338.976	17.82 ± 0.12	0.23

Table 8.54: Values of the initial density dependence of the thermal conductivity $(\partial\kappa/\partial\rho)$, its standard deviation σ and deviation δ from the smoothing equation at each experimental temperature in CHF_3 from the S-T method.

$\mathbf{T/K}$	$(\partial\boldsymbol{\kappa}/\partial\boldsymbol{\rho})_{\text{S-T}} \pm\boldsymbol{\sigma}/\mathbf{mW{\cdot}m^2{\cdot}K^{-1}{\cdot}kg^{-1}}$	$\boldsymbol{\delta}/\mathbf{mW{\cdot}m^2{\cdot}K^{-1}{\cdot}kg^{-1}}$
229.946	0.49 ± 0.02	0.06
240.971	0.51 ± 0.04	0.08
253.095	0.44 ± 0.03	0.00
266.652	0.31 ± 0.02	-0.12
281.503	0.29 ± 0.03	-0.14
298.262	0.46 ± 0.04	0.03
317.375	0.53 ± 0.04	0.10
338.976	0.55 ± 0.03	0.12

which has a standard deviation of 0.11 $\text{mW} \cdot \text{m}^2{\cdot}\text{K}^{-1}{\cdot}\text{kg}^{-1}$,

$$(\partial\kappa/\partial\rho)_{\text{E-U}}\,/\text{mW} \cdot \text{m}^2 \cdot \text{K}^{-1} \cdot \text{kg}^{-1} = 0.41, \tag{8.35}$$

which has a standard deviation of 0.10 $\text{mW} \cdot \text{m}^2{\cdot}\text{K}^{-1}{\cdot}\text{kg}^{-1}$, and

$$(\partial\kappa/\partial\rho)_{\text{M-E}}\,/\text{mW} \cdot \text{m}^2 \cdot \text{K}^{-1} \cdot \text{kg}^{-1} = 0.45, \tag{8.36}$$

which has a standard deviation of 0.10 $\text{mW} \cdot \text{m}^2{\cdot}\text{K}^{-1}{\cdot}\text{kg}^{-1}$. These coefficients are to some extent an artifact of the analysis and might be a factor of 10 too high but nevertheless the values given above describe the experimental data. The error is probably due in part to the term for the density dependence of κ and η in the half-width analysis absorbing the contribution from the density dependence of the vibrational relaxation time which was found to be important in other acoustic work[1],[4],[44]. The value at 241 K was again retained and the experimental results, their standard deviations σ and deviations $\delta = (\partial\eta/\partial\rho)_{\text{exp}} - (\partial\eta/\partial\rho)_{\text{calc}}$ from the equations above are given in tables (8.54), (8.55) and (8.56).

The differences between the coefficients in the expressions for the transport properties generated using the three methods of half-width analysis may be used to estimate their associated uncertainties. The general form of the expressions describing the thermal conductivity, shear viscosity and their initial density de-

Table 8.55: Values of the initial density dependence of the thermal conductivity $(\partial\kappa/\partial\rho)$, its standard deviation σ and deviation δ from the smoothing equation at each experimental temperature in CHF_3 from the E-U method.

$\mathbf{T/K}$	$(\partial\boldsymbol{\kappa}/\partial\boldsymbol{\rho})_{\text{E-U}} \pm\boldsymbol{\sigma}/\mathbf{mW{\cdot}m^2{\cdot}K^{-1}{\cdot}kg^{-1}}$	$\boldsymbol{\delta}/\mathbf{mW{\cdot}m^2{\cdot}K^{-1}{\cdot}kg^{-1}}$
229.946	0.51 ± 0.02	0.06
240.971	0.53 ± 0.04	0.08
253.095	0.45 ± 0.04	0.00
266.652	0.32 ± 0.03	-0.13
281.503	0.31 ± 0.03	-0.15
298.262	0.48 ± 0.04	0.03
317.375	0.56 ± 0.04	0.10
338.976	0.59 ± 0.03	0.13

Table 8.56: Values of the initial density dependence of the thermal conductivity $(\partial\kappa/\partial\rho)$, its standard deviation σ and deviation δ from the smoothing equation at each experimental temperature in CHF_3 from the E-U method.

$\mathbf{T/K}$	$(\partial\boldsymbol{\kappa}/\partial\boldsymbol{\rho})_{\text{M-E}} \pm\boldsymbol{\sigma}/\mathbf{mW{\cdot}m^2{\cdot}K^{-1}{\cdot}kg^{-1}}$	$\boldsymbol{\delta}/\mathbf{mW{\cdot}m^2{\cdot}K^{-1}{\cdot}kg^{-1}}$
229.946	0.47 ± 0.02	0.06
240.971	0.49 ± 0.03	0.08
253.095	0.42 ± 0.03	0.00
266.652	0.30 ± 0.02	-0.12
281.503	0.28 ± 0.03	-0.13
298.262	0.44 ± 0.03	0.02
317.375	0.50 ± 0.04	0.09
338.976	0.52 ± 0.03	0.11

pendencies are given below together with the estimated uncertainties in the coefficients.

$$\eta/\mu\mathrm{Pa}\cdot\mathrm{s} = (0.0502 \pm 0.0007)\,T \tag{8.37}$$

$$(\partial\eta/\partial\rho)\,/\mu\mathrm{Pa}\cdot\mathrm{s}\cdot\mathrm{m}^3\cdot\mathrm{kg}^{-1} = 0.49 \pm 0.01 \tag{8.38}$$

$$\kappa/\mathrm{mW}\cdot\mathrm{m}^{-1}\cdot\mathrm{K}^{-1} = (0.0268 \pm 0.0002)\,T + (0.64 \pm 0.09) \times 10^{-4}T^2 \tag{8.39}$$

$$(\partial\kappa/\partial\rho)\,/\mathrm{mW}\cdot\mathrm{m}^2\cdot\mathrm{K}^{-1}\cdot\mathrm{kg}^{-1} = 0.43 \pm 0.02 \tag{8.40}$$

Vibrational Relaxation Times

In contrast to the thermal conductivity and the shear viscosity, the vibrational relaxation time is essentially independent of the method used to analyse the resonance half-widths. The estimates presented here were determined by separating out the different density dependencies of the known loss mechanisms that contribute to the resonance halfwidths and the spread of the results indicates the reliability with which the terms may be resolved. The smoothing equations resulting from the weighted non-linear regression analysis are shown in figure (8.47) together with the result obtained by *Rossing et al.*[45] of 1.373 μs at a density of 1 $\mathrm{kg}\cdot\mathrm{m}^3$. The variation between the methods is about 0.2 % and the good agreement observed with published results for all three experimental systems,in particular with the acoustic measurements of Boyes[1]for the mixture, give confidence in the vibrational relaxation times presented here. The good agreement may also be taken as evidence that there are no unknown loss mechanisms operating in the resonator that result in perturbations to the resonance half-widths with the same density dependence as the vibrational relaxation time. Values of $\tau\rho$ at a density of 1 $\mathrm{kg}\cdot\mathrm{m}^3$ and their associated standard deviations σ are given in tables (8.57), (8.58) and (8.59) for the three methods. The values may be represented over the experimental temperature range by

$$(\tau\rho)_{\text{S-T}}\,/\mu\mathrm{s}\cdot\mathrm{kg}\cdot\mathrm{m}^{-3} = \frac{0.443\times10^3}{T} - \frac{0.58\times10^7}{T^3}, \tag{8.41}$$

$$(\tau\rho)_{\text{E-U}}\,/\mu\mathrm{s}\cdot\mathrm{kg}\cdot\mathrm{m}^{-3} = \frac{0.442\times10^3}{T} - \frac{0.57\times10^7}{T^3}, \tag{8.42}$$

and

$$(\tau\rho)_{\text{M-E}}\,/\mu\mathrm{s}\cdot\mathrm{kg}\cdot\mathrm{m}^{-3} = \frac{0.441\times10^3}{T} - \frac{0.57\times10^7}{T^3}. \tag{8.43}$$

Figure 8.47: Comparison of the vibrational relaxation times $\tau\rho$ of CHF_3 at a density of 1 kg·m^3 determined in this work with published values.

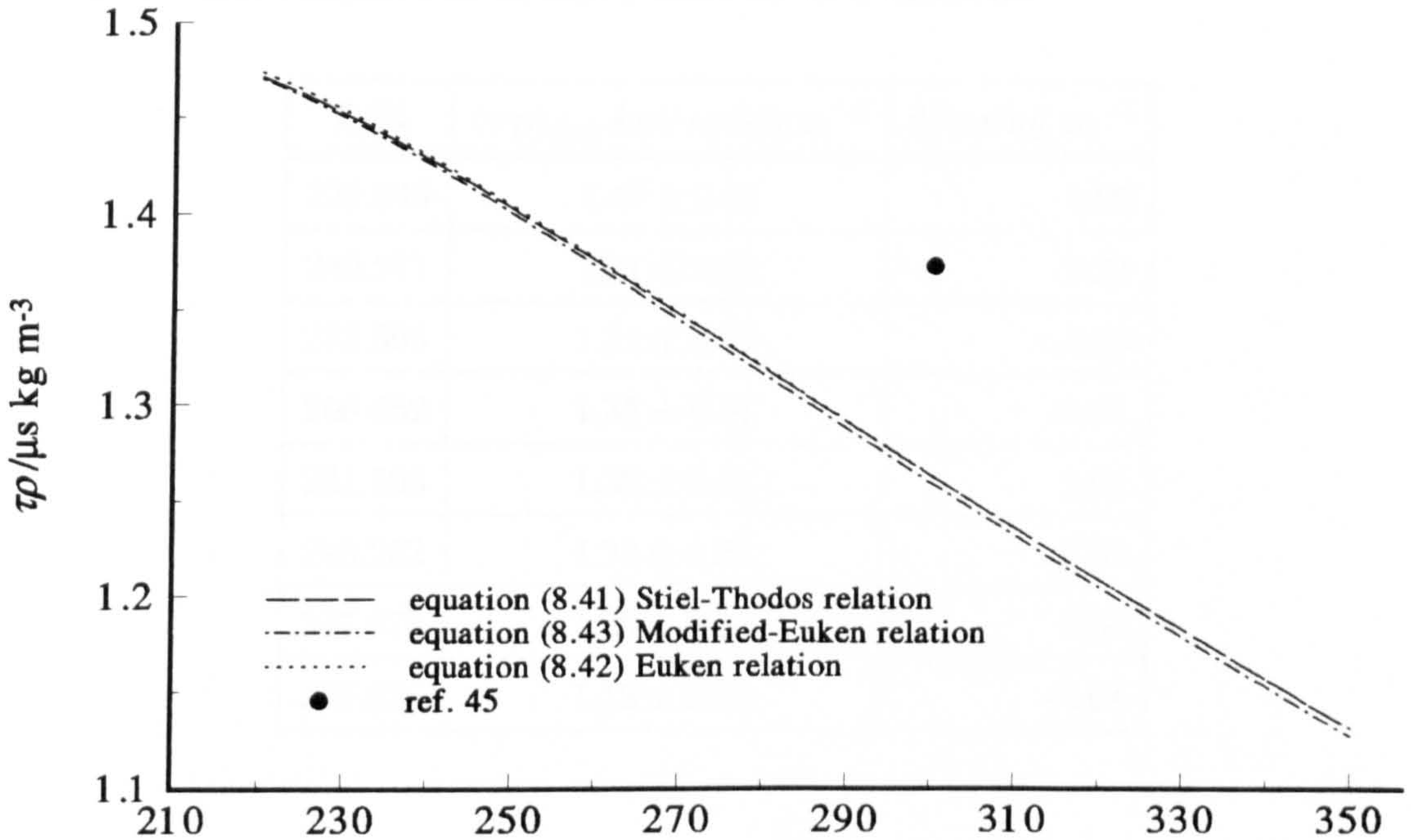

Table 8.57: Values of the vibrational relaxation time ($\tau\rho$) at a density of 1 kg·m^3, its standard deviation σ and deviation δ from the smoothing equation at each experimental temperature in CHF_3 from the S-T method.

T/K	$(\tau\rho)_{\text{S-T}} \pm \sigma$/μs·kg·m^{-3}	δ/μs·kg·m^{-3}
229.946	1.47 ± 0.02	0.02
240.971	1.21 ± 0.02	-0.21
253.095	1.31 ± 0.02	-0.08
266.652	1.34 ± 0.01	-0.01
281.503	1.32 ± 0.01	0.01
298.262	1.30 ± 0.02	0.03
317.375	1.26 ± 0.01	0.04
338.976	1.12 ± 0.01	-0.04

Table 8.58: Values of the vibrational relaxation time ($\tau\rho$) at a density of 1 kg·m^3, its standard deviation σ and deviation δ from the smoothing equation at each experimental temperature in CHF_3 from the E-U method.

T/K	$(\boldsymbol{\tau\rho})_{\text{E-U}} \pm \boldsymbol{\sigma}/\boldsymbol{\mu}$**s·kg·m**$^{-3}$	$\boldsymbol{\delta}/\boldsymbol{\mu}$**s·kg·m**$^{-3}$
229.946	1.48 ± 0.02	0.02
240.971	1.21 ± 0.02	-0.21
253.095	1.31 ± 0.02	-0.08
266.652	1.35 ± 0.01	-0.01
281.503	1.32 ± 0.01	0.01
298.262	1.29 ± 0.02	0.02
317.375	1.26 ± 0.01	0.04
338.976	1.12 ± 0.01	-0.04

Table 8.59: Values of the vibrational relaxation time ($\tau\rho$) at a density of 1 kg·m^3, its standard deviation σ and deviation δ from the smoothing equation at each experimental temperature in CHF_3 from the M-E method.

T/K	$(\boldsymbol{\tau\rho})_{\text{M-E}} \pm \boldsymbol{\sigma}/\boldsymbol{\mu}$**s·kg·m**$^{-3}$	$\boldsymbol{\delta}/\boldsymbol{\mu}$**s·kg·m**$^{-3}$
229.946	1.47 ± 0.02	0.02
240.971	1.21 ± 0.02	-0.21
253.095	1.31 ± 0.02	-0.08
266.652	1.34 ± 0.01	-0.01
281.503	1.32 ± 0.01	0.01
298.262	1.29 ± 0.02	0.03
317.375	1.26 ± 0.01	0.04
338.976	1.12 ± 0.01	-0.03

Figure 8.48: Deviations δ of the vibrational relaxation times $\tau\rho$ of CHF_3 at a density of 1 kg·m^3 extracted using the Stiel-Thodos method of half-width analysis from equation (8.41).

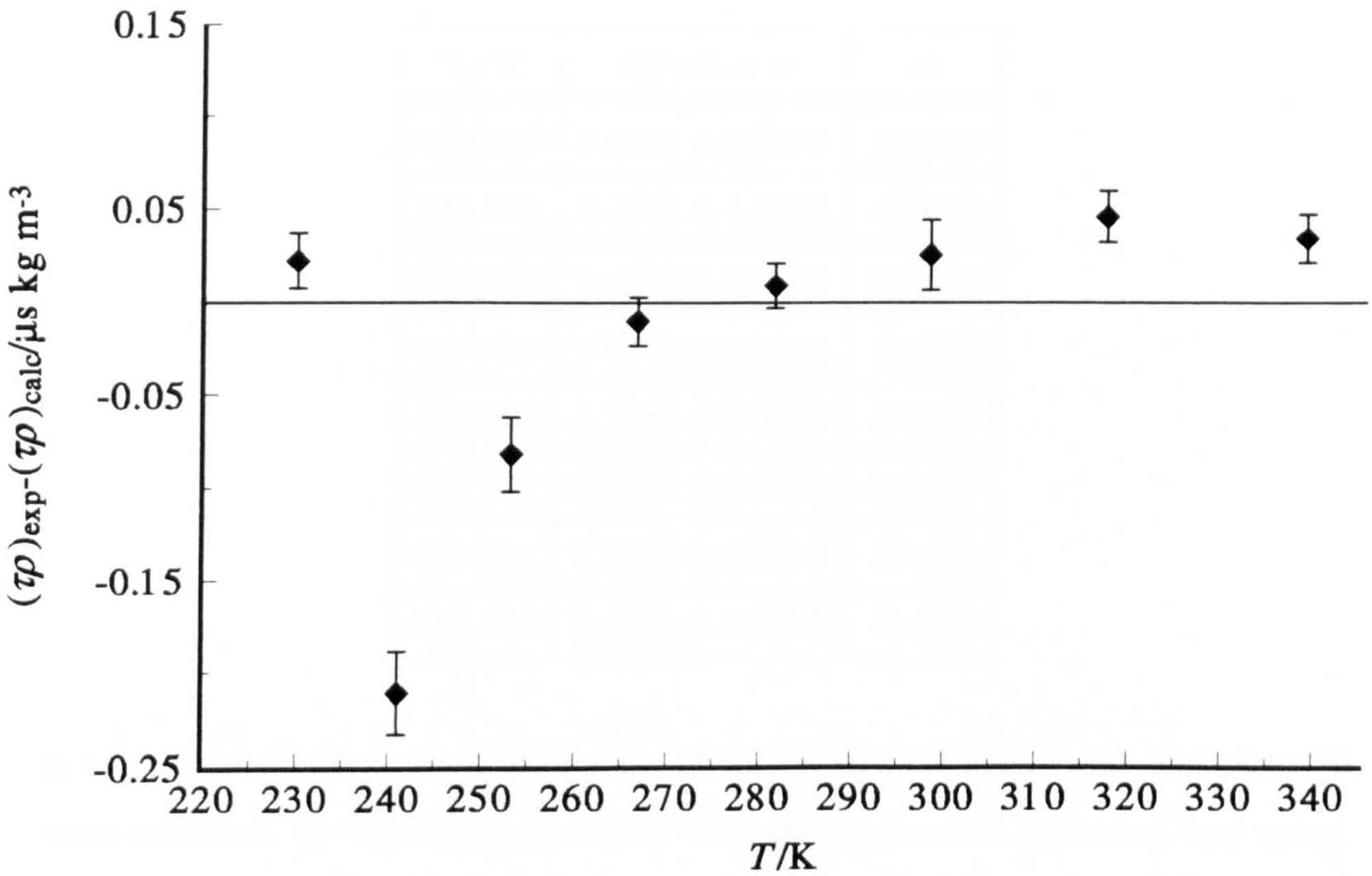

Equations (8.41) to (8.43) all have a standard deviation of 0.10 $\mu s \cdot kg \cdot m^{-3}$. Again using the small differences between the results of the three methods to estimate the uncertainty associated with the coefficients, the vibrational relaxation time in CHF_3 is given by

$$\tau\rho/\mu s \cdot kg \cdot m^{-3} = \frac{(0.442 \pm 0.001) \times 10^3}{T} - \frac{(0.573 \pm 0.007) \times 10^7}{T^3}. \qquad (8.44)$$

The deviations $\delta = (\tau\rho)_{exp} - (\tau\rho)_{calc}$ of the results from equations (8.41) to (8.43) are also listed in tables (8.57), (8.58) and (8.59). The deviations are essentially the same for the three methods of half-width analysis and the deviations for the Steil-Thodos method are illustrated in figure (8.48). The datum at 241 K was again removed from the regression and all the remaining data could be fitted to within a few multiples of their standard deviations.

8.4.4. Results Derived from the Speed of Sound

Values of the perfect gas heat capacity C_p^{pg} and second acoustic virial coefficient β_a were determined by analysis of the speed of sound data along each isotherm

Table 8.60: Perfect-gas heat capacities C_p^{pg} derived from the density and pressure series, estimated standard deviations σ, and deviations Δ from the smoothing equations for CHF_3.

T/K	$\mathbf{C_p^{pg}/R \pm \sigma}$	$\boldsymbol{\Delta}$
229.946	5.2382 ± 0.0008	0.0010
240.971	5.3371 ± 0.0014	-0.0029
253.095	5.4632 ± 0.0005	-0.0012
266.652	5.6177 ± 0.0008	0.0046
281.503	5.7837 ± 0.0008	0.0002
298.262	5.9770 ± 0.0009	-0.0032
317.375	6.2058 ± 0.0006	0.0005
338.976	6.4548 ± 0.0006	0.0000

in terms of a density series. Estimates of the (p, V, T) second virial coefficient B were extracted by combining the data with the square-well potential and using equation (1.15).

Heat Capacity Results

The perfect-gas heat capacities determined from the first terms of the density series representing the speed of sound data at each temperature are given in table (8.60) together with their associated standard deviations σ. The value of the heat capacity was found to be independent of the method used to analyse the half-widths. This indicates that the sum of the corrections to the resonance frequencies made using transport properties derived from the half-width analyses employing the Stiel-Thodos, Euken and Modified-Euken relations were essentially identical. This important conclusion could also be inferred by examining the excess half-widths for each method which never differed by more than a couple of ppm. The values of C_p^{pg} were fit to a function determined using the adaptive regression algorithm which gave

$$C_p^{\mathrm{pg}}/R = 0.01845T - 0.309 \times 10^{-10}T^4 + \frac{0.187 \times 10^3}{T} + \frac{0.75 \times 10^9}{T^4} \qquad (8.45)$$

Figure 8.49: Deviations Δ of the perfect gas heat capacities C_p^{pg} of CHF_3 determined from the density series from equation (8.45).

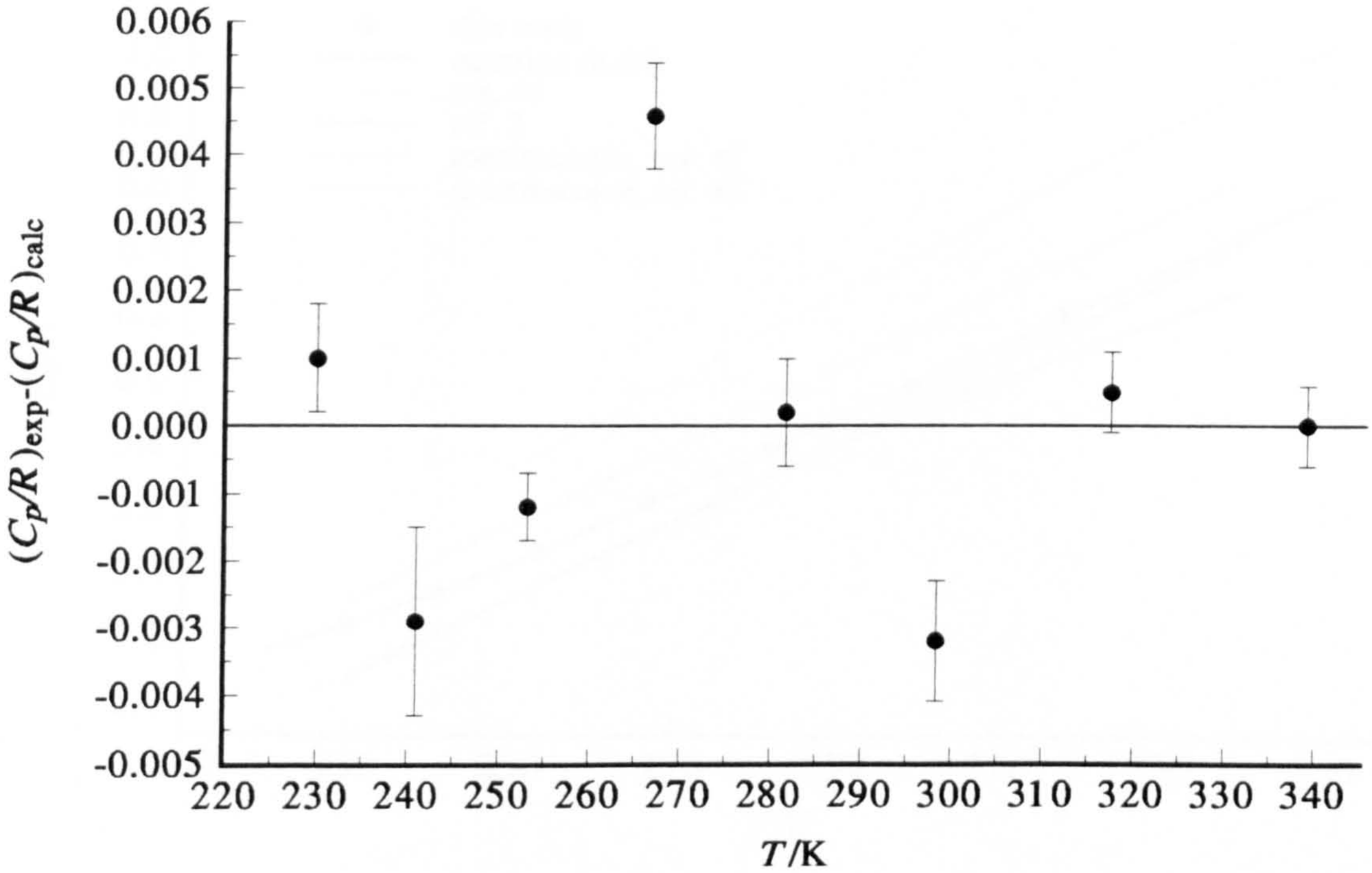

with a standard deviation of 0.004 R. The deviations $\Delta = \left(C_p^{pg}/R\right)_{exp} - \left(C_p^{pg}/R\right)_{calc}$ of the experimental results from equation (8.45) are also given in table (8.60) and are plotted in figure (8.49). With the exception of the datum at 267 K, the deviations are always only a few multiples of the standard deviations, but this point was retained in the regression as its removal did not significantly reduce the overall standard deviation of the fit. Comparison with published data is by means of figure (8.50) which shows the experimentally determined values, equation (8.45), results by Glockler *et al.*[46], heat capacities calculated from spectroscopic information[47],[48] and from an experimental correlation[3]. The correlation based on experimental data was found in reference [3] but no indication of the accuracy, source material or temperature range over which the expression is valid was given. This correlation agrees very closely with the results calculated using the vibrational frequencies of Bernstein *et al.*[48] at temperatures below 280 K. These spectroscopic values converge with the results of this work as the temperature increases to 340 K whereas the heat capacities calculated from the vibrational frequencies given by Plyler *et al.*[47] diverge from the data reported here as the temperature increases. The two spectroscopic calculations show a systematic de-

Figure 8.50: Comparison of the perfect gas heat capacities C_p^{pg} of CHF_3 determined in this work with published values.

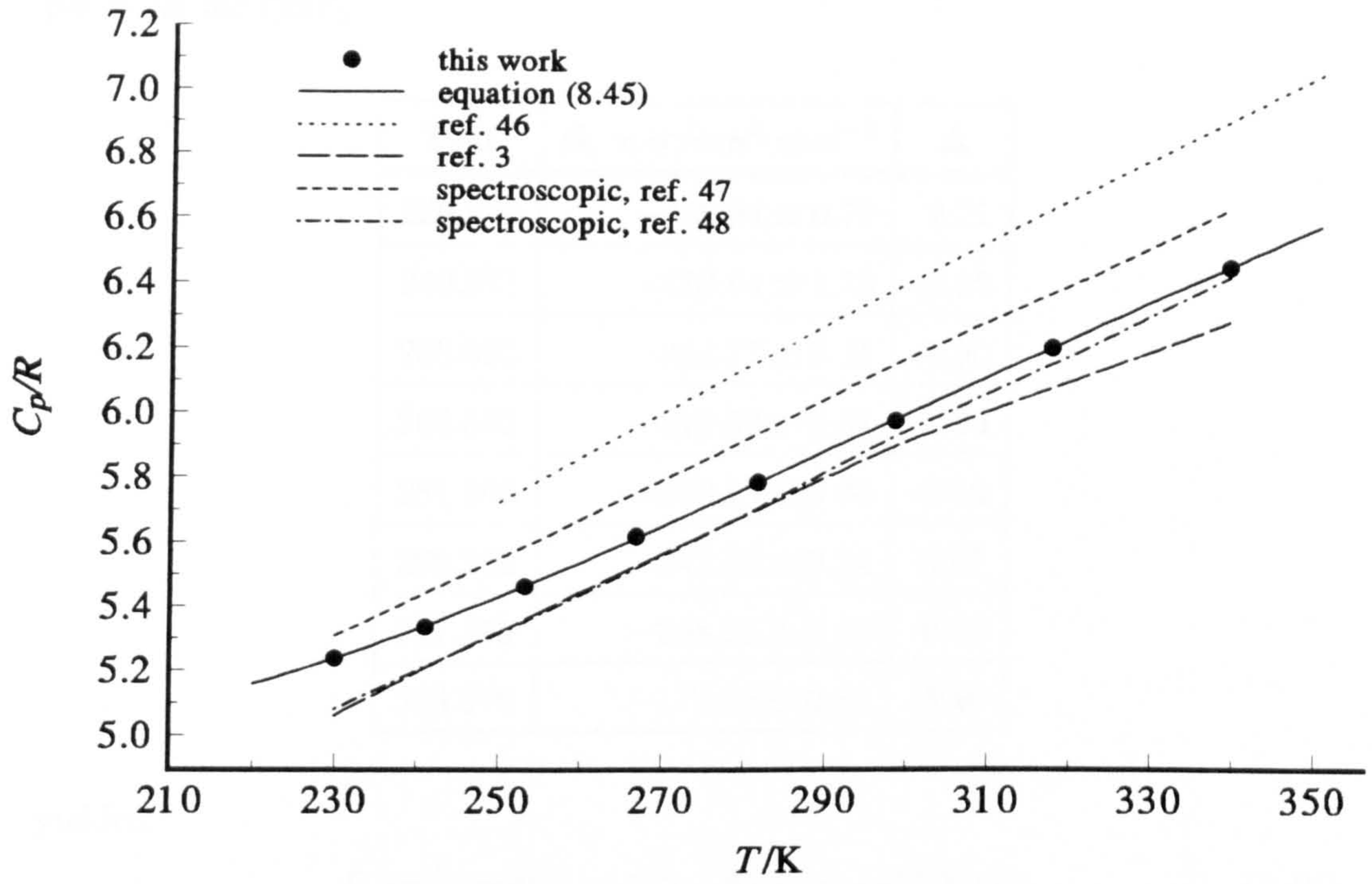

viation from one another of about 0.2 R and equation (8.45) always lies between these bounds. The results of Glockler *et al.*[46] were calculated using a semi-empirical method based on additive contributions of the bonds and angles in the molecule. These results are systematically high and appear to be significantly in error. In the absence of recent calorimetric data equation (8.45) represents the most accurate method of calculating the heat capacity of CHF_3 between 230 and 340 K published to date.

Second Virial Coefficients of CHF_3

The second acoustic virial coefficients determined from fitting the speed of sound results to a three term density series at each of the eight experimental temperatures are given in table (8.61) together with their standard deviations σ. The extraction of (p, V, T) second virial coefficients was again by means of regression analysis using the square-well potential. The experimental determinations of C_p^{pg} were used in conjunction with the acoustic second virial coefficients β_a. Weighted non-linear analysis of the experimental β_a with γ^{pg} and the square-well function

Table 8.61: Values of the second acoustic virial coefficient β_a from the density series, estimated standard deviations σ, and deviations Δ from the square well potential for CHF_3.

T/K	$\beta_a \pm \sigma$/cm^3·mol^{-1}	**Δ**
229.946	-458.94 ± 0.72	2.21
240.971	-419.64 ± 1.13	-9.95
253.095	-364.77 ± 0.41	-1.90
266.652	-319.33 ± 0.51	0.23
281.503	-280.13 ± 0.48	-0.09
298.262	-242.62 ± 0.24	0.57
317.375	-208.31 ± 0.28	0.35
338.976	-177.05 ± 0.24	-0.46

yielded

$$B/\mathrm{cm}^3 \cdot \mathrm{mol}^{-1} = 123 - 65.1 \exp\left(470\ \mathrm{K}/T\right) \tag{8.46}$$

which fit the results from the density series with a weighted standard deviation of 1.0 cm^3·mol^{-1}. In figure (8.51) the experimental β_a are shown as deviations $\Delta = (\beta_a)_{exp} - (\beta_a)_{calc}$ from equations (8.46) with equation (1.15). These deviations Δ are also given in table (8.61). The datum at 241 K was removed from the regression as it could not be accommodated in the fit, altered the values of B significantly and its removal led to a significant reduction in the overall standard deviation of the fit. The values of B extracted from this analysis are likely to be more accurate than the results for the other two experimental systems as three term density series were required to describe the speed of sound data leading to smaller systematic errors in β_a due to truncation of the series.

Figure (8.52) shows the variation of the (p, V, T) second virial coefficient B with temperature and gives all the literature data[49]-[54]. Figure (8.53) shows the published results as deviations $\Delta B = B - B_{\text{equation (8.46)}}$ from equation (8.46). Above 250 K equation (8.46) is in very good agreement with all the literature data except that of Hajjar *et al.*[51] which shows systematic deviations of 40 to 80 cm^3·mol^{-1}. In particular there is excellent agreement with the high temperature data of Sutter *et al.*[52] of better 1 cm^3·mol^{-1} even at 405 K which is 60 K above

Figure 8.51: Deviations Δ of the second acoustic virial coefficients β_a of CHF_3 determined from the density series from equation (8.46) with equation (1.15).

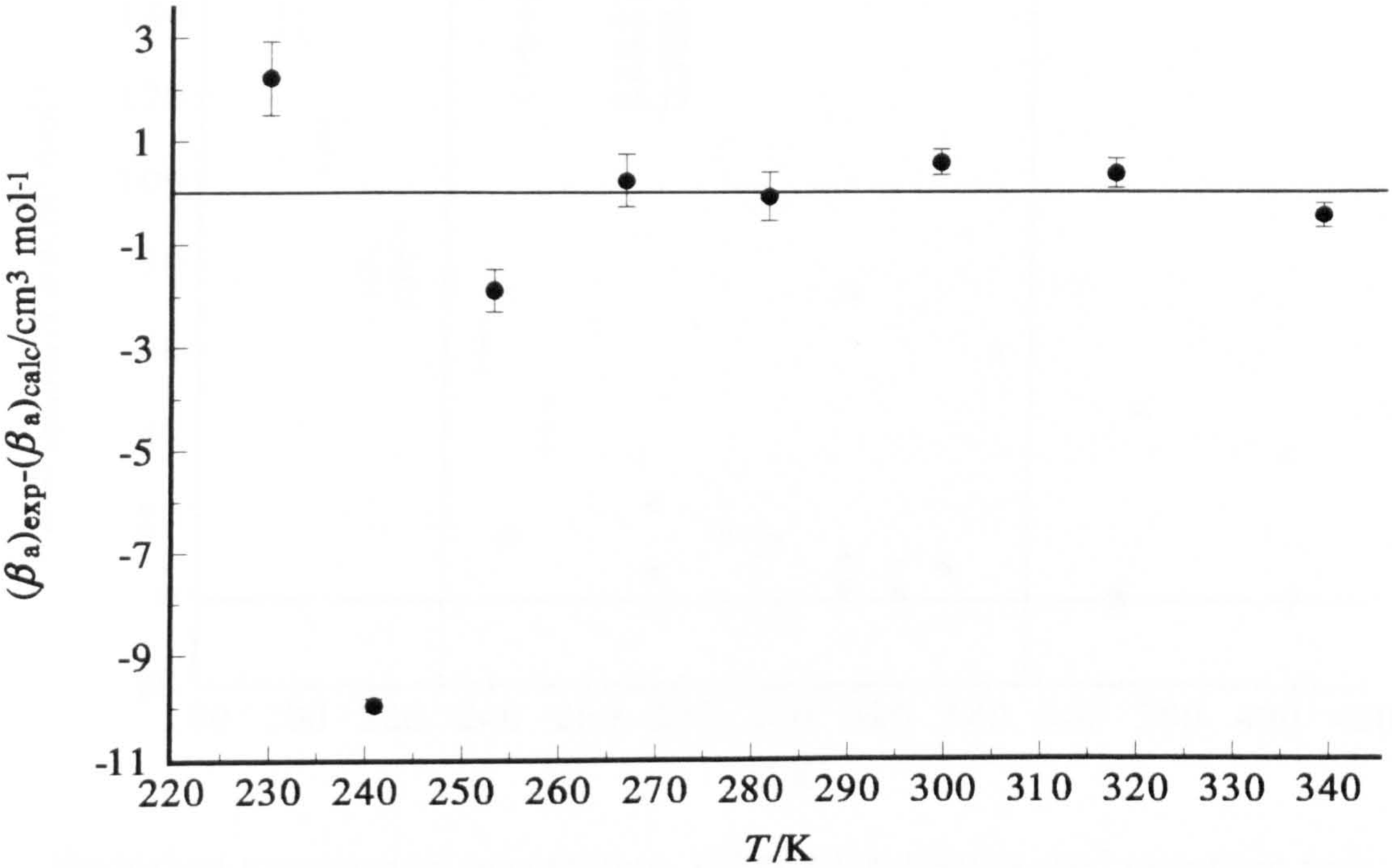

Figure 8.52: Comparison of the second virial coefficients B of CHF_3 determined from the density series with published results.

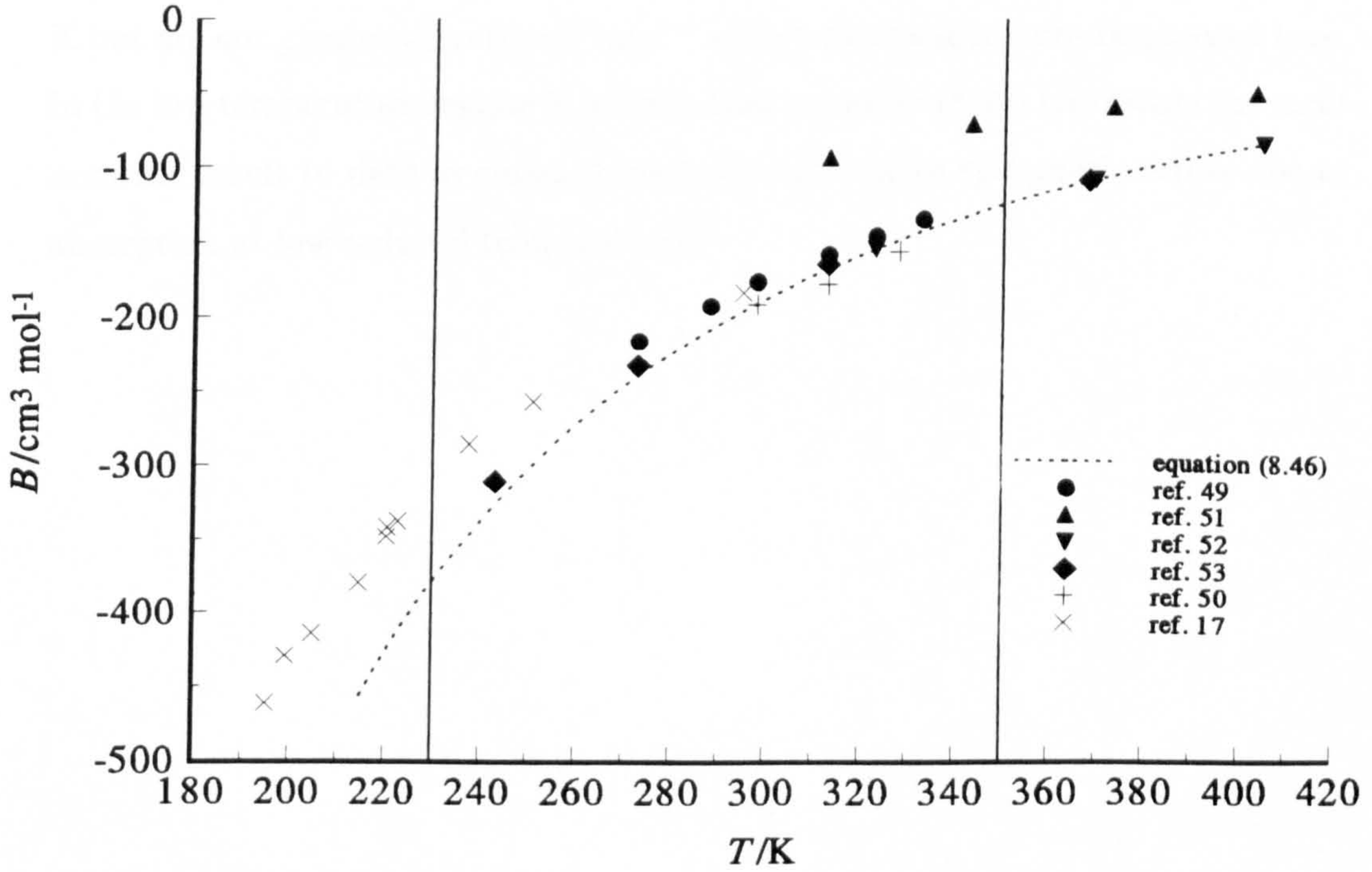

Figure 8.53: Deviations ΔB of the second virial coefficients of CHF_3 from equation (8.46).

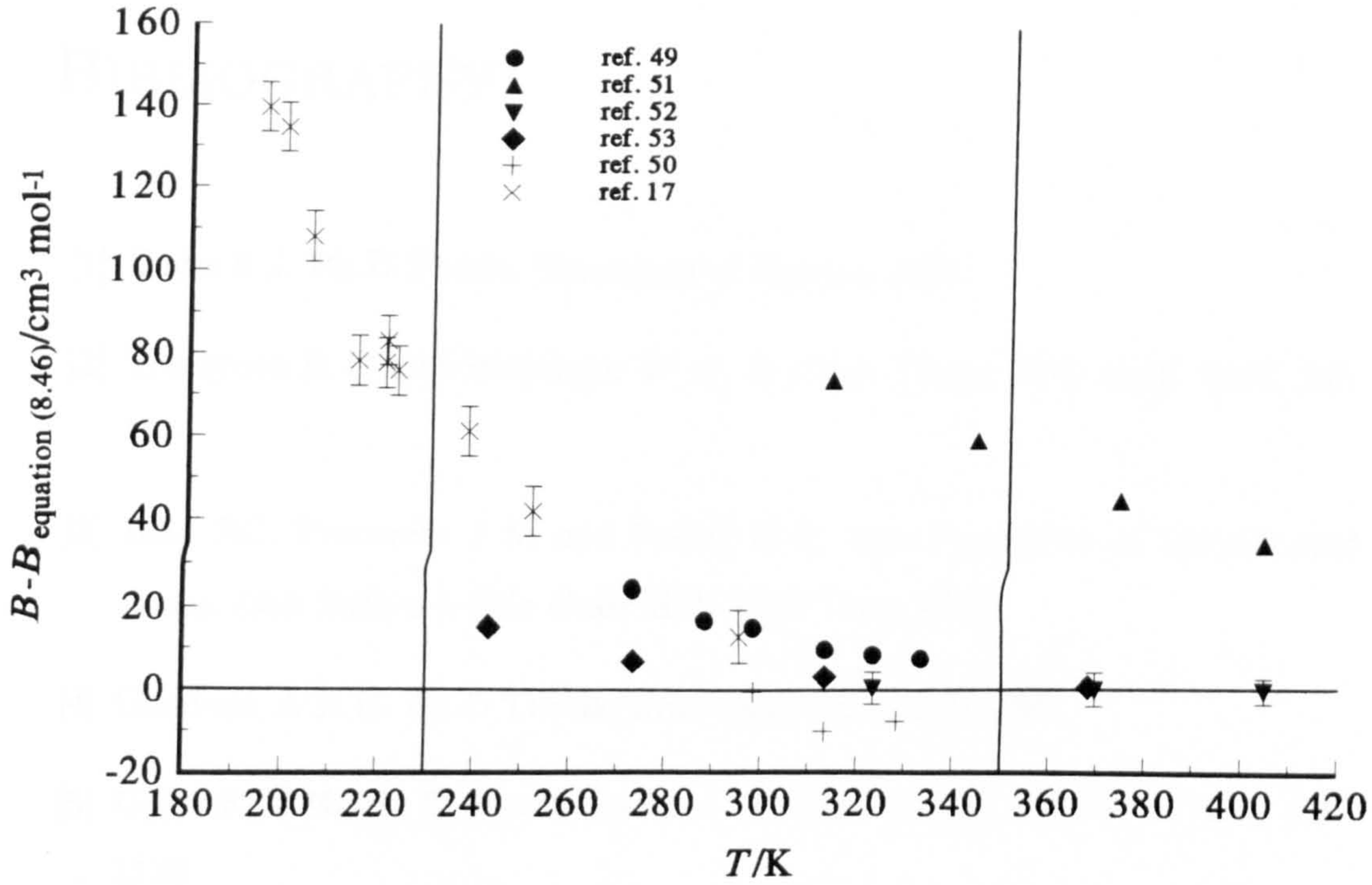

the highest experimental temperature. Below 250 K there is good agreement with the result of Lange *et al.*[53] which is less negative by about 15 $cm^3 \cdot mol^{-1}$, but the lower temperature results of Schramm *et al.*[17] quoted by Dymond and Smith show systematic deviations from this work that increase to 140 $cm^3 \cdot mol^{-1}$ at 200 K but are not greater than 60 $cm^3 \cdot mol^{-1}$ within the temperature range used here. In the low temperature regime it is likely that equation (8.46) represents the most accurate result to date as classical methods suffer large systematic errors due to absorption at low reduced temperatures.

BIBLIOGRAPHY

[1] Boyes S J. Ph.D Thesis, University of London 1988.

[2] Trengrove R D and Wakeham W A. *J. Phys. Chem. Ref. Data.* 1987, **16,** 175.

[3] Reid RC, Prausnitz J M and Poling B E. *The Properties of Liquids and Gases. (4th Edition).* (Mc Graw Hill: New York, 1986).

[4] Goodwin A R H. Ph.D Thesis, University of London 1988.

[5] Uribe F J, Mason E A and Kestin J. *J. Phys. Chem. Ref. Data.* 1990, **19,** 1123.

[6] Hermans L J F, Koks J M, Hengeveld A F and Knaap H F P. *Physica.* 1970, **50**, 410.

[7] Plank R. *Kaltetechnik.* 1958, **10**, 30.

[8] Tanaka Y, Noguchi M, Kubota H and Makita T. *J. Chem. Eng. Japan.* 1979, **12**, 171.

[9] Bousheri A, Bzowski J, Kestin J and Mason E A. *J. Phys. Chem. Ref. Data.* 1987, **16,** 445.

[10] Hoogland J H B, Van Den Berg H R and Trappeniers N J. *Physica A.* 1985, **134**, 169.

[11] Strehlow T and Vogel E. *Physica A.* 1989, **161**, 101.

[12] Lambert J D, Parks-Smith D G and Stretton J L. *Proc. R. Soc.* 1964, **A282**, 380.

[13] Lambert J D. *Vibrational and Rotational Relaxation in Gases.* (Clarendon Press: Oxford, 1977).

[14] Gaunt J. *Trans. Faraday. Soc.* 1953, **49**, 1122.

[15] Yost D M, Steffens C C and Gross S T. *J. Chem. Phys.* 1934, **2**, 311.

[16] Herzberg G. *Infrared and Raman Specta.* (Van Nostrand Reinhold: New York, 1945).

[17] Dymond J H and Smith E B. *The Virial Coefficients of Pure Gases and Mixtures.* (Clarendon Press: Oxford, 1980).

[18] MacCormack K E and Shneider W G. *J. Chem. Phys.* 1951, **19**, 845.

[19] Hamann S D, McManamey W J and Pearse J F. *Trans. Faraday. Soc.* 1953, **49**, 351.

[20] Clegg H P, Rowlinson J S and Sutton J R. *Trans. Faraday. Soc.* 1955, **51**, 1327.

[21] Mears W H, Rosenthal E and Sinka J V. *J. Phys. Chem.* 1969, **73,** 2254.

[22] Bellm J, Reineke W, Schäffer K and Schramm B. *Ber. Bunsenges. Phys. Chem.* 1974, **78**, 282.

[23] Sigmund P M, Silberberg I H and McKetta J J. *J. Chem. Eng. Data.* 1972, **17**, 168.

[24] Hahn R, Schäffer K and Schramm B. *Ber. Bunsenges. Phys. Chem.* 1974, **78**, 287.

[25] Hosticka C and Bose T K. *J. Chem. Phys.* 1974, **60**, 1318.

[26] Santafe J, Urieta J S and Gutierrez C. *Chem. Phys.* 1976, **18**, 341.

[27] Hajjar R F and MacWood G E. *J. Chem. Eng. Data.* 1970, **15**, 3.

[28] Nelson R D and Cole R H. *J. Chem. Phys.* 1971, **54**, 4033.

[29] Wilke C R. *J. Chem. Phys.* 1950, **18**, 517.

[30] De Rocco A G and Halford J O. *J. Chem. Phys.* 1958, **28**, 1152.

[31] Mostert R, van den Berg H R, van der Gulik P S and Sengers J V. *J. Chem. Phys.* 1990, **92**, 5454.

[32] Mason E A and Saxena S C. *Phys. Fluids.* 1958, **1**, 361.

[33] Johnston H L and Grilly E R. *J. Chem. Phys.* 1946, **14**, 233.

[34] Peek D J. M.Sc Thesis, University of London 1992.

[35] McDowell R S and Kruse F H. *J. Chem. Eng. Data.* 1963, **8**, 547.

[36] Gunn R D. M.S. Thesis, University of California 1958.

[37] Mason D and Eakin B E. *J. Chem. Eng. Data.* 1961, **6**, 499.

[38] Hoover A E, Nagata I, Leland T W and Kobayashi R. *J. Chem. Phys.* 1968, **48**, 2633.

[39] Dantzler E M, Knobler C M and Windsor M L. *J. Phys. Chem.* 1968, **72**, 676.

[40] Wormald C J, Lewis E J and Hutchings D J. *J. Chem. Thermodyn.* 1979, **11,** 1.

[41] Dunlop P J. *J. Chem. Phys.* 1994, **100**, 3149.

[42] Thijsse B J, Denissen W A P, Hermans L J F, Knaap H F P and Beenakker J J M. *Physica A.* 1979, **97**, 467.

[43] Tommasini F, Levi A C, Scoles G, De Groot J J, Van Den Broeke J W, Van Den Meijdenberg C J N and Beenakker J J M. *Physica.* 1970, **49**, 1970.

[44] Trusler J P M. Ph.D Thesis, University of London 1984.

[45] Rossing T D and Legvold S. *J. Chem. Phys.* 1955, **23**, 1118.

[46] Glockler G and Edgell W F. *J. Chem. Phys.* 1941, **9**, 527.

[47] Plyler E K and Benedict W S. *J. Res. Nat. Bur. Stand.* 1951, **47,** 202.

[48] Bernstein H J and Herzberg G. *J. Chem. Phys.* 1948, **16**, 30.

[49] Dymond J H and Smith E B. *Trans. Faraday. Soc.* 1964, **60**, 1378.

[50] Sutter H and Cole R H. *J. Chem. Phys.* 1967, **46**, 2014.

[51] Hajjar R F and MacWood G E. *J. Chem. Eng. Data.* 1970, **15**, 3.

[52] Sutter H and Cole R H. *J. Chem. Phys.* 1970, **52**, 132.

[53] Lange H B (Jr) and Stein F P. *J. Chem. Eng. Data.* 1970, **15**, 56.

[54] Haworth W S and Sutton L E. *Trans. Faraday. Soc.* 1971, **67**, 2907.

9. CONCLUDING REMARKS

Measurements in the novel annular resonator have shown that it is possible to measure the speed of sound u over the temperature range 230 to 340 K, at pressures between 10 and 1000 kPa with a fractional precision of 20 ppm for gases which show severe dispersion. Low pressure speed of sound measurements are important because perfect gas heat capacities C_p^{pg} are determined from the limit of u^2 as the density ρ tends to zero and second acoustic virial coefficients β_{a} from the limiting slope of the speed of sound measurements $(du^2/d\rho)$ as $\rho \to 0$. The annular resonator described in this work allows speed of sound measurements to be carried out in gases with relatively long vibrational relaxation times τ_{vib} at pressures a factor of 10 lower than would be possible for a practical spherical resonator. Typically an accuracy of 0.1 % was achieved for the second virial coefficients B determined from the experimental γ^{pg} and β_{a} together with the square-well potential. This compares favourably with classical (p, V, T) measurements and the expressions obtained for B agree with published results even when extrapolated to well above the experimental temperature range. At low temperatures the estimates of B published here represent the most accurate measurements to date for these gases because, unlike classical methods they do not suffer from systematic errors due to gas adsorption. A precision of 0.01 % was typically achieved for the heat capacities determined in this work. The measurements agreed favourably with the estimates calculated from the vibrational frequencies but, due to a lack of recent calorimetric results, a more rigorous comparison could not be made.

Over the whole range of temperatures and pressures at least three azimuthal modes were used to determine $\langle u/b \rangle$ at a given state point. At pressures below 100 kPa more modes were used in the determination of $\langle u/b \rangle$. The limited number of low frequency modes retained at the highest pressures was due to the influence of shell motion. For the gases under study it was unfortunate that the shell resonance overlapped the lower frequency azimuthal modes which the apparatus was

specifically designed to exploit. This problem was overcome by the use of higher order modes but could not have been avoided because the modes of motion of an annular shell were not known. The problem was most severe for sulfur hexafluoride due to the lower gas resonance frequencies and in consequence the data above 110 kPa was rejected in the final analysis. For the methane-ethane mixture, the shell resonance caused smaller perturbations to the data but there was a loss of accuracy at low pressure due to the relatively large transport coefficients causing the modes to have large half-widths. In addition, fractionation of the mixture as the pressure was reduced caused further loss of precision but the estimated mole fraction of ethane present at the end of the measurements varied less in this work than for previous acoustic studies on this system[1],[2]. The measurements in trifluoromethane were considerably better due to the high pressure measurements being affected only slightly by the shell resonance as for the mixture, but the precision at low pressures was not compromised to the same extent by large resonance half-widths. The greater curvature observed in the measurements for CHF_3 further increased the precision of the results by reducing the systematic errors due to truncation of the virial series. Adverse effects due to the coupling of gas and shell motion could be reduced by the use of different materials for the resonator. An obvious choice would be stainless steel which is much less elastic than aluminium. However, it would not be possible to achieve the same level of temperature control because the lower thermal conductivity would cause larger temperature gradients and the time required to bring the system back to the set-point temperature after the pressure was reduced along an isotherm would be greater due to the higher heat capacity.

One of the limitations on the precision of the results generated in this work was the accuracy to which the geometry of the resonator was known. The geometry of the resonator under vacuum as a function of temperature could be determined with greater precision using dimensional microwave resonance techniques providing that suitable microwave antennae could be designed which would themselves not cause significant perturbations to the cavity geometry. The dependence of the microwave resonance frequencies on the geometry of the cavity are available in the literature[3] and the probable fractional accuracy of such measurements would be of the order of 1 in 10^8. The extension of the theory to enable the technique

to be applied with the cavity filled with gas in order to investigate the response of the resonator to pressurisation was carried out, but unfortunately no time was available for the validation of this work.

Novel features in the design of the resonator included the use of a model of the thermal environment of the resonator and the use of a digital computer and a programmable power supply to provide a flexible temperature control algorithm. In addition, the design of transducer inserts enabled the optimum performance to be achieved without the need for dismantling the transducer and the design only requires one seal reducing the problems associated with pressure leaks. As well as the extension of the acoustic theory to cover the annular geometry, a new iterative method was developed for the analysis of the results which does not rely on equation of state or transport property data being available in the literature. In addition, this method provides limiting values as $\rho \rightarrow 0$ of the viscosity η and thermal conductivity κ which have an accuracy of approximately 5 %. The accuracy of the transport properties could be increased by a different choice of resonance modes that would allow the shear and thermal losses occurring at the walls of the resonator to be resolved. This would eliminate the requirement for expressions such as the Euken relation to reduce the number of variables in the analysis. Analysis of the resonance half-widths also provides estimates of the vibrational relaxation time as $\tau\rho$. For the results published here the precision varied between 1 and 15 % depending on the magnitude of $\tau\rho$. Although it is beyond the scope of this work analysis of such data may provide valuable information on intramolecular dynamics and intermolecular interactions.

In conclusion, this work again proves the validity of using the resonance technique to provide high quality acoustic measurements from which heat capacity and equation of state data for gases may be derived. The acoustic theory was extended to cover the annular geometry and the flexibility for the optimisation of the technique to suit particular applications by varying the resonator geometry was illustrated. Here, the apparatus was optimised for acoustic measurements in relaxing gases at low pressures over the temperature range 230 to 340 K. In particular this work highlights the importance of cavity resonance measurements in determining the transport properties of gases. Although the resonator constructed for this work was not ideal for measurements of vibrational relaxation

time, shear viscosity and thermal conductivity, the consistent quality of the data prove the potential of this approach.

Bibliography

[1] Boyes S J. Ph.D Thesis, University of London 1988.

[2] Peek D J. M.Sc Thesis, University of London 1992.

[3] Waldron R A. *Theory of Guided Electromagnetic Waves.* (Van Nostrand-Reinhold: New York, 1969).